AN INVESTIGATION OF THE MAGNETIC FIELD STRUCTURE OF FLARING SOLAR ACTIVE REGIONS USING GLOBAL MAGNETIC FIELD MODELS AND AUTOMATED TECHNIQUES

Teri Love

A Thesis Submitted for the Degree of PhD
at the
University of St Andrews

2022

DOI: https://doi.org/10.17630/sta/511
https://hdl.handle.net/10023/27806

An Investigation of the Magnetic Field Structure of Flaring Solar Active Regions Using Global Magnetic Field Models and Automated Techniques

Teri Love

University of
St Andrews

This thesis is submitted in partial fulfilment for the degree of
Doctor of Philosophy (PhD)
at the University of St Andrews

October 2021

Abstract

In this thesis we explore methods for analysing flaring active regions, in particular studying X-class flares. We use global magnetic field models and machine learning techniques to carry out this analysis.

Using both potential field source surface (PFSS) models and magnetohydrostatic (MHS) models, the global magnetic skeletons for dates where X-class flares occurred are created. This allows the investigation of topological features found around flaring active regions. The flares analysed all have observable signatures found in Atmospheric Imaging Assembly data (onboard the Solar Dynamics Observatory), in the form of solar flare ribbons which can be mapped by eye to the footpoints of the separatrix structures located in the active regions.

Additionally, we consider techniques for identifying and locating the solar flare ribbons observed. The first technique utilises a convolutional neural network trained using images of M and C-class flares to allow the detection and classification of the types of flare ribbons observed. This includes two-ribbon, compact and limb flares, as well as quiet sun images. After training the network and identifiying the flare ribbons in the data, we present an edge detection method which identifies the edges of the flare ribbons, making it easier to compare with the topological features previously found in the global field models. To find the best edge, two methods are presented which correct saturated pixels in the flare ribbon data. Afterwards the corrected images are passed into the edge detector which returns the ribbon edges, which are subsequently compared to the topological features previously found by calculating the Hausdorff and modified Hausdorff distances.

Overall these methods could be put into an automated pipeline which would identify solar flare ribbons in the observations using a CNN, then subsequently creating 3D magnetic field models to investigate the toplogy around the flare. With the final step taking both the observational and modelled data to be processed by the edge detection method and subsequently outputting a metric which identifies whether they are related. Note however this pipeline was not created in this thesis.

Candidate's declaration

I, Teri Love, do hereby certify that this thesis, submitted for the degree of PhD, which is approximately 45,000 words in length, has been written by me, and that it is the record of work carried out by me, or principally by myself in collaboration with others as acknowledged, and that it has not been submitted in any previous application for any degree. I confirm that any appendices included in my thesis contain only material permitted by the 'Assessment of Postgraduate Research Students' policy.

I was admitted as a research student at the University of St Andrews in September 2017.

I received funding from an organisation or institution and have acknowledged the funders in the full text of my thesis.

Date: 02 October 2021 Signature of candidate:

Supervisor's declaration

I hereby certify that the candidate has fulfilled the conditions of the Resolution and Regulations appropriate for the degree of PhD in the University of St Andrews and that the candidate is qualified to submit this thesis in application for that degree. I confirm that any appendices included in the thesis contain only material permitted by the 'Assessment of Postgraduate Research Students' policy.

Date: 02 October 2021 Signature of supervisor:

Permission for publication

In submitting this thesis to the University of St Andrews we understand that we are giving permission for it to be made available for use in accordance with the regulations of the University Library for the time being in force, subject to any copyright vested in the work not being affected thereby. We also understand, unless exempt by an award of an embargo as requested below, that the title and the abstract will be published, and that a copy of the work may be made and supplied to any bona fide library or research worker, that this thesis will be electronically accessible for personal or research use and that the library has the right to migrate this thesis into new electronic forms as required to ensure continued access to the thesis.

I, Teri Love, confirm that my thesis does not contain any third-party material that requires copyright clearance.

The following is an agreed request by candidate and supervisor regarding the publication of this thesis:

Printed copy
No embargo on print copy.

Electric copy
No embargo on electronic copy.

Date: 02 October 2021 Signature of candidate:

Date: 02 October 2021 Signature of supervisor:

Underpinning Research Data or Digital Outputs

Candidate's declaration

I, Teri Love, understand that by declaring that I have original research data or digital outputs, I should make every effort in meeting the University's and research funders' requirements on the deposit and sharing of research data or research digital outputs.

Date: 02 October 2021 Signature of candidate:

Permission for publication of underpinning research data or digital outputs

We understand that for any original research data or digital outputs which are deposited, we are giving permission for them to be made available for use in accordance with the requirements of the University and research funders, for the time being in force. We also understand that the title and the description will be published, and that the underpinning research data or digital outputs will be electronically accessible for use in accordance with the license specified at the point of deposit, unless exempt by award of an embargo as requested below.

The following is an agreed request by candidate and supervisor regarding the publication of underpinning research data or digital outputs:

No embargo on underpinning research data or digital outputs.

Date: 02 October 2021 Signature of candidate:

Date: 02 October 2021 Signature of supervisor:

Acknowledgements

First of all, I have to thank both Clare and Thomas. I have really enjoyed working with both of them on my PhD for the past four years, and I'm pretty sure they will be glad when they don't have to listen to me talk about everything and anything apart from my PhD work!

Secondly, thank you to my office mates who have had to listen to my incessant chatting for the past four years (I'm sure some of them were glad when we had to work from home - I'm looking at you Alex and Hendrik). In particular I'd like to thank Lianne who sent me countless memes to keep me going with writing - I'll miss our morning catch-up chats!

Thank you to my family for supporting me during my PhD, in particular thank you to my parents and to my sisters Chloe and Jodie and my brother Jordan. For mum putting up with me using her as a sounding board for ideas even when she had no idea what I was talking about, to Dad for always giving good advice without judgement, to Jordan for always asking ”who cares?” and finally to Chloe and Jodie; my triplets, best friends and sisters for always being there for me. I also have to thank my grandparents for all the encouragement and support they have given.

Finally, I suppose I should thank the cats for disturbing EVERY teams meeting, walking over my keyboard all the time and making as much noise as possible while I've been working from home.

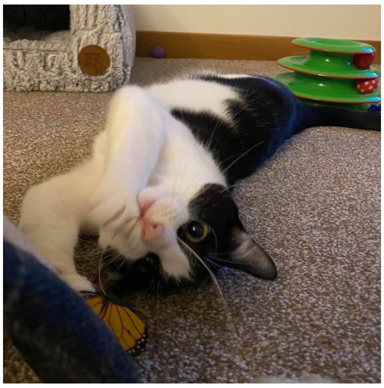

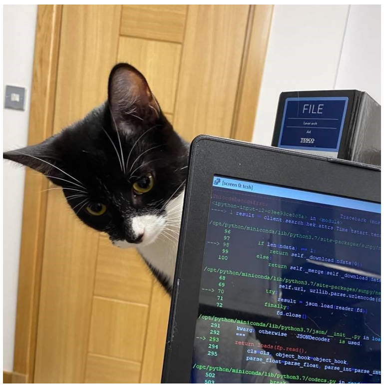

Contents

Chapter 1

Introduction

The Sun is the star at the centre of our solar system at a distance of 1.496×10^8 km (1 AU) from Earth. It is made up of plasma, primarily consisting of electrons, hydrogen and helium ions. The solar mass, $M_\odot = 1.988 \times 10^{30}$kg, contributes to approximately 99% of all mass in our solar system and is almost $333,000$ times greater than the mass of Earth. The solar radius is $R_\odot = 6.957 \times 10^8$m = 695.7Mm, approximately 109 times that of the Earth.

The lowest temperatures typically occur at the solar surface, also known as the photosphere, where temperatures are approximately 5000K, however at the Sun's core temperatures of over 1.5×10^7K occur. The charged particles in the plasma naturally create magnetic and electric fields, which subsequently affect how the particles move. This creates a cause and effect process for the dynamics of the plasma on the Sun. The Sun's magnetic field originates from what is known as the solar dynamo, where an electrically conducting fluid and plasma flows generate a magnetic field. The Sun's magnetic field plays a determining role in the dynamical processes we observe on the Sun and hence understanding them is important.

1.1 Structure of the Sun

The layers of the Sun, shown in Figure 1.1, can be split into two main groups: the solar interior and the solar atmosphere. This thesis concentrates mainly on solar phenomena occurring in the Sun's atmosphere, however the solar interior is briefly described below.

The solar interior consist of three layers; the core, the radiative zone and the convective zone. The previously mentioned high temperatures found in the Sun's core causes nuclear fusion of hydrogen to helium to occur whilst releasing energy in the process.

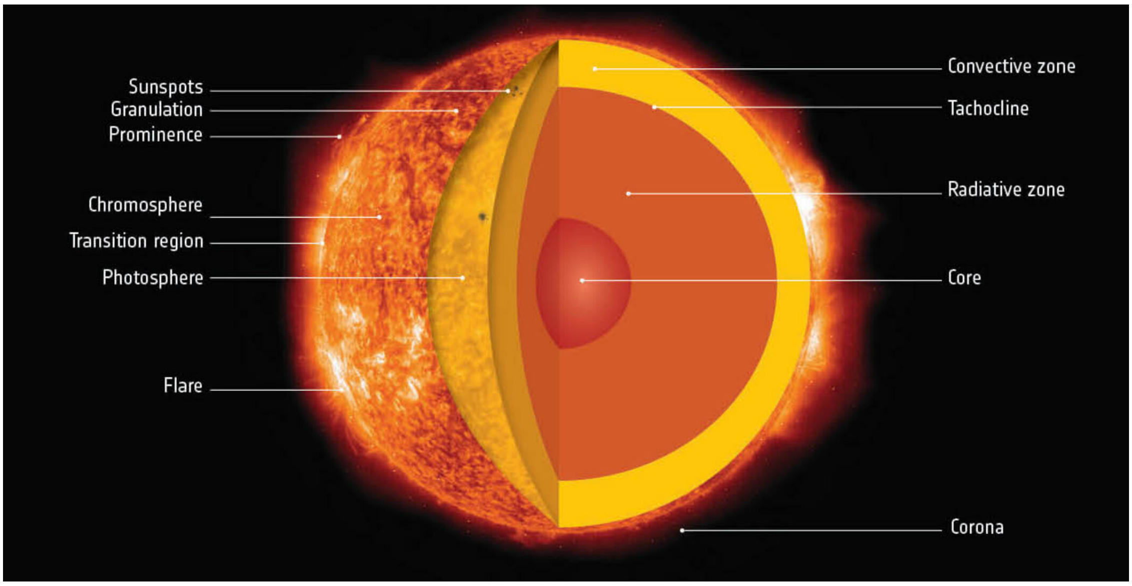

Figure 1.1: Structure of the Sun. The solar interior includes the core, radiative zone, tachocline and convection zone. The solar atmosphere includes the photosphere, chromosphere, transition region and the corona. Some features and events commonly found on the Sun are also labelled. Credit: ESA (2019).

Around the core is the radiative zone, where energy is transported through a process known as radiative diffusion. This process is carried out by photons which are subject to scattering due to the presence of the hydrogen and helium ions. It can take more than 170,000 years for photons to leave the radiative zone. Note that convection cannot occur in this layer due to an insufficient temperature gradient.

Between the radiative zone and the convective zone lies the tachocline (Spiegel and Zahn, 1992), where below this region the Sun rotates as a solid body but above the Sun rotates at varying speeds according to latitude. This is thought to be the location of the solar dynamo, (e.g. Bushby and Mason, 2004). Above the tachocline lies the convection zone; here the temperature gradient is large enough that the process of convection is more efficient for energy transport. In convection the hot plasma rises to the photosphere, transferring heat, and the cooler plasma falls back into the convection zone.

As well as the solar interior previously discussed, there are also four outer layers that make up the solar atmosphere. The first layer is known as the photosphere, also considered as the surface of the Sun starting at $1R_\odot$ (measured where optical depth is ≈ 1 (Williams, 2018b)). The temperature here is much cooler than in the Sun's interior with a temperature range between 4500K and 6000K (ranging due to the presence of cooler regions such as sunspots), where at the start of the convection zone temperatures could reach 2×10^6K. Most of the electromagnetic radiation produced by the Sun is emitted in this layer which is the upper boundary of the convection zone.

The photosphere exhibits granulation, which is one of the observable signatures of convection, see Figure 1.2. These granules are caused by the plasma rising and falling as it is being heated and cooled. Individual granules may last for about 20 minutes and can be thousands of kilometres in size. This granulation is visible across the whole solar surface (Leighton, 1963), however can be suppressed when sunspots form, due to the intense magnetic fields inhibiting the convection process.

Another observable feature in the photosphere are sunspots, with an example shown in Figure 1.2. Large sunspots can be found to be several tens of thousand kilometres wide. They are formed when patches of magnetic field break through the photosphere where the plasma in the region is not as hot due to the strong magnetic fields inhibiting heat transport. Hence, they are identified by their dark centers, also known as umbra.

Larger regions of strong magnetic fields, known as *active regions*, can be found around the solar equator. The regions are the site of intense solar activity, with many solar phenomena (see Section 1.2) occurring there. Two examples of the line-of-sight (LOS) solar magnetic fields at the photosphere are shown in Figure 1.3, one occurring at solar minimum and the other at solar maximum

The layer above the photosphere, known as the chromosphere, is approximately 2000km thick with a temperature, ranging from 4000K to approximately 20000K at the top. The temperature minimum region occurs in the chromosphere with the subsequent temperatures increasing with height.

The thin transition region lies between the chromosphere and the final region known as the solar corona. This region is where the temperature increases rapidly from the chromospheric temperature, to the much hotter temperature in the corona of approximately 1×10^6K. However temperatures in the corona can reach as high as 20×10^6K in some regions. The reason why the corona is much hotter than the other outer layers is known as the *coronal heating problem* (e.g. De Moortel and Browning, 2015). Unlike the photosphere, the corona is dominated by magnetic fields which forces the plasma to move along fieldlines rather than moving freely. The solar corona is where many phenomena such as coronal loops, solar flares and CMEs can be observed, although solar flare radiation is chromospheric as discussed in Section 1.2. Although there are many interesting solar phenomena, flaring active regions are the focus of this thesis. These phenomena can affect the flow of plasma outwards from the Sun which is known as the solar wind. The solar wind carries charged particles away from the Sun along with the heliospheric magnetic field.

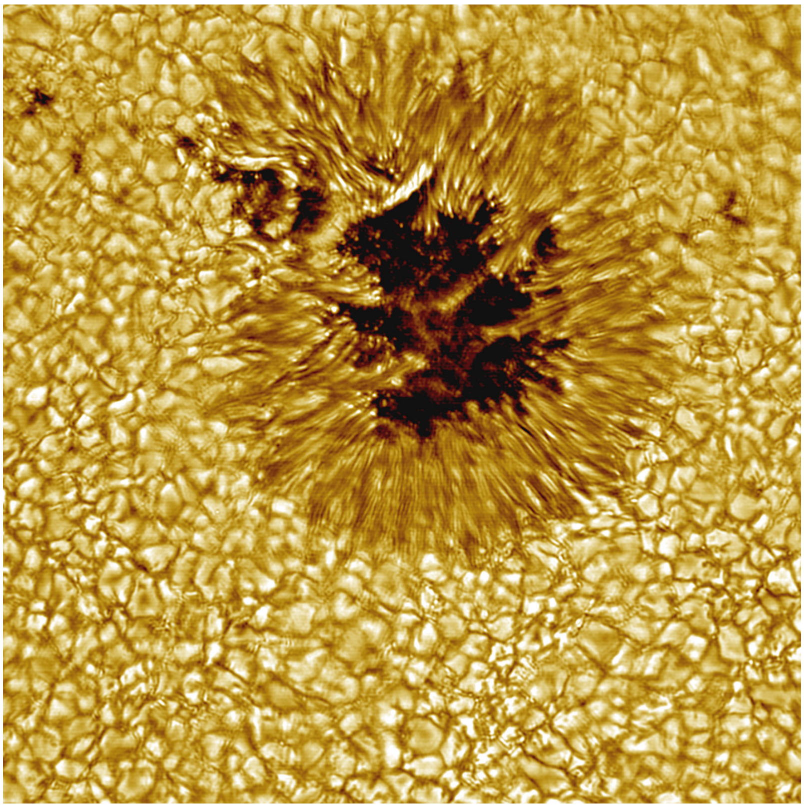

Figure 1.2: A sunspot and granulation shown on the Photosphere. Credit: Vacuum Tower Telescope, NSO, NOAO.

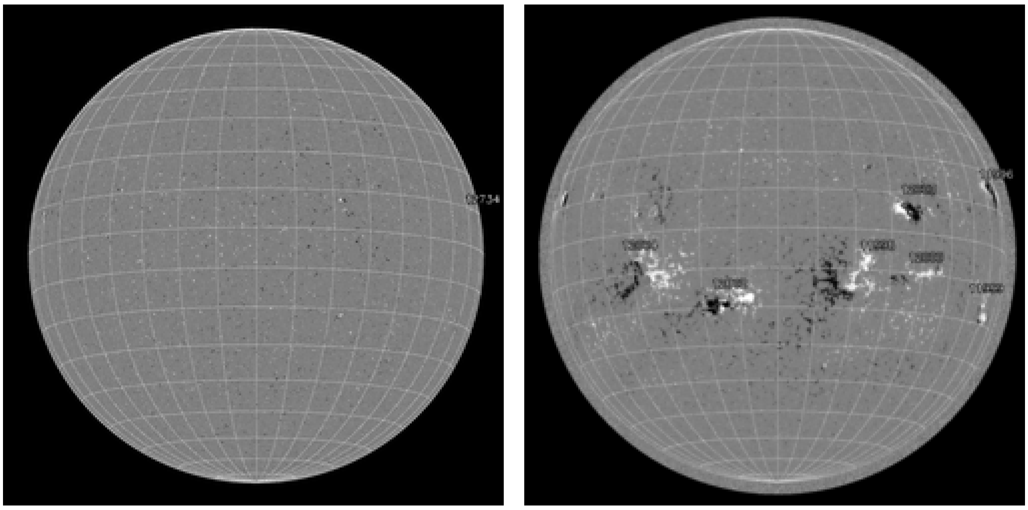

(a) Solar minimum, 13 March 2019 **(b)** Solar maximum, 13 March 2014

Figure 1.3: HMI magnetograms taken onboard SDO showing solar minimum and maximum. Courtesy of NASA/SDO and the HMI science team.

1.2 Solar Phenomena

Many observable phenomena in the solar atmosphere have been associated with the highly complex magnetic fields found there. Throughout this thesis we mainly focus on observations and data linked to solar flares, see Section 1.2.1. Another type of eruptive event often, but not always, associated with flares are coronal mass ejections (CMEs), which can also be directly linked to the release of stored magnetic energy. However these events are not the main focus of this work.

1.2.1 Solar Flares

Solar flares occur when stored magnetic energy is released, emitting radiation which is visible across much of the electromagnetic spectrum, (e.g. Fletcher et al., 2011). One of the processes which can assist in the the conversion of magnetic energy is *magnetic reconnection*. This process implies changing the connectivity of the magnetic field whilst converting magnetic energy into kinetic energy and energetic particles.

The process thought to occur during a two-ribbon solar flare is schematically shown in Figure 1.4. This model is known as the *standard model* or CSHKP model (Carmichael, 1964; Sturrock, 1966; Hirayama, 1974; Kopp and Pneuman, 1976). At the top of a coronal loop magnetic reconnection; the process in which magnetic field lines reconnect producing thermal and kinetic energy; occurs causing a burst of radiation and hard X-rays (HXR) to be emitted. However as well as propagating into the solar atmosphere, within this model it is thought that some of the energised particles travel down the coronal loop and interact with the chromosphere at the footpoints causing *flare ribbons* to occur. In the later stages of the flare, chromospheric evaporation occurs and the chromospheric plasma rises back into the coronal loop. The strong magnetic fields needed for flares to occur, are typically found in active regions.

Following this flare model, flare dynamics can be split into three phases; the *preflare* phase, the *impulsive* phase and the *gradual* phase. The preflare phase is where indicators may be spotted in observations that a flare is about to occur such as small UV brightenings that may be visible a few minutes before the impulsive phase, weak SXR emission or spectral line broadening, (e.g. Fárník et al., 1996; Fárník and Savy, 1998). The second phase, known as the impulsive phase is where the initial flare energy release occurs, lasting anywhere from tens of seconds to minutes. Here the HXRs, γ-rays and white-light emissions are dominant, with UV and EUV emission also visible (e.g. Hudson, 1972; Chupp et al., 1973). In this phase the main emission is concentrated at the chromospheric flare foot-points. As previously discussed this results in HXR

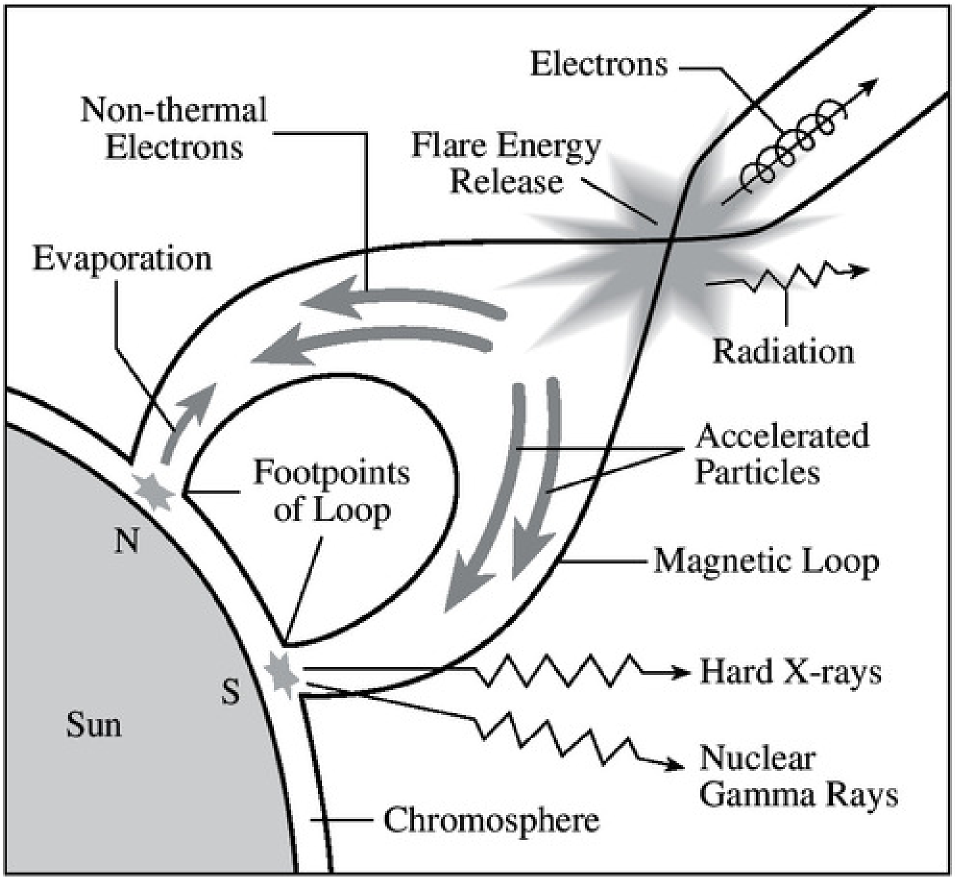

Figure 1.4: Standard flare model is shown with different types of emission labelled. Credit: Lang (2010).

foot-points and Hα flare ribbons (also visible in UV and EUV wavelengths, which are discussed further in Section 1.2.1). It is thought that during this phase magnetic reconnection occurs in the low corona, resulting in the release of the emissions previously discussed. The final phase, known as the gradual phase, is linked to the previously mentioned chromospheric evaporation. Here the SXR signatures decay and the coronal loops visible in SXR and EUV begin to change due to the evaporation effects. This final part of the flare evolution may last for hours after the impulsive phase (which can last only minutes).

Note that although the CSHKP model is discussed above, this model may not be suitable for some of the flares analysed here. In particular circular ribbon flares may differ dynamically to the process described above, with some 3D models (e.g. Janvier, M. et al., 2013) more suited to describing the flare process. See below also for a discussion on how the topology of the magnetic fields around the flaring regions may affect the flare ribbons observed.

Solar flares can be classified by their SXR intensities, typically measured by XRS

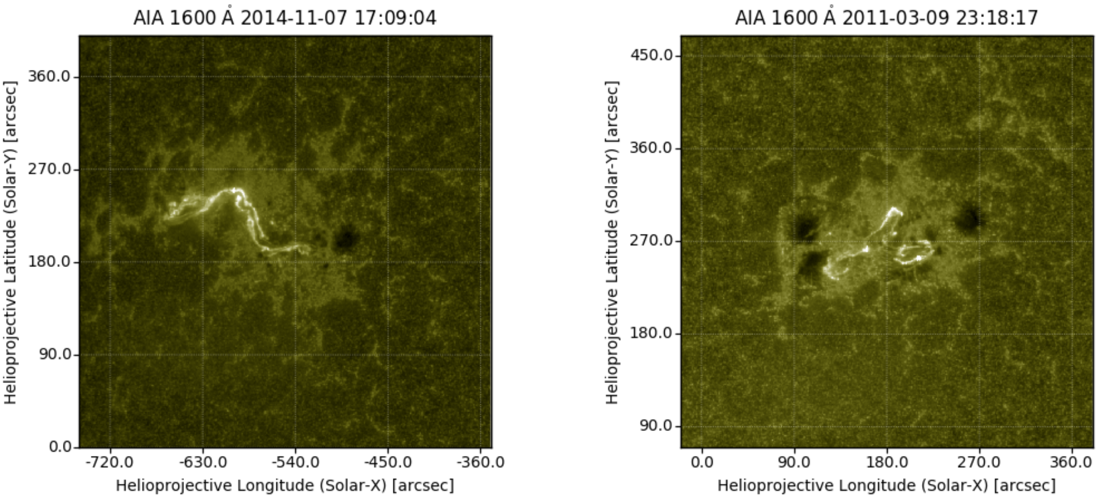

(a) **(b)**

Figure 1.5: Solar flare ribbons from two X-class flares observed by AIA are shown.

onboard GOES (*Geostationary Operational Environmental Satellite*). This classification starts at A class, which are flares with an intensity above 10^{-8}Wm^{-2} measured at the satellite, and ends with the highest classification of X class flares, which have intensities above 10^{-4}Wm^{-2}. Each classification between these two have an intensity threshold ten times higher than the previous with B (10^{-7}Wm^{-2}), C (10^{-6}Wm^{-2}) and M (10^{-5}Wm^{-2}) class flares. Within each of these classes there are subclasses from 1 to 9; for example an X2 flare is twice as large as a X1 flare. This means that an M7.5 class flare would have an approximate intensity of 7.5×10^{-5}Wm^{-2}.

Solar Flare Ribbons

As previously mentioned, one of the observable signatures from solar flares are flare ribbons. Although historically viewed in Hα emission, ribbons can also be observed in EUV and UV wavelengths, (e.g. Fletcher and Hudson, 2001). Ribbons typically occur at the HXR brightenings, considered the footpoints of the flare. Examples of flare ribbons observed by AIA in the 1600$\mathring{A}$ UV wavelength are shown in Figure 1.5 for two X-class solar flares.

These examples show some of the variations in flare ribbon structures, with most flares observed to have two ribbons visible. These two flare ribbons typically form in opposing polarity magnetic fields, with one lying in positive field and the other in negative field. Alternatively flares can produce what is known as a circular flare ribbon, observed to be a bright spot in the chromosphere.

Typically found in active regions where the flaring events have taken place, flare ribbons can be thousands of kilometres long and can be observed on the solar disc for extended periods of time. The ribbon structures can change throughout the flaring event with the flare ribbons lying close to the PIL (polarity inversion line) during the impulsive phase of the flare, and moving apart during the gradual phase. The flare ribbons positions have been linked to the topological structures (see Chapter 4) found in the flaring regions (e.g. Gorbachev and Somov, 1988; Mandrini et al., 1991, 1993; Priest and Démoulin, 1995; Demoulin et al., 1997). This is thought to be due to how these flare ribbons are produced, with the high energy particles that are produced at the reconnection site (see Figure 1.4) interacting with the chromospheric plasma to produce the elongated ribbon shapes. These ribbons are then commonly found at the footpoints of the magnetic fieldlines in the region.

Note circular flare ribbons, previously mentioned here and studied later in Chapter 4, have been shown to relate to topological features found in magnetic field models. A *dome-spine* topology, see Figure 1.6, in particular has been the main structure studied that is thought to relate to circular flare ribbons (e.g. Masson et al., 2009; Song and Tian, 2018). This is where there is a magnetic null point present, with magnetic field lines extending from it to make a dome shape. This dome shape intersecting with the chromosphere is thought to give rise to the circular flare ribbon shape observed in AIA images for example. Although dome-spine topology is mainly studied in relation to circular flare ribbons, later in Chapter 4, these features are also studied in relation to other flare ribbon shapes observed.

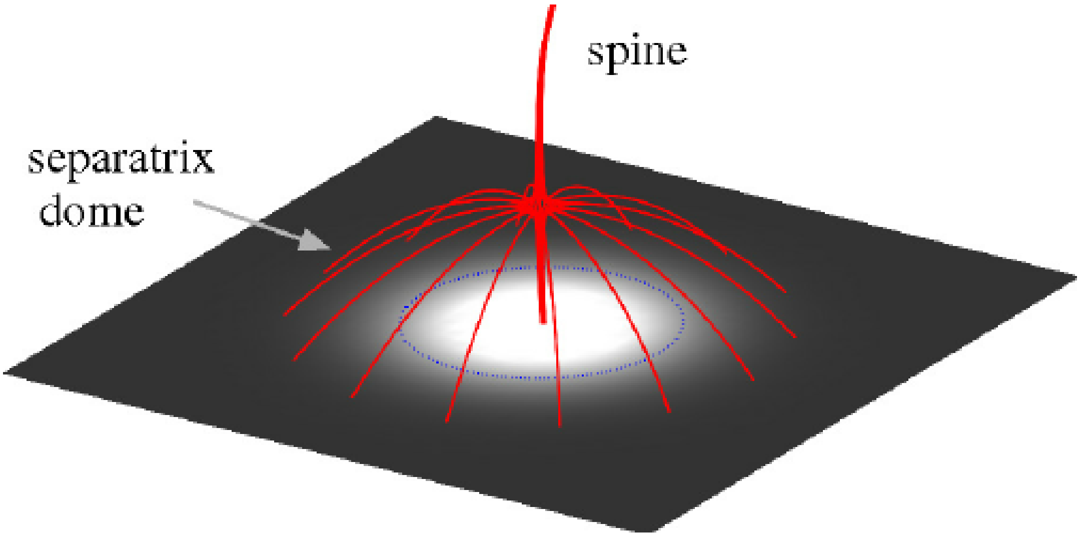

Figure 1.6: Figure from Pontin et al. (2013), a magnetic dome is shown with associated spine line originating from a null point lying in the solar atmosphere.

1.3 Solar Observations

Observations of the Sun have become more high-resolution and detailed since the launch of the first solar satellites in the 1960s. There are many ground and space-based observatories currently in use, however here we will mainly focus on observations taken by the Solar Dynamics Observatory (SDO) which has 3 onboard instruments; Helioseismic and Magnetic Imager (HMI), the Atmospheric Imaging Assembly (AIA) and the Extreme Ultraviolet Variability Experiment (EVE), (Pesnell et al., 2012). Throughout this thesis data collected by HMI and AIA will be used.

HMI takes high resolution (1 arcsecond) measurements of the Sun's magnetic field at the photosphere, (Schou et al., 2012). Although HMI produces four data products, only the line-of-sight (LOS) magnetograms are used in this work.

Figure 1.3 shows two examples of HMI LOS magnetograms taken five years apart at both extremes of the Sun's 11 year cycle. Figure 1.3a shows an example taken at solar minimum where there are no active regions visible. Figure 1.3b shows the Sun during solar maximum where there are many more active region patches visible. From these magnetograms synoptic maps can be created by taking sections of the LOS magnetograms and piecing them together to create a view of the whole solar surface. These synoptic maps can be created daily or for whole Carrington rotations, and are used extensively in Chapters 2 to 4.

AIA provides full-disk observations of the solar atmosphere, in particular the solar corona, at various wavelengths. Seven EUV wavelengths are observed (all from different source ions), with $1600 \AA$, $1700 \AA$ and continuum observations also taken. This allows AIA to observe the photosphere, chromosphere and the corona at various temperatures. Examples of AIA images are shown in Figure 1.7, with three EUV observations and one $1600 \AA$ observation shown. Note that in Figure 1.7c the bright spots highlight active regions, with both Figures 1.7b and 1.7d showing coronal loop structures and active regions. Throughout this work however most of the AIA observations used will be taken from the $1600 \AA$ wavelength, which observes the upper photosphere and transition region. This is due to solar flare ribbons, as previously discussed in Section 1.2.1, being clearly observable in this wavelength.

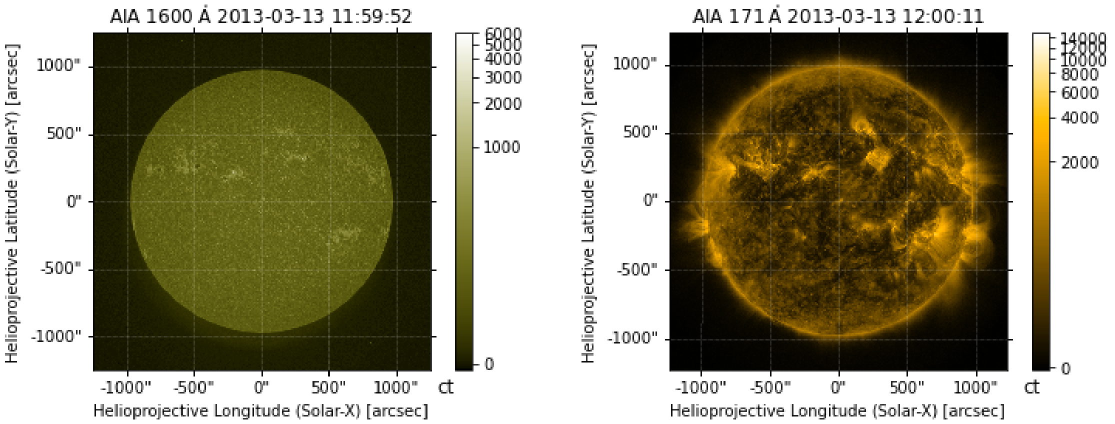

(a) 160nm, Transition Region and Photosphere (10^5K and 5000K)

(b) 17.1nm, Transition Region and Corona (6.3×10^5K)

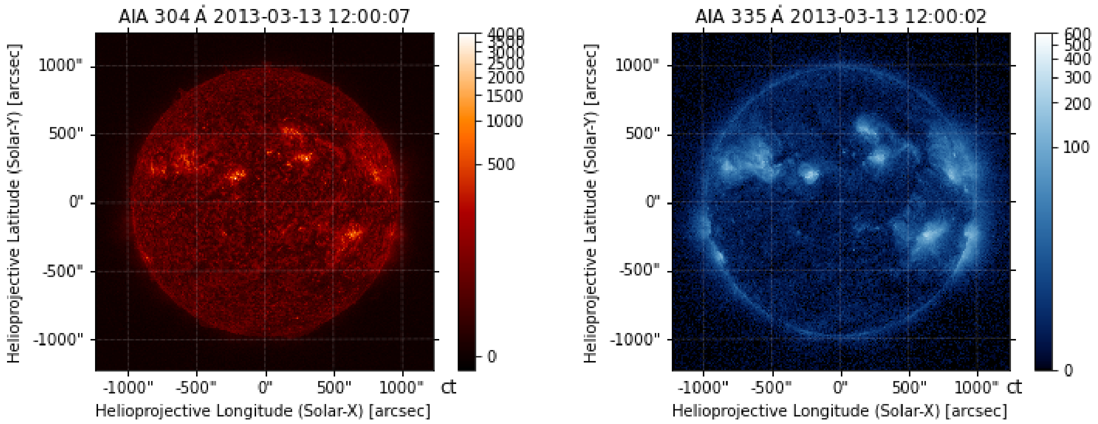

(c) 30.4nm, Chromosphere (50,000K)

(d) 33.5nm, Corona (2.5×10^6K)

Figure 1.7: Examples of images taken by AIA onboard SDO on 13 March 2013 at approximately 12UT. Courtesy of NASA/SDO and the AIA science team.

1.4 MHD Equations

The *magnetohydrodynamic* (MHD) equations are a combination of Maxwell's equations and the fluid equations. These equations together are based on the assumption that the plasma is a single fluid which is continuous in space and is electrically conducting. The presence of magnetic fields leads to forces which can act on the plasma, which can subsequently change the strength and topology of the magnetic fields.

Note that in this thesis, these MHD equations are used in Chapters 2 and 3, with mostly potential fields considered. The MHD equations are therefore only briefly discussed below, (for further information see e.g. Priest, 2014; Galtier, 2016).

1.4.1 Maxwell's Equations

Here we describe Maxwell's equations in the form known as *magnetohydrodynamics* (MHD), these partial differential equations are used to describe electromagnetism. The four equations that make up Maxwell's equations are;

1. **Ampère's Law:**
   $$\nabla \times \mathbf{B} = \mu_0 \mathbf{j}, \tag{1.1}$$
   indicates that magnetic fields can be produced by changing electric currents. Note this is the MHD approximation of Ampère's Law where the displacement current is negligible.

2. **Solenodial Constraint:**
   $$\nabla \cdot \mathbf{B} = 0, \tag{1.2}$$
   indicates that there are no magnetic monopoles present (or no sources or sinks in the magnetic fields).

3. **Faraday's Law:**
   $$\nabla \times \mathbf{E} = -\frac{\partial \mathbf{B}}{\partial t}, \tag{1.3}$$
   which describes how a spatially varying electric field can induce magnetic fields.

In these equations $\mathbf{B}$ denotes the magnetic field, $\mathbf{j}$ is the current density, $\mathbf{E}$ is the electric field and μ_0 is the magnetic permeability in a vaccum ($4\pi \times 10^{-7}\mathrm{Hm}^{-1}$).

Note that although we state that $\mathbf{B}$ and $\mathbf{E}$ are the magnetic and electric fields respectively, $\mathbf{B}$ is actually the magnetic induction with the magnetic field usually denoted in other works as $\mathbf{H} = \dfrac{\mathbf{B}}{\mu_0}$. The electric displacement is also denoted as $\mathbf{D} = \epsilon_0 \mathbf{E}$, however neither $\mathbf{H}$ or $\mathbf{D}$ are used here.

1.4.2 Ohm's Law and the Fluid Equations

Ohm's law and the fluid equations make up another part of the magnetohydrodynamic (MHD) equations.

1. **Ohm's law:**
   $$\mathbf{E} + \mathbf{v} \times \mathbf{B} = \frac{1}{\sigma}\mathbf{j}, \tag{1.4}$$
   connects the plasma that is governed by the fluid equations with the electromagnetic fields previously given in Maxwell's Equations.

Note that $\mathbf{v}$ is the plasma velocity and σ is electrical conductivity, with the $\frac{1}{\sigma}$ term known as the resistivity.

2. **Mass continuity:**

$$\frac{\partial \rho}{\partial t} + \nabla \cdot (\rho \mathbf{v}) = 0, \tag{1.5}$$

where ρ is the density of the plasma. This equation shows that mass is conserved within a comoving volume, such that matter is neither created or destroyed.

3. **Equation of motion:**

$$\rho \frac{D\mathbf{v}}{Dt} = \mathbf{j} \times \mathbf{B} - \nabla p + \rho \mathbf{g} + \mathbf{F}, \tag{1.6}$$

where $-\nabla p$ is the pressure force, $\mathbf{j} \times \mathbf{B}$ is known as the Lorentz force, $\rho\mathbf{g}$ is the gravitational force (where $\mathbf{g}$ is gravitational acceleration) and $\mathbf{F}$ is any other force. This equation includes the Lorentz force due to the magnetic fields being considered here and describes Newton's second law for the whole plasma instead of just one particle.

Note that the Lorentz force present in this equation, is a force acting on fluid particles due to the surrounding magnetic fields. The Lorentz force can be written as;

$$\mathbf{j} \times \mathbf{B} = \frac{1}{\mu_0}(\mathbf{B} \cdot \nabla)\mathbf{B} - \nabla\left(\frac{\mathbf{B} \cdot \mathbf{B}}{2\mu_0}\right), \tag{1.7}$$

with one term denoting the magnetic tension and the other term the magnetic pressure force. The magnetic tension force tries to straighten magnetic fieldlines whereas the magnetic pressure force attempts to make the magnetic field strength uniform everywhere.

4. **Ideal gas law:**

$$p = \frac{\rho R T}{\bar{\mu}}, \tag{1.8}$$

where T is the plasma temperature, R is the gas constant and $\bar{\mu}$ is the mean molecular weight. $\bar{\mu}$ varies depending on the fluid, however it is approximately 0.6 in the solar corona and 1 for a neutral hydrogen gas.

This equation describes the relationship between plasma pressure, density and temperature assuming that the plasma behaves like a perfect gas i.e. between particles there are no interactions.

5. **Energy equation:**
$$\frac{\rho^\gamma}{\gamma - 1}\frac{D}{Dt}\left(\frac{p}{\rho^\gamma}\right) = -\mathcal{L}, \tag{1.9}$$
where $\mathcal{L}$ is the total energy loss function and γ is the ratio of specific heats.

   This equations describes the conservation of energy in a fluid. Note that if $\mathcal{L} = 0$ this is known as an adiabatic plasma and the energy equation can be simplified to;
$$\frac{D}{Dt}\left(\frac{p}{\rho^\gamma}\right) = 0,$$
where entropy is conserved.

1.4.3 Induction Equation

Using Ohm's law to remove the electric field component ($\mathbf{E}$) from Faraday's law (Equation 1.3) and using Ampère's law (Equation 1.1) we can define the *induction equation* as;
$$\frac{\partial \mathbf{B}}{\partial t} = \nabla \times (\mathbf{v} \times \mathbf{B}) + \eta \nabla^2 \mathbf{B}, \tag{1.10}$$
where η is a constant of the form; $\eta = \dfrac{1}{\mu_0 \sigma}$ describing the magnetic diffusivity.

This equation describes how magnetic fields change with time with respect to two terms; the *advection term*, $\nabla \times (\mathbf{v} \times \mathbf{B})$, which determines how the magnetic field moves with the plasma and the *diffusion term*, $\eta \nabla^2 \mathbf{B}$, which determines how the magnetic field lines slip through the plasma.

The ratio of the magnitude of these two terms is known as the magnetic Reynolds number (R_m);
$$R_m = \frac{|\nabla \times (\mathbf{v} \times \mathbf{B})|}{|\eta \nabla^2 \mathbf{B}|} = \frac{v_0 l_0}{\eta},$$
where v_0 and l_0 are typical velocities and length scales. If $R_m \gg 1$ then we can say the magnetic field is *frozen-in* to the plasma and the advection term dominates the induction equation (note that the diffusion term must not have a large second derivative i.e. the current density does not vary strongly). This means the magnetic field lines move with the plasma flows. However, if $R_m \ll 1$ the diffusion term dominates the induction equation.

1.5 Magnetic Skeleton

1.5.1 Magnetic Null Points

Magnetic null points are points where the magnetic field vanishes locally (e.g. $\mathbf{B}=\mathbf{0}$). In general we can consider the field around a null point, and express it as;

$$\mathbf{B}=\mathbf{M}\cdot\mathbf{r} \ = \left.\begin{pmatrix} \frac{\partial B_x}{\partial x} & \frac{\partial B_x}{\partial y} & \frac{\partial B_x}{\partial z} \\ \frac{\partial B_y}{\partial x} & \frac{\partial B_y}{\partial y} & \frac{\partial B_y}{\partial z} \\ \frac{\partial B_z}{\partial x} & \frac{\partial B_z}{\partial y} & \frac{\partial B_z}{\partial z} \end{pmatrix}\right|_{null} \begin{pmatrix} x \\ y \\ z \end{pmatrix}, \tag{1.11}$$

where we have assumed that the null point is located at the origin.

Two-dimensional Null Points

In two-dimensions Equation 1.11 can be reduced to;

$$\mathbf{B}=\left.\begin{pmatrix} \frac{\partial B_x}{\partial x} & \frac{\partial B_x}{\partial y} \\ \frac{\partial B_y}{\partial x} & \frac{\partial B_y}{\partial y} \end{pmatrix}\right|_{null} \begin{pmatrix} x \\ y \end{pmatrix},$$

and we can let the arguments of matrix $\mathbf{M}$ take the form;

$$\mathbf{M}=\begin{pmatrix} a & b \\ c & d \end{pmatrix},$$

where $a,b,c,d\in\mathbb{R}$. Using the solenodial constraint ($\nabla\cdot\mathbf{B}=0$), we know that $a=-d$ therefore allowing the magnetic field to be written in the form;

$$\mathbf{B}=\begin{pmatrix} ax+by \\ cx-ay \end{pmatrix}.$$

To determine what the fieldlines are doing around these points we can solve,

$$\begin{pmatrix} x'(s) \\ y'(s) \end{pmatrix}=\mathbf{M}\begin{pmatrix} x(s) \\ y(s) \end{pmatrix},$$

and consider the eigenvalues and eigenvectors of $\mathbf{M}$. This results in “O” type null points if the eigenvalues are complex (i.e. $a^2+bc<0$) and “X” type null points if the eigenvalues are real (i.e. $a^2+bc>0$). Typically in 2D studies it is assumed that the null points are either “X” type or “O” type null points.

Three Dimensional Null Points

In three-dimensions we can use Equation 1.11 and the solenodial constraint again to find the structure of the field around null points. Here instead of a two-dimensional "X" or "O" type point, the null points have a fan plane (e.g. Priest and Titov, 1996), which is a surface of field lines and two specific lines known as *spine lines* going out of/into the null points. The fan plane is where we only consider the linear version of the null point structure, however this fan-plane is known as a *separatrix surface* when non-linear terms dominate and this surface separates regions of different connectivity. Overall null points in 3D are categorised by their sign (positive or negative), where the spine line lies in relation to the separatrix surface and finally the fieldlines in the separatrix surface. How the sign of the null point is determined is shown below.

In 3D, the matrix $\mathbf{M}$ can be defined as shown in Equation 1.11, and using the solenoidal constraint ($\nabla \cdot \mathbf{B} = 0$) the trace of this matrix must sum to zero;

$$\frac{\partial B_x}{\partial x} + \frac{\partial B_y}{\partial y} + \frac{\partial B_z}{\partial z} = 0.$$

Due to the trace of the matrix summing to zero this means that the eigenvalues associated with matrix $\mathbf{M}$ must also sum to zero;

$$\lambda_1 + \lambda_2 + \lambda_3 = 0,$$

where we define the eigenvalues as λ_1, λ_2 and λ_3 and the corresponding eigenvectors as $\mathbf{e_1}, \mathbf{e_2}$ and $\mathbf{e_3}$. Following this we can use the methods presented by Parnell et al. (1996) to calculate the spine lines and fan planes associated with the 3D null points.

If a magnetic field line is considered which lies close to a null point with a position vector $\mathbf{r}$ which is dependent on some parameter s which lies along the fieldline, then we know;

$$\frac{\mathrm{d}\mathbf{r}(s)}{\mathrm{d}s} = \mathbf{M} \cdot \mathbf{r}(s) = \mathbf{B}.$$

This can be written in terms of the matrix eigenvectors of $\mathbf{M}$, which we call $\mathbf{P}$, by using the substitution $\mathbf{r}(s) = \mathbf{Pu}(s)$ such that;

$$\frac{\mathrm{d}\mathbf{u}}{\mathrm{d}s} = \mathbf{P^{-1}MPu}. \tag{1.12}$$

This results in two cases to solve depending on whether $\mathbf{M}$ can be diagonalised or not.

First, consider when $\mathbf{M}$ is diagonalisable to a matrix $\mathbf{\Lambda}$ then;

$$\mathbf{\Lambda} = \mathbf{P^{-1}MP} = \begin{pmatrix} \lambda_1 & 0 & 0 \\ 0 & \lambda_2 & 0 \\ 0 & 0 & \lambda_3 \end{pmatrix}.$$

This allows Equation 1.12 to be solved to obtain an expression for $\mathbf{u}$ which gives;

$$\mathbf{u} = \mathbf{A}e^{\Lambda s} = \begin{pmatrix} Ae^{\lambda_1 s} & 0 & 0 \\ 0 & Be^{\lambda_2 s} & 0 \\ 0 & 0 & Ce^{\lambda_3 s} \end{pmatrix},$$

where $\mathbf{A}$ is a matrix containing values constant along the fieldline. This allows the fieldline position vector, $\mathbf{r}(s)$, to be written in terms of eigenvalues and eigenvectors of $\mathbf{M}$ such that,

$$\mathbf{r}(s) = Ae^{\lambda_1 s}\mathbf{e_1} + Be^{\lambda_2 s}\mathbf{e_2} + Ce^{\lambda_3 s}\mathbf{e_3} \tag{1.13}$$

Initially considering the real part of the eigenvalues, at least one must be of opposite sign to allow the sum of the eigenvalues to equal zero for example, $\mathbb{R}(\lambda_1), \mathbb{R}(\lambda_2) > 0$ and $\mathbb{R}(\lambda_3) < 0$. In this case, tracing the fieldlines, if $s \rightarrow -\infty$ then Equation 1.13 becomes,

$$\mathbf{r}(s) \rightarrow Ce^{\lambda_3 s}\mathbf{e_3}.$$

This implies that the fieldlines moving towards the null point are lying parallel to the eigenvector $\mathbf{e_3}$. This eigenvector with the negative eigenvalue (λ_3) is what defines the *spine line*, with the two other eigenvectors defining the *fan plane* with these fieldlines moving outwards from the null point in the opposite direction to the spine line. This is shown by considering $s \rightarrow \infty$ such that,

$$\mathbf{r}(s) \rightarrow Ae^{\lambda_1 s}\mathbf{e_1} + Be^{\lambda_2 s}\mathbf{e_2}.$$

This implies that fieldlines moving away from the null point are lying parallel to the plane formed by the eigenvectors $\mathbf{e_1}$ and $\mathbf{e_2}$. These type of null points are known as *positive* null points. Figure 1.8 shows an example of a positive null point, with the spine line and fan plane clearly shown.

Alternatively, considering where the eigenvalue signs are the opposite of those previously considered such that $\mathbb{R}(\lambda_1), \mathbb{R}(\lambda_2) < 0$ and $\mathbb{R}(\lambda_3) > 0$, the arguments stated above reverse and a *negative* null point occurs. This is where the spine line is pointing

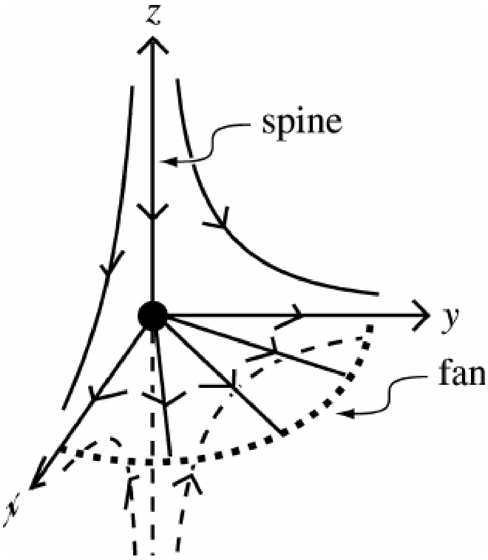

Figure 1.8: A positive null point is shown in the xyz plane. The spine points into the null point, with the fan plane lying in the xy plane moving radially outwards from the null. Credit: Close et al. (2004)

out of the null point and the fan plane consists of fieldlines moving towards the null point.

The matrix $\mathbf{M}$ can be reduced to a simpler form where its elements are dependent on the fewest number of free parameters without any loss of generality. Here it is assumed that the eigenvalue associated with the spine line is located in the z-direction and the matrix is rotated so the x-axis lies in the same direction as the current present in the xy plane. This allows the matrix $\mathbf{M}$ to be written as;

$$\mathbf{M} = \begin{pmatrix} 1 & \frac{1}{2}(q - j_{\parallel}) & 0 \\ \frac{1}{2}(q + j_{\parallel}) & p & 0 \\ 0 & j_{\perp} & -(p+1) \end{pmatrix}, \tag{1.14}$$

after the use of a scaling factor with $p \geq -1$ and $q^2 \leq j_{\parallel}^2 + 4p$. The parameters p and q correspond to the potential field and the current is defined as $\mathbf{j} = \frac{1}{\mu_0}(j_{\perp}, 0, j_{\parallel})$, where $j_{\parallel}$ is the current parallel to the spine and $j_{\perp}$ is the current perpendicular to the spine.

As shown in Parnell et al. (1996) the eigenvalues of matrix $\mathbf{M}$ are,

$$\lambda_1 = \frac{p + 1 + \sqrt{(p-1)^2 + q^2 - j_{\parallel}^2}}{2},$$

$$\lambda_2 = \frac{p + 1 - \sqrt{(p-1)^2 + q^2 - j_{\parallel}^2}}{2},$$

$$\lambda_3 = -(p+1).$$

Note that as $p \geq -1$ then λ_3 is always negative and so corresponds to the spine line of a positive null point, with λ_1 and λ_2 corresponding to the fan plane. However by changing the sign of the scaling factor the signs here would change and would correspond to a negative null point.

Here we assume that all eigenvalues are real, however note that if one eigenvalue is real and two are complex then *spiral nulls* occur. This is where the fan plane fieldlines spiral towards the null point instead of moving radially outwards. This spiralling effect comes from the $j_{||}$ term located in λ_1 and λ_2. The $j_\perp$ component also has an effect on the fan plane, however it causes a tilt effect rather than a spiral effect. This means $j_\perp$ causes the fan plane to tilt away from the perpendicular position found in potential field configurations. The tilt angle of this fan plane can be defined as:

$$\cos\theta = \frac{9(p+1^2-(p-1)^2-q^2+j_{||})}{|\mathbf{n_f}|},$$

where the normal vector to the fan plane is defined as,

$$\mathbf{n_f} = \begin{pmatrix} 2j_\perp(q+j_{||}) \\ -4j_\perp(p+2) \\ 9(p+1)^2-(p-1)^2-q^2+j_{||}^2 \end{pmatrix}.$$

All possible combinations of the variables $p, q, j_\perp$ and $j_{||}$ are considered in Parnell et al. (1996). However for the magnetic fields that we consider in Chapter 4, the matrix $\mathbf{M}$ is reduced to,

$$\mathbf{M} = \begin{pmatrix} 1 & 0 & 0 \\ 0 & p & 0 \\ 0 & 0 & -(p+1) \end{pmatrix},$$

where $p > 0, j_\perp = 0, j_{||} = 0$ and a threshold current is set as $j_{thresh} = \sqrt{4p^2+q^2}$. Null points, spine lines and fan planes all contribute to what is known as the *magnetic skeleton*. As discussed above the spine lines and fan planes originate from the null points found in the magnetic field, however as distance increases between the null and the magnetic field lines that create the spine line and fan plane non-linear effects will take over. Although these lines continue they are no longer the flat fan-plane shown in Figure 1.8 but become warped. These fieldlines continue until they stop at one of the boundaries set in the domain or if they reach another null point.

If the fieldlines that originate from the fan plane continue until reaching a domain boundary, then the fan plane develops into what is known as a *separatrix surface*. This is where the infinite number of fieldlines originating from a null point separates two regions of magnetic field. No fieldlines cross this separatrix surface from either region.

Alternatively, fieldlines that connect one null point to another are known as *separators*. These are considered to be the fourth component of the magnetic skeleton. These separators are found where two separatrix surfaces intersect. The intersection of separatrix surfaces create many smaller regions of different topology within the magnetic field. An example of this type of separator is shown in Figure 1.9, where two separatrix surfaces from opposite polarity nulls intersect creating a separator between the two. Note spine lines can also be associated with separators, however these types of separators are topologically unstable and so are not considered throughout our analysis.

1.5.2 Heliospheric Current Sheet

The final global magnetic skeleton feature considered here is the *heliospheric current sheet* (HCS), (see Smith, 2001). This is a feature included in the magnetic field models

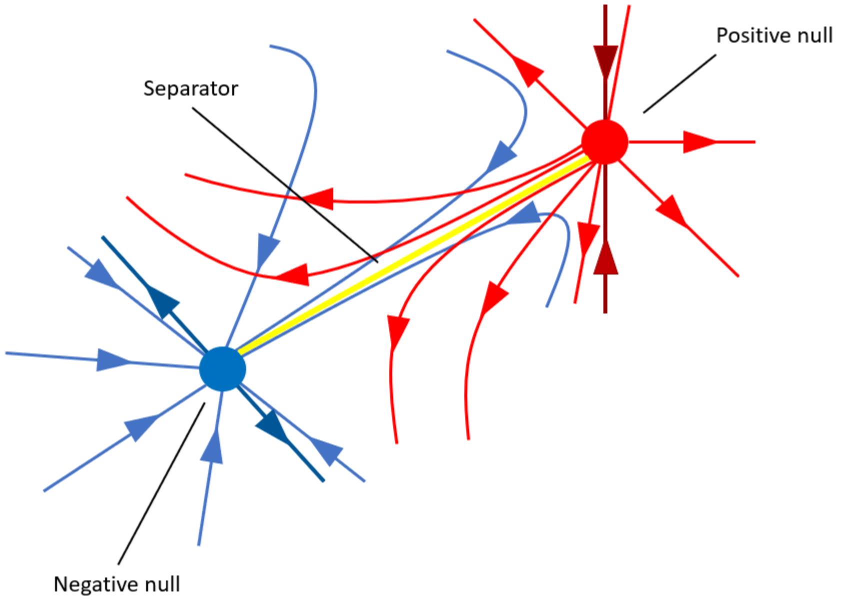

Figure 1.9: Sketch showing the formation of a separator due to the intersection of separatrix surfaces of two 3D null points. A positive and negative null point are shown with their correspoding spine lines, in dark red and dark blue respectively. The separatrix surface for the positive null point is shown in red and the corresponding separatrix surface for the negative null point shown in blue. The separator between both nulls (shown in yellow) indicates where the two separatrix surfaces intersect.

used in Chapters 2, 3 and 4. Note that although magnetic field models are used as an example here, the HCS is an observed feature and not only associated with models.

The Sun's magnetic field is assumed to be purely radial after a certain radius due to the solar wind, note this radius is considered to be $R = 2.5R_{\odot}$ throughout this work. This assumption implies that any change in sign in the magnetic field will create what is known as the *null line*. In the *potential field source surface model* (PFSS) which is discussed in Chapter 2, it is assumed that this null line creates the base of what is known as the heliospheric current sheet (HCS) which extends into the solar atmosphere.

Fieldlines can be traced from the HCS to create what are known as *HCS curtains*, an example of these are shown in Figure 1.10. Note that the fieldlines in the HCS curtains may intersect with separatrix surfaces from null points located in the magnetic field, this will create separators (as previously discussed in Section 1.5.1).

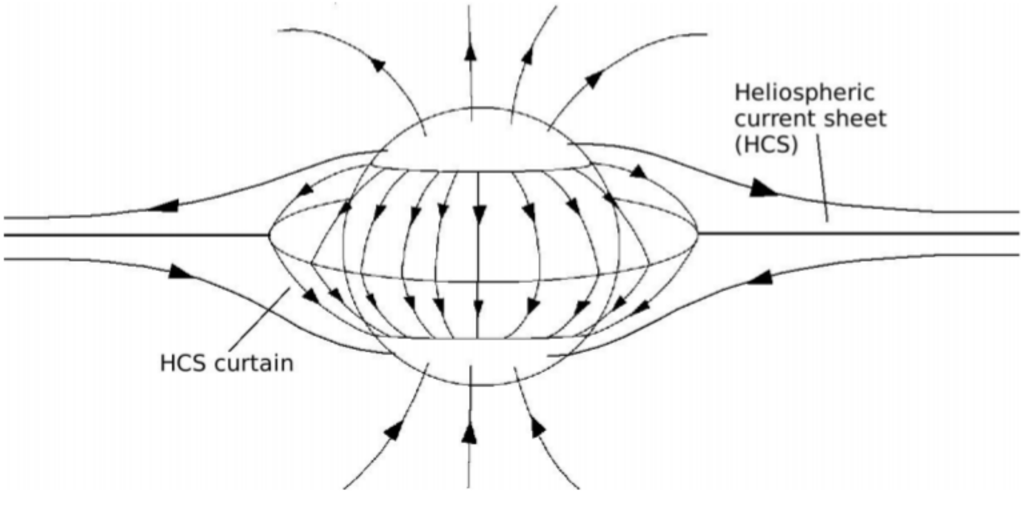

Figure 1.10: An example of the heliospheric current sheet (HCS) and its associated HCS curtains. Credit: Edwards (2014)

1.6 Machine Learning Techniques

Machine learning (ML) techniques can be used to develop algorithms that for example will automatically learn and detect patterns in the input data. ML covers a large range of techniques with applications such as support vector machines (SVMs), neural networks (NN), decision trees and random forests all suitable for predicting or classifying data. Methods can be carried out by supervised or non-supervised learning, dependent upon whether there is human input teaching the method what to learn. The ML methods typically take in a set of input data, known as the *training* dataset, and output a prediction or classification for each portion of the data. They typically learn during the training phase and produce an output during the prediction phase.

Currently for solar data, with SDO producing approximately 1.5TB of solar data each day and with more data from current and upcoming observatories such as Parker Solar Probe, Solar Orbiter, DKIST (Daniel K. Inouye Solar Telescope) and the SKA (Square Kilometre Array), it is vital to be able to process the large amounts of data produced. ML techniques have been applied to different aspects of solar research such as space weather forecasting and solar flare predictions (e.g. Colak and Qahwaji, 2009; Li et al., 2008; Bobra and Couvidat, 2015; Barnes et al., 2016), classification of solar events (e.g. Armstrong and Fletcher, 2019), detecting solar events and regions of interest (e.g. Schuh et al., 2013; Banda and Angryk, 2015), predicting photospheric velocities (Asensio Ramos et al., 2017) and correction of solar image data (Tree et al., 2019) to name a few.

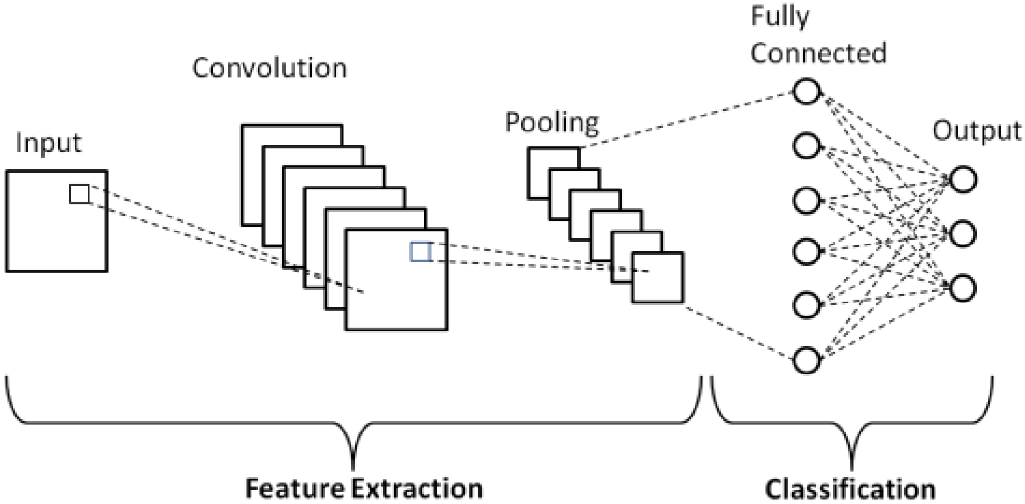

Figure 1.11: A basic convolutional neural network (CNN) with one convolutional layer. Credit: Phung and Rhee (2019)

In this thesis, particularly in Chapter 5, we consider a *convolutional neural network* (CNN) for the classification of flare ribbon data observed by SDO. Although we concentrate on CNNs for classification they can also be used for prediction, for example as previously mentioned above for predicting the onset of solar flares. A training dataset allows the CNN to learn the features required for each class and a test dataset can be implemented to test how well the CNN is classifying the images in the prediction phase.

A basic CNN is shown in 1.11, where the layers required to build a CNN are shown. In general, there is one input layer and one classification (output) layer with as many hidden layers as the programmer wishes in between. The number of hidden layers chosen is typically dependent on the complexity of the dataset being analysed.

The first layer initalises the data input which will be passed onto the hidden layers, which are key to CNN training. The types of hidden layers used throughout our analysis are;

1. Convolutional layers

   Convolutional layers are what give the CNNs their name, applying convolutions to the image matrices to extract features for each class. Applying these image convolutions helps reduce the dimensionality of the image data which can reduce overfitting and overtraining.

2. Activation layers The layers use what is known as an *activation function* to help the CNN decide which neurons activate for the next layer e.g., what individual feature maps produced by the previous convolutional layer are passed onto and used by the next layer in the network.

3. Pooling layers

   Pooling layers help reduce the size of the data being considered. These typically include maximum or average pooling; where the data is converted into a reduced matrix containing only maximum or averaged values of the previous layers data.

4. Fully connected (FC) layers

   Used as both a hidden layer and the final output layer, these FC layers are used to gather results from previous layers. These are the layers implemented in non-convolutional neural networks (NNs).

All of these are discussed in more detail in Chapter 5, with each layer broken down to analyse the part it plays in the CNN training process.

1.7 Outline

In Chapter 2, the *potential field source-surface* (PFSS) model is described, with a detailed explanation of how the model is used to calculate potential magnetic fields. The codes used to reproduce and calculate the potential fields dicussed here are the same as those previously described in Williams (2018a), with that work following on from the PFSS model codes created by Ballegooijen et al. (1998). The global potential magnetic fields discussed in this chapter are used extensively for magnetic field analysis in the rest of this thesis but particularly in Chapter 4.

In Chapter 3, the *magnetohydrostatic* (MHS) model is derived with the same derivation carried out as in Neukirch (1995). Further derivations that are pertinent to this chapter are also included in Appendix A.2. With the creation of the MHS codes and analysis into some of the parameters of the model previously done by Williams (2018a), we continue this work here with the pressure, plasma beta and density values calculated for varying parameter values. This work was introduced to finish the investigation into the magnetic field parameters that can be freely chosen as well as the global models being used as an alternative to the PFSS model previously discussed.

In Chapter 4, active regions where X-class flares occurred from 2011 to 2017 and were observed by SDO were analysed. The PFSS model was used to analyse the active regions and the resulting magnetic skeleton features are mapped by eye to the flare ribbons observed at peak flare times. Subsequently, the MHS model is also used to see if a non-potential field will give different topological features that could be mapped to the flare ribbons. The squashing factor Q (see Titov, 2007) is also calculated to compare whether high Q values are found in the presence of flare ribbons where no topological features were found, perhaps highlightling the presence of *quasi-separatrix layers* (QSLs), (e.g. Priest and Démoulin, 1995; Titov, 1999).

In Chapter 5, a *convolutional neural network* (CNN) is created to classify flare ribbons into three categories, two-ribbon flares, circular (compact) ribbon flares and limb flares as well as the control classifcation, the quiet sun. This CNN is trained on $1600 \mathring{A}$ AIA images which were being used for the previous flare and edge detection analysis in Chapters 4 and 6. This chapter discusses the work previously published in Love et al. (2020), however also shown is subsequent work done to include flare ribbon clasifications with the use of numerical parameters along with the classification of the

AIA images.

In Chapter 6, observations of solar flares taken by the Atmospheric Imaging Assembly (AIA) onboard the Solar Dynamics Observatory (SDO) are considered. The Canny edge detection method (Canny, 1986) is implemented and used to identify the flare ribbons observed at peak flare times. De-saturation of 1600$\mathring{A}$ AIA images is also discussed due to pixel saturation during some of the flares analysed. Subsequently distance metrics are chosen to mathematically compare the flare ribbon edges detected to the topological features found in Chapter 4.

Finally in Chapter 7, a summary is presented with discussion on possible future work included. This includes the possibility of merging the work discussed into an automated pipeline which could analyse flare ribbon observations. This would result in an output of a mathematical metric which could describe whether the flare ribbons observed were correlated to any topological features within the flaring region.

Chapter 2

Potential Field Source-Surface Model

The *Potential Field Source Surface* (PFSS) Model (e.g. Schatten et al., 1969; Altschuler and Newkirk, 1969) generates an analytical approximation of the Sun's magnetic field in spherical coordinates. Here we use the PFSS model codes previously discussed and updated by Williams (2018a).

The model itself can be used to analyse various aspects of the solar atmosphere for example, modelling coronal null points and their associated features (e.g. Platten, S. J. et al., 2014).

The model produces a *potential* magnetic field such that

$$\mathbf{j} = \frac{\nabla \times \mathbf{B}}{\mu_0} = \mathbf{0}, \tag{2.1}$$

where $\mathbf{j}$ is the current density and μ_0 is the permability of free space. By using the above result the magnetic field, $\mathbf{B}$, can be written in terms of a harmonic scalar potential, *f*,

$$\mathbf{B} = -\nabla f, \tag{2.2}$$

allowing the magnetic field, $\mathbf{B}$, in spherical coordinates to be defined as,

$$\begin{aligned} B_r(r,\theta,\phi) &= -\frac{\partial f}{\partial r}, \\ B_\theta(r,\theta,\phi) &= -\frac{1}{r}\frac{\partial f}{\partial \theta}, \\ B_\phi(r,\theta,\phi) &= -\frac{1}{r\sin(\theta)}\frac{\partial f}{\partial \phi}. \end{aligned}$$

Using the solenodial constraint where,

$$\nabla \cdot \mathbf{B} = 0,$$

and substituting Equation 2.2, produces Laplace's equation,

$$\nabla^2 f = 0. \tag{2.3}$$

Hence the PFSS model solves the Laplace equation in spherical coordinates (r, θ, ϕ);

$$\frac{1}{r^2}\frac{\partial}{\partial r}\left(r^2\frac{\partial f}{\partial r}\right) + \frac{1}{r^2 \sin(\theta)}\frac{\partial}{\partial \theta}\left(\sin(\theta)\frac{\partial f}{\partial \theta}\right) + \frac{1}{r^2 \sin^2(\theta)}\frac{\partial^2 f}{\partial \phi^2} = 0, \tag{2.4}$$

to produce a potential magnetic field.

The solution to Laplace's equation is well known (e.g. Altschuler and Newkirk, 1969; Schatten et al., 1969), where

$$f(r, \theta, \phi) = \sum_{l=0}^{\infty}\sum_{m=-l}^{l}(a_l^m r^l + b_l^m r^{-(l+1)})Q_l^m(\cos(\theta))e^{im\phi}. \tag{2.5}$$

Note that the derivation of this solution and the definitions of the Legendre polynomials is discussed in Appendix A.1. Here Q_l^m are normalised Legendre polynomials and $-l \leq m \leq l$, where $l > 0$.

From Equation 2.2 and 2.5 the magnetic field components can be derived,

$$B_r(r, \theta, \phi) = \sum_{l=0}^{\infty}\sum_{m=-l}^{l} B_l^m(r)Q_l^m(\cos(\theta))e^{im\phi}, \tag{2.6}$$

$$B_\theta(r, \theta, \phi) = -\sum_{l=0}^{\infty}\sum_{m=-l}^{l} A_l^m(r)\frac{\mathrm{d}Q_l^m}{\mathrm{d}\theta}e^{im\phi}, \tag{2.7}$$

$$B_\phi(r, \theta, \phi) = -\sum_{l=0}^{\infty}\sum_{m=-l}^{l} A_l^m(r)\frac{Q_l^m(\cos(\theta))}{\sin(\theta)}e^{im\phi}im. \tag{2.8}$$

The r dependence in Equations 2.6 to 2.8 has been written in terms of two newly defined functions A_l^m and B_l^m. These functions have been defined as follows,

$$\begin{aligned} A_l^m(r) &= \frac{R(r)}{r} \\ &= a_l^m r^{l-1} + b_l^m r^{-(l+2)}, \end{aligned} \tag{2.9}$$

$$\begin{aligned} B_l^m(r) &= -\frac{\mathrm{d}}{\mathrm{d}r}(R(r)) \\ &= (l+1)b_l^m r^{-(l+2)} - l a_l^m r^{l-1}. \end{aligned} \tag{2.10}$$

Both $A_l^m(r)$ and $B_l^m(r)$ are found by applying inner and outer boundary conditions.

2.1 Boundary Conditions

The PFSS model has two boundary conditions that must be imposed to find the unknown constants a_l^m and b_l^m that are required to calculate the magnetic field components.

The model uses synoptic maps to initialise the magnetic field values at the solar surface. These synoptic maps are created by averaging out HMI observations. In general for each Carrington longitude 20 HMI magnetograms are averaged that lie closest in time to the central meridian passage. In Chapter 4 daily synoptic maps are used, which are created by replacing the Carrington synoptic maps with the data that occurred on that day for 120° in longitude, see Figure 2.1. Note however that Carrington rotation synoptic maps can also be used.

Overall the boundary conditions can be summarised as,
BC1: At the solar surface the r-component of the potential magnetic field is defined by the radial synoptic map (see Figure 2.1):

$$B_r(R_\odot, \theta, \phi) = B_\odot(\theta, \phi). \tag{2.11}$$

BC2: When r = R_{max} the magnetic field becomes purely radial, indicating the position of the *source-surface.* This results in the following assumptions;

$$B_\theta(R_{max}, \theta, \phi) = B_\phi(R_{max}, \theta, \phi) = 0, \tag{2.12}$$

$$\mathbf{B} = B_r(R_{max}, \theta, \phi)\hat{\mathbf{e}}_r.$$

These boundary conditions along with Equations 2.6 and A.16, expressing the orthogonality condition for the spherical harmonics as an integral, can be used to find an expression for $B_l^m(r)$.

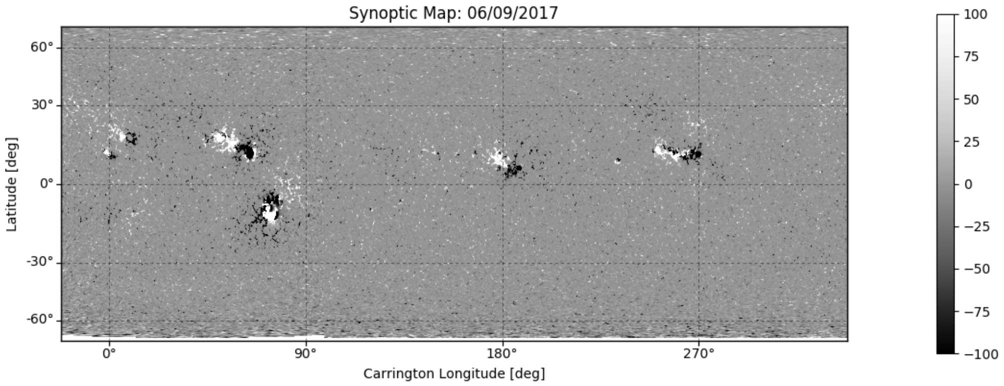

Figure 2.1: Example of a HMI daily synoptic map, these maps are used as the lower boundary condition of the PFSS model.

$$
\begin{aligned}
\int\limits_{\theta=0}^{\pi}\int\limits_{\phi=0}^{2\pi} B_r(r,\theta,\phi)\overline{Y}_l^m(\theta,\phi)\mathrm{d}S &= \int\limits_{\theta=0}^{\pi}\int\limits_{\phi=0}^{2\pi}\left(\overline{Y}_l^m(\theta,\phi)\sum_{l'=0}^{\infty}\sum_{m'=-l'}^{l'} B_{l'}^{m'}(r)Y_{l'}^{m'}(\theta,\phi)\right)\mathrm{d}S,\\
&= \sum_{l'=0}^{\infty}\sum_{m'=-l'}^{l'}\left(B_{l'}^{m'}(r)\int\limits_{\theta=0}^{\pi}\int\limits_{\phi=0}^{2\pi}\left(\overline{Y}_l^m(\theta,\phi)Y_{l'}^{m'}(\theta,\phi)\right)\mathrm{d}S\right),\\
&= B_l^m(r).
\end{aligned}
$$

By using BC1 for r=$R_\odot$, at the solar surface,

$$
B_l^m(R_\odot) = \int\limits_{\theta=0}^{\pi}\int\limits_{\phi=0}^{2\pi} B_\odot(\theta,\phi)\overline{Y}_l^m\mathrm{d}S. \tag{2.13}
$$

Equation 2.13 gives all the values of $B_l^m(r)$ at the solar surface which can be calculated using the synoptic map data. However to get the values for all $r \leq R_{max}$, the ratio of $\dfrac{B_l^m(r)}{B_l^m(R_\odot)}$ must be considered to get an expression for $B_l^m(r)$. First note that BC2 implies,

$$
A_l^m(R_{max}) = 0,
$$

as both the B_θ and B_ϕ components of the magnetic field are to be set to zero at the outer boundary. This allows Equation 2.9 to be rearranged such that,

$$
a_l^m = -b_l^m R_{max}^{-(2l+1)}. \tag{2.14}
$$

The original expression for $B_l^m(r)$, Equation 2.10, can be used to express the ratio,

$$\frac{B_l^m(r)}{B_l^m(R_\odot)} = \frac{l a_l^m r^{l-1} - (l+1) b_l^m r^{-(l+2)}}{l a_l^m R_\odot^{l-1} - (l+1) b_l^m R_\odot^{-(l+2)}}, \tag{2.15}$$

and substituting Equation 2.14 here and rearranging we get,

$$B_l^m(r) = B_l^m(R_\odot) \frac{l a_l^m r^{l-1} + (l+1) a_l^m r^{-(l+2)} R_{max}^{2l+1}}{l a_l^m R_\odot^{l-1} + (l+1) a_l^m R_\odot^{-(l+2)} R_{max}^{(2l+1)}},$$

$$= B_l^m(R_\odot) \frac{(l+1)\left(\dfrac{r}{R_\odot}\right)^{-(l+2)} + l\left(\dfrac{r}{R_\odot}\right)^{l-1}\left(\dfrac{R_\odot}{R_{max}}\right)^{(2l+1)}}{(l+1) + l\left(\dfrac{R_\odot}{R_{max}}\right)^{(2l+1)}}. \tag{2.16}$$

This gives an expression for $B_l^m(r)$ where all terms are known. Equation 2.16 and 2.9 can be used to find a similar expression for $A_l^m(r)$,

$$A_l^m(r) = B_l^m(R_\odot) \frac{\left(\dfrac{r}{R_\odot}\right)^{-(l+2)} - \left(\dfrac{r}{R_\odot}\right)^{l-1}\left(\dfrac{R_\odot}{R_{max}}\right)^{(2l+1)}}{(l+1) + l\left(\dfrac{R_\odot}{R_{max}}\right)^{(2l+1)}}. \tag{2.17}$$

Note that although all terms here can be calculated, the $(r/R_\odot)^{l-1}$ terms can become large for large values of l and so it is best to use the following forms of Equations 2.16 and 2.17,

$$B_l^m(r) = B_l^m(R_\odot)\left(\frac{r}{R_\odot}\right)^{-(l+2)} \frac{l+1+l\left(\dfrac{r}{R_{max}}\right)^{2l+1}}{l+1+l\left(\dfrac{R_\odot}{R_{max}}\right)^{2l+1}}, \tag{2.18}$$

$$A_l^m(r) = B_l^m(R_\odot)\left(\frac{r}{R_\odot}\right)^{-(l+2)} \frac{1-\left(\dfrac{r}{R_{max}}\right)^{2l+1}}{l+1+l\left(\dfrac{R_\odot}{R_{max}}\right)^{2l+1}}. \tag{2.19}$$

Using these definitions, the magnetic field components in Equations 2.6 to 2.8 can be written without any unknown constants, giving the equations needed to calculate the magnetic fields for the PFSS Model.

$$B_r(r,\theta,\phi) = \sum_{l=0}^{\infty}\sum_{m=-l}^{l} Y_l^m(\theta,\phi) B_l^m(R_\odot)\left(\frac{r}{R_\odot}\right)^{-(l+2)} \frac{l+1+l\left(\dfrac{r}{R_{max}}\right)^{2l+1}}{l+1+l\left(\dfrac{R_\odot}{R_{max}}\right)^{2l+1}} \tag{2.20}$$

$$B_\theta(r,\theta,\phi) = \sum_{l=0}^{\infty}\sum_{m=-l}^{l} \frac{\mathrm{d}Q_l^m}{\mathrm{d}\theta} e^{im\phi} B_l^m(R_\odot)\left(\frac{r}{R_\odot}\right)^{-(l+2)} \frac{\left(\dfrac{r}{R_{max}}\right)^{2l+1} - 1}{l+1+l\left(\dfrac{R_\odot}{R_{max}}\right)^{2l+1}} \tag{2.21}$$

$$B_\phi(r,\theta,\phi) = \sum_{l=0}^{\infty}\sum_{m=-l}^{l} im\frac{Y_l^m(\theta,\phi)}{\sin(\theta)} B_l^m(R_\odot)\left(\frac{r}{R_\odot}\right)^{-(l+2)} \frac{\left(\dfrac{r}{R_{max}}\right)^{2l+1} - 1}{l+1+l\left(\dfrac{R_\odot}{R_{max}}\right)^{2l+1}} \tag{2.22}$$

2.2 PFSS Codes

The codes used to produce the PFSS magnetic fields and 3D models are the BMW2016 codes discussed in Williams (2018a). These codes are mainly used in Chapter 4 where flaring active regions are analysed using potential magnetic fields. In this section the general steps of calculating the potential magnetic fields produced by the model are discussed.

2.2.1 Synoptic Map Processing

To run these codes synoptic maps are used as the bottom boundary condition, as discussed in Section 2.1. These maps are obtained from the *Joint Science Operations Centre*, JSOC and are 3600 × 1440 radial magnetograms that are created from HMI 720s line-of-sight magnetograms. Although Carrington synoptic maps can be used for the PFSS model, daily synoptic maps will be used for most of our analysis. These daily synoptic maps replace 120 degrees of data in longitude with the HMI data observed on the solar disk at any one time.

To produce a global potential field the polar field values must be determined and placed into the synoptic map. This is required as some of the polar values are missing from the original synoptic map data as the HMI instrument on SDO cannot observe all points on the solar disc. As in Williams (2018a), these polar values are found by using the mean polar field values which are given in other HMI data files over several latitudes. This is calculated by converting LOS magnetograms to a radial field and taking a weighted 27.2 day average, (see JSOC for data products *hmi.meanpf_720s* and for more information Sun et al. (2015)). The mean values were used for latitudes greater than 70 degrees, as these positions are where we start to see gaps in the observational data. For the daily synoptic maps a 30 day average was taken of all the polar values around the date given. If the synoptic map had some values already at the poles - perhaps when one pole was visible - then the data is smoothed such that no discontinuities occur. This data smoothing is assumed to have little affect on the fields later analysed in Chapter 4 as many of the regions analysed are lying far from the polar regions and most features found were local to those regions.

The final step in preparing the data is ensuring that the solenodial constraint is satisfied over the whole field. To do this the mean net magnetic field value is subtracted from all the pixels in the synoptic map.

2.2.2 Model Calculations

The PFSS Model uses the Legendre polynomials, Q_m^l discussed in Section A.1.1, particularly using Eqns A.18 to A.23 to create an equidistant grid for the θ components. This results in two arrays being formed containing the polynomials such that:

- a ***plm*** array is created where the Legendre polynomials used are calculated for a grid equidistant in $\cos(\theta)$,
- a ***qlm*** array is created where the Legendre polynomials used are calculated for a grid equidistant in θ.

Both of these arrays are calculated in the PFSS routine. The original synoptic map data used has a grid equidistant in $\cos(\theta)$, hence the *plm* array is needed. However the final grid used in the PFSS model must be equidistant in θ and ϕ, hence both arrays must be formed.

There are also two routines in the code which calculate the derivatives of the Legendre polynomials. Instead of calculating derivatives numerically we use recurrance relations to get the exact values. These derivatives are needed to calculate the final B_θ component of the magnetic field as in Equation 2.21.

The final potential field in the PFSS code is calculated and stored on a $n_r \times n_\theta \times n_\phi$ grid. To do this a maximum number of harmonics, l, must be set due to being unable to computationally add an infinite number of terms as needed in Equations 2.20 to

2.22. Hence the field is calculated in the range $l = [0, L]$ and $m = [-l, l]$. This L is picked depending on the memory available within the computing resources used. However it should be noted that the original synoptic map $n_\theta = 1440$ so as L gets closer to this value, the resolution and accuracy of the field calculated will become better. However note that typically $L \leq 1440$ so the field is not extrapolated past the original synoptic map size. This also means that $n_\phi \leq 3600$ so that the ϕ grid is also not over extrapolated.

Before this final field is calculated a Gaussian filter is applied to the magnetic field components where,

$$B_l^m(R_\odot) = I_l^m e^{\frac{-\pi^2 l(l+1)}{4a^2}},$$

$$I_l^m = \int\int_S B_\odot(\theta, \phi)\overline{Y_l^m}(\theta, \phi)dS.$$

Note that a is a parameter that can be chosen, the value used here is consistent with that used by (Williams, 2018a). This smoothing could cause the loss of smaller scale features if they depend on small changes in the magnetic field that may be lost when the Gaussian filter is applied. Therefore, it is important to apply an appropriate strength filter such that it does not impact the magnetic field features found. The affect of this parameter was not investigated in this work, however could provide further insight into finding small scale null features.

Smoothing allows the use of a high number of spherical harmonics whilst preventing the occurrence of *ringing.* This ringing (also known as the Gibbs Phenomenon) occurs when there are large variations or discontinuities in the magnetic field causing a oscillating pattern to occur. This can occur frequently at regions of strong varying polarity, such as sunspots, which are found in active regions - studied in Chapter 4.

Within these PFSS codes, fast Fourier transforms (FFTs) are used to calculate the magnetic fields. Due to this method being used there must be a limit on the size of the ϕ grid due to the array sizes and computation time needed to calculate the fields. As used in the BMW2016 codes, the grid sizes are set such that,

$$n_r = \frac{2(L+1)}{\pi} log \frac{R_{max}}{R_\odot},$$

$$n_\theta = L + 2,$$

$$n_\phi = 2L + 3.$$

Where the final grid has values between, $1 \leq r \leq 2.5, 0 \leq \theta \leq \pi$ and $0 \leq \phi \leq 2\pi$. It should be noted that the values of r are calculated on an exponential grid such that there are more points closer to the solar surface, with less towards the upper limit at $r = 2.5$.

2.2.3 Summation of Harmonics

As previously discussed FFTs are used to calculate the magnetic field components, however instead of carrying out the summation terms initially over $-l \leq m \leq l$ as in Equations 2.6 to 2.8, here the FFT routines are initially summed over $|m| \leq l \leq L$, (e.g., see Ballegooijen et al., 1998; Williams, 2018a). For example Equation 2.6 would become,

$$B_r(r,\theta,\phi) = \sum_{m=-L}^{L} e^{im\phi}\Bigg(\sum_{l=|m|}^{L} B_l^m(r)Q_l^m(\theta)\Bigg), \tag{2.23}$$

which can subsequently be calculated using a discrete Fourier transform.

For a continuous function, f, the Fourier transform is given by,

$$\hat{f}(y) = \int_{-\infty}^{\infty} e^{-2\pi ixy} f(x)dx, \tag{2.24}$$

with its equivalent discrete Fourier transform written as,

$$y_k = \sum_{n=0}^{N-1} e^{-\frac{2n\pi ki}{N}} x_n. \tag{2.25}$$

Here both x_n and y_n are points in two one-dimensional arrays of length N, with x denoting the input array and y denoting the output array. We also define the discrete inverse Fourier transform as,

$$x_k = \frac{1}{N}\sum_{n=0}^{N-1} e^{\frac{i2kn\pi}{N}} y_n. \tag{2.26}$$

The exponential terms in Equations 2.23 and 2.26 can be equated to note that each $\phi = \frac{2\pi k}{N}$. This makes it easier to see how the Fourier transforms would be applied here.

Note that the summation in Equation 2.26 only calculates the values where $m \geq 0$, so using Equation A.22 the values for Q_l^{-m} can be calculated. This can be done by simply taking the conjugate of FFT values for $m \geq 0$, similarly to what is done in Williams (2018a) where

$$B_l^{-m}(x)Y_l^{-m}(x) \equiv \overline{B_l^m(x)Y_l^m(x)}.$$

As in the original codes an FFT is used to calculate both the inner and outer summations which significantly improves the computation time, which is longer when calculating the outer sum directly.

Chapter 3

Global Magnetohydrostatic Model

This chapter discusses extensions to the global magnetohydrostatic (MHS) model developed by Williams (2018a) which was previously developed for the case of no parallel currents ($\alpha = 0$). As this model is used for the analysis of magnetic field regions in this work, the derivations of the magnetic field components that are calculated in the subsequent code are shown below.

In contrast to Williams (2018a) we allow the component of the current parallel to the magnetic field to be non-zero. Although this method was discussed in that work, it was never investigated how varying the parallel current would affect the global MHS models created. Below we carry out a similar analysis as that done for the case where the parallel current is zero.

3.1 Magnetic field derivations

We will now derive the theory of analytical MHS equilibria, where we make the assumptions that:

1. A spherical coordinate system is being implemented, where we assume the gravitational potential $\psi = -\frac{GM}{r}$ such that;

$$\nabla\psi = \frac{GM}{r^3}\mathbf{r}. \tag{3.1}$$

2. M is assumed to be the mass of the star (here the Sun) being studied.

Initially we consider similar equations as those previously discussed in Chapter 2 with the magnetohydrostatic (MHS) equations given as follows,

$$\mathbf{j} \times \mathbf{B} - \nabla p - \rho \nabla \psi = \mathbf{0}, \tag{3.2}$$

$$\nabla \times \mathbf{B} = \mu_0 \mathbf{j}, \tag{3.3}$$

$$\nabla \cdot \mathbf{B} = 0, \tag{3.4}$$

where Equation 3.2 shows the force balance equation, Equation 3.3 shows Ampères Law and Equation 3.4 shows the solenodial constraint.

We also assume that the current density takes the form;

$$\mathbf{j} = \alpha \mathbf{B} + \nabla F \times \nabla \psi, \tag{3.5}$$

as suggested by (e.g. Bogdan and Low, 1986; Low, 1991). Note, throughout we assume $\alpha = \textit{constant}$ and F is a free function. First, we can substitute Equation (3.5) into Ampére's Law (Equation (3.3) to get,

$$\nabla \times \mathbf{B} = \mu_0(\alpha \mathbf{B} + \nabla F \times \nabla \psi). \tag{3.6}$$

Taking the curl of Equation 3.6, which is shown in Appendix A.2, and dotting the result, Equation A.26, with $\mathbf{r}$, we get the following;

$$\mathbf{r} \cdot (\nabla \times (\nabla \times \mathbf{B})) = \mu_0(\alpha^2 \mu_0 \mathbf{r} \cdot \mathbf{B} + \mathbf{r} \cdot \nabla \times (\nabla F \times \nabla \psi)). \tag{3.7}$$

To expand this equation further we must first find a form for $\nabla F \times \nabla \psi$, therefore we let F take the form;

$$\begin{aligned} F &= \kappa(\psi) \nabla \psi \cdot \mathbf{B} \\ &= \kappa(\psi) \frac{GM}{r^3} \mathbf{r} \cdot \mathbf{B}, \end{aligned} \tag{3.8}$$

and following this definition we find,

$$\begin{aligned} \nabla F \times \nabla \psi &= \nabla(\kappa(\psi) \frac{GM}{r^3} \mathbf{r} \cdot \mathbf{B}) \times \frac{GM}{r^3} \mathbf{r}, \\ &= \xi(r) \nabla(\mathbf{r} \cdot \mathbf{B}) \times \mathbf{r}, \end{aligned} \tag{3.9}$$

with the full derivation of this result shown in Appendix A.2 (Equation A.28).

Using this result we can substitute this back into Equation 3.7 and rearrange to get;

$$\nabla^2(\mathbf{r}\cdot\mathbf{B}) + \alpha^2\mu_0^2(\mathbf{r}\cdot\mathbf{B}) + \mu_0\mathbf{r}\cdot\nabla\times(\xi(r)\nabla(\mathbf{r}\cdot\mathbf{B})\times\mathbf{r}) = 0, \tag{3.10}$$

where the simplification of the LHS of Equation 3.7 is shown in Equation A.27.

To simplify Equation 3.10 we consider the 3rd term. This can be simplified by considering;

$$\begin{aligned}
\nabla\times(\xi(r)\nabla(\mathbf{r}\cdot\mathbf{B})\times\mathbf{r}) &= (\mathbf{r}\cdot\nabla)\xi(r)\nabla(\mathbf{r}\cdot\mathbf{B}) - (\xi(r)\nabla(\mathbf{r}\cdot\mathbf{B})\cdot\nabla)\mathbf{r}\\
&\quad + (\nabla\cdot\mathbf{r})\xi(r)\nabla(\mathbf{r}\cdot\mathbf{B}) - (\nabla\cdot\xi(r)\nabla(\mathbf{r}\cdot\mathbf{B}))\mathbf{r},\\
&= (\mathbf{r}\cdot\nabla)\xi(r)\nabla(\mathbf{r}\cdot\mathbf{B}) - \xi(r)\nabla(\mathbf{r}\cdot\mathbf{B}) + 3\xi(r)\nabla(\mathbf{r}\cdot\mathbf{B})\\
&\quad - (\nabla\cdot\xi(r)\nabla(\mathbf{r}\cdot\mathbf{B}))\mathbf{r},\\
&= (\mathbf{r}\cdot\nabla)\xi(r)\nabla(\mathbf{r}\cdot\mathbf{B}) + 2\xi(r)\nabla(\mathbf{r}\cdot\mathbf{B}) - (\nabla\cdot\xi(r)\nabla(\mathbf{r}\cdot\mathbf{B}))\mathbf{r},\\
&= 2\xi(r)\nabla(\mathbf{r}\cdot\mathbf{B}) - (\nabla\cdot\xi(r)\nabla(\mathbf{r}\cdot\mathbf{B}))\mathbf{r} + r\frac{\partial}{\partial r}(\xi(r)\nabla(\mathbf{r}\cdot\mathbf{B})),\\
&= 2\xi(r)\nabla(\mathbf{r}\cdot\mathbf{B}) - (\nabla\cdot\xi(r)\nabla(\mathbf{r}\cdot\mathbf{B}))\mathbf{r} + r\frac{\partial\xi(r)}{\partial r}\nabla(\mathbf{r}\cdot\mathbf{B})\\
&\quad + r\xi(r)\frac{\partial}{\partial r}(\nabla(\mathbf{r}\cdot\mathbf{B})),\\
&= 2\xi(r)\nabla(\mathbf{r}\cdot\mathbf{B}) - \mathbf{r}\nabla\xi(r)\cdot\nabla(\mathbf{r}\cdot\mathbf{B}) - \xi(r)\mathbf{r}(\nabla\cdot\nabla(\mathbf{r}\cdot\mathbf{B}))\\
&\quad + r\frac{\partial\xi}{\partial r}\nabla(\mathbf{r}\cdot\mathbf{B}) + r\xi(r)\frac{\partial}{\partial r}(\nabla(\mathbf{r}\cdot\mathbf{B})).
\end{aligned}$$

Following this result we can now consider,

$$\begin{aligned}
\mathbf{r}\cdot(\nabla\times(\xi(r)\nabla(\mathbf{r}\cdot\mathbf{B})\times\mathbf{r})) &= \mathbf{r}\cdot(2\xi(r)\nabla(\mathbf{r}\cdot\mathbf{B}) - \mathbf{r}\nabla\xi(r)\cdot\nabla(\mathbf{r}\cdot\mathbf{B}) - \xi(r)\mathbf{r}(\nabla^2(\mathbf{r}\cdot\mathbf{B}))\\
&\quad + r\frac{\partial\xi}{\partial r}\nabla(\mathbf{r}\cdot\mathbf{B}) + r\xi(r)\frac{\partial}{\partial r}(\nabla(\mathbf{r}\cdot\mathbf{B}))),\\
&= 2r\xi(r)\frac{\partial}{\partial r}(\mathbf{r}\cdot\mathbf{B}) - r^2\frac{\partial\xi}{\partial r}\frac{\partial}{\partial r}(\mathbf{r}\cdot\mathbf{B}) - r^2\xi(r)\nabla^2(\mathbf{r}\cdot\mathbf{B})\\
&\quad + r^2\frac{\partial\xi}{\partial r}\frac{\partial}{\partial r}(\mathbf{r}\cdot\mathbf{B}) + r^2\xi(r)\frac{\partial^2}{\partial r^2}(\mathbf{r}\cdot\mathbf{B}),\\
&= \xi(r)\bigg(2r\frac{\partial}{\partial r}(\mathbf{r}\cdot\mathbf{B}) - r^2\nabla^2(\mathbf{r}\cdot\mathbf{B}) + r^2\frac{\partial^2}{\partial r^2}(\mathbf{r}\cdot\mathbf{B})\bigg),\\
&= \xi(r)\bigg(\frac{\partial}{\partial r}\bigg(r^2\frac{\partial}{\partial r}(\mathbf{r}\cdot\mathbf{B})\bigg) - r^2\nabla^2(\mathbf{r}\cdot\mathbf{B})\bigg).
\end{aligned} \tag{3.11}$$

We can introduce the operator, $\mathbf{L}$, such that;

$$\mathbf{L} = \frac{1}{i}\mathbf{r} \times \nabla, \tag{3.12}$$

and this definition can be used to simplify Equation 3.11 where,

$$\mathbf{r} \cdot \nabla \times (\nabla F \times \nabla \psi) = \xi(r)\mathbf{L}^2(\mathbf{r} \cdot \mathbf{B}). \tag{3.13}$$

This equation can be substituted back into Equation 3.10 to get the radial component of the magnetic field in the form of a partial differential equation;

$$\begin{aligned} \nabla^2(\mathbf{r} \cdot \mathbf{B}) + \alpha^2\mu_0^2(\mathbf{r} \cdot \mathbf{B}) + \mu_0\mathbf{r} \cdot \nabla \times (\xi(r)\nabla(\mathbf{r} \cdot \mathbf{B}) \times \mathbf{r}) &= 0, \\ \nabla^2(\mathbf{r} \cdot \mathbf{B}) + \alpha^2\mu_0^2(\mathbf{r} \cdot \mathbf{B}) + \mu_0\xi(r)\mathbf{L}^2(\mathbf{r} \cdot \mathbf{B}) &= 0, \\ \nabla^2(\mathbf{r} \cdot \mathbf{B}) + \bar{\alpha}^2(\mathbf{r} \cdot \mathbf{B}) + \bar{\xi}(r)\mathbf{L}^2(\mathbf{r} \cdot \mathbf{B}) &= 0, \end{aligned} \tag{3.14}$$

where,

$$\bar{\alpha} = \alpha\mu_0 \qquad \text{and} \qquad \bar{\xi}(r) = \xi(r)\mu_0. \tag{3.15}$$

Equation 3.14 can be used to find the B_r component of the magnetic field, however to solve the partial differential equation separation of variables is used to simplify the $\mathbf{r} \cdot \mathbf{B}$ component. Therefore we let,

$$\mathbf{r} \cdot \mathbf{B} = R(r)T(\theta)P(\phi),$$

and substituting into Equation 3.14 we get,

$$\begin{aligned} \frac{TP}{r^2}\frac{\partial}{\partial r}\left(r^2\frac{dR}{dr}\right) + \frac{RP}{r^2\sin\theta}\frac{\partial}{\partial\theta}\left(\sin\theta\frac{dT}{d\theta}\right) + \frac{RT}{r^2\sin^2\theta}\frac{d^2P}{d\phi^2} + \bar{\alpha}^2RTP \\ -\bar{\xi}\frac{RP}{r^2\sin\theta}\frac{d}{d\theta}\left(\sin\theta\frac{dT}{d\theta}\right) - \bar{\xi}\frac{RT}{r^2\sin^2\theta}\frac{d^2P}{d\phi^2} = 0; \end{aligned}$$

$$\frac{1}{r^2R}\frac{d}{dr}\left(r^2\frac{dR}{dr}\right) + \left(\frac{1}{r^2} - \bar{\xi}\right)\left(\frac{1}{T\sin\theta}\frac{d}{d\theta}\left(\sin\theta\frac{dT}{d\theta}\right) + \frac{1}{P\sin^2\theta}\frac{d^2P}{d\phi^2}\right) + \bar{\alpha}^2 = 0.$$

Using a separation constant, λ, to carry out separation of variables we get;

$$\frac{1}{T\sin\theta}\frac{d}{d\theta}\left(\sin\theta\frac{dT}{d\theta}\right) + \frac{1}{P\sin^2\theta}\frac{d^2P}{d\phi^2} = -\lambda, \tag{3.16}$$

$$\frac{1}{r^2R}\frac{d}{dr}\left(r^2\frac{dR}{dr}\right)-\lambda\left(\frac{1}{r^2}-\bar{\xi}\right)+\bar{\alpha}^2=0. \tag{3.17}$$

Equation 3.16 is the same equation we solve for the PFSS model, shown in Chapter 2 which has spherical harmonics $Y_l^m(\theta,\phi)$, (see Jackson, 1975), as solutions where $\lambda=l(l+1)$ and $-l\leq m\leq l$. Finding the solution to Equation 3.16 is shown in Section A.1.1.

Therefore there is only the r-dependent solution to consider here, which differs to the r-dependent solution of the PFSS model. To find solutions to Equation 3.17 we must choose $\bar{\xi}(r)$ such that the differential equation becomes solvable using known functions. This means we can assume that the solutions are a sum of two functions with a linear dependence on r, for example;

$$\mathbf{r}\cdot\mathbf{B}=\sum_{l=0}^{\infty}\sum_{m=-l}^{l}B_l^m(r)Y_l^m(\theta,\phi). \tag{3.18}$$

Therefore we can define B_r as;

$$B_r=\sum_{l=0}^{\infty}\sum_{m=-l}^{l}\frac{B_l^m(r)}{r}Y_l^m(\theta,\phi), \tag{3.19}$$

and to find B_θ and B_ϕ we must again consider $\mathbf{L}$, previously defined as,

$$\mathbf{L}=\frac{1}{i}\mathbf{r}\times\nabla=\frac{1}{i}\left(0,-\frac{1}{\sin\theta}\frac{\partial}{\partial\phi},\frac{\partial}{\partial\theta}\right). \tag{3.20}$$

From this we can find $\mathbf{L}^2$;

$$\mathbf{L^2}=\mathbf{L}\cdot\mathbf{L}=-\frac{1}{\sin\theta}\frac{\partial}{\partial\theta}\left(\sin\theta\frac{\partial}{\partial\theta}\right)-\frac{1}{\sin^2\theta}\frac{\partial^2}{\partial\phi^2}.$$

Returning to Equation 3.6 we can find the magnetic field components by first taking;

$$\mathbf{r}\cdot\nabla\times\mathbf{B}=\mu_0\alpha\mathbf{r}\cdot\mathbf{B},$$

which can be simplified using vector identities and the angular momentum where;

$$\begin{aligned}\mathbf{r}\times\nabla\cdot\mathbf{B}&=\mu_0\alpha\mathbf{r}\cdot\mathbf{B},\\ i\mathbf{L}\cdot\mathbf{B}&=\mu_0\alpha\mathbf{r}\cdot\mathbf{B}.\end{aligned} \tag{3.21}$$

As $\mathbf{L}$ has no radial component we can simplify Equation 3.21 by using Equation 3.18;

$$\begin{aligned}
\mathbf{L}\cdot\mathbf{B_t} &= \frac{\mu_0\alpha}{i}\mathbf{r}\cdot\mathbf{B},\\
\mathbf{L}\cdot\mathbf{B_t} &= \frac{\bar{\alpha}}{i}\mathbf{r}\cdot\mathbf{B},\\
\mathbf{L}\cdot\mathbf{B_t} &= \frac{\bar{\alpha}}{i}\sum_{l=0}^{\infty}\sum_{m=-l}^{l} B_l^m(r)Y_l^m(\theta,\phi),
\end{aligned}\tag{3.22}$$

where we let $\mathbf{B_t} = B_\theta\mathbf{e}_\theta + B_\phi\mathbf{e}_\phi$. From Neukirch (1995) we can assume that $\mathbf{B_t}$ takes the form:

$$\mathbf{B_t} = \sum_{l=0}^{\infty}\sum_{m=-l}^{l} v_{l,m}(r)\mathbf{L}Y_l^m(\theta,\phi) + w_{l,m}\nabla Y_l^m(\theta,\phi). \tag{3.23}$$

We can find the general forms of both $v_{l,m}(r)$ and $w_{l,m}(r)$ by substituting this definition of $\mathbf{B_t}$ into Equations 3.22 and 3.4, with the details of both derivations shown in Appendix A.2 (see Equations A.30 and A.31). If we substitute Equation 3.23 into Equation 3.22 and consider a single order element,

$$v_{l,m}(r) = \frac{\bar{\alpha}}{i}\frac{B_l^m(r)}{l(l+1)}. \tag{3.24}$$

We consider $\nabla\cdot\mathbf{B} = 0$ such that;

$$\nabla\cdot\mathbf{B} = \frac{1}{r^2}\frac{\partial}{\partial r}\left(r^2\frac{B_l^m(r)}{r}Y_l^m(\theta,\phi)\right) + \nabla\cdot(v_{l,m}\mathbf{L}Y_l^m(\theta,\phi)) + \nabla\cdot(w_{l,m}(r)\nabla Y_l^m(\theta,\phi)) = 0,$$

where,

$$w_{l,m} = \frac{1}{l(l+1)}\frac{d}{dr}(rB_l^m(r)). \tag{3.25}$$

We can now write the final form of the magnetic field as;

$$\begin{aligned}
\mathbf{B} = \sum_{l=0}^{\infty}\sum_{m=-l}^{l}\Bigg(&\mathbf{r}\frac{B_l^m(r)}{r^2}Y_l^m(\theta,\phi) + \frac{\bar{\alpha}}{i}\frac{B_l^m(r)}{l(l+1)}\mathbf{L}Y_l^m(\theta,\phi)\\
&+\frac{d}{dr}(rB_l^m(r))\frac{\nabla Y_l^m(\theta,\phi)}{l(l+1)}\Bigg),
\end{aligned}\tag{3.26}$$

and using Equation A.17 this can also be written component-wise;

$$B_r(e,\theta,\phi) = \sum_{l=0}^{\infty}\sum_{m=-l}^{l}\frac{B_l^m(r)}{r}Y_l^m(\theta,\phi), \tag{3.27}$$

$$\begin{aligned} B_\theta(r,\theta,\phi) = \sum_{l=0}^{\infty}\sum_{m=-l}^{l}\frac{1}{l(l+1)}\bigg(&\bar{\alpha}B_l^m(r)im\frac{Q_l^m(\theta)}{sin\theta}e^{im\phi} \\ &+\frac{1}{r}\frac{d}{dr}(rB_l^m(r))\frac{dQ_l^m(\theta)}{d\theta}e^{im\phi}\bigg), \end{aligned} \tag{3.28}$$

$$\begin{aligned} B_\phi(r,\theta,\phi) = \sum_{l=0}^{\infty}\sum_{m=-l}^{l}\frac{1}{l(l+1)}\bigg(&-\bar{\alpha}B_l^m(r)\frac{dQ_l^m(\theta)}{d\theta}e^{im\phi} \\ &+\frac{1}{r}\frac{d}{dr}(rB_l^m(r))im\frac{Q_l^m(\theta)}{sin\theta}e^{im\phi}\bigg). \end{aligned} \tag{3.29}$$

3.2 Plasma Pressure and Density derivations

The plasma pressure and density of the magnetohydrostatic (MHS) magnetic fields can be calculated to check that the parameters chosen for the magnetic field models $(\bar{\alpha}, d)$ keep these quantities physical, whilst also investigating how the parameters change these quantities. To derive the relevant plasma pressure and density equations we return to the force balance equation (see Equation 3.2),

$$\mathbf{j}\times\mathbf{B} - \nabla p - \rho\nabla\psi = \mathbf{0},$$

and use the definition of the current density, see Equation 3.5, to obtain

$$\begin{aligned} \nabla p + \rho\nabla\psi - (\alpha\mathbf{B} + \nabla F\times\nabla\psi)\times\mathbf{B} &= \mathbf{0}; \\ \nabla p + \rho\nabla\psi - (\mathbf{B}\cdot\nabla F)\nabla\psi + (\mathbf{B}\cdot\nabla\psi)\nabla F &= \mathbf{0}. \end{aligned} \tag{3.30}$$

Here we assume that $\nabla\psi$ and ∇F are linearly independent such that $p = p(F,\psi)$ and hence Equation 3.30 becomes

$$\frac{\partial p}{\partial F}\nabla F + \frac{\partial p}{\partial\psi}\nabla\psi + \rho\nabla\psi + (\mathbf{B}\cdot\nabla\psi)\nabla F - (\mathbf{B}\cdot\nabla F)\nabla\psi = \mathbf{0}. \tag{3.31}$$

Since we have assumed linear independence, the equation can be split into the two following equations,

$$\frac{\partial p}{\partial F} + \mathbf{B}\cdot\nabla\psi = 0, \tag{3.32}$$

$$\frac{\partial p}{\partial\psi} + \rho - \mathbf{B}\cdot\nabla F = 0. \tag{3.33}$$

We can use the definition of F, Equation 3.8, to simplify Equation 3.32,

$$\frac{\partial p}{\partial F} + \frac{F}{\kappa(\psi)} = 0,$$

this equation can subsequently be integrated with respect to F to get an equation for pressure where;

$$p(r,\theta,\phi) = p_0(\psi) - \frac{F^2}{2\kappa(\psi)}. \tag{3.34}$$

Again using the definition of F we get,

$$\begin{aligned} p(r,\theta,\phi) &= p_0(r) - \frac{\xi(r)}{2}(\mathbf{r}\cdot\mathbf{B})^2 \\ &= p_0(r) - \frac{\bar{\xi}(r)}{2\mu_0}(\mathbf{r}\cdot\mathbf{B})^2, \end{aligned} \tag{3.35}$$

where $p_0(r)$, which is a free function, represents a background pressure.

Using Equations 3.33 and 3.35 we can derive an expression for the density of the global MHS model, (for details see Bogdan and Low, 1986; Neukirch, 1995). Using both equations and changing the derivative of the pressure with respect to ψ in Equation 3.33 to the derivative with respect to r, along with the definition of F (as in Equation 3.8) we get the following expression for the density of the model;

$$\rho(r,\theta,\phi) = \frac{r^2}{\mu_0 GM}\left(\frac{1}{2}\frac{d\bar{\xi}}{dr}(\mathbf{r}\cdot\mathbf{B})^2 + r\bar{\xi}\mathbf{B}\cdot\nabla(\mathbf{r}\cdot\mathbf{B}) - \mu_0\frac{dp_0}{dr}\right). \tag{3.36}$$

Both the pressure and density of the MHS fields can now be calculated and in principle the ideal gas law can be used to define the plasma temperature,

$$T = \frac{\mu p}{\rho R_{gas}}, \tag{3.37}$$

where μ is the mean molecular weight and R_{gas} is the gas constant.

We can now apply the boundary conditions of the model to calculate the function B_l^m which is used to define the magnetic field components.

3.3 Imposing Boundary Conditions on the MHS Model

As shown in Williams (2018a) the MHS model created could have a source surface similar to that which is present in the potential field source surface (PFSS) model in Chapter 2. In total two different boundary conditions were used for the MHS model created. These included:

1. when $\alpha = 0$ the same BCs used for the PFSS model are applied,

2. when $\alpha \neq 0$ we relax the PFSS BCs previously used (parts of $B_\theta, B_\phi \neq 0$, however an outer boundary is still set, which is discussed below) which we refer to as the source-surface.

To implement boundary condition 1 i.e. when $\alpha = 0$ we can use similar assumptions to those used in the potential field model. Boundary condition 2 is created by setting parts of the magnetic field which are not dependent on α to zero at the outer boundary, this is discussed in Section 3.3.1.

We can first choose a form for $\bar{\xi}(r)$, the function we use was initially used by Bogdan and Low (1986) and again implemented by Neukirch (1995) where,

$$\bar{\xi}(r) = \frac{1}{r^2} - \frac{1}{(r+d)^2}, \tag{3.38}$$

and d is a constant which relates to the amount of current in the model which is perpendicular to the gravitational force (which is radial for a spherical mass). This constant can now be used to find the analytical solutions of Equation 3.17 which were previously denoted by some function $B_l^m(r)$. Hence equation 3.17 becomes,

$$\frac{1}{r}\frac{d}{dr}\left(r^2\frac{dR}{dr}\right) + \left(\bar{\alpha}^2 - \frac{l(l+1)}{(r+d)^2}\right)rR = 0,$$

which can be simplified to,

$$\frac{d^2}{dr^2}(rR) + \left(\bar{\alpha}^2 - \frac{l(l+1)}{(r+d)^2}\right)rR = 0. \tag{3.39}$$

Equation 3.39 can now be solved for varying values of α. If we first consider $\alpha = 0$, the solutions are similar to those found in the PFSS model, such that

$$\frac{d^2}{dr^2}(rR) - \frac{l(l+1)}{(r+d)^2}rR = 0.$$

This equation is simplified further by creating two new variables such that the equation becomes a simple second order differential equation. These variables are chosen to be,

$$u(r) = rR \quad \text{and} \quad v(r) = \log(r+d),$$

and so the differential equation can be written as,

$$\frac{d^2u}{dv^2} - \frac{du}{dv} - l(l+1)u = 0.$$

This equation can be solved for $u(v)$, however as we want an equation with respect to r, we can rearrange the solution so that,

$$R(r) = \frac{(r+d)^{l+1}}{r}a + \frac{(r+d)^{-l}}{r}b,$$

where a and b are constants of integration. As previously mentioned we chose to call the solutions of the equation $B_l^m(r)$ and so we can transform the solutions with constants a_l^m and b_l^m which are dependent on l and m. The final solutions have the form,

$$B_l^m(r) = \frac{(r+d)^{l+1}}{r}a_l^m + \frac{(r+d)^{-l}}{r}b_l^m. \tag{3.40}$$

Equation 3.39 has different solutions when $\alpha \neq 0$. First a substitution must be made to transform the equation into a second order differential equation. Hence, we substitute:

$$rR = (r+d)^{\frac{1}{2}}u(v) \quad \text{with} \quad v(r) = \bar{\alpha}(r+d),$$

to get a differential equation of the form:

$$v^2\frac{d^2u}{dv^2} + v\frac{dv}{du} + \left(v^2 - \left(l + \frac{1}{2}\right)^2\right)u = 0.$$

Therefore, the solutions for $u(v)$ are Bessel functions and our solution is,

$$B_l^m(r) = \frac{\sqrt{r+d}}{r}\big(a_l^m J_{l+\frac{1}{2}}(\bar{\alpha}(r+d)) + b_l^m N_{l+\frac{1}{2}}(\bar{\alpha}(r+d))\big). \tag{3.41}$$

Note that J_z and N_z are half-integer Bessel functions (`https://dlmf.nist.gov/10.47`). This solution was originally derived in Neukirch (1995) and discussed further in Williams (2018a). Similarly to those works we simplify our equation further by defining two new functions $\bar{J}_z(r)$ and $\bar{N}_z(r)$, which will allow the MHS field components to be written in a similar format to those previously derived in Chapter 2 for the PFSS model. Hence we can write Equation 3.41 as,

$$B_l^m(r) = \frac{\sqrt{r+d}}{r}\big(a_l^m \bar{J}_{l+\frac{1}{2}}(r) + b_l^m \bar{N}_{l+\frac{1}{2}}(r)\big). \tag{3.42}$$

This allows the boundary conditions to be applied to calculate the unknown constants a_l^m and b_l^m.

The boundary condition applied at the base of the magnetic field is identical to that used in the PFSS model. It requires the radial component of the magnetic field at the bottom boundary to be equivalent to that taken from the radial component of the synoptic map used, for example;

$$B_r(R_\odot, \theta, \phi) = B_\odot(\theta, \phi).$$

In a similar way to the B_l^m derived for the PFSS model, we can define our variable as,

$$B_l^m(R_\odot) = R_\odot \int_{\phi=0}^{2\pi} \int_{\theta=0}^{\pi} B_\odot(\theta, \phi) \bar{Y_l^m}(\theta, \phi) dS. \tag{3.43}$$

3.3.1 Outer Boundary Conditions

The outer boundary conditions for $\bar{\alpha} = 0$ and $\bar{\alpha} \neq 0$ were previously discussed in Williams (2018a). The boundary conditions used in the MHS models here are unchanged from those previously discussed in the PFSS model (see Chapter 2). They are reproduced here for the benefit of the reader.

For $\bar{\alpha} = 0$, a source-surface similar to that seen in the PFSS model is present with the magnetic field becoming purely radial at $R = R_{ss}$. This means that,

$$\frac{d}{dr}(rB_l^m)|_{R=R_{ss}} = 0, \tag{3.44}$$

to allow the B_θ and B_ϕ terms to go to zero. When applying this to find the value of $B_l^m(r)$ we get,

$$a_l^m = -\frac{l+1}{l}(R_{ss}+d)^{2l+1} b_l^m,$$

with a similar technique applied here as to what was previously carried out in the PFSS model analysis, where by substituting this into Equation 3.40 and using the lower boundary condition we find,

$$\frac{B_l^m(r)}{r} = B_l^m(R_\odot)\frac{R_\odot^2}{r^2}\left(\frac{R_\odot+d}{r+d}\right)^l \frac{l+1+l\left(\dfrac{r+d}{R_{ss}+d}\right)^{2l+1}}{l+1+l\left(\dfrac{R_\odot+d}{R_{ss}+d}\right)^{2l+1}},$$

and,

$$\frac{1}{r}\frac{d}{dr}(rB_l^m) = l(l+1)B_l^m(R_\odot)\frac{R_\odot^2}{r^2}\frac{(R_\odot+d)^l}{(r+d)^{l+1}} \frac{\left(\dfrac{r+d}{R_{ss}+d}\right)^{2l+1} - 1}{l+1+l\left(\dfrac{R_\odot+d}{R_{ss}+d}\right)^{2l+1}}.$$

For $\bar{\alpha} \neq 0$ one part of the tangential magnetic field is set to zero, this is the part of Equation 3.26 which does not depend on $\bar{\alpha}$. This will allow the creation of an outer boundary similar to that produced when $\bar{\alpha} = 0$. Here we cannot set $B_l^m(r) = 0$ at $R = R_{ss}$ as the radial component of the magnetic field would be zero at the maximum R value, therefore we assume $B_l^m(r) \neq 0$. This allows us to use the same assumption as shown in Equation 3.44 which subsequently results in the value of a_l^m when $\bar{\alpha} \neq 0$ to be,

$$a_l^m = -\frac{2\bar{\alpha}(R_{ss}+d)\bar{N}'_{l+\frac{1}{2}}(R_{ss}) + \bar{N}_{l+\frac{1}{2}}(R_{ss})}{2\bar{\alpha}(R_{ss}+d)\bar{J}'_{l+\frac{1}{2}}(R_{ss}) + \bar{J}_{l+\frac{1}{2}}(R_{ss})} b_l^m.$$

This can be substituted into Equation 3.42 to get,

$$\frac{B_l^m(r)}{r} = B_l^m(R_\odot)\frac{R_\odot^2}{r^2}\sqrt{\frac{r+d}{R_\odot+d}}\frac{\bar{N}_{l+\frac{1}{2}}(r) - C_R\bar{J}_{l+\frac{1}{2}}(r)}{\bar{N}_{l+\frac{1}{2}}(R_\odot) - C_R\bar{J}_{l+\frac{1}{2}}(R_\odot)},$$

where we define,

$$C_R = \frac{2\bar{\alpha}(R_{ss}+d)\bar{N}'_{l+\frac{1}{2}}(R_{ss}) + \bar{N}_{l+\frac{1}{2}}(R_{ss})}{2\bar{\alpha}(R_{ss}+d)\bar{J}'_{l+\frac{1}{2}}(R_{ss}) + \bar{J}_{l+\frac{1}{2}}(R_{ss})}. \tag{3.45}$$

3.4 Comparison of MHS and PFSS fields

3.4.1 Pressure and Density values

As previously discussed in Section 3.2 both the pressure and density values for an MHS field can be calculated. We can therefore calculate these values for different values of $\bar{\alpha}$ and d to get a better insight into which of these values are suitable for a physical MHS field i.e. both pressure and density values stay positive for all heights, r, in the magnetic field. If required, the temperature in relation to the plasma pressure could also be calculated - however this will not be discussed here.

In Williams (2018a) an investigation was carried out into what suitable values the parameter d, the current which is perpendicular to the radial magnetic field component, could take. There it was found that $0 \leq d \leq 1$, however values between $-10 \leq d \leq 10$ were also considered in that study. Throughout that analysis it was assumed that $\bar{\alpha} = 0$, here we will consider the changes in the MHS magnetic field pressure, density and plasma beta for varying values of $\bar{\alpha}$. This will give us suitable values of both d and $\bar{\alpha}$ that can be used for the MHS models created in Chapter 4. We continue our analysis with two values of d, $d = 0.005$ and $d = 0.05$ this allows us to see the change in the calculated parameters when $\bar{\alpha}$ is varied.

From Equation 3.35 recall that the MHS pressure takes the form,

$$p(r,\theta,\phi) = p_0(r) - \frac{\bar{\xi}(r)}{2\mu_0}(\mathbf{r}\cdot\mathbf{B})^2,$$

and the plasma beta is,

$$\beta = \frac{2\mu_0 p}{\mathbf{B}\cdot\mathbf{B}}.$$

To fit in with the ideal values for the low corona the plasma beta would have a value which is very small i.e. $\beta \ll 1$, with the value rising to values of order one or higher in the corona (e.g. Gary, 2001). Therefore to ensure that the pressure is kept positive everywhere, $p_0(r)$ is chosen such that it is just slightly larger than the other pressure term i.e;

$$p_0(r) > \frac{\bar{\xi}(r)}{2\mu_0}(\mathbf{r}\cdot\mathbf{B})^2.$$

To calculate the pressure at each height the mean value of the pressure for that radius is taken. The plasma beta is also calculated across the full disk for each radius, with the mean value taken. The pressure and the plasma beta values calculated for varying values of $\bar{\alpha}$ are shown in Figure 3.1 with $d = 0.05$. The values of $\bar{\alpha}$ that were chosen for this analysis were picked to give a range of values and to push the bounds of what may be physically meaningful i.e. in keeping pressure (and density) positive. These values ranged from $-9 \leq \bar{\alpha} \leq 9$ and included the potential field value at $\bar{\alpha} = 0$ and $d = 0$.

Note that Figure 3.1a shows some oscillating pressure values with respect to height above the solar surface for certain $\bar{\alpha}$ values. We see that values from $0 \leq \bar{\alpha} \leq 1$ give suitable pressure values with the pressure decreasing continuously from 0 to 1000Mm above the solar surface. For values where $\bar{\alpha} < 0$ we see that the pressure values decrease close to the surface, however steadily start to rise again, which is not physical. For the remaining values considered, $\bar{\alpha} > 1$, the pressure values start to oscillate with increasing distance from the solar surface, this is also not desirable. Figure 3.1b shows the corresponding plasma beta values with the corresponding $\bar{\alpha}$ values. These values seem to drop off with increasing height, however for some values of $\bar{\alpha}$ we see small peaks in the plasma beta values.

Figure 3.2 also shows pressure and plasma beta values for a smaller value of $d = 0.005$. Although the d value has been changed, we see the same patterns in the pressure values calculated as previously discussed. Note however that both the pressure and plasma beta values are smaller that those calculated for $d = 0.05$, with a more smooth, continuous curve of the plasma beta values shown.

Hence from this analysis it is shown that to keep pressure decreasing as R increases and to ensure that the plasma beta drops off to $\beta \ll 1$ in the solar corona we must choose $0 \leq \bar{\alpha} \leq 1$.

To further confirm our choices for the $\bar{\alpha}$ values we plotted the mean density against the change in height from the solar surface. To do this we used the density equation previously derived (Equation 3.36) such that,

$$\rho(r,\theta,\phi) = \frac{r^2}{\mu_0 GM}\left(\frac{1}{2}\frac{d\bar{\xi}}{dr}(\mathbf{r}\cdot\mathbf{B})^2 + r\bar{\xi}\mathbf{B}\cdot\nabla(\mathbf{r}\cdot\mathbf{B}) - \mu_0\frac{dp_0}{dr}\right).$$

The value previously chosen for the $p_0(r)$ term will make an impact here.

Figure 3.3 gives examples of average density values for varying values of $\bar{\alpha}$ when $d = 0.05$. These density values are relatively small i.e. in the region of 10^{-9}kg m^{-3}, hence so we can deduce which values of $\bar{\alpha}$ keep the average density positive we have shown the density values on a log axis as in Figure 3.3b. For most of the $\bar{\alpha}$ values chosen, we see that the density oscillates from positive to negative values (where the curves go off the plot). For the values of $\bar{\alpha}$ that were previously found to have suitable pressure and plasma beta values ($0 \leq \bar{\alpha} \leq 1$) we find that they also always have positive density values - although sometimes these values can become extremely small, $\approx 10^{-19}$kg m^{-3}. In particular we find positive density values where $\bar{\alpha} = 0, \bar{\alpha} = 0.3$ and $\bar{\alpha} = 1$.

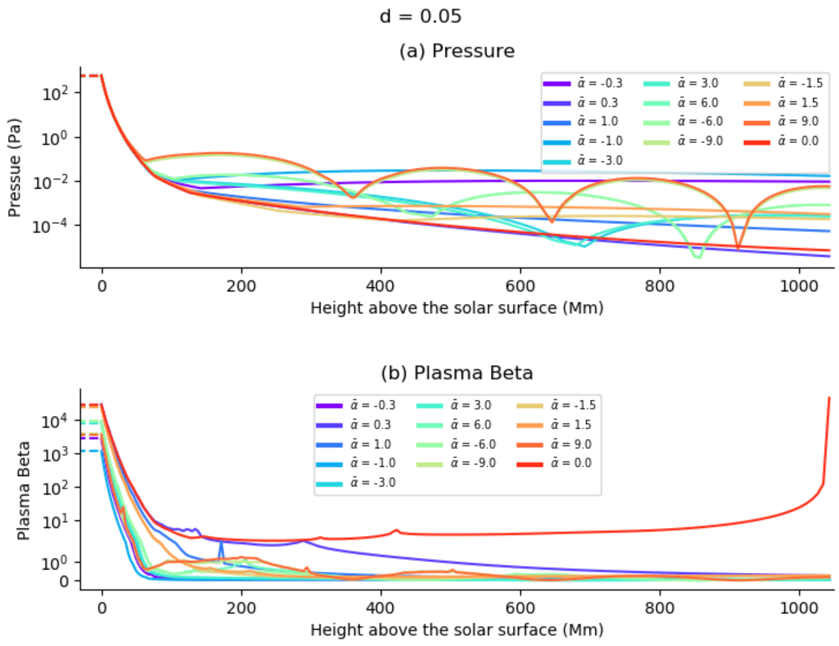

Figure 3.1: (a) shows the mean plasma pressure calculated for $d = 0.05$ and $-9 \leq \bar{\alpha} \leq 9$, (b) the mean plasma beta is calculated for the same values.

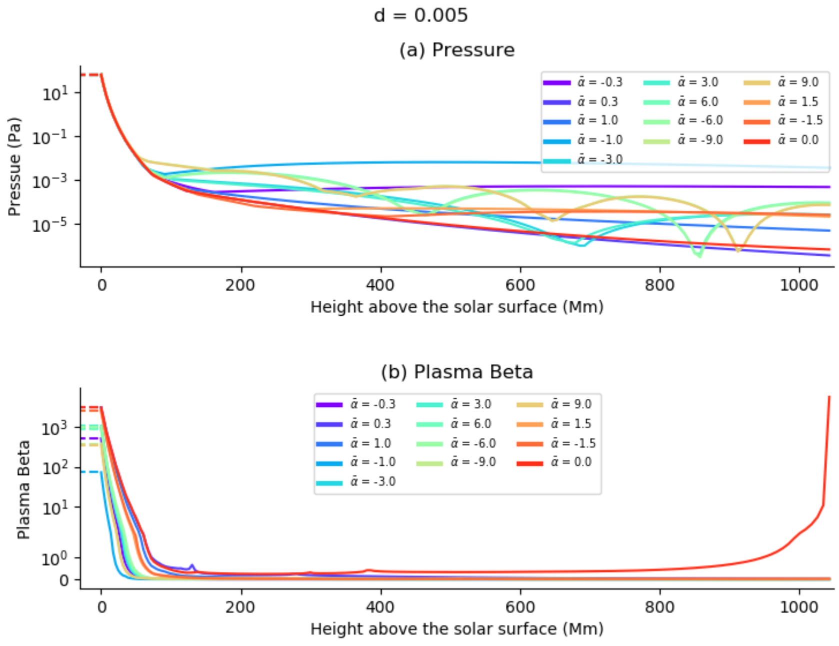

Figure 3.2: (a) shows the mean plasma pressure calculated for $d = 0.005$ and $-9 \leq \bar{\alpha} \leq 9$, (b) the mean plasma beta is calculated for the same values.

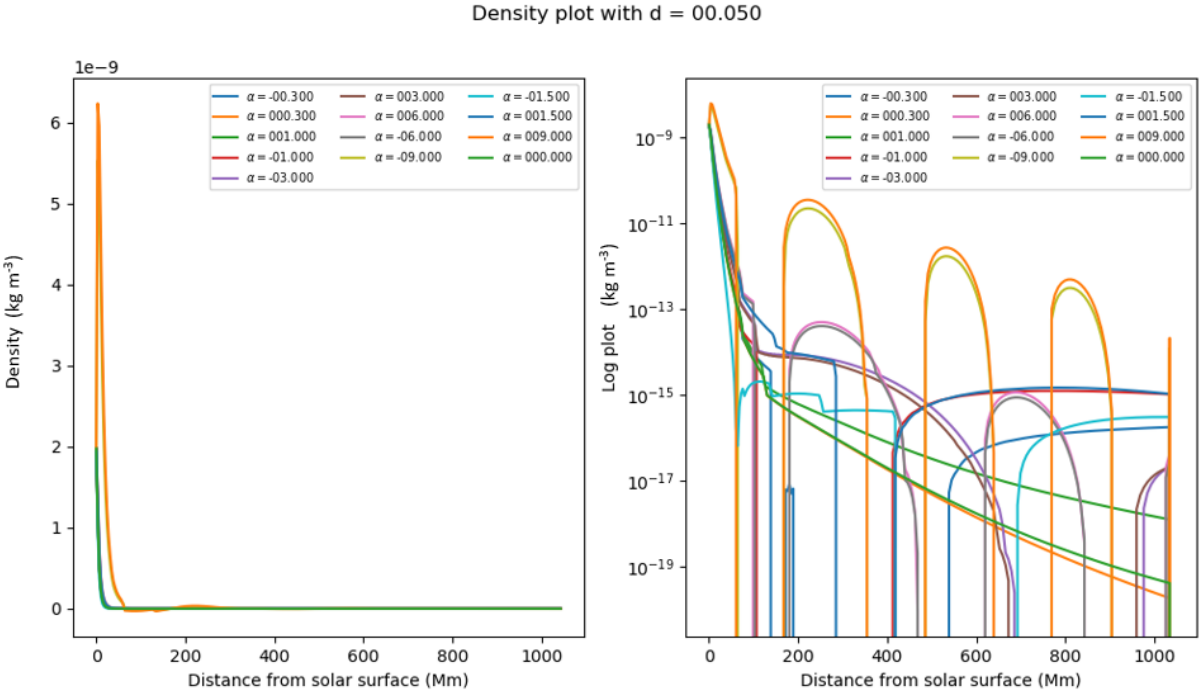

Figure 3.3: (a) shows the change in density against height with (b) showing the log plot of the density against height allowing us to investigate whether density is becoming negative.

3.4.2 Global Magnetic Field Models

As we can achieve suitable pressure and density values by setting $0 \leq \bar{\alpha} \leq 1$ and $0 \leq d \leq 1$ we can investigate the general changes in the overall magnetic field features found around active regions for both potential magnetic fields ($\bar{\alpha} = 0, d = 0$) and the MHS fields ($\bar{\alpha} \neq 0$ and/or $d \neq 0$).

From the analysis in Williams (2018a), we use the value of $d = 0.05$ here and vary the α values between the range $0 \leq \bar{\alpha} \leq 1$. This allows a general overview of how varying the $\bar{\alpha}$ values can alter the global magnetic field features.

Initially surface cuts of three magnetic fields were taken at $R = 1.2R_{\odot}$; these are shown in Figure 3.4. A potential field is shown along with two MHS fields where $\bar{\alpha} = 0.3$ and $\bar{\alpha} = 1$. Comparing the separatrix surfaces (calculated using the MSAT codes (Williams, 2018a)), which are shown in red (positive) and blue (negative) between all three figures, shows differences in their shapes and locations. Both the potential field and the MHS field where $\bar{\alpha} = 0.3$ and $d = 0.05$, see Figures 3.4a and 3.4b, have very similar separatrix structures present in many parts of the surface cut, with many of the large structures having the same shapes and positions but some of the smaller structures differing between the two. This differs a lot from the MHS field where $\bar{\alpha} = 1$ and $d = 0.05$, as many of the larger separatrix structures are different from those previously shown in the potential and other MHS fields. Note that the yellow and orange dots on the surface cuts indicate the presence of separators, with the yellow marking null-null separators and the orange marking HCS separators. The presence of these separators also vary between all three surface cuts due to the changing position of the HCS and the separatrix surfaces originating from null points. However the main differences between the three magnetic fields shown is in the HCS positions. Both the potential field and the MHS field where $\bar{\alpha} = 0.3$ are shown to have a HCS present (shown in green) with some slight variations in where it intersects with the surface. However Figure 3.4c shows that the MHS field where $\bar{\alpha} = 1$ does not have any HCS intersecting at this height, which lead us to investigate further using 3D global magnetic field models.

The 3D magnetic field models for $\bar{\alpha} = 0$, $\bar{\alpha} = 0.3$ and $\bar{\alpha} = 1$ are shown in Figure 3.5. The HCS present in both Figures 3.5a and 3.5b lie mainly across the centre of the solar surface resulting in regions of open and closed magnetic field. Both HCS are similar in shape with slight differences visible. However the 3D magnetic skeleton reveals that the HCS for $\bar{\alpha} = 1$ (Figure 3.5c), is almost torus-like around the centre of the Sun, which is not physical. This shows that where $\bar{\alpha} = 1$ we may have chosen a value for $\bar{\alpha}$ that is too large and results in unusual changes in the toplogy of the magnetic field. The values which are suitable for constant-α fields have been discussed previously (e.g. Berger, 1985). For our use of the MHS models in Chapter 4, we limit the value of $\bar{\alpha}$ to lower values.

As well as the differences in the HCS shown, differences can also be seen in the position and polarity of the separatrix structures and spine lines in the global magnetic field models. As α increases fewer structures lie across the solar equator; instead it seems they move towards the poles with the spine lines also pointing in the polar directions also.

Overall through analysis of the pressure, density and plasma beta values shown in Section 3.4.1 and the global magnetic field models analysed here the final values that are suitable to create MHS magnetic fields are $0 \leq d \leq 1$ and $0 \leq \bar{\alpha} \leq 1$ (note, $\bar{\alpha}$ values may have to be investigated further as although pressure values etc. look suitable, the field itself may have become unstable due to the larger $\bar{\alpha}$ values).

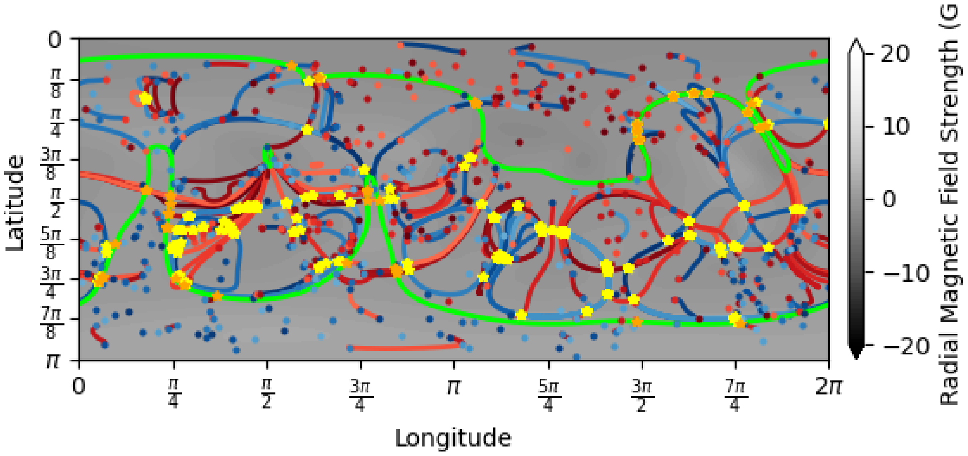

(a) $\bar{\alpha} = 0, \ d = 0$

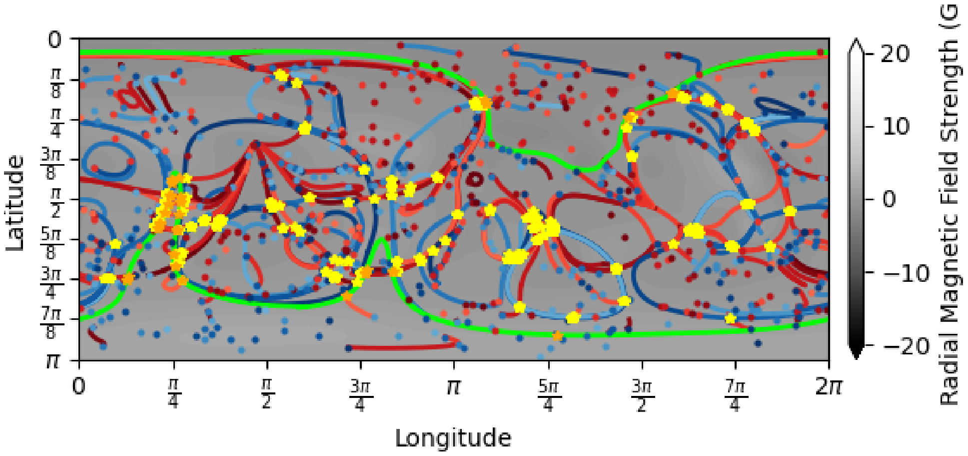

(b) $\bar{\alpha} = 0.3, \ d = 0.05$

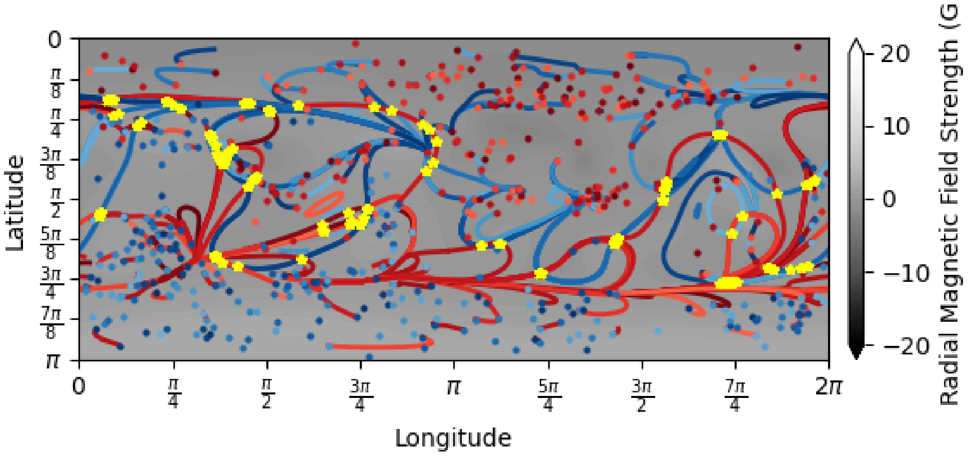

(c) $\bar{\alpha} = 1, \ d = 0.05$

Figure 3.4: Surface cuts at $r = 1.2R_{\odot}$ are shown for MHS magnetic fields calculated for various d and α values. For Carrington rotation 2097; (a) a potential field, (b) a MHS field where $\bar{\alpha} = 0.3, \ d = 0.05$ and (c) a MHS field where $\bar{\alpha} = 1, \ d = 0.05$. These include positive nulls (separatrix surfaces - red lines; spine lines - red dots), negative nulls (separatrix surfaces - blue lines; spine lines - blue dots), null-null separators (yellow), HCS-null separators (orange) and the HCS curtains (green line)

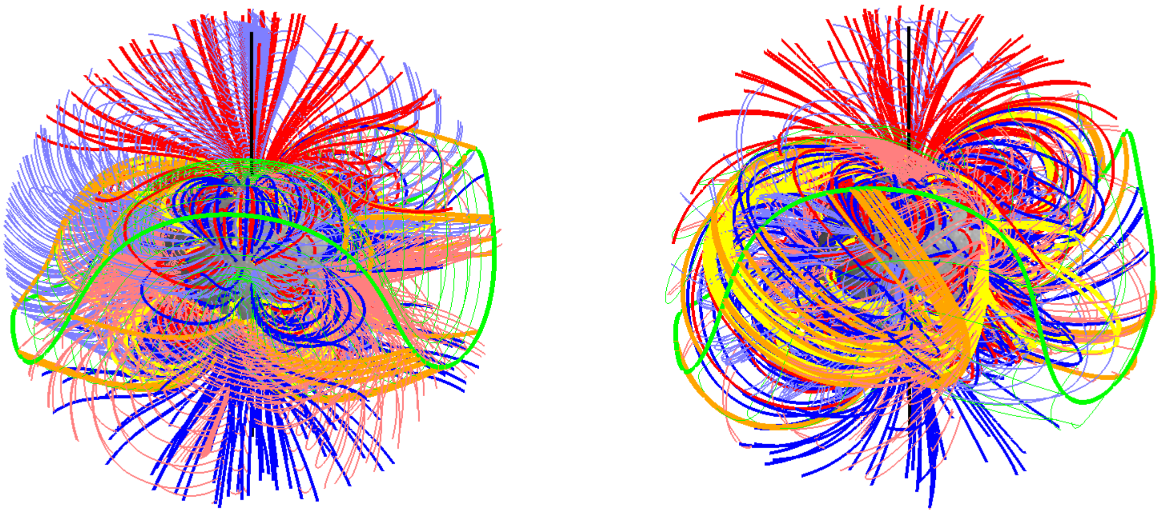

(a) $\bar{\alpha} = 0,\ d = 0$

(b) $\bar{\alpha} = 0.3,\ d = 0.05$

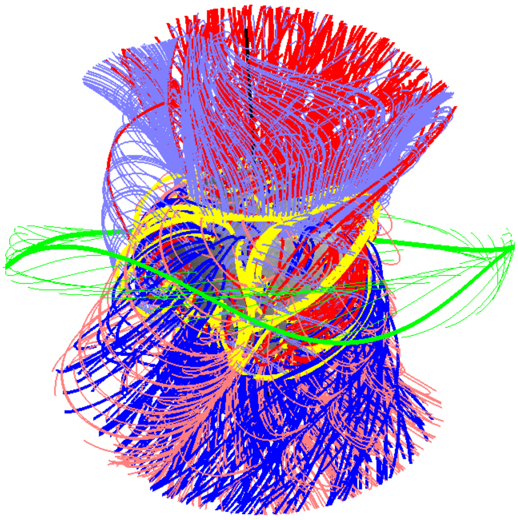

(c) $\bar{\alpha} = 1,\ d = 0.05$

Figure 3.5: 3D magnetic skeletons are shown for MHS magnetic fields calculated for various d and α values. All fields were calculated for Carrington rotation 2097. (a) shows a potential field, (b) shows a field where $\bar{\alpha} = 0.3,\ d = 0.05$ and (c) shows a field where $\bar{\alpha} = 1,\ d = 0.05$.

Chapter 4

Analysing Global Magnetic Field Features Found in Flaring Active Regions

Analysis of the magnetic fields and their global magnetic skeletons around flaring active regions can give us an insight into the properties needed for flaring events to occur. In this Chapter, we will discuss fourteen flaring active regions that were observed on the solar surface from February 2011 to September 2017. Six of the regions are discussed in detail here, showcasing the main features and problems found in the analysis. The remaining eight active regions are discussed further in Appendix A.3. All of these regions were found to have at least one X-class flare occur whilst they were passing across the solar disc. The data used is taken from the peak flare time and flare ribbons are visible in the AIA observations. Additionally the magnetic fields are extrapolated globally and their magnetic skeletons are constructed. Following this, a study was carried out to investigate whether the presence of these global magnetic field features, in particular the separatrix surfaces, could be correlated with the appearance of the flare ribbons observed.

To start this study, data products from the *Solar Dynamics Observatory* (SDO) (Pesnell et al., 2012) are used. The flare ribbon observations required are taken from the 1600$\mathring{A}$ emission line data from the *Atmospheric Imaging Assembly* (AIA). These images have a 24-second cadence, with a resolution of 0.6 arcsecs per pixel and are of size 4096 × 4096 pixels. The corresponding magnetograms must be obtained to model the magnetic fields at the flare times, hence line-of-sight magnetograms with a resolution of 0.5 arcsecs per pixel from the *Heliopsheric and Magnetic Imager* (HMI) are used. Daily synoptic maps created by HMI data products are used by the magnetic field models to carry out the field extrapolations.

To extrapolate the global magnetic fields at the flare times, the *Potential Field Source Surface* (PFSS) model (e.g. Schatten et al., 1969; Altschuler and Newkirk, 1969; Platten et al., 2014; Williams, 2018a) is used initially.

As previously discussed in Chapter 2, this PFSS model has two boundary conditions imposed. The first lower boundary condition, at $R = 1.0$, uses the daily HMI radial synoptic maps as the magnetic field values at the solar surface. Instead of the Carrington rotation synoptic maps which are HMI magnetograms averaged over 27 days, these daily maps have all data within 60° of the central meridian replaced by the average magnetic field values of the magnetograms taken between 10UT and 14UT. For these synoptic maps however, there is missing data at the polar regions which is needed for the PFSS model extrapolations. Therefore polar field values taken from HMI data products are averaged for the whole Carrington rotation with the synoptic map values replaced by these mean values with more information on this given in Chapter 2. The second outer boundary condition imposed assumes that where $R > 2.5$ the magnetic fields become purely radial, hence marking where the source-surface is located. For the remainder of this Chapter the number of spherical harmonics used is assummed to be $l = 1201$, resulting in potential magnetic fields ($\mathbf{B}$) of size $(702 \times 1203 \times 2405)$ in r, θ and ϕ respectively being extrapolated.

After the magnetic fields have been extrapolated, global magnetic skeletons are created (Bungey et al., 1996). These magnetic skeletons are made up of null points, spine lines, separatrix surfaces, separatrices and the heliospheric current sheet (HCS), for more information on how all of these are calculated see Chapter 1.5. Throughout this analysis however features created by the separatrix surfaces found will be classified as in Platten et al. (2014). This allows the larger scale structures created to be easily picked out and compared to the flare ribbons observed.

Three main topological features will be considered as shown in Figure 4.1, with separatrix domes, separatrix caves and separatrix tunnels expected to be found in and around the flaring regions. Firstly, the separatrix domes form over opposite polarity regions and consist of separatrix surfaces from one or more null points. Commonly separatrix domes consist of a single null point and its corresponding spine line, with the separatrix surface fieldlines arching down to intersect completely with the solar surface. They are also found to occur within both open and closed fields, in open fields the spine line will intersect at one end with the solar surface and the other end with reach up to the outer boundary. However in closed fields the spine line footpoints are found to both intersect with the solar surface. Secondly, separatrix caves are also considered. These are extremely similar to separatrix domes, however are found to have an opening bounded by spine lines from an opposite polarity null point. This opening makes the structure almost cave-like in shape. The final structure considered are separatrix tunnels, which have two openings where the separatrix fieldlines intersect with the solar surface. The openings are shown by yellow arrows in Figure 4.1f, with both opening bounded by spine lines of opposite polarity nulls whilst the tunnel itself originates from a single null point.

Other magnetic field features have previously been found to contribute to the presence of flare ribbons. The main field feature that has been widely analysed is the presence of *quasi separatrix layers* (QSLs), (Priest and Démoulin, 1995), in the flaring regions. Although very similar to separatrix surfaces there is no associated null point for QSLs. They can be identified by the large gradient of footpoint mapping that occurs in the magnetic field, the best measure of this is given by the squashing factor, Q. Note that in the presence of separatrices $Q \to \infty$ due to the jump in connectivity of the field. Both QSLs and separatrices have been analysed using various magnetic field methods (Demoulin et al., 1997; Titov, 1999; Aulanier, 2011; Savcheva et al., 2015; Pontin et al., 2016; Janvier et al., 2016; Zhao et al., 2016, e.g.).

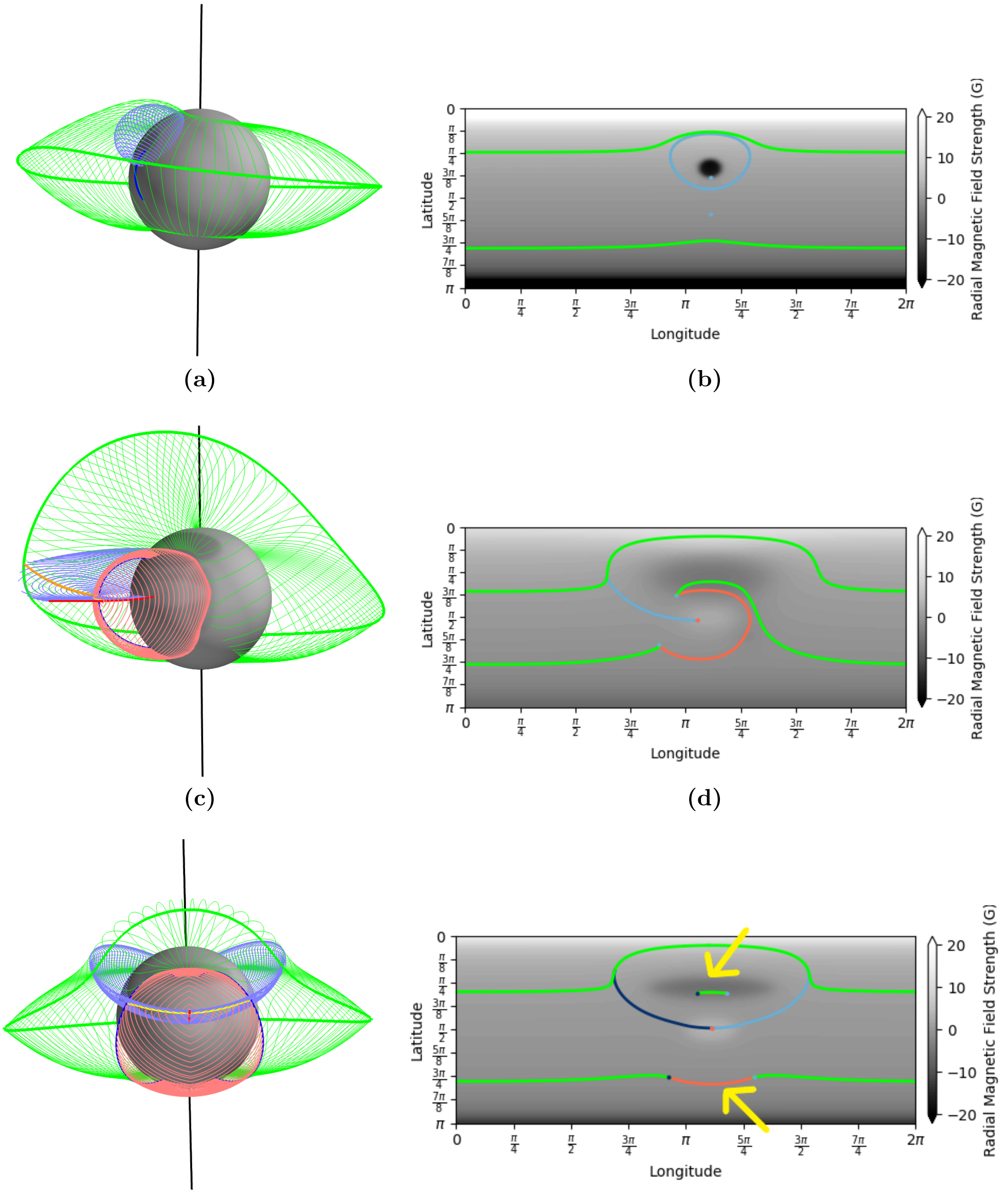

(a) (b)

(c) (d)

(e) (f)

Figure 4.1: (a) and (b) show a separatrix dome and its cut along the surface $R = 1.001$, (c) and (d) show a separatrix cave and its respective surface cut, (e) and (f) show a separatrix tunnel and its respective surface cut with the yellow arrows indicating the tunnel openings.

4.1 Calculating the Squashing Factor

The squashing factor Q, can be calculated using the method described in Titov (2007). The method is discussed in detail here to calculate Q in terms of spherical coordinates. Following the derivation of the squashing factor, the flaring active regions considered in this Chapter can also be analysed for the presence of QSLs if no separatrix surfaces are present, as well as showing high values of Q where separatrix surfaces are present.

Initially, we can consider two surfaces, a launch surface and a target surface, with a coordinate systems defined as (u^1, u^2) and (w^1, w^2) respectively at both boundaries. Note that here our launch surface is typically the photosphere, with the target surface for closed fieldlines also the photosphere and the target surface for open fieldlines marked at the source-surface $R = R_{ss} = 2.5R_{\odot}$.

As in Titov (2007), we can define the magnetic field lines mapping from one surface to the other, $(u^1, u^2) \to (w^1, w^2)$, by defining a vector function $[W^1(u^1, u^2), W^2(u^1, u^2)]$. The properties of this fieldine mapping can be described by,

$$D = \left[\frac{\partial W^i}{\partial u^j}\right], \tag{4.1}$$

where D is a Jacobian matrix which determines the mappings from the tangent plane at the photosphere to the tangent plane at the target surface. This mapping can be generalised to give a definition of the *squashing factor*, Q, of an infinitesimal circle at the photosphere being projected onto an ellipse at one of the target surfaces.

To derive an expression for Q, we introduce a vector function $\mathbf{R}(u^1, u^2)$ which describes the location of the fieldline footpoints at the photosphere in a 3D coordinate system. Therefore we can subsequently define a set of vectors that determine the covariant vector basis tangent to the u-coordinates at the photosphere where,

$$\boldsymbol{\epsilon}_k = \frac{\partial \mathbf{R}}{\partial u^k}; \quad k = 1, 2. \tag{4.2}$$

The local length and angles here can be determined using,

$$g_{lk} = \boldsymbol{\epsilon}_l \cdot \boldsymbol{\epsilon}_k; \quad l, k = 1, 2; \tag{4.3}$$

which is the corresponding covariant metric tensor, with $g \equiv det[g_{lk}]$.

The orthonormal basis vectors can be constructed using Equation 4.2 and the Gram-

Schmidt procedure such that;

$$\begin{aligned}\boldsymbol{e}_1 &= \frac{\boldsymbol{\epsilon}_1}{\|\boldsymbol{\epsilon}_1\|}\\ &= \frac{\boldsymbol{\epsilon}_1}{\sqrt{g_{11}}},\end{aligned} \tag{4.4}$$

$$\boldsymbol{e}_2 = \frac{g_{12}}{\sqrt{g_{11}}}\boldsymbol{\epsilon}_1 - \sqrt{\frac{g_{11}}{g}}\boldsymbol{\epsilon}_2. \tag{4.5}$$

Any point on the circle with unit radius on the tangent plane to the photosphere is defined by,

$$\boldsymbol{o} = \cos\vartheta\boldsymbol{e}_1 + \sin\vartheta\boldsymbol{e}_2; \tag{4.6}$$

where $\vartheta \in [0, 2\pi)$.

Similarly, we can define $\tilde{\boldsymbol{R}}(w^1, w^2)$ which determines the footpoints at the target surface where,

$$\tilde{\boldsymbol{o}} = o^k \frac{\partial W^i}{\partial u^k}\tilde{\boldsymbol{\epsilon}}_i, \tag{4.7}$$

is the mapping of the fieldlines to the tangent plane of the target surface with the corresponding covariant basis vectors defined by;

$$\tilde{\boldsymbol{\epsilon}}_i = \frac{\partial \tilde{\boldsymbol{R}}}{\partial w^i}. \tag{4.8}$$

By varying ϑ we can define the ellipse traced by $\tilde{\boldsymbol{o}}$ such that;

$$\begin{aligned}\tilde{\boldsymbol{o}}^2 &= g^*_{ij}\tilde{o}^i\tilde{o}^j\\ &= \frac{1}{2}g^*_{ij}\frac{\partial W^i}{\partial u^k}\frac{\partial W^j}{\partial u^l}\left[e^k_1e^l_1 + e^k_2e^l_2 + \cos 2\vartheta(e^k_1e^l_1 - e^k_2e^l_2) + \sin 2\vartheta(e^k_1e^l_2 + e^l_1e^k_2)\right],\end{aligned} \tag{4.9}$$

where $g^*_{ij}(u^1, u^2)$ is $\tilde{g}_{ij}(w^1, w^2)$ evaluated at the tangent surface footpoint.

Equation 4.9 can be simplified using Equations 4.2→4.5 such that;

$$\tilde{\boldsymbol{o}}^2 = \frac{1}{2}\left(N^2 + \sqrt{N^4 - 4\Delta^2}\right)\sin 2\vartheta, \tag{4.10}$$

where,

$$N^2 = \frac{\partial W^i}{\partial u^k}g^*_{ij}\frac{\partial W^j}{\partial u^l}g_{lk}, \tag{4.11}$$

$$\Delta = \sqrt{\frac{g^*}{g}}\frac{\partial(W^1, W^2)}{\partial(u^1, u^2)}. \tag{4.12}$$

These equations allow us to consider the major and minor axes of the ellipse at the target surface such that,

$$\begin{aligned} \frac{\tilde{o}_{max}}{\tilde{o}_{min}} &= \left(\frac{N^2 + \sqrt{N^4 - 4\Delta^2}}{N^2 - \sqrt{N^4 - 4\Delta^2}} \right) \\ &= \frac{N^2}{2|\Delta|} + \sqrt{\left(\frac{N^2}{2|\Delta|} \right)^2 - 1}. \end{aligned} \tag{4.13}$$

It was assumed in Titov et al. (2002) that $\frac{N^2}{\Delta} \gg 1$ when a QSL is present, which allows us to reduce Equation 4.13 to;

$$\begin{aligned} Q &= \frac{N^2}{2|\Delta|} + \sqrt{\left(\frac{N^2}{2|\Delta|} \right)^2 - 1}, \\ &\approx \frac{N^2}{2|\Delta|} + \frac{N^2}{2|\Delta|}. \end{aligned}$$

Therefore we can conclude, as in Titov (2007), that the larger values of this ratio do not deviate much from the value;

$$Q = \frac{N^2}{|\Delta|}, \tag{4.14}$$

this is the definition of the squashing factor that is used in the remainder of this chapter. This quantity provides an indication of whether QSLs or separatrices are present within a model. If a separatrix is present then the value of $Q \to \infty$. Throughout our analysis of each flaring active region it was decided to calculate Q, allowing us to give any indication of the value of Q around the flare ribbons observed in AIA data.

Instead of a Cartesian system, a typical spherical configuration is used with the global coordinate system (r, θ, ϕ). This configuration changes for open and closed field-lines. Generally, the photospheric boundary is defined when $r = R_\odot$. The outer boundary is said to occur here where, $r = R_*$. Hence for open field-lines $R_* = 2.5R_\odot$ and for closed field-lines $R_* = R_\odot$. We define the endpoints as $[\Phi(\phi, \theta), \Theta(\phi, \theta)]$. Equation 4.11 can be expanded from the Cartesian case to give,

$$N^2 = \frac{R_*^2}{R_\odot^2} \left[\left(\frac{\sin\Theta}{\sin\theta} \frac{\partial\Phi}{\partial\phi} \right)^2 + \left(\sin\Theta \frac{\partial\Phi}{\partial\theta} \right)^2 + \left(\frac{1}{\sin\theta} \frac{\partial\Theta}{\partial\phi} \right)^2 + \left(\frac{\partial\Theta}{\partial\theta} \right)^2 \right]. \tag{4.15}$$

Δ is defined as the ratio of the radial field components at the launch and target points along an infinitesimal flux tube,

$$\Delta = \frac{B_r}{B_r^*} = \frac{R_*^2}{R_\odot^2} \frac{\sin\Theta}{\sin\theta} \frac{\partial(\Phi, \Theta)}{\partial(\phi, \theta)}. \tag{4.16}$$

Both equations 4.15 and 4.16 are used to find Q as defined in equation 4.14.

For each active region we trace fieldlines in spherical coordinates from the photosphere to either the outer source-surface located at $R = 2.5R_{\odot}$ or back down to the photosphere at $R = R_{\odot}$. By tracing these fieldlines and using the definition of Q, see Equation 4.14, we can calculate the squashing factor around the active regions which can indicate the presence of QSLs as well as separatrix surfaces.

The remainder of this chapter concentrates on analysing fourteen active regions that were observed from February 2011 to September 2017, with six of the active regions discussed in Section 4.2 and the remaining eight regions discussed in Appendix A.3. The global magnetic skeleton features found around each active region are compared by eye to the flare ribbons observed in the AIA data. This allows for a comparsion to be made as to whether the flare ribbons observed have their position and shape due to the presence of the magnetic field features modelled here. Although we initially consider potential magnetic fields, Section 4.3 studies the differences found when using a non-potential field. Furthermore as well as locating the separatrix surfaces, if any, in the magnetic field models, we calculate the squashing factor, Q (see Titov, 2007, reproduced above) and locate quasi-separatrix layers (QSLs), (Priest and Démoulin, 1995) which could be present in regions where no separatrix surfaces are found whilst also showing high values of Q where separatrix surfaces have been found in the magnetic field models. Furthermore Section 4.4 analyses the change in topological features found in an active region by using the PFSS model, with two active regions analysed over four days.

4.2 Analysis of Flaring Active Regions using Potential Magnetic Fields

A study of the magnetic field structures found in flaring active regions is carried out here. The chosen active regions were selected due to X-class flares being observed in all the regions as they crossed the solar disc. X-class flares are the strongest flaring events to occur on the Sun, however they are also the rarest and so only 18 events were recorded to have happened within 45° of central meridian (see the flare ribbon database Kazachenko et al., 2017) between April 2010 and April 2016. Hence all of these active regions were included in this study as well as active region NOAA 12673 which in September 2017 was the site of multiple X-class flares. Therefore in total fourteen active regions were analysed by extrapolating the potential magnetic fields using the PFSS model and creating their global magnetic skeletons which allows for comparisons to be made between the flare ribbons observed and the magnetic skeleton structures, in particular the separatrix surfaces found.

The analysis of each active region was completed by extrapolating the potential magnetic fields on the dates where the X-class flares occurred. This would allow for a more accurate comparison between the flare ribbons observed and the magnetic field structures. A comparison between the flare ribbons and the separatrix structures found allows us to determine what type of structures are typically found around flaring active regions and whether their shapes correspond to the ribbon shapes observed. In previous studies separatrix domes were found to commonly occur where cicrular (or compact) flare ribbons were observed (e.g. Masson et al., 2009; Liu et al., 2011; Reid et al., 2012; Sun et al., 2013; Janvier et al., 2016), here we will investigate whether different structures such as separatrix caves or tunnels may also be present.

Six active regions are presented here as representative classes of the types of flare ribbons and their associated separatrix structures we find lying in and around the flaring regions. The six active regions are NOAA 11158, NOAA 11890, NOAA 12192, NOAA 12205, NOAA 12242 and NOAA 12297. These regions were found to have varying sizes and shapes of flare ribbons observed in the AIA data, and when analysing their magnetic fields, the 3D magnetic skeletons were all found to have different variations of separatrix structures lying in the active regions. The other eight active regions analysed; NOAA 11166, NOAA 11283, NOAA 11429, NOAA 11520, NOAA 11944, NOAA 12017, NOAA 12158 and NOAA 12673; were found to have separatrix structures and flare ribbons similar to the six active regions already analysed, and are discussed in Appendix A.3.

4.2.1 Active Region NOAA 11158

Active region NOAA 11158 emerged on the solar disc on 12 February 2011 and crossed the disc until 20 February 2011, during that time it was the location of over 30 C-class and 4 M-class flares as well as one X-class flare. Also known as the *Valentine's day flare*, the X2.2 solar flare occurred on 15 February 2011 and was observed from 01:44UT to 01:56UT.

This flare and active region have been included in many previous studies (e.g. Schrijver et al., 2011; Beauregard et al., 2012; Maurya et al., 2012; Sun et al., 2012b,a; Liu and Schuck, 2012; Aschwanden et al., 2013; Petrie, 2013; Inoue et al., 2014). Some studies in particular focus on the associated earth-directed coronal mass ejection (CME), (Schrijver et al., 2011; Sun et al., 2012b), which occurred after the X-class flare event. The corresponding AIA observations have been extensively analysed in comparison to varying magnetic field parameters and velocity flows around the active region. Here we consider only the $1600\mathring{A}$ AIA observation taken just after the peak time of the X-class flare which clearly shows the flare ribbons at a snapshot in time which are found to lie in the chromosphere, shown in Figure 4.2a and Figure 4.2b where the ribbons have been contoured onto the associated HMI magnetogram.

Our analysis compares the 3D magnetic field structures found from the potential field extrapolations and the two flare ribbons observed in the AIA data. Figures 4.2c, 4.2d show the 3D magnetic skeleton and the associated cut along the surface $R = 1.001$ around the active region. Here a separatrix dome was found, originating from a negative null point and overlying most of the active region. The dome itself is found to lie under a closed magnetic field, with another larger separatrix structure originating from further across the disc overlying the region also, therefore the spine line was found to intersect the solar surface at two different locations. Figures 4.2e, 4.2f show the magnetic field structure locations with respect to the active region and the flare ribbons observed there. The two flare ribbons are found to lie close to the separatrix dome structure, with the larger ribbon lying along a section of where the dome intersects with the solar surface. Note in Figure 4.2f the flare ribbons are contoured in orange and the separatrix dome is found overlying the active region in blue. The smaller ribbon, found lying above the larger ribbon, is not found to have a magnetic field structure lying close by apart from the separatrix dome. However the spine lines present in the region and lying close to the edges of the flare ribbons observed could also contribute to the shape of the flare ribbons observed (Pontin et al., 2016).

The Q map was also calculated, normally used to indicate the presence of QSLs. However, here we see values of approximately 10^7 around where the separatrix surfaces were found to lie in the PFSS model. High values in particular were noted around the negative separatrix dome lying close to the flare ribbons observed during the X-class flare, shown in orange in Figure 4.3. These higher values were to be expected due to $Q \to \infty$ at true separatrices.

4.2.2 Active Region NOAA 11890

Active region NOAA 11890 was the location of two X1.1 solar flares that occurred on 8 and 10 November 2013, with both observed X-class flares having durations of approximately half an hour. The active region was visible on the solar disc from 2

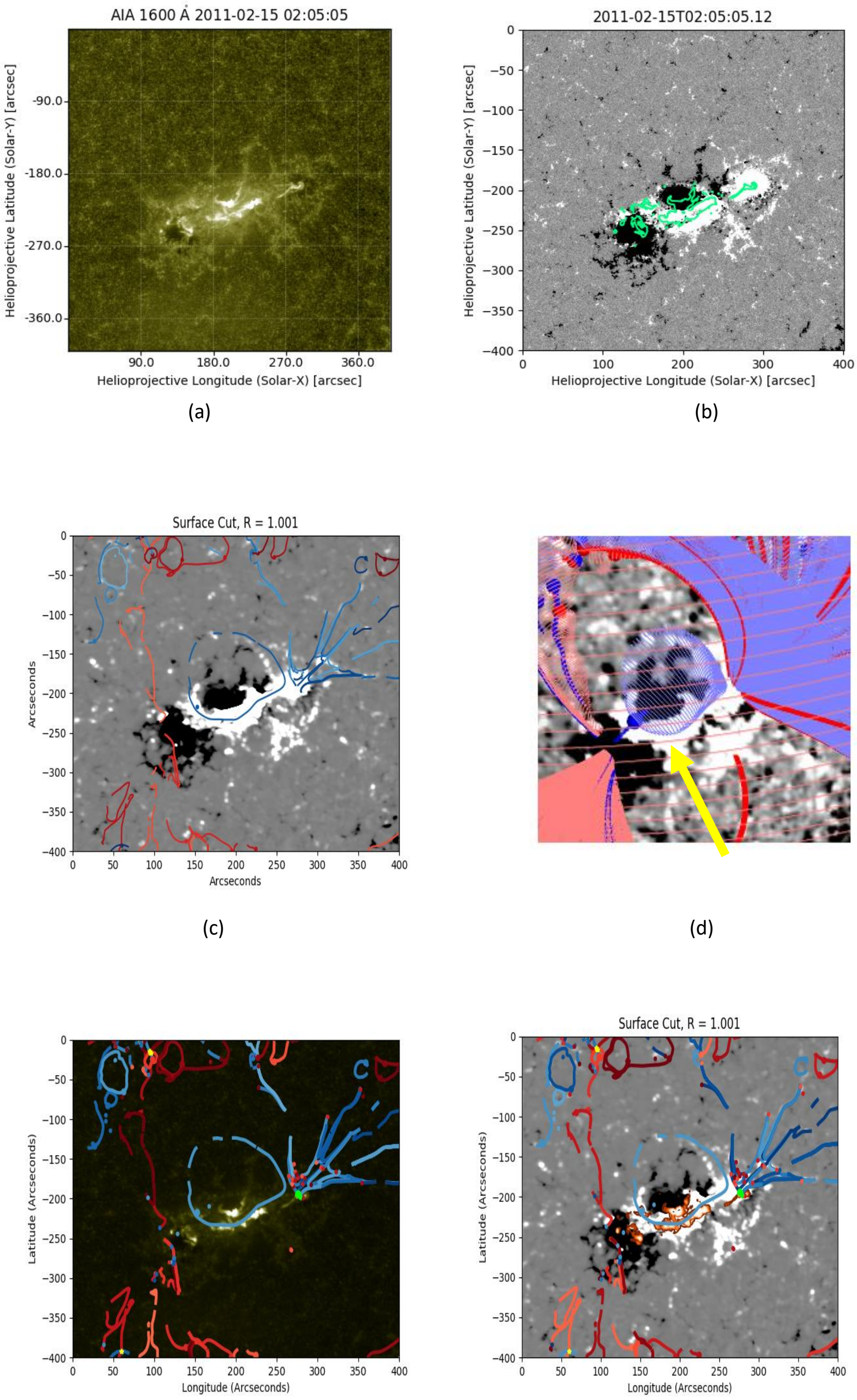

(a) (b)

(c) (d)

(e) (f)

Figure 4.2: Analysis of AR NOAA 11158. (a) an AIA observation taken during the X2.2 flare. (b) the HMI data at the date and time of the flare with the corresponding Hα ribbons contoured in green. (c) the surface cut of the PFSS model at $R = 1.001$, with a negative separatrix structure overlying the active region. (d) a separatrix dome originating from a negative null point overlying the active region (highlighted by yellow arrow) (e) the surface cut ($R = 1.001$) is imposed onto the AIA image. (f) surface cut of the 3D model at $R = 1.001$ with the UV ribbons contoured in orange.

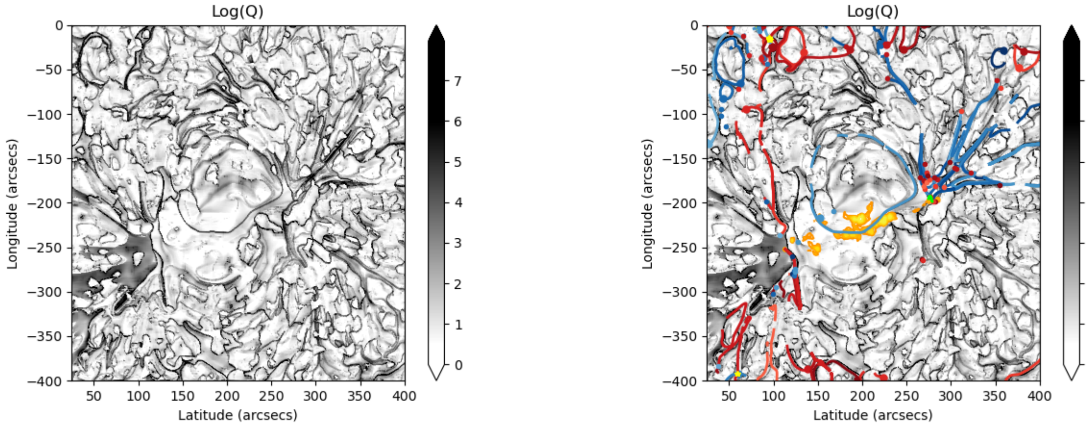

(a) (b)

Figure 4.3: Q map calculated for NOAA 11158. (a) the Q map, (b) Q map with ribbons contoured in orange, with separatrix surface cut overplotted. Shows how high Q values of the order $\approx 10^7$ correlate to the presence of separatrix surfaces around the active region.

November 2013 to 14 November 2013 and was the site of many flaring events. Although separate analysis was carried out for both days where the X-class flares were observed, the structures and results found were consistent, hence only the analysis and results for 10 November are shown here.

Figures 4.4a and 4.4b shows the presence of two flare ribbons which create a circular brightening on the solar surface, as observed by SDO (AIA 1600 $\mathring{A}$), lying over a small bipolar region within the active region itself. The flare ribbons are also shown projected onto a HMI magnetogram in green contours. This active region has been analysed previously due to the presence of the circular brightening (e.g., Xu et al., 2016; Song and Tian, 2018; Liu et al., 2020) where the connection between a separatrix dome structure originating from a single null point has been analysed along with studying the magnetic field parameters needed during the flare.

As expected from the presence of the circular flare ribbons shape observed (e.g. Masson et al., 2009), Figure 4.4c shows the surface cut, taken at $R = 1.001$, which is the result of the presence of a single separatrix dome. Figure 4.4d highlights the 3D structure, with the dome originating from a single positive null point and lying in a region of open magnetic field. Similarly to active region NOAA 11158 (see Section 4.2.1), the separatrix dome is the only structure in the active region, with the spine lines from the dome intersecting at both footpoints with the solar surface.

Figures 4.4e and 4.4f shows the separatrix structures found in relation to the flare

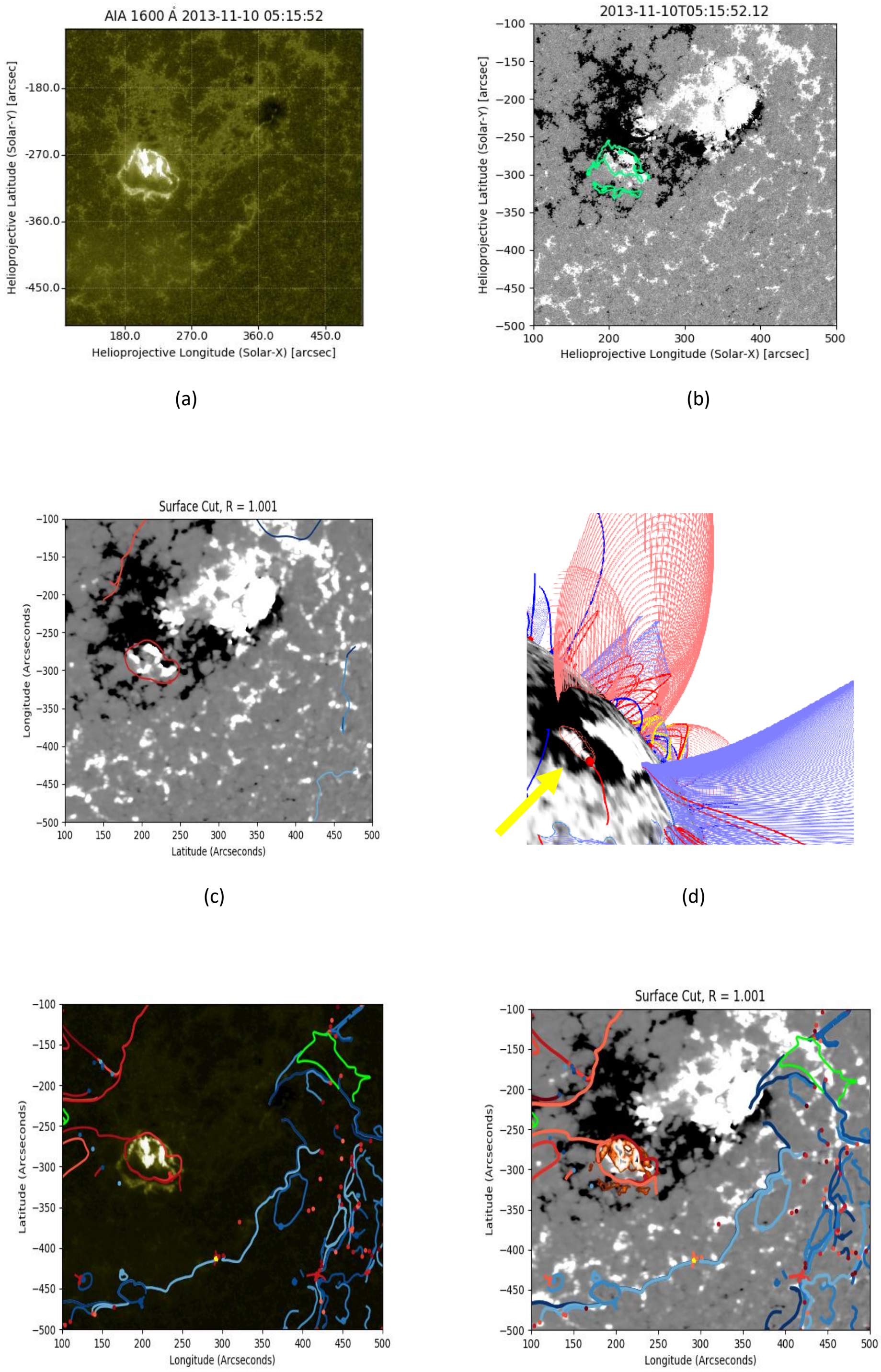

(a) (b)

(c) (d)

(e) (f)

Figure 4.4: Analysis of AR NOAA 11890. (a) - (f) as shown in 4.2, with a small positive separatrix dome overlying a portion of the active region (highlighted by yellow arrow).

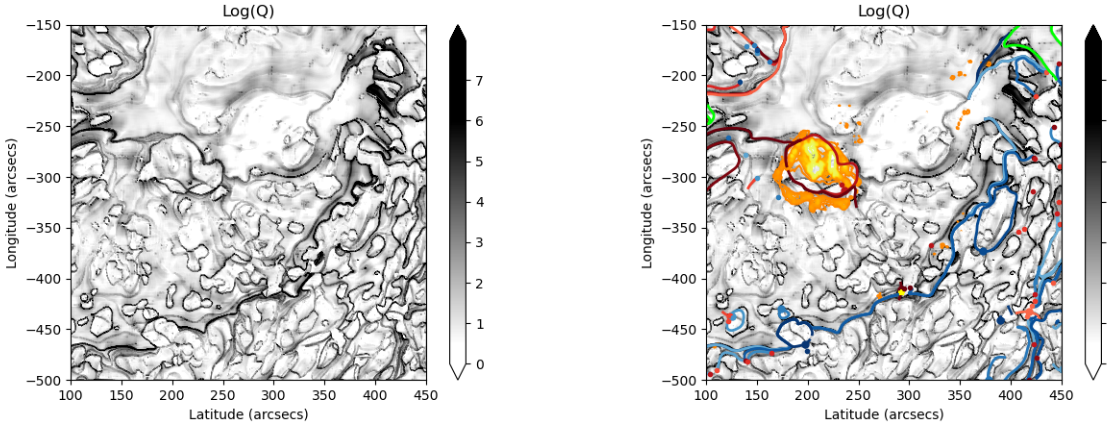

(a) **(b)**

Figure 4.5: Q map calculated for NOAA 11890. (a) the Q map, (b) Q map with ribbons contoured in orange, with separatrix surface cut overplotted. Shows how high Q values of the order $\approx 10^7$ correlate to the presence of positive separatrix dome where the flare ribbons are located.

ribbons observed. There seems to be, from the figures shown, a clear correlation between the separatrix dome structure found in the active region and the circular shape the flare ribbons observed make. The Q map was investigated here and similarly to NOAA 11158 again (see Figure 4.3), high Q values were found around the separatrix surface structures found using the PFSS model. Again Q values were in the region of 10^7 around these separatrix surfaces. The Q maps for this active region highlighting the flare ribbons observed and the positive separatrix dome found by the PFSS model are shown in Figure 4.5.

4.2.3 Active Region NOAA 12192

Active region NOAA 12192 crossed the solar disc from 16 October 2014 to 29 October 2014, during that time four X-class flares occurred in the region along with multiple C and M-class flares. The details of these four X-class flares are shown in Table 4.1. The active region analysis shown here was carried out using data from 26 October 2014, however all four days were analysed with the results found to be consistent.

The X2.0 flare that occurred on 26 October 2014 had two associated flare ribbons which are shown in Figure 4.6a. The active region itself was quite large, see Figure 4.6b, with the flare ribbons only lying within a small portion of it. The 3D magnetic skeleton constructed here is shown in Figure 4.6d, with many separatrix surfaces and their spine line footpoints lying along the edge of the active region. However no separatrix surfaces

Date	Class	Start Time	End Time
22/10/14	X1.6	14:02:00	14:50:00
24/10/14	X3.1	21:07:00	21:41:00
25/10/14	X1.0	16:55:00	17:08:00
26/10/14	X2.0	10:04:00	11:18:00

Table 4.1: Data for the Solar flares that occurred in NOAA 12192

were found within a large portion of the active region, including where the flare ribbons lie. This is shown more clearly in Figure 4.6c, where the active region has very few separatrix structures intersecting with the solar surface at $R = 1.001R_{\odot}$. A further comparsion of the flare ribbons observed and the magnetic skeleton was analysed in Figures 4.6e and 4.6f. Here it is confirmed that there are no separatrix surfaces lying in the region that could possibly contribute to the presence of the flare ribbons observed.

4.2.4 Active Region NOAA 12205

Many flares were observed in active region NOAA 12205 as it crossed the solar disc from 4 November 2014 to 16 November 2014. During this period one X-class flare was observed by SDO from 16:53UT to 17:54UT on the 7 November 2014. This active region has been the subject of previous studies (e.g., Sobotka et al., 2016; Zuccarello et al., 2019; Tei et al., 2018), however we will consider the global magnetic field features found around the active region which have not been previously studied.

Figure 4.7a shows the two 'J' shaped sigmoidal flare ribbons observed by SDO that were observed during the X-class flare event, with the ribbons shown in relation to the HMI magnetogram in Figure 4.7b. Multiple structures were found overlying the active region from the potential field extrapolation, with many of these possibly contributing to the ribbon shapes observed. In particular Figure 4.7d shows the 3D magnetic skeleton structures lying around the active region, with five smaller structures lying close to where the ribbons were observed as shown in Figure 4.7 where the surface cut along $R = 1.001$ was taken. On closer inspection, three of the five separatrix structures found lying in the centre of the active region were separatrix domes, with two originating from single positive null points (shown in red) and one originating from a negative null point (shown in blue). The other two structures originate from one positive and one negative null point, with both structures found to be separatrix caves. The spine lines from the oppposite polarity nulls bound the edges of the separatrix

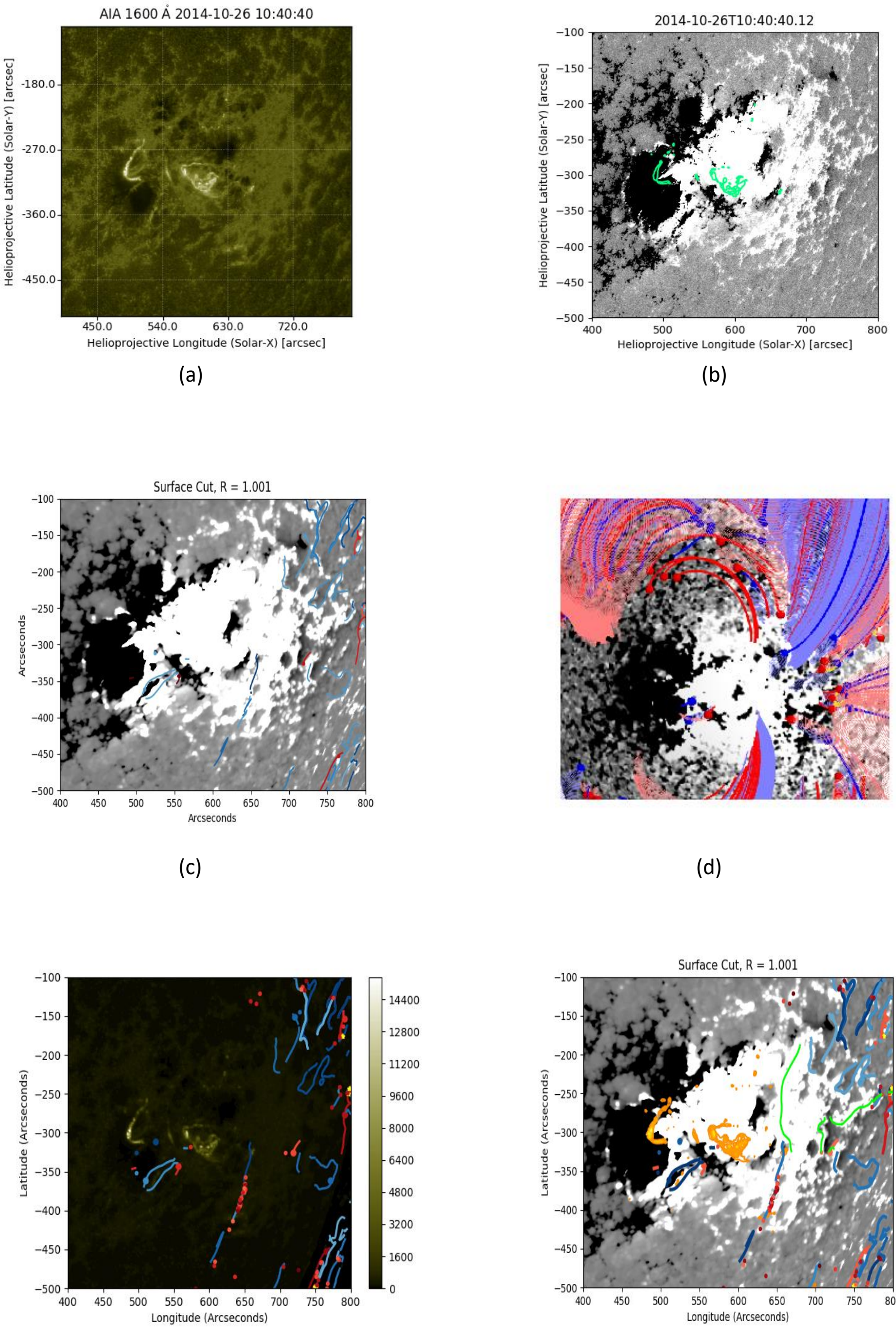

(a) (b)

(c) (d)

(e) (f)

Figure 4.6: Analysis of AR NOAA 12192. (a) - (f) as shown in 4.2, with no larger features found in the active region.

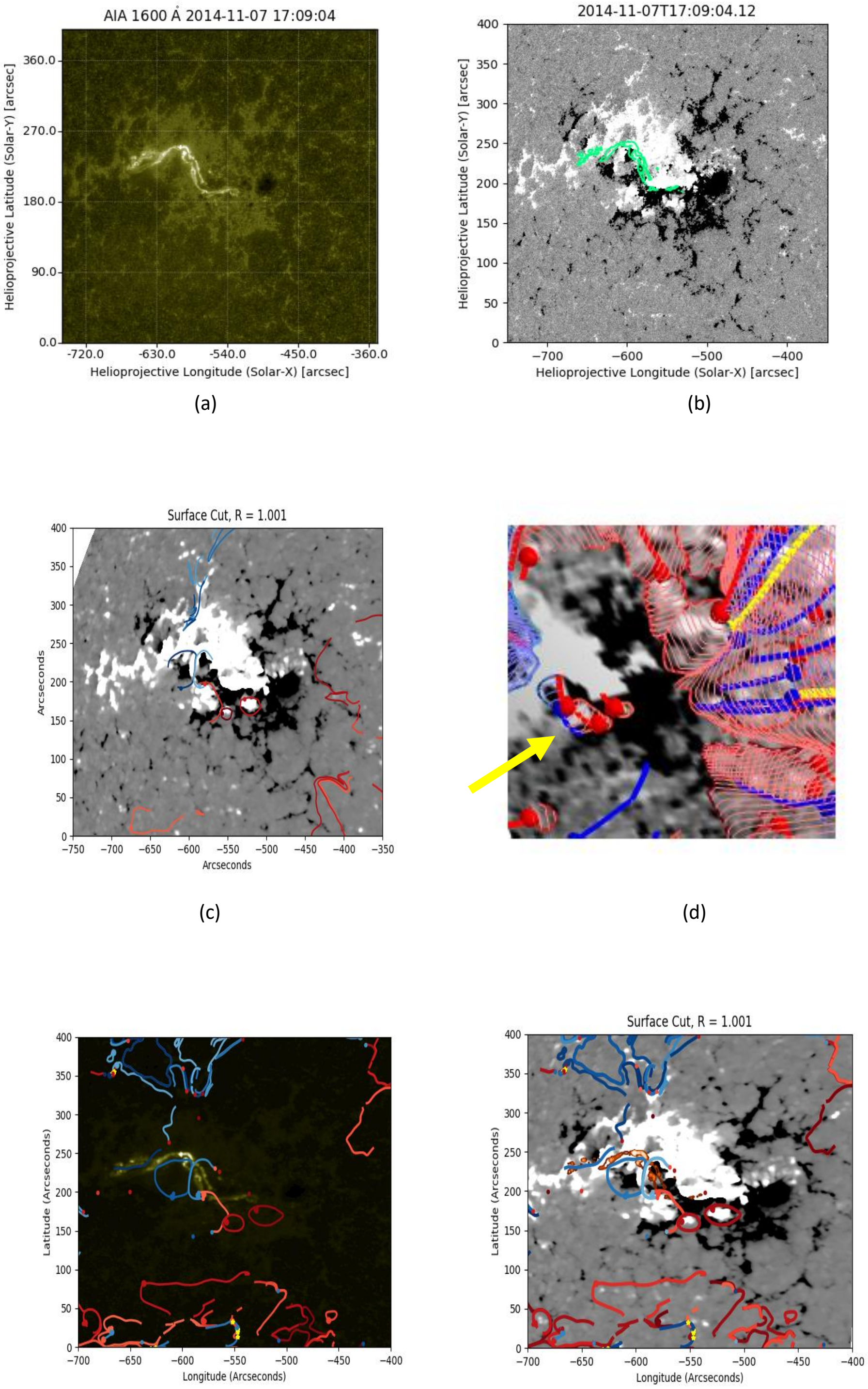

(a) (b)

(c) (d)

(e) (f)

Figure 4.7: Analysis of AR NOAA 12205. (a) - (f) as shown in 4.2, with mixed topology found around the flaring site (three separatrix domes and two separatrix caves are shown).

caves.

Figures 4.7e and 4.7f show the separatrix surfaces, in particular where the structures intersect with the solar surface, in relation to the location of the flare ribbons observed. The flare ribbons are found to lie along the five structures discussed above. It is thought that the presence of these separatrix structures could contribute to the shape and location of the flare ribbons observed.

In particular, notice that one of the flare ribbons is completely covered by the edges of the separatrix structures, however the second, slightly lower lying flare ribbon does not completely map onto the edges of the five structures discussed above. Note that a spine line from one of the positive separatrix domes lies at one ribbon edge and the spine line from one of the negative domes lies at the other ribbon edge, which may be the cause of the ribbon location (Pontin et al., 2016). Note that as with the previous two active regions analysed the Q maps were calculated here, again as expected high values were found around the separatrix surfaces produced by the PFSS model.

4.2.5 Active Region NOAA 12242

Active region NOAA 12242 crossed the solar disc from 15 December 2014 to 24 December 2014, this active region was the site of a X1.8 solar flare on the 20 December 2014 from 00:11UT to 00:55UT. When this flare occurred the active region was only a few days old as it had emerged on the solar disc on 15 December 2014, with the region the site of a further 50 C-class and 4 M-class flares as well as the single X-class flare discussed here. Due to the interesting dynamics found in this active region it has been the subject of previous studies (e.g., Zhou and Zhan, 2015; Abramov-Maximov et al., 2017; Zhu et al., 2018; Liu et al., 2019).

The X-class flare studied here was found to have two flare ribbons observed by SDO, with both shown at a snapshot in time during the flare in Figure 4.8a. To get a clearer understanding of where these ribbons lie in relation to the whole active region, the ribbons are also shown in green imposed onto the HMI magnetogram taken at the same time, see Figure 4.8b. These ribbons look to make a large semi-circular shape lying across a large portion of the active region. To investigate whether there were any separatrix surface features lying around the active region that may contribute to the shapes of the flare ribbons observed the PFSS model was analysed for the flare date. The 3D magnetic field model created is shown in Figure 4.8d, with a large separatrix cave found overlying the active region. The separatrix cave originated from a positive null point which was found lying at the edge of the active region, a negative null

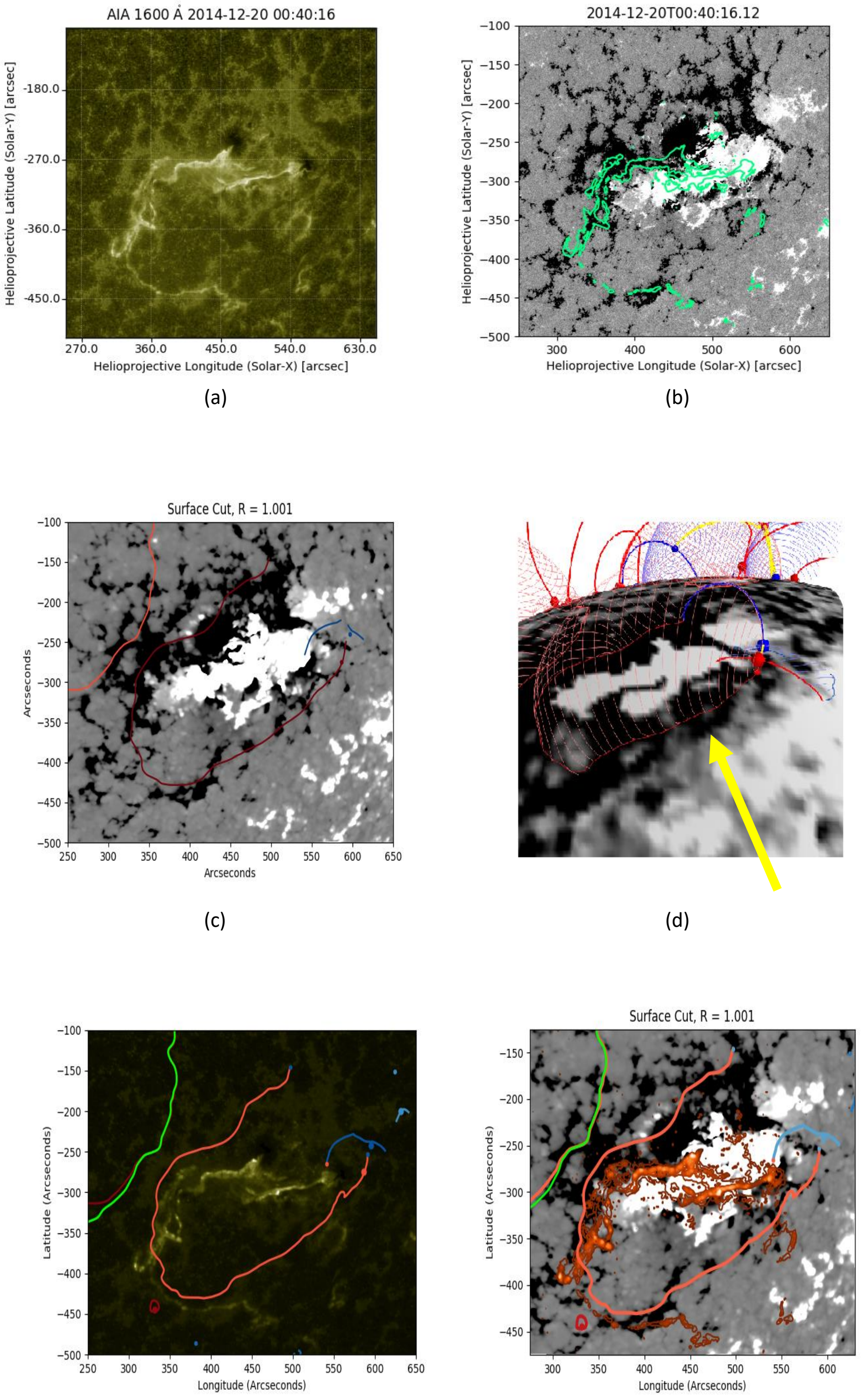

(a) (b)

(c) (d)

(e) (f)

Figure 4.8: Analysis of AR NOAA 12242. (a) - (f) as shown in 4.2, with a positive separatrix cave bounded by a negative null spine line overlying the flaring region (see yellow arrow).

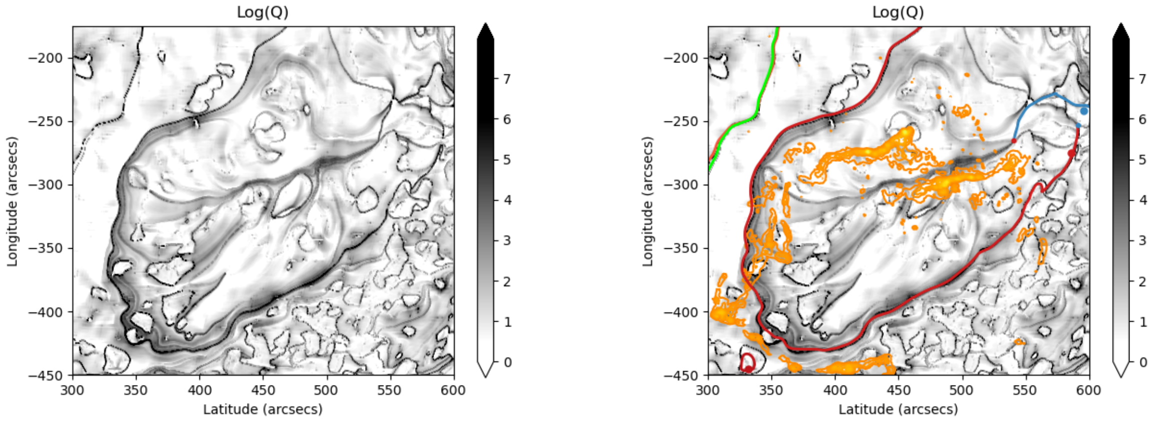

(a) (b)

Figure 4.9: Q map calculated for NOAA 12242. (a) the Q map, (b) Q map with ribbons contoured in orange, with separatrix surface cut overplotted. High Q values are found around separatrix surfaces as expected, however high Q values are also located close to where one of the ribbons lie, where no separatrix surface is present.

point lying close by is connected by a separator to the positive null with the spine line bounding the cave opening. An overview of what this feature looks like intersecting with the solar surface at $R = 1.001$ is shown in Figure 4.8c, with the positive separatrix cave lying over the active region. Note also that the separatrix cave lies in open magnetic field with the HCS intersecting with the solar surface not far from the active region.

To compare the separatrix cave and the flare ribbons observed, the separatrix cave cut was merged with the AIA observation of the flare ribbons see Figure 4.8e. A clearer comparison is also given in Figure 4.8f, with the flare ribbons and separatrix cut both compared to the HMI observation. Here it is clear to see that although the separatrix cave has a shape very similar to the flare ribbons observed there is a slight offset between both. The Q map was calculated for this active region and is shown in Figure 4.9a. Note that there are high Q values of approximately 10^7 located in regions where separatrix surfaces were located in the PFSS model. In Figure 4.9b the flare ribbons are shown along with the Q values and the separatrix surfaces. For the shorter ribbon there is a region of high Q close by which could possibly correspond to the presence of a QSL being indicated. Here this could indicate that the separatrix cave may only correspond to the larger semi-circular ribbon and the smaller ribbon could correspond to a QSL.

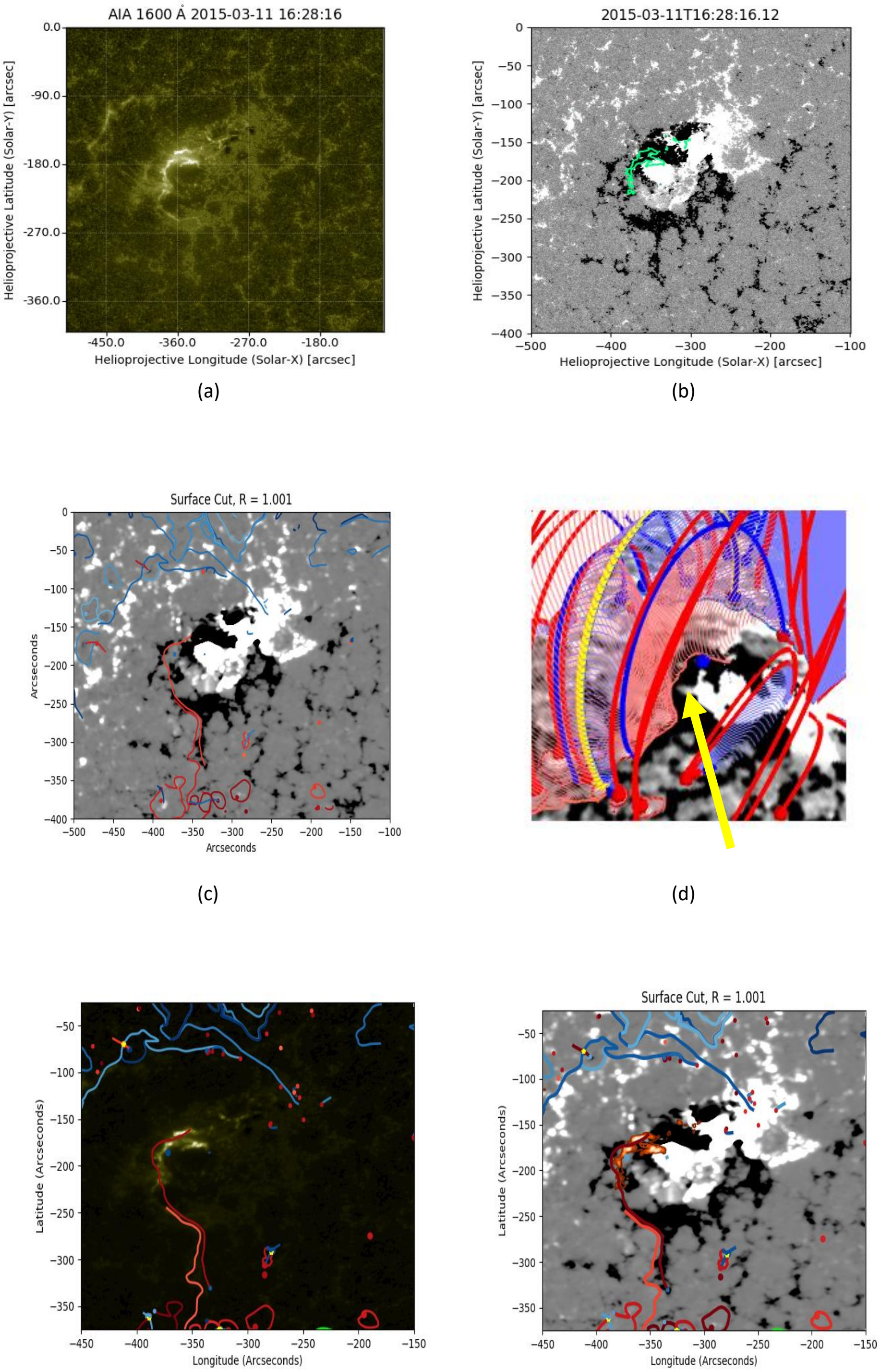

(a) (b)

(c) (d)

(e) (f)

Figure 4.10: Analysis of AR NOAA 12297. (a) - (f) as shown in 4.2, with a positive separatrix cave found overlying the region.

4.2.6 Active Region NOAA 12297

From 16:11UT to 16:29UT on 11 March 2015, an X2.1 solar flare was observed in active region NOAA 12297. Whilst crossing the solar disc from 6 March 2015 to 19 March 2015 over 50 C-class and 20 M-class flares were observed in the active region as well as the X-class flare which will be discussed and analysed here. As this flare was the only X-class event that occurred in 2015 it has been the subject of previous studies (e.g., Lacatus et al., 2016; Dhakal and Zhang, 2018; Qiu et al., 2020). Here we want to investigate whether there is a connection between the separatrix structures found from the 3D magnetic skeleton and the shape and positions of the flare ribbons observed by SDO.

During the X-class flare two flare ribbons were observed on the solar disc (see Figure 4.10a, with one smaller ribbon lying beside a large sigmodial shaped ribbon. Figure 4.10b shows the flare ribbons observed by AIA projected onto the relevant part of the HMI magnetogram, with both ribbons lying at the outer edge of the active region. To investigate whether there is a separatrix surface in the region which may be contributing to the shape and position of the flare ribbons the 3D magnetic skeleton was created using a potential field extrapolation on the date the X-class flare occurred. The structures found in the active region are shown in Figure 4.10d with the corresponding cut along the solar surface at $R = 1.001R_{\odot}$. A positive null point located in the active region results in the presence of a separatrix cave which could contribute to the presence of the flare ribbons. The positive separatrix cave is bounded by the spine lines of a negative null point also located in the active region. The active region itself is quite noisy with many separatrix structures and their spine lines lying over the region.

The correlation between the presence of the separatrix cave and the two flare ribbons observed are shown in Figures 4.10e and 4.10f. The separatrix cave seems to lie in the region of the larger flare ribbon observed. The smaller ribbon observed lies just below the edge of the separatrix cave, however one of the spine lines that bound the cave opening intersect with the solar surface at one end of the flare ribbon. As with previous active regions, when the Q map was calculated the high Q values were found around the regions where separatrix surfaces were located in the PFSS model.

4.2.7 Results

Here we presented six active regions which had been analysed using the *potential field source-surface* (PFSS) model. Each of the active regions presented were representative of the types of topological features that were found in the remaining eight active regions analysed in Appendix A.3.

Active region NOAA 11158 (15 February 2011) was found to have a single separatrix dome originating from a negative null point lying over the region. The dome intersected the photosphere everywhere and both spine lines had footpoints also intersecting with the solar surface, see Figure 4.2d. This region had a similar topological structure to active region NOAA 11890 (10 November 2013) which was also discussed here. Active region NOAA 11890 also had a separatrix dome present (see Figure 4.4d), however it originated from a positive null point. Both of these active regions were found to have their topological structures correlate slightly to the flare ribbons observed, although active region NOAA 11158 was found to have a flare ribbon that occurred during the X-class flare which did not have a corresponding topological feature. Active region NOAA 11890 was found to map the separatrix dome almost exactly to the almost circular flare ribbons observed during the X1.1 flare that occurred on 10 November 2013. The region exhibits the expected topology associated with circular flare ribbons, (e.g., Masson et al., 2009) and active region NOAA 11158 shows an example where dome-spine topology occurs in connection to two J-shaped ribbons being observed. Of the other eight regions analysed active region NOAA 11166 (9 March 2011) was found to have a separatrix dome in the region where the X-class flare occurred. However this dome did not correspond to the flare ribbons observed unlike active regions NOAA 11890 and NOAA 11158 and is discussed in Appendix A.3.

Next, active region NOAA 12192 (26 October 2014) was discussed. This region was the largest of all the regions analysed and one of the most active, with four X-class flares occurring in it. However, the region was found to have no topological features that could be related to the flare ribbons observed, see Figure 4.6c. This could be due to the limitations of the potential field model used, which are discussed later in this Section. Of the remaining active regions analysed (see Appendix A.3), three were found to have no separatrix surfaces in the active region; NOAA 11520 (12 July 2012), NOAA 11944 (7 January 2014) and NOAA 12158 (10 September 2014). No main topological features were found in the active regions thought to contribute to the flare ribbon shapes and positions observed throughout the X-class flares, however both NOAA 11944 and 12158 had other features lying at the edges of the active regions with separatrix domes creating closed fields above the regions.

Active region NOAA 12205 (7 November 2014) was chosen to show an example of mixed topology around the flaring region. Here, it was found that the two flare ribbons were thought to correspond to a group of topogical structures rather than a single structure. Three small separatrix domes and two small separatrix caves were found to originate from both positive and negative nulls lying across the centre of the active region, this is shown in Figure 4.7d. This was the only region found to have more than two separatrix structures located in it that were thought to correspond to the flare ribbons observed. It highlights that more intricate networks of topological features could be found in relation to the shape and position of the flare ribbons observed during an X-class flare event.

Next, active region NOAA 12242 was analysed using data from 20 December 2014 and was found to be the site of a large separatrix cave originating from a positive null point and bounded by spine lines from a nearby negative null point, see Figure 4.8d. At the time of the X-class flare two large ribbons were found to stretch across the active region, by comparing the AIA observations and the 3D magnetic field model it can be seen that, although the ribbons made a similar shape to the separatrix cave observed there was a slight offset in flare ribbon position and the cave position. Although some of the other regions analysed were found to have separatrix caves lying in the active region, only this region was found to have a cave on such a large scale and with no overlying closed magnetic field. Active regions NOAA 11429 (7 March 2012) and NOAA 12673 (6 September 2017), both discussed in Appendix A.3, were found to have small cave structures lying in the active regions, however both were contained within an overlying separatrix dome structure. Both of these regions were also found to have topological features that could not be related in position or shape to the X-class flare ribbons observed.

Note that the final active region discussed in detail, NOAA 12297 (11 March 2015), was found to also have a cave structure present in the region that could be mapped to the flare ribbons observed. Both active region NOAA 12242 and NOAA 12297 were shown as examples of where separatrix caves were found as the main feature in the active regions. Active region NOAA 12017 (29 March 2014) was found to have a *cave-like* structure in the active region surrounded by many other topological features, however the cave shape looked to match the observed flare ribbons. This was very similar to the topology found around where the flare ribbons were observed in active region NOAA 11283 (7 September 2011), where a separatrix cave structure was observed, however it was surrounded by many other features intersecting the photosphere such as spine lines and other separatrix structures fan planes.

Table 4.2 shows the total number of each type of topological structure found in each active region analysed. Separatrix caves and domes were found most often, with no separatrix tunnels found at all throughout the analysis. Two active regions were found to have mixed topology, where both active regions had a combination of both

Type of Separatrix Feature	Number of ARs	Percentage(%)
Cave	5	35
Tunnel	0	0.00
Dome	4	29
None	4	29
Mixed	1	7

Table 4.2: A list of the different types of topological structures that are present around the active regions analysed.

separatrix domes and caves present. This shows that a diverse range of topological features can be found in active regions, not just separatrix domes which have been the main focus of previous studies, however due to the composition of these active regions where there are small regions of mixed polarities this is not surprising.

Note that the Q values around the active regions were also calculated, see Figure A.3. However it was found that for regions where topological features were present, Q values $> 10^7$ were present, and for regions where no topological features were found, no high Q values were found where the flare ribbons were observed.

Although some regions analysed have topological features that can be mapped accurately by eye (see Section 4.2.2), some of the fourteen active regions studied had one or more of the following problems;

1. An offset between the position of the topological features found and the flare ribbons observed in the AIA data. (For example, see Section 4.2.5 which discusses AR12242.)

2. The topological features found did not correspond in shape and/or position of the flare ribbons observed. (For example, see Appendix A.3 which discusses AR11944.)

3. There were no topological features found in the region that could be mapped by eye to the flare ribbons observed. (For example, see Section 4.2.3 which discusses AR12192).

All of these issues may be caused by some of the limitations of using a potential field model. The PFSS model has no electric currents present, this may cause some of the issues listed above. The inclusion of global currents is discussed when implementing the MHS model in Section 4.3, although it would perhaps be the inclusion of local currents around the active regions analysed which would alter the position or shape of the topological features found. These localised currents could be included by using a non-linear force free (NLFF) model, however implementing such a model is not discussed here.

Another limitation of the PFSS model used is the resolution issues that may occur. For example, in Active region NOAA 12192 (see Section 4.2.3) where there were no topological features found, this active region was particularly large and so resolution issues may become a problem. In the PFSS model the resolution of the model is defined by the number of spherical harmonics used, which can limit in particular the resolution in the ϕ-direction, see Chapter 2. Due to this limitation unless we had the computational capacity to create the PFSS model using an extremely large number of spherical harmonics, this issue may not be resolved.

One of the final limitations of the PFSS model used here is that a Gaussian filter is used to smooth the magnetic field, however this filter may lead to a loss in valuable data which could explain why some regions where small bipolar regions are observed do not have any null topology overlying them, see Section 4.2.3. To rectify this an alternative smoothing method could be chosen, or a check could be implemented which only smooths the data using a weaker gaussian filter. See Chapter 2 for further discussion on the smoothing method of the PFSS model.

Although some of the limitations discussed above can not be recitified by using a PFSS model, our analysis shows that the topology found using a potential field model can still produce features which can be mapped to the observed flare ribbons. To investigate the inclusion of a global current in the model, the following section discusses the implementation of a MHS model and the analysis of the same active regions discussed here.

4.3 Analysis of Flaring Active Regions using Non-Potential Magnetic Fields

In the previous section, potential fields are used to calculate the 3D magnetic skeletons analysed. However, they do not include any currents moving through the field which could cause some of the issues seen such as the offset of the separatrix structures in comparison to the flare ribbons observed in 1600$\AA$ AIA data. Here, we consider active region NOAA 12242 which was previously analysed in Section 4.2.5. We found a large separatrix cave structure that lay over most of the active region, with two flare ribbons observed in the AIA data which looked to have similar shapes. When the flare ribbons were compared to the separatrix cave there was an offset between the two which is thought to be due to the use of the PFSS model.

To analyse an alternative magnetic field the MHS model discussed in Chapter 3 is used here. In that chapter we discuss the parameters which can be chosen for the model that result in different MHS fields being calculated. Here we calculate MHS fields where $\bar{\alpha} = 0.3$ and $d = 0.005$, recall that when $\bar{\alpha} = 0$ the field is potential and the d variable relates to the amount of current perpendicular to the radial magnetic field component. The values for these parameters are chosen such that the plasma beta, pressure and density of the model have suitable values, as shown previously in Figures 3.2 and 3.3.

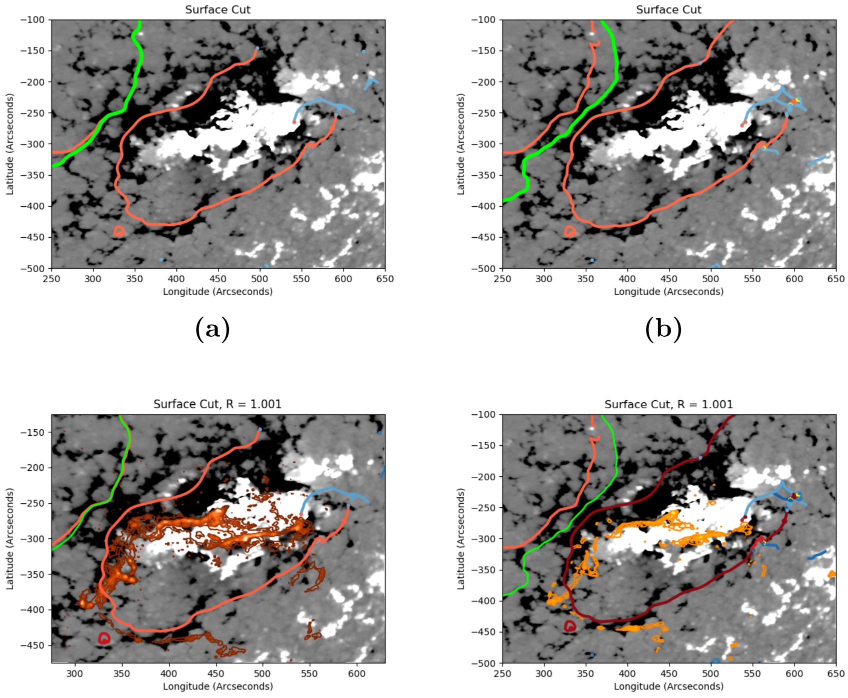

(a) (b)

(c) (d)

Figure 4.11: Comparison of potential field and MHS field models, (a) surface cut of potential field, (b) surface cut of MHS field ($\bar{\alpha} = 0.3, d = 0.005$), (c) and (d) show the surface cuts with AIA contours for (a) and (b) respectively. All surface cuts are taken at $R = 1.001R_\odot$.

Figure 4.11 shows the comparison between the potential and magnetohydrostatic field models with the surface cuts taken along $R = 1.001R_\odot$. By comparing Figures 4.11a and 4.11b, we can investigate whether the introduction of a current component to the magnetic field alters the topological structures found in the potential field models to lie closer to the flare ribbon positions observed. Figure 4.11a shows the previous potential field model analysed in Section 4.2.5 with a large separatrix cave originating form a positive null point found overlying the active region in an open field region, with the HCS intersecting close to the edge of the region. A corresponding MHS field was analysed with $\bar{\alpha} = 0.3$ and $d = 0.005$, the resultant topological features are shown in Figure 4.11b, where there were found to be very few alterations to the original structures found in and around the active region. The cave structure has been extended into a larger structure with another negative null point found lying close to the other negative null points boundary spine line. There is also a positive separatrix structure found to connect to the other side of the cave opening. The position of the cave structure is the same in both the potential and MHS models. The other main difference shown between the surface cuts is that the edge of the HCS has been moved to lie closer to the edge of the cave structure.

By analysing the differences in topological features found in relation to the active region position, a comparison was also made for the surface cut with respect to the AIA data, shown contoured in orange in Figures 4.11c and 4.11d which show the PFSS and MHS results respectively. As previously stated the differences in the topological features found between the PFSS and MHS models were small and there were no obvious changes to the larger topological structures that were thought to be connected to the flare ribbons observed. Hence, even when using a MHS magnetic field instead of a potential magnetic field there are no obvious improvements to the relation between the AIA ribbons observed and the topological features found. Note that although active region NOAA 12242 is discussed here, the other active regions were also analysed using MHS fields instead of the PFSS model. All active regions where topological features were found showed little difference between the separatrix structures in the MHS or PFSS fields, with any changes happening globally in the HCS or smaller changes in null positions. However the topological feature positions and general overall shapes were not changed from the PFSS to the MHS model. For active regions where no topological features were found, for example NOAA 12192, there were no topological features found in the MHS model which could relate to the flare ribbons observed.

To further the analysis of these active regions NLFFF models could be used. This would differ from the MHS models discussed here, which introduce global electric currents, to introduce regions in which the current density is more localised within the model. These NLFFF models would create a more realistic view of the global magnetic field and perhaps change the topology of the field around the flaring active regions. NLFFFs are not used throughout this work, however would be the next step in investigating whether the topology of the magnetic fields would greatly differ from those already found here using the MHS model and previously using the PFSS model.

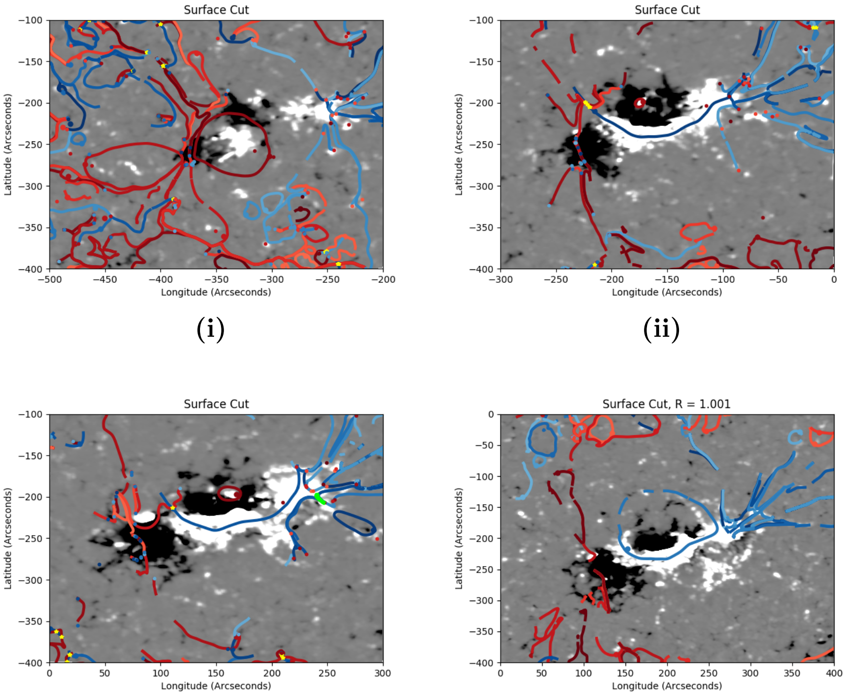

(i)

(ii)

(iii)

(iv)

Figure 4.12: Active Region NOAA 11158. The change in separatrix structures present over the region from 12 February 2011 to 15 February 2011 is shown, (i) A positive separatrix dome (12 February), (ii) A negative separatrix cave and small positive separatrix dome (13 February), (iii) A negative separatrix cave and small positive separatrix dome (14 February) and (iv) A negative separatrix dome (15 February) is overlying the flaring active region.

4.4 Topological Structure Development of an Active Region

The previous sections consisted of a study of fourteen active regions analysed on a single day where an X-class flare occurred. This analysis included the creation and investigation of a 3D magnetic skeleton extrapolated from the PFSS model. Two main types of topological features were found to occur in the active regions, separatrix domes and separatrix caves, however here we investigate whether these structures change over the course of 4-days when the active region was visible on the solar disc.

4.4.1 Active Region NOAA 11158

Here we consider active region NOAA 11158 which emerged on the solar disc on the 12 February 2011 and crossed the disc until 20 February 2011. This active region was previously analysed in Section 4.2.1 where the 3D magnetic skeleton was created for data observed on 15 February 2011, the date on which an X-class flare occurred.

For the date previously analysed, 15 February 2011, Figure 4.12iv shows the negative separatrix dome overlying most of the active region, with other topological structures lying to the side. Here we investigate whether the topological structures in the days leading up to this were different or similar to those found here. The change in active region structures over four days from 12 February 2011 to 15 February 2011 is shown in Figure 4.12.

On the 12 February 2011, when the active region emerged, there was a positive null with a separatrix dome overlying the active region shown in Figure 4.12i. As well as the dome structure there is a collection of negative separatrix surfaces lying along the outer edge of the active region with a group of positive spine footpoints also visible. These topological features are vastly different from those observed on 15 February when the X-class flare occurred, with there being no sign of a negative separatrix structure lying in the centre of the active region.

On the 13 February 2011, see Figure 4.12ii, there is a small positive dome present in the centre of the region which overlies a very small opposite polarity region. The positive separatrix dome that was present the previous day is no longer present, however there is what looks to be a large negative separatrix crossing over the lower positive flux in the active region. From the analysis done in Section 4.2.1, we know that the main feature of this active region when the X-class flare occurs is a large negative dome. Both of these structures are still present on 14 February 2011, Figure 4.12iii, where it looks like the large negative separatrix structure may be a separatrix cave lying above the active region. This is due to the presence of spine lines and a separator at the edge of the separatrix structure.

This indicates that when the active region is first emerging on the 12 February there are some difference in the topological features observed, however over the following three days the features settle into a negative separatrix cave which finally changes into a separatrix dome as observed on 15 February 2011.

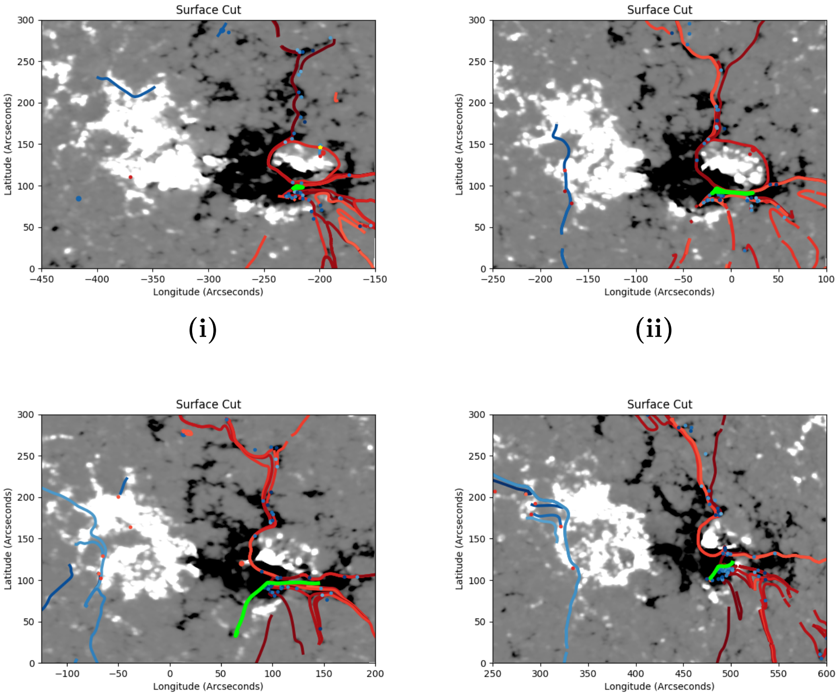

(i) (ii)

(iii) (iv)

Figure 4.13: Active Region NOAA 11283. The change in separatrix structures present over the region from 4 September 2011 to 7 September 2011 is shown, (i) A positive separatrix dome is surrounded by other positive separatrix surfaces (4 September), (ii) A positive separatrix dome is surrounded by other positive separatrix surfaces (5 September), (iii) A positive separatrix cave surrounded by other positive separatrix surfaces (6 September) and (iv) A positive separatrix cave surrounded by other positive separatrix surfaces (7 September) are overlying the flaring active region.

4.4.2 Active Region NOAA 11283

Active region NOAA 11283 crossed the disc from 30 August 2011 to 12 September 2011. Two X-class flares were observed on 6 and 7 September, along with some C and M-class events. We investigate the change in the active region topology in the days before the X-class flares occurred. The active region was analysed on the 4 September 2011 initially, see Figure 4.13i. It was found that there was a single positive separatrix dome overlying a portion of the active region, with many footpoints of negative spines also lying along the edges of the positive separatrix surfaces. This feature lay across one side of the active region with the other side of the active region mostly clear of any topological features. On the 5 September, see Figure 4.13ii, the topology of the active region was very similar to that found in the previous day's analysis with the positive separatrix dome still present in the region.

On the 6 September, it was found that the topology around the region had altered slightly as shown in Figure 4.13iii. There was still a positive null present in the region, however it is low lying and no longer producing a separatrix dome. The positive separatrices in the region have become a separatrix cave lying at the edge of an opposite polarity region. It should also be noted that the HCS still cuts through the edge of this region. This topology is the same as that found on 7 September, shown in Figure 4.13iv. However, the cave present on 7 September looks to have become smaller in the region to match the reduction of the smaller positive polarity region. This region was also analysed previously in Appendix A.3, where the 3D magnetic skeleton is also shown with the correlation to one of the X-class flare observations.

4.5 Discussion

In this chapter we have analysed 14 active regions where X-class flares have occurred using a potential field source-surface (PFSS) model. The active regions analysed were NOAA 11158, NOAA 11166, NOAA 11283, NOAA 11429, NOAA 11520, NOAA 11890, NOAA 11944, NOAA 12017, NOAA 12158, NOAA 12192, NOAA 12205, NOAA 12242, NOAA 12297 and NOAA 12673. Note that six active regions are analysed in Section 4.2, with the rest of the active regions discussed in Appendix A.3. These regions were chosen as they were all the site of at least one X-class flare that had flare ribbons visible in $1600\mathring{A}$ AIA data. The study was conducted to investigate whether certain types of topological features could be found in the active regions, noting which type was more prevalent and whether they could be associated with the observed flare ribbons.

The three main types of topologial structures that were looked for in the active regions were separatrix domes, separatrix caves and separatrix tunnels. All of these structures originate from at least a single null point, with the separatrix dome intersecting everywhere at the photosphere, the separatrix cave should have an obvious single opening where it does not intersect with the photosphere and finally the separatrix tunnel should have two openings where it does not intersect with the photosphere. Examples of all of these structures were shown in Figure 4.1.

To analyse all of the regions the 3D magnetic skeleton of the PFSS model was created, with a surface cut taken along $R = 1.001R_\odot$. This surface cut was subsequently compared to the active region HMI data and the $1600\mathring{A}$ AIA data to compare the separatrix structures found with the flare ribbons observed. Note that for the PFSS models the polar field values were averaged using HMI data products (see Chapter 2), this may affect the larger scale features such as the HCS but as the active regions are mainly located between poles and here smaller localised features are being analysed.

In relation to the flare ribbons observed during the X-class flare events, many of the features found in the active regions were of a similar shape and position to the flare ribbons observed. This indicates that the topological features found in the active regions influence the structure of the flare ribbons observed. However we can only currently map the flare ribbons to the separatrix surfaces by eye, Chapter 6 discusses methods to allow for a mathematical comparison. This will allow a more robust method of understanding whether the flare ribbons can be associated with the topological structures found. A summary of all the X-class flares analysed is shown in Table 4.3. The table highlights whether the flare ribbons are thought to map (by eye) to the topological features found, the type of features located in the active region and whether the structures occur under open or closed field. As well as showing the results for all the flares analysed in Section 4.2, the table shows all the X-class flares that occurred in the active regions while they crossed the solar disc, along with those discussed in Appendix A.3. Note that in the regions where more than one solar flare occurred, the separatrix structure type did not change between flares but may have changed slightly in shape. For example, active region NOAA 12192 where four X-class flares occurred, was always found to have no relevant topoological features in the active region no matter when the analysis was carried out.

To investigate whether it could be the potential fields affecting some regions lacking topological structures, or the structures lying slightly offset in relation to the flare ribbons observed the magnetohydrostatic (MHS) model discussed in Chapter 3 is used as an alternative magnetic field extrapolation in Section 4.3. Active region NOAA 12242 was analysed, with the MHS field extrapolated using $\bar{\alpha} = 0.3$ and $d = 0.005$. When comparing the MHS and PFSS models in Figure 4.11 it is shown that the cave structure remains the same overlying the active region, with the main differences occurring in the position of the HCS intersecting with the solar surface. The other flares discussed were also analysed using the MHS method, however it quickly became clear that the topological features found in the regions were not changing with the use of the MHS model. In some regions, like in the example given, small structures originating from null points were also found. Overall it was decided that the use of the PFSS model was sufficent in deducing what topological features lie in a region for the purpose of this work. This is due to the MHS model finding the same local topology in the active regions analysed and mostly changes were seen in the global structures such as the HCS, with the PFSS field much easier to calculate than the MHS fields. However further improvements could be made with the use of a NLFFF model, which is not covered in this work.

Date	Start Time	End Time	Flare Class	AR Number	AR Type	Ribbons Map?	Topological Feature around AR	Open/Closed Field
15/02/11	01:44:00	01:56:00	X2.2	11158	$\beta\gamma$	Yes	Dome	Open
09/03/11	23:13:00	23:23:00	X1.5	11166	$\beta\gamma\delta$	Partial	Dome	Open
06/09/11	22:12:00	22:52:00	X2.1	11283	$\beta\gamma\delta$	Yes	Cave	Closed
07/09/11	22:32:00	22:38:00	X1.8	11283	$\beta\gamma\delta$	Yes	Cave	Closed
07/03/12	00:30:00	01:15:00	X1.3	11429	$\beta\gamma\delta$	Partial	Cave	Closed
12/07/12	15:37:00	16:49:00	X1.4	11520	$\beta\gamma\delta$	No	None	Closed
08/11/13	04:20:00	04:45:00	X1.1	11890	$\beta\gamma\delta$	Yes	Dome	Open
10/11/13	05:04:00	05:38:00	X1.1	11890	$\beta\gamma\delta$	Yes	Dome	Open
07/01/14	18:04:00	18:32:00	X1.2	11944	$\beta\gamma\delta$	No	Dome	Closed
29/03/14	17:35:00	17:54:00	X1.0	12017	$\beta\delta$	Yes	Cave	Open
10/09/14	17:21:00	17:45:00	X1.6	12158	$\beta\gamma\delta$	No	None	Closed
22/10/14	14:02:00	14:50:00	X1.6	12192	$\beta\gamma\delta$	No	None	Open
24/10/14	21:07:00	21:41:00	X3.1	12192	$\beta\gamma\delta$	No	None	Open
25/10/14	16:55:00	17:08:00	X1.0	12192	$\beta\gamma\delta$	No	None	Open
26/10/14	10:04:00	11:15:00	X2.0	12192	$\beta\gamma\delta$	No	None	Open
07/11/14	16:53:00	17:54:00	X1.6	12205	$\beta\gamma\delta$	Yes	Mixed	Open
20/12/14	00:11:00	00:55:00	X1.8	12242	$\beta\gamma\delta$	Yes	Cave	Open
11/03/15	16:11:00	16:29:00	X2.1	12297	$\beta\gamma\delta$	Yes	Cave	Closed
06/09/17	11:53:00	12:10:00	X9.3	12673	$\beta\gamma\delta$	Partial	Cave	Closed

Table 4.3: Summary of all flares analysed and their active region properties.

As an alternative to creating the 3D magnetic skeletons and comparing the topological features found with the flare ribbons observed, quasi-separatix layers (QSLs) could also be considered. Here we studied the flares already analysed by calculating the squashing factor, Q, to deduce whether QSLs could be present in the regions. This was of particular interest to the regions where we found no separatrix surfaces that could be mapped to the flare ribbons observed.

For regions where separatrix structures had already been located by using the PFSS model, regions of Q greater than 10^7 were found around the points of intersection of the separatrix structure footpoints with the solar surface. Examples of this are shown in Figures 4.5 and 4.9, where large Q regions correlate to the separatrix dome and caves located in these active regions. However it is more important to analyse regions where no separatrix structures were found or only one flare ribbon was thought to correlate to a structure found. Figure A.3 shows examples of this. Active region NOAA 11520 was found to have no topological features lying very close to the observed flare ribbons (although some were found on the edge of the active region). When the Q map was calculated a region of large Q was found close to the flare ribbons which with a slight offset looked to lie across it. This could indicate the presence of a QSL where no separatrix surface was located by the PFSS model. However, active region NOAA 12158 which was found to have no separatrix structures that could correlate to the observed flare ribbons was also found to have no regions of high Q that could possibly indicate QSLs either. For the other active region where no interesting topological features were found (NOAA 12192) this was also the case.

In addition to analysing the active regions during an X-class flare, two active regions were chosen to be analysed as they crossed the solar disc. This would allow the investigation of the development of topological features as the active regions developed in the days leading up to and following the X-class flare events. Active region NOAA 11158 was chosen as one of these regions with PFSS models created for all days from 12 February 2011 to 15 February 2011. Here we saw the development of the negative separatrix dome which was present on the 15 February when the X-class flare occurred. Initially a small separatrix dome was found to lie over the region, which eventually reduced in size before disappearing completely by day four. In addition to this a negative separatrix cave was present on days two and three which eventually developed into the separatrix dome analysed previously. In addition to this, active region NOAA 11283 was also analysed from 4 September 2011 to 7 September 2011 (the day when the X-class flare occurred). Here a positive separatrix dome was found to lie over a region of positive magnetic field at the edge of the active region which slowly over the following days developed into the separatrix cave previously analysed. There were other features in this region which also changed structure. This analysis shows that the PFSS model can show the development of topological features as the active regions age, with a simple model such as the PFSS showing that further analysis could take place using more complex methods such as NLFFFs to gain further insight into the development of magnetic field features.

Overall in this chapter we have shown that a range of topological features can be found in active regions that have had flaring activity, in particular X-class flares. Through the analysis of fourteen active regions from February 2011 to September 2017 and the extrapolation of their potential magnetic fields, the main topological features found in the regions were separatrix domes and caves. These separatrix structures could subsequently be mapped to the flare ribbons by eye to deduce whether it was thought that their presence could have determined the flare ribbon shapes and positions as observed by AIA. In the majority of regions where separatrix surfaces were located, they were found to partially map to parts of the flare ribbons observed. In active regions where no separatrix structures were found it was thought the use of an MHS model or locating QSLs in the active region could possibly help find structures that correlate to the flare ribbons. The use of the MHS models did not result in the finding of more topological features in the active regions and in active regions where features had already been found using the PFSS model, those same features were located with perhaps small changes in feature positions or shape. Subsequently, the Q values were calculated to look for the presence of QSLs, again however in regions where features had already been found regions of high Q were also located but in regions where no topological features had been found, regions of high Q were also not present. However for some of the active regions where only one flare ribbon was thought to correlate to the feature found, there were also regions of high Q located close to the second ribbon, for example see analysis of active region NOAA 12242. This was also the case for active region NOAA 11520 where high Q values were found that could correlate to the ribbons observed but not to any topological feature in the region. Furthermore two active regions were analysed to allow an insight into the topologcial feature development that occurred over a period of a few days where the regions were visible on the solar disc.

To further the work done here, the use of a NLFFF model globally or locally would result in the finding of topological features in the regions where none were located previously. Including local currents which are implemented through the NLFFF model, would alter the magnetic field structure around the flaring active regions to become more dynamic and realistic to the actual magnetic field properties of the active regions. As previously mentioned the flare ribbons mapped to the topological features by eye to indicate whether they could match each other, this is investigated further in Chapter 6 where we introduce quantitative metrics to try to indicate whether the topological features could match the flare ribbons in shape and position. All of the work carried out here is taken at a snapshot in time, with the flare ribbon observations taken around the peak flare time with the ribbons unsaturated. The magnetic field models use daily synoptic maps, taken from the day when the flares occurred. Further work could investigate the use of HMI magnetograms taken during the flare and analyse how the topological structures can change during the flare period, in a similar fashion to the work done in Section 4.4 which shows the change in separatrix structures across each day for active regions NOAA 11283 and NOAA 11158.

92

Chapter 5

Analysing Observations using Convolutional Neural Networks

In this chapter, we discuss the use of *Convolutional Neural Networks* (CNNs) as a method of automatically detecting events observed on the solar disk. Due to the vast amounts of data being generated by both ground-based and space-based instruments, for example 1.5 terabytes of data is collected every day by the *Solar Dynamics Observatory* (SDO), the detection of solar events can be made more efficent by implementing machine learning techiques such as CNNs.

Here we intitally analyse full disk observations taken by the *Atmospheric Imaging Assembly* (AIA) onboard SDO. In particular, we concentrate on detecting flaring active regions and further classifying the shape of the flare ribbons observed. It is shown that a CNN can be created and trained with approximately 93% accuracy to correctly classify 1600$\AA$ AIA data that contains one of the following; quiet sun, two-ribbon flare, compact ribbon flare or a limb flare. However, throughout our classification process we see some confusion between the compact flare class and the limb flare class.

We go on to show that a separate single-layer neural network model can be added to our CNN to allow the use of numerical and categorical variables that may help with the classification of the flaring regions. By training the new model, it is shown that with the addition of positional data there is no longer confusion between compact and limb flares. We also briefly discusss how the model could be changed to accommodate the detection of other solar events such as filaments.

As discussed in Chapter 4, the geometry and topology of the solar magnetic field around the flaring active regions are thought to contribute to the locations and shapes of the flare ribbons observed. In particular, the presence of separatrix surfaces and/or quasi-separatrix layers (QSLs) (e.g. Aulanier et al., 2000; Savcheva et al., 2015; Hou et al., 2019; Janvier et al., 2016) have been connected to the lengths and shapes of some flare ribbons. Although, in most previous studies two-ribbon flares are the most commonly analysed, it is known that flares with compact (or circular) flare ribbons can also be observed. A key motivation of this work is to create a tool which can be easily used to analyse large amounts of data quickly, whilst confirming whether flares (or other features) occur in the region of the image or observation analysed.

Within the remainder of this chapter we aim to show how the networks previously discussed can be created and trained, whilst showing how accurately they work on unseen datasets.

5.1 Methods

Convolutional neural networks (CNNs) are one type of machine-learning techniques that can be used to detect objects or patterns in data and classify them, (e.g. LeCun and Bengio, 1998; LeCun et al., 2015b; Alzubaidi et al., 2021). They were created to get a more regularized version of a multi-layer perceptron (MLP) or a normal neural network. To do this, unlike MLPs they share information (or weights) across each convolutional node, meaning that the amount of data used is greatly reduced. To identify trends and patterns in the image data, instead of being given instructions or mathematical functions they learn through the use of a *training data* set, allowing for a more natural learning method and the ability to pick up similarities and differences in each class chosen by the creator. The training data is used as the inputs for the CNN and usually consists of a subset of the data that the programmer would want to classify or detect objects in, allowing the network to learn the patterns in the data which it can subsequently use to classify previously unseen data sets.

5.1.1 CNN Design

To create a convolutional neural network (CNN) there must be at least 3 three layers; an input layer, a hidden layer and an output layer (e.g. Cun et al., 1990; Hinton et al., 2012; Krizhevsky et al., 2017; LeCun et al., 2015a; Szegedy et al., 2015). In general, there is one input layer and one classification (output) layer with as many hidden layers as the programmer wishes in between. The number of hidden layers chosen however is usually dependent on the complexity of the data being classified.

The input layer is the initial network layer which initalises the input data size for the network and accesses the image input to pass onto the first hidden layer. The data input should be pre-processed before being passed into the input layer; the data used in our network is processed as described in Section 5.1.2.

After the input layer, hidden layers are added to the the CNN. The types of hidden layers used throughout our analysis are;

1. convolutional layers
2. activation layers
3. pooling layers
4. fully connected (FC) layers

Each of these hidden layers contributes to how a CNN learns how to distingush between classes.

The convolutional layers apply mathematical convolutions to the image data. To carry-out these convolutions a kernel is created which contains a set of weights that are applied to each image to produce what is known as a *feature map*. This image convolution process is where the kernels have their rows and columns flipped, then the kernel values are multipled with the corresponding local values in the image and these are then summed together. The kernels used throughout our analysis are chosen to be 3×3 in size, however can be larger or smaller depending on the use of the convolutional layers. Another parameter affecting how the convolutional layers operate is the *stride* of the kernel across the image data. This indicates how many pixels the kernel should skip before applying the convolution to the data again, with the stride chosen to be 1 in the CNN created here. Again this parameter can be altered depending on the use of the CNN for example, if larger features were to be found the stride may be increased. An example of a image convolution being carried out is shown in Figure 5.1. Convolutional layers are used as, applying these image convolutions helps reduce the dimensionality of the image data which can reduce overfitting and overtraining.

Hence the kernel will apply the convolution to the whole image similar to that shown in Figure 5.1. For the first convolutional layer the input will be,

$$\text{number of images} \times \text{image width} \times \text{image height} \times \text{image channels},$$

with a 3×3 kernel being applied where $\textit{stride} = 1$. This will result in a feature map of size,

$$\text{number of images} \times \text{image width}{-}2 \times \text{image height}{-}2 \times \text{number of kernels}\ ,$$

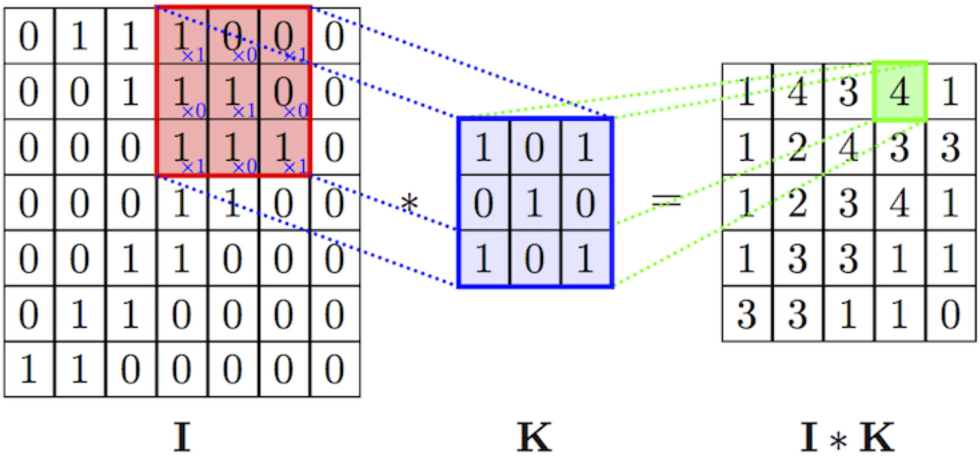

Figure 5.1: A 3×3 kernel (K) is applied to a 7×7 image (I) via an image convolution. The resultant array is summed together and the value passed into a new *feature map* (I∗K)which will be 5 × 5 in size. (Originally shown in S. Mohamed (2017))

where the number of kernels applied can be chosen. The overall size of the data being used in each subsequent convolutional layer will be smaller than the previous layer, with the height and width of the feature map calculated using the following formula,

$$n_{out} = \left[\frac{n_{in} + 2p + k}{s} \right] + 1, \tag{5.1}$$

where n_{out} is the size of a feature map height or width, n_{in} is the original feature map height or width size, p is the size of the padding used, k is the kernel size and s is the stride length. Note that throughout, our CNN has $p = 0$ in every convolutional layer. Once a set of feature maps has been produced by a convolutional layer, they are passed onto an activation layer.

An activation layer uses what is known as an *activation function* to help the CNN decide which neurons fire in the next layer i.e; what individual feature maps produced by the previous convolutional layer are passed onto and used by the next layer in the network. It can also be described as deciding which convolutional nodes are turned on during training and which are turned off. There are many activation functions to choose from, however there are features that are desirable for activation functions to possess such that they do not create problems when training the network.

One of the most desirable features of an activation function, is for it to prevent the *vanishing gradient* problem. This occurs during the training process when *back-propagation* (see Section 5.1.3) is being carried out. Backpropagation is the process carried out during training which updates the weights (values in kernels) used in the convolutional and fully connected layers. During the process the values from the chosen activation functions, usually between 0 and 1, are used to calculate gradients needed for the weight updates. If the values from the activation functions are close to or equal to zero then the gradients calculated will tend to zero (or vanish). These zero gradients will cause the weights to stop being updated and results in the network no longer training on the data. This training process of updating weights by backpropagation is discussed in further detail in Section 5.1.3. This is known as the vanishing gradient problem and hence activation functions are selected to minimise the possibly of this occurring. Note, that as activation functions must be differentiated to update the weights during training, the function itself must be differentiable.

As well as the vanishing gradient problem, activation functions should try to be zero-centered i.e; the output from the activation functions should be symmetrical about zero to prevent the gradients being calculated during training shifting in either direction. Finally, as activation functions are calculated after each layer they can be calculated thousands of times during training and so should also be computationally inexpensive.

There are various activation functions to choose from, and for the CNN created here a *rectified linear unit* (ReLU (Nair and Hinton, 2010)) activation function was used for every layer except the output layer. The ReLU function is defined by;

$$f(x) = max(0, x). \tag{5.2}$$

Note that this function is not differentiable everywhere (i.e. at $x = 0$), although it is commonly used in CNNs as it deals well with the vanishing gradient problem, however it can suffer from another problem known as the *dying ReLU* problem. This is where, due to all-negative inputs to the activation function returning 0, the convolutional node will be turned off and hence not learn or help the network train. The ReLU function can also become unstable as its upper bound is infinity and so this can sometimes lead to unstable nodes. Note that when differentiating to calculate the weights the reason ReLU can be used although it is not differentiable here is that the value of $x = 0.000000$ is very rarely reached, however where this value is reached it is assummed the derivative value is taken at the nearest x-value i.e the derivative can be set to zero.

Other activation functions such as *linear, exponential* or *softmax* (see Equation 5.3) can be used for convolutional or FC layers, however both the linear and exponential activation functions can also suffer from the vanishing gradient problem and so are rarely used.

As previously discussed, convolutional layers and their subsequent activation layers are the main contributors to the hidden layers present in CNNs. Usually implemented after convolutional layers, as an optional layer to prevent over-training, *pooling* layers can also be used. Pooling layers help to reduce the number of parameters calculated during training whilst also preventing and helping to reduce over-fitting of the training data sets. This reduction in training parameters also allows the CNN to train faster. Pooling layers are typically implemented by either *max-pooling* or *average-pooling*. A max-pooling layer similarly to a convolutional layer contains a kernel which passes over the data, however instead of appling an image convolution, the pooling layer takes the maximum value of the pixels the kernel has passed over. That maximum value is then passed into a new and smaller feature map. Note that, average-pooling layers work in a similar way, taking the average of the data instead of the maximum.

The kernel sizes used in pooling layers can be varied similarly to those in convolutional layers; throughout this work the neural networks created all use max-pooling layers with a kernel size of 2×2. By using pooling layers, it is thought that the most important features of the network will still be passed onto the next layers with a smaller, more easily trained feature map being used.

Although not listed above as a possible hidden layer, another layer which is used in our CNN is a *dropout* layer, (see e.g. Hinton et al., 2012, for further information on dropout layers). Similarly to pooling layers, these layers are implemented to prevent over-training of the input dataset. These layers are usually implemented before FC layers to indicate the percentage of random nodes that should be switched off during training of the next layer i.e. they have *dropped out* of the training process for that current iteration (or epoch). These layers are used to prevent nodes memorising input data and therefore not learning properly.

Once the hidden layers have been chosen, the final layer type that can be implemented are fully-connected (FC or dense) layers. These layers can be used as hidden layers, however they also act as the output layer which returns the final classification of the data. FC layers only work on one-dimensional data and so input coming from previous hidden layers must be converted into a one-dimensional array before being passed into the FC nodes. As their name suggests, each node in a FC layer receives an input from all the nodes in the previous layer. Hence, unlike convolutional layers that rely on patterns in the image data, FC layers return features that are combinations of those previously found. The FC layer itself carries out the dot product between the input tensor and the kernel for each node, before passing that output and the bias vector (if one has been used) onto an activation function.

As previously mentioned, after the hidden layer, the final step is to pass the data into an output layer which is always a final FC layer. This layer carries out the final classification which indicates what class an input belongs to. The final FC layer is chosen to have,

$$\text{number of nodes} = \text{number of classes.}$$

As this layer is indicating what class the data belongs to, the activation layer associated with it has to correspond to what the network is trying to classify. Here the final activation function used is a *softmax* activation; this allows the probabilities of whether the data belongs to a certain class to be produced. Hence, the probability, $p(x_i)$, of each class is calculated using a softmax distribution such that;

$$p(x_i) = \frac{e^{x_i}}{\sum_k e^{x_k}}. \tag{5.3}$$

This function should tend towards 1 if an observation belongs to a single class and tends to 0 for the other model classes to indicate that the network does not recognise it as belonging to those classes.

The CNN created here was used to analyse flare ribbons observed in AIA data. The four classes were chosen to be,

1. **Quiet Sun**

   No brightenings present on the surface, hence should give an indication of general background values. (It should be noted that none of these observations are taken on the limb.)

2. **Two-ribbon Flare**

   Two flare ribbons must be clearly defined in the observations. However the shape does not matter here e.g. if there are 2 semi-circular ribbons the flare is classified as a two-ribbon flare and not a circular flare.

3. **Limb Flares**

   The solar limb must be clearly observed in this snapshot observation with a flare brightening being visible. The limb class was chosen to start at a specific distance from the solar limb to reduce confusion with other classes. This will be discussed further in Section 5.2.

4. **Circular Flare Ribbons**

   Here a circular ribbon shape of any size must be observed. It should be ideally a singular ribbon so as not to be confused with the two-ribbon flare class. Compact

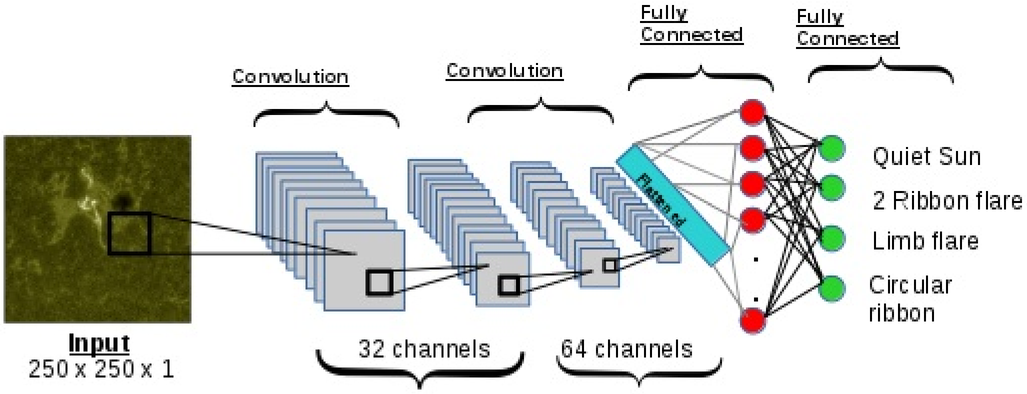

Figure 5.2: Layout of CNN created, including two convolutional and max pooling layers and two fully connected layers. The first convolutional layer has 32 channels followed by max pooling layer and the second convolutional layer has 64 channels followed by a max pooling layer. The fully connected layer has 128 nodes and then the final fully connected layer has four nodes which correspond to each of the classes - Quiet Sun, two-ribbon flares, limb flares and circular/compact flares.

flares were also included here, they appear in the data as round 'dot' like shapes.

The CNN created had two convolutional layers and one fully connected layer implemented as the hidden layers. All of the layers were chosen to have ReLU activations, with the first convolutional chosen to have 32 nodes and the second convolutional layer chosen to have 64 nodes before passing onto the FC layer with 128 nodes. A max-pooling layer with a stride of 2, was present after each convolutional layer. A drop-out layer was also used between the final convolutional layer and the hidden FC layer. The output FC layer had four output nodes with softmax probabilities being calculated. All layers were chosen to have padding, $p = 0$, indicating that the outputs will get smaller in size.

The final model layout is shown in Figure 5.2 with the training parameters calculated during the training process shown in Table 5.1. The CNN was created and trained using Keras (Chollet et al., 2015), with the training process and outcomes discussed in Section 5.1.3.

5.1.2 Data preparation

The CNN was created to locate whether a solar flare occurred in the observations and to classify it by the shape or location of the flare ribbons observed. Hence, a robust data set of flaring regions was created to train the network. To ensure the CNN would

Layer	Number of nodes	Kernel Size (Weights)	Stride	Activation Function
Convolution	32	3×3	1	ReLU
Max Pooling	/	2×2	2	/
Convolution	64	3×3	1	ReLU
Max Pooling	/	2×2	2	/
Fully Connected	128	$61 * 61 * 64 \times 128$	/	ReLU
Fully Connected (Output)	4	128×4	/	Softmax

Table 5.1: Details of each CNN layer with the number of filters, size of kernels and activation functions used shown.

train on the correct features in each image, observations from the same instrument with a specific wavelength were chosen for the training and test datasets. This would ensure that the network would not train on varying parameters such as wavelength or solar features that are perhaps only observed using specific instruments. Due to this the data has been collected from the *Atmospheric Imaging Assembly* (AIA) on board the *Solar Dynamics Observatory* (SDO) at the 1600 $\AA$ wavelength. The flare observations in this wavelength give a clear overview of what the flare ribbons look like without any interference from other features like nearby coronal loops; this is due to the observation in this wavelength showing the upper chromosphere and transition region, (Simões et al., 2019), giving a clearer view than the AIA observations in EUV wavelengths.

To create the training and test sets, observations where known flares had already occurred were used. Flares documented in a flare ribbon database, (see Kazachenko et al., 2017), were chosen such that any flare that took place between February 2011 and March 2015 were included in the training and test datasets.All of these flare observations have to be labelled corresponding to one of the four classes chosen for the CNN. Throughout the labelling process the flares that were found to have saturated flare ribbons, where the shapes were not visible, or other errors in the data were removed from the dataset. This resulted in a training set containing 540 image samples with 160 quiet Sun regions, 160 two-ribbon flares, 95 limb flares and 125 circular flares.

When creating the training and test sets, flares have been chosen such that they should clearly fall into a particular class. To be able to classify each image the following process was implemented.

Using the *Heliophysics Event Knowledgebase* (HEK) (Hurlburt et al., 2012), the observations used for each flare were chosen at the peak flare time. It should be noted that the evolution of the flare ribbons from the start to the end of the flare is not taken into account by the CNN, although this could be included in further work. As the images processed are full disk images, sometimes more than one flare is visible. In those cases both flares are processed and classified separately.

Once the flares have been located in each image, a bounding box of size 500 × 500 × 1 pixels is created around each flare position. Due to the the number of training parameters increasing as image size increases, this step was added to reduce the size of image the CNN would have to process whilst also reducing the training times. The original AIA level 1 data files are 4096 × 4096 × 1 in size, so the network must extract boxes around the flares as the full disk images are too large for CNNs to work with. This code works in a similar way to that of an object detector creating bounding boxes around objects to be classified further.

Once each flare has been located and a bounding box created around it, the image must be labelled according to one of the classes previously discussed in Section 5.1.1; two ribbon flare, compact ribbon flare, a limb flare or a quiet sun image. To find which

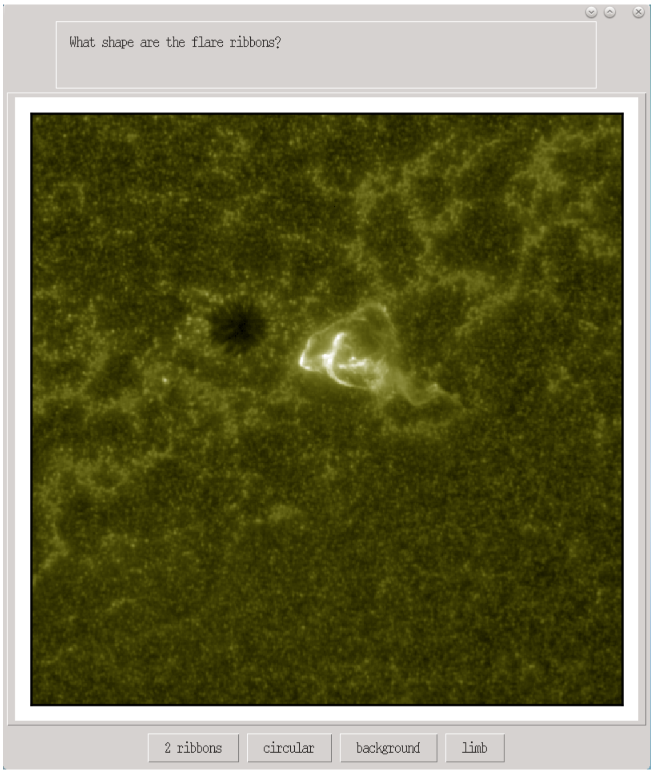

What shape are the flare ribbons?

Figure 5.3: The graphical user interface created to classify each flare by hand.

class an image belongs to, each image was labelled by hand. This was done using a *graphical user interface* (GUI) as shown in Figure 5.3, allowing a clear overview of what class each image belongs to. This interface was created using the python package easygui. Each image must be labelled for the model to train, allowing it to learn why an image belongs to a certain class, see Section 5.1.3.

After each image has been classified the overall size of the image data must again be reduced to allow a suitable size for training the CNN. Hence each image was downsampled to become an image of size 250 × 250 × 1, where the final set of input data would contain n ROI samples such that the final size of the data inputted to the initial CNN layer would be $n \times 250 \times 250 \times 1$.

The final step for the data preparation was to normalise the data before training, this will ensure the best results when training the CNN and so all of the ROIs were normalised using their z-scores as follows:

$$\text{z-score} = \frac{\text{data} - mean(\text{data})}{standard\, deviation(\text{data})}.$$

Once all of the above processes had been carried out on the observations the CNN could begin training as discussed in Section 5.1.3. All flares used for training and testing occurred between February 2011 and March 2015, with a subset of flares that occured during this time being used. Some were removed due to corrupt image pixels or pixels blooming into adjacent pixels. Note that the training set contained 540 1600$\mathring{A}$ AIA images used for model training and the test set contained 430 1600$\mathring{A}$ AIA images which were used to test the robustness of the model as shown in Section 5.2.1. The test dataset used contained 160 quiet sun, 160 two-ribbon flares, 63 compact ribbon flares and 47 limb flares.

5.1.3 Model Training

In this section we will describe how the convolutional neural network (CNN) created *trains* i.e. learns how to distinguish between the classes chosen.

To learn to distinguish between the classes a gradient descent method must be implemented to update the weights at each kernel in all the fully connected and convolutional layers within the network. To do this weight update a loss function must be chosen so the network can learn the optimal classifcations for each training image. A *categorical cross-entropy* loss function was implemented here, which can be calculated by;

$$E = -\sum_{c=1}^{M} y(x_i) log(p(x_i)), \tag{5.4}$$

where M is the number of classes (here $M = 4$) and y is the binary indicator (0 or

1) such that if $y = 1$ the observation belongs to the class and $y = 0$ if it does not. Finally p is the probability that the observation belongs to a class, c. This loss is chosen dependent on whether the labels are one-hot encoded or integers and whether it is a binary classification problem or not. Due to our network having four classes and one-hot encoded labels (i.e., $[0, 1, 0, 0]$ etc.) categorical cross-entropy loss is used.

Here, to update the weights, w, and hence minimise this loss function, E, *stochastic gradient descent* (SGD) with Nesterov momentum, p_{mom}, included is used (Sutskever et al., 2013). This means the weights are updated by;

$$velocity = p_{mom} * velocity - l_{rate} * \frac{\partial E}{\partial w},$$

$$w = w + p_{mom} * velocity - l_{rate} * \frac{\partial E}{\partial w}. \tag{5.5}$$

The learning rate, l_{rate} must be chosen, indicating how fast or slow the network updates the weights during training. The inital $velocity = 0$ and $p_{mom} = 0.1$, with the velocity getting updated throughout training. The learning rate for our model was chosen to be 10^{-4} with a mini-batch size of 32. This indicates that with the SGD optimiser, mini-batch gradient descent is also being used. Hence instead of training on the whole dataset, it trains and updates the weights after every 32 images have been trained on. Note that although larger batch sizes can be used to speed up the training process, this batch size of 32 was chosen as it gave the optimal training results for the CNN. Where momentum, $p_{mom} = 0$, the Nesterov momentum is turned off and standard SGD is used.

To calculate the gradients needed to minimise the loss function, a process known as *backpropagation* (Hecht-Nielson, 1989) is carried out. There are four main steps to the backpropagation process; forward pass, calculating the loss function, backwards pass and the weight update. This process is derived in Appendix A.4.

Figure 5.4 shows an example of how the gradients are applied to the convolutional layer inputs to calculate new weight functions. One whole iteration of the backpropagation process over the whole training dataset is known as an *epoch*.

Once the network set-up has been chosen as discussed in Section 5.1.1, the network can begin training using the backpropagation process discussed above.The CNN was trained using 540 $1600\mathring{A}$ AIA images, with the data being processed before training as discussed in Section 5.1.2 and each image labelled to indicate which of the four classes it belongs to. Recall that the four classes chosen were; quiet sun, two-ribbon flares, compact ribbon flares and limb flares.

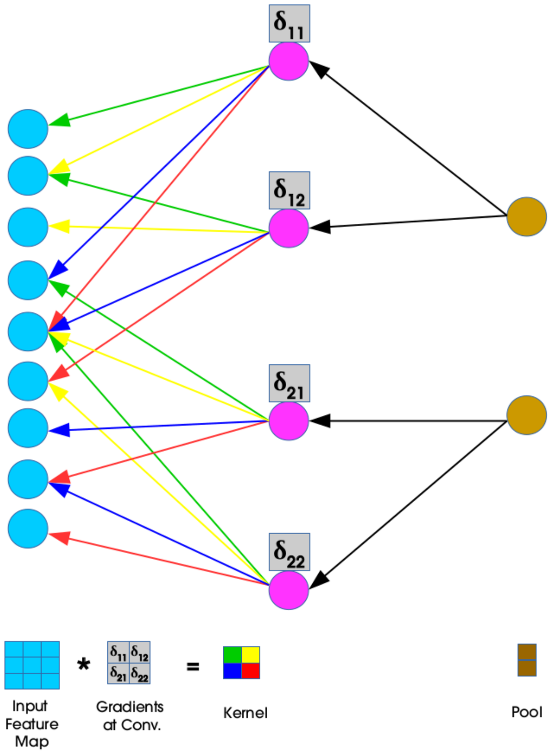

Figure 5.4: Illustrates how the backpropagation process uses the gradient values to update the model weights. (Originally shown in jefkine (2016).)

For the 540 images used, the number of images belonging to each class were divided almost evenly to ensure that observational bias would not affect the model during training. The slight imbalance between classes that does occur is not large enough to affect the training of the model. From this set of images, 60% were used as the main training dataset with the other 40% used as the *validation dataset*. The validation dataset is used during training to ensure that the training dataset is not being memorised by testing the network on unseen data to ensure it is still achieving the same accuracy as on the training dataset.

To investigate whether the network was training properly and learning which parts of each class were important we plotted the feature map outputs for both convolutional and max-pooling layers. An example of what the feature map looks like for a two-ribbon flare is shown in Figure 5.5i. Note that there are 32 nodes in the first convolutional layer, so 32 feature maps are produced (shown in a 16×2 grid) and 64 nodes are used in the second convolutional layer, so 64 feature maps are produced there (shown in a 16×4 grid. Note that for each group of four intermediate feature maps shown (e.g. Figure 5.5ii), both convolutional and max-pooling layers are presented. As an alternative view of what the CNN is training on, heatmaps are also produced which highlight where the

CNN concentrates it's training of features on (e.g. see Figure 5.5iii).

Figure 5.5i shows where the CNN is concentraing its training on. For the two-ribbon flares this highlights that the network is definitely concentrating on the two ribbons present in the image and not training on any of the possible background noise. Similar layer outputs and heatmaps were produced for the other 3 classes. Figure 5.6ii shows where the network is learning for compact flares. Note again that the compact ribbon itself is highlighted in the heatmap which means the network is training properly on the flare and ignoring the background, similar to the two-ribbon flares previously discussed. For the limb flares note that in Figure 5.7ii that although the strongest part of the heatmap is concentrated on the flare, the limb itself is highlighted along with some of the noise around it, this could lead to problems later where instead of picking up a flare on unseen data the CNN may just pick up the limb. The feature maps for the limb flares, shown in Figure 5.7i, help to visualise where each convolution is concentrating on training - it seems that similarly to the heatmaps, some of the convolutions are picking up the limb only, whereas others are locating the flare itself. The final set of heatmaps and feature maps calculated are for the quiet sun class shown in Figure 5.8 where it shows the network only picking up the background noise in the AIA data used.

The training results are shown in Figure 5.9. The training and validation accuracies are shown in Figure 5.9a, with the network only being trained for 10 epochs to prevent overfitting it is shown that even with so few epochs the training accuracy was found to be $\approx 98\%$ and the validation accuracy was slightly lower at $\approx 94\%$. The training and validation losses were also calculated throughout training with the results shown in Figure 5.9b. Both losses fall sharply and then start to level off over the 10 epochs. As the losses begin to level out the training of the CNN should be stopped as this indicates were over-fitting may occur if training continues. For both the accuracies and losses calculated note that, all values could be improved by increasing the number of images included in the training dataset.

To further validate the model training and its outputs, k-fold cross validation was implemented, similar to that implemented by Bobra and Couvidat (2015). This means that the model is trained from scratch k times, using the same training datasets to allow for generalisation of what values the training accuracies and losses would be at the final epoch. Here, we carried out 5-fold cross validation with the loss and accuracy values shown in Figure 5.9e. This means we trained the model 5 times using the same training and test datasets. Note that the mean training accuracy was found to be approximately $92.9\% \pm 2.98\%$.

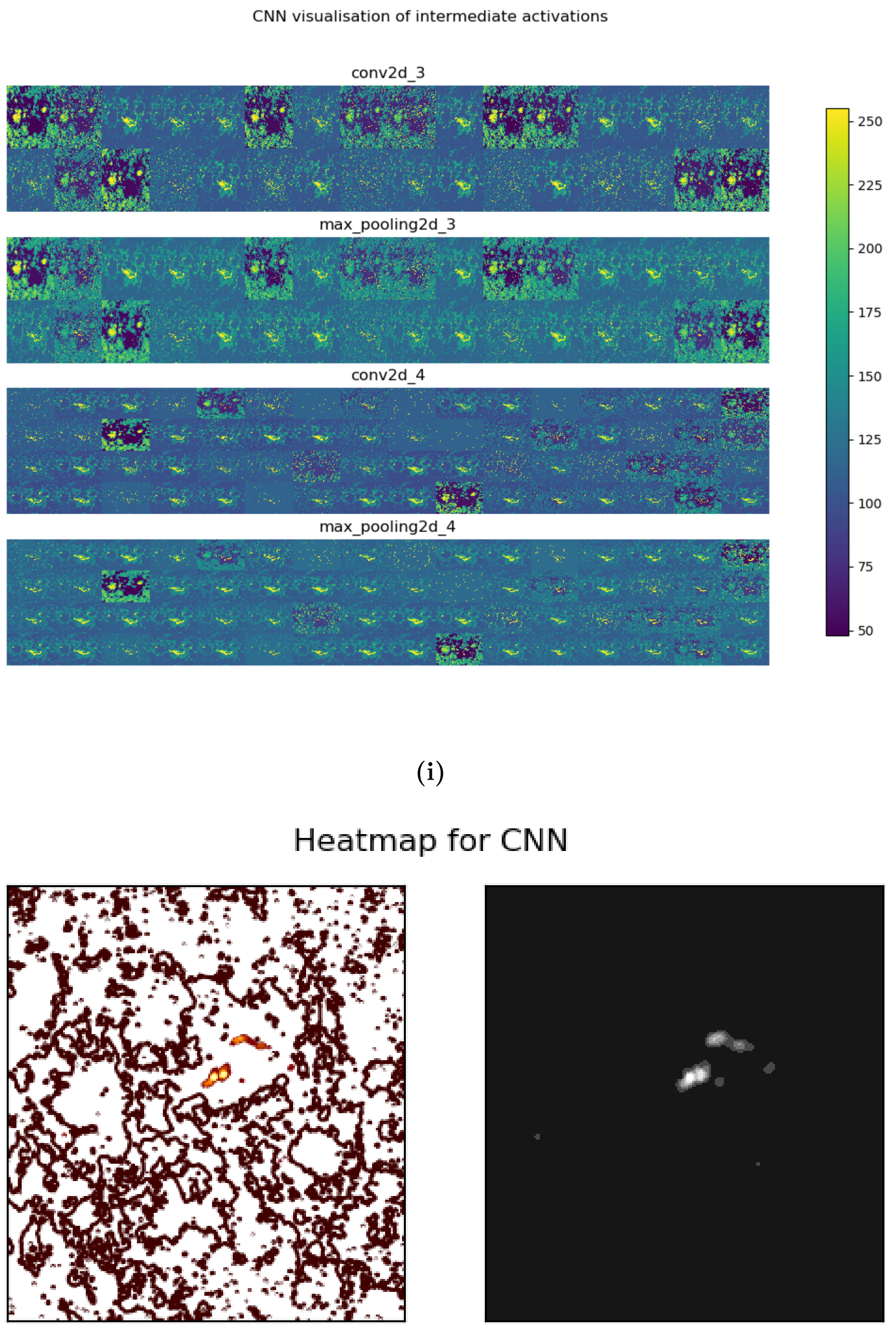

(i)

(ii)

Figure 5.5: Feature maps and heatmaps for two-ribbon flares; (i) visualises the outputs for each layer of the network and (ii) shows an example of the key parts of the image the network is training on to gain the correct classification.

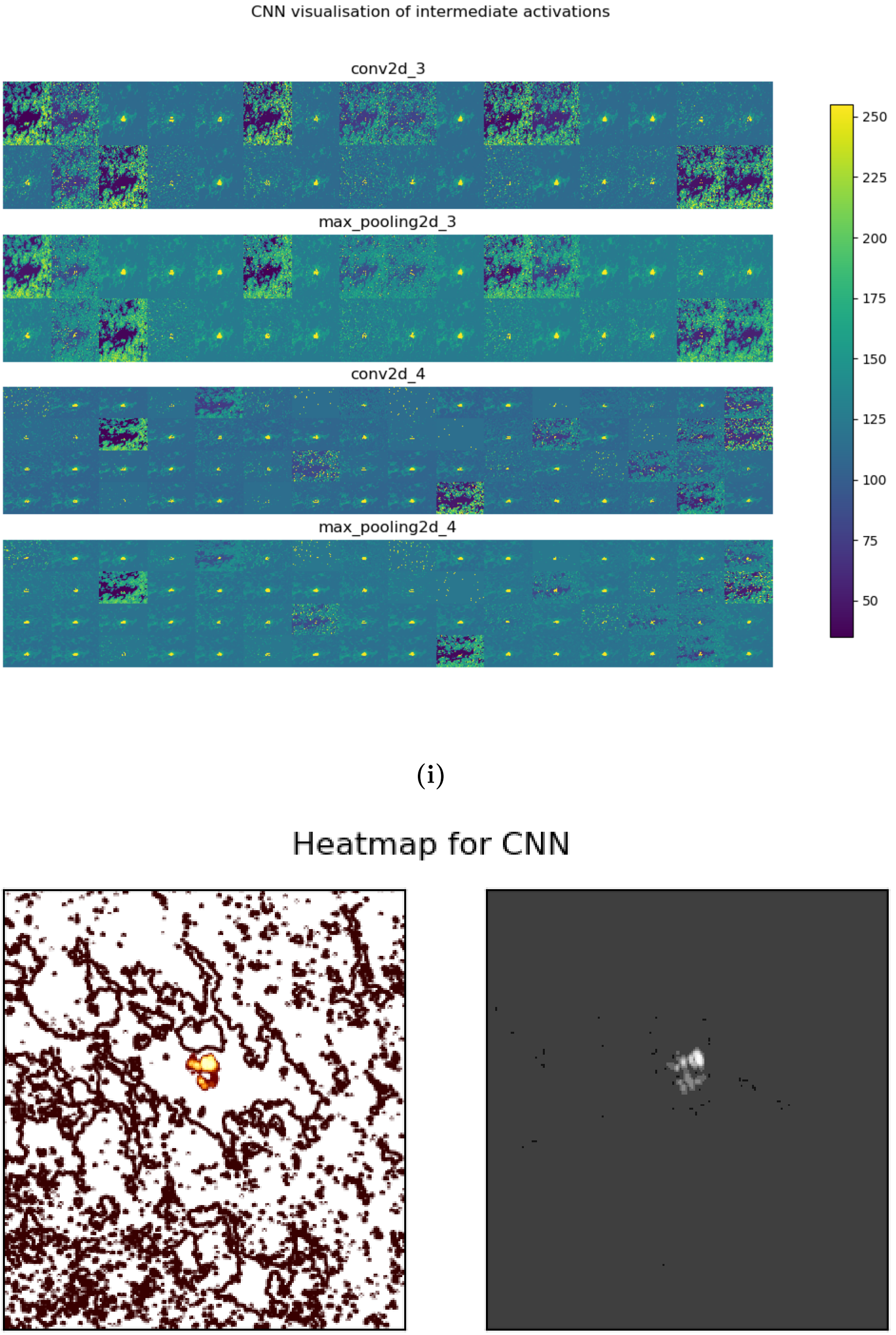

(i)

(ii)

Figure 5.6: Feature maps and heatmaps for compact ribbon flares; (i) visualises the outputs for each layer of the network and (ii) shows an example of the key parts a compact flare image the network is training on to gain the correct classification.

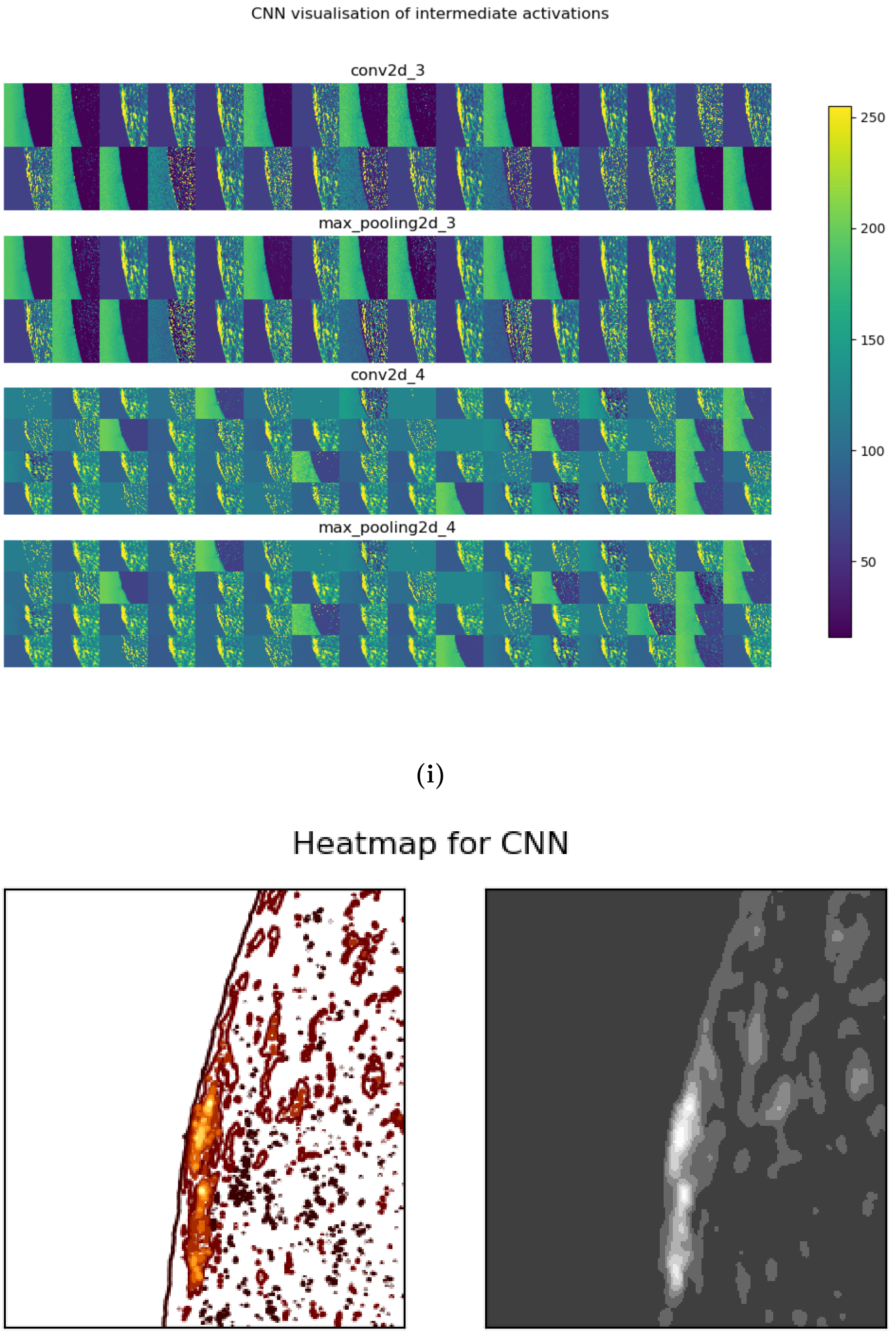

(i)

(ii)

Figure 5.7: Feature maps and heatmaps for limb flares; (i) visualises the outputs for each layer of the network and (ii) shows an example of the key parts of a limb flare image the network is training on to gain the correct classification.

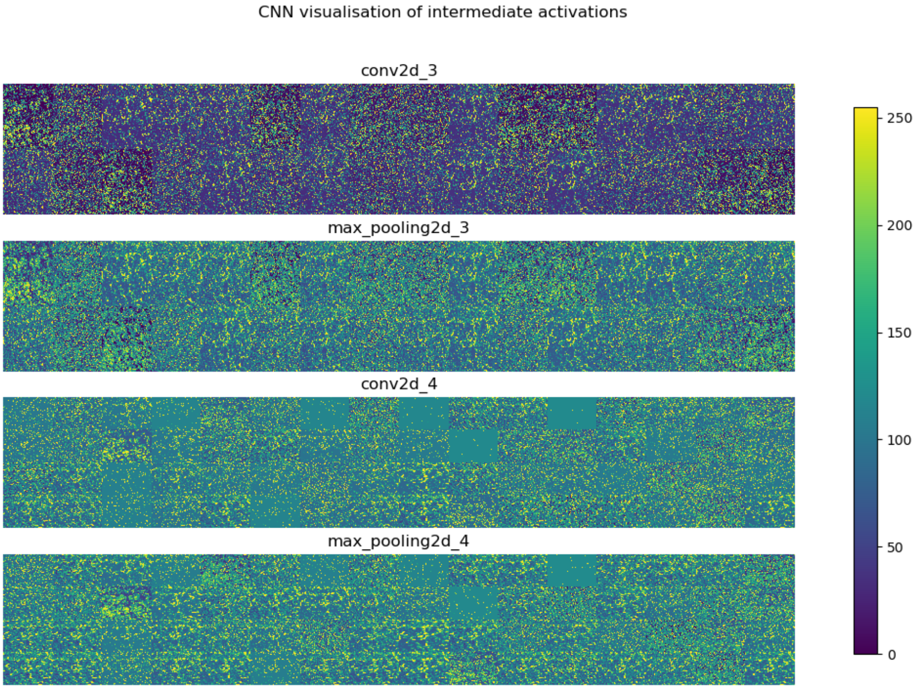

(i)

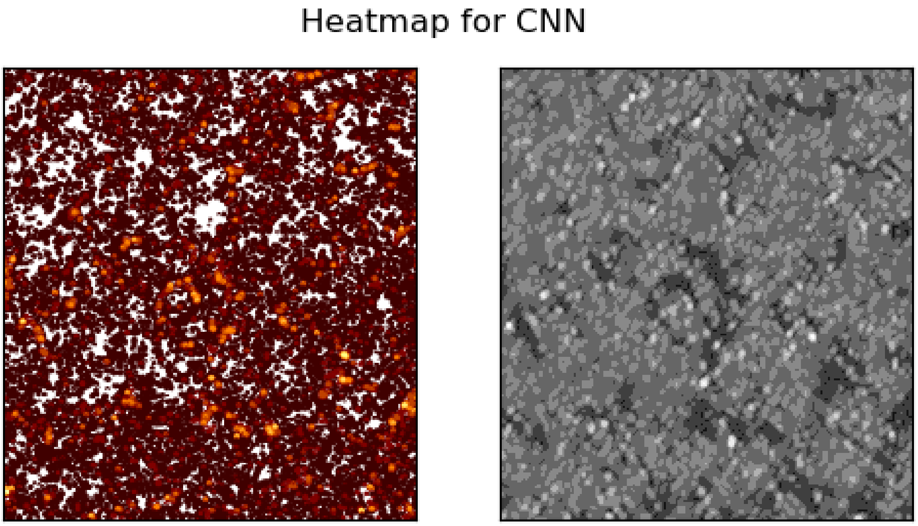

(ii)

Figure 5.8: Feature maps and heatmaps for quiet sun images; (i) visualises the outputs for each layer of the network and (ii) shows an example of the key parts of a quiet sun image the network is training on to gain the correct classification.

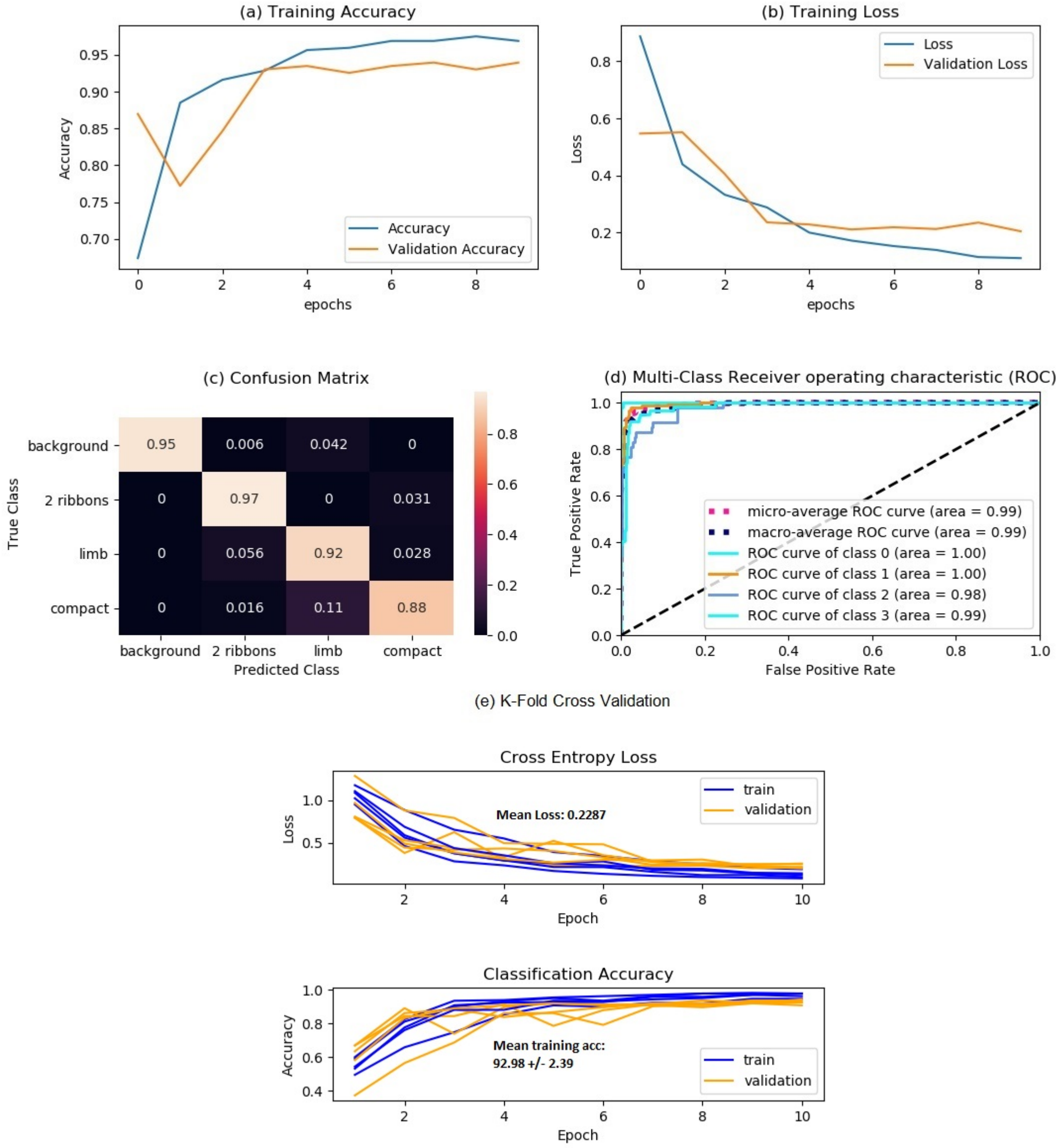

Figure 5.9: (a) Training accuracies with both validation and training accuracies shown over 10 epochs; (b) Training and validation loss shown over 10 epochs; (c) Shows the confusion matrix created on the test set, with the diagonal showing the correctly identified ribbon types; (d) shows the receiver operating characteristic (ROC) curve which has been modified to include a curve for each class and the micro and macro average curves; (e) Shows the results for loss and accuracy whilst using k-fold cross validation, where k = 5.

5.2 Results

5.2.1 Testing

After training the model the network accuracy can be checked by testing on a previously unseen dataset. This test set contained 430 images consisting of 160 quiet sun images, 160 two-ribbon flares, 47 limb flares and 63 circular ribbon flares. Some of the flares included in the test set may have occurred in the same active regions as those contained in the training datset. The outputs from the model classification of the test dataset are shown in Figure 5.9c and d.

To test whether the model is correctly classifying unseen data, a confusion matrix was created to show what percentage of the test dataset were being correctly classified, see Figure 5.9c. The confusion matrix creates a summary of the number of correct and incorrect classifiations with the predicted classes plotted against the true classes of the data. The percentage of correct classifications are shown in the diagonal of the matrix with all other entries showing the percentage of incorrect classifications. Approximately 95% of the quiet sun, two-ribbon flares and limb flares present in the test dataset were correctly classified, with only 88% of the compact ribbon flares correctly classified. Note that 11% of the incorrectly classified compact ribbon flares were classified as limb flares, this may be due to the limb flares lying close to the limb looking like compact ribbon flares. To remove this confusion between compact ribbon and limb flare classes a larger more robust dataset would have to be used during training.

To further investigate this confusion between classes, three different images belonging to the limb flare class were analysed further. Figure 5.10 shows the limb flares and the classification outputs of the CNN, with the probability of the flare belonging to a class shown as a barplot. The first flare is correctly identified as a limb flare, with the flare positioned almost exactly on the limb. Note that the flare here looks larger and more widespread than the other two examples given. For the second limb flare shown there is a small flare that occurs just away from the limb. The classsification output shows the model is confused with it predicting almost 50/50 as to whether the flare belongs to the limb or compact flare class. For the final limb flare shown the model is almost 100% confident it is a compact ribbon flare. This means that for this image the network may not be picking up the limb but only what looks like a compact ribbon flare. To rectify these problems some changes to the network could be made such as adding spatial coordinates to the input such that the limb classes should always be correctly classified. This proposed change is applied and discussed in Section 5.3.

The final testing output is the *receiver operating characteristic* (ROC) curves, shown in Figure 5.9d. A ROC curve is plotted as the true positive rate (TPR) against the false positive rate (FPR) at various thresholds. The area under the ROC curve (AUC) indicates the performance of the model as a classifier. The closer to 1 the AUC is indicates how well the model works, with 0 indicating that the model is not classifying anything correctly. Hence the further to the left of the diagonal the ROC curve lies the better the classifier. The ROC curves in Figure 5.9d show how well the model works for each class, with high AUC values found - all approximately 99%.

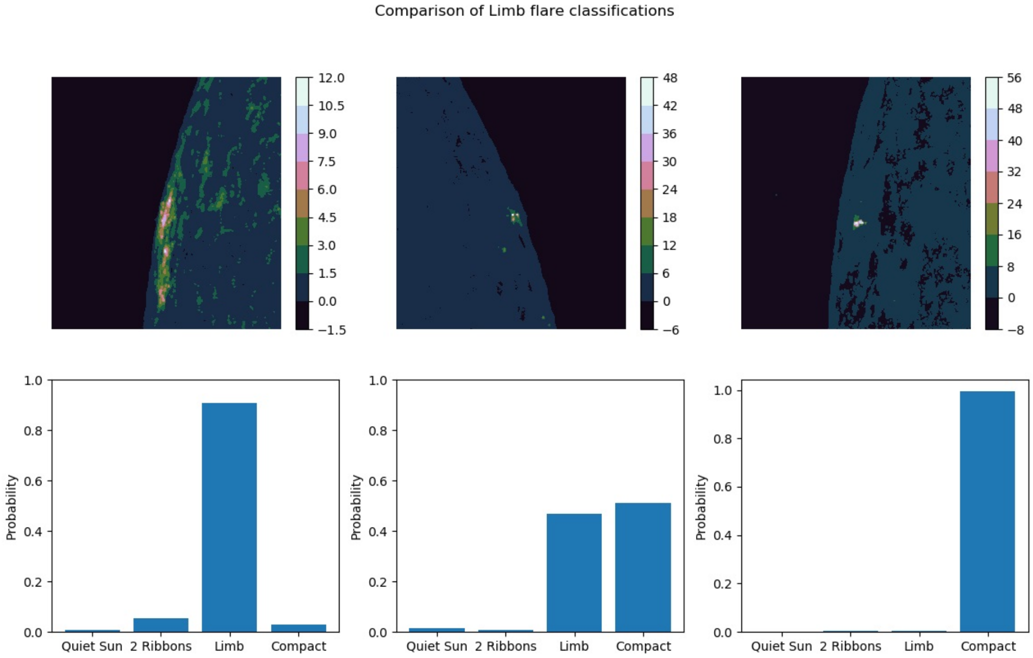

Figure 5.10: Model output on previously unseen images in the test set. All of the data should belong to the limb flare class, however confusion is seen between limb flares and compact flares.

5.2.2 Classification of X-class flare data

A dataset containing 14 X-class flares were processed through the neural network to investigate what shape their ribbons were and to test the robustness of the network. This dataset is further analysed for topological features occurring around the flares in Chapter 4.

Figure 5.11 shows the classification results of each flare, with the final class shown in red. Out of the fourteen flares classified, eleven are found to be two-ribbon flares

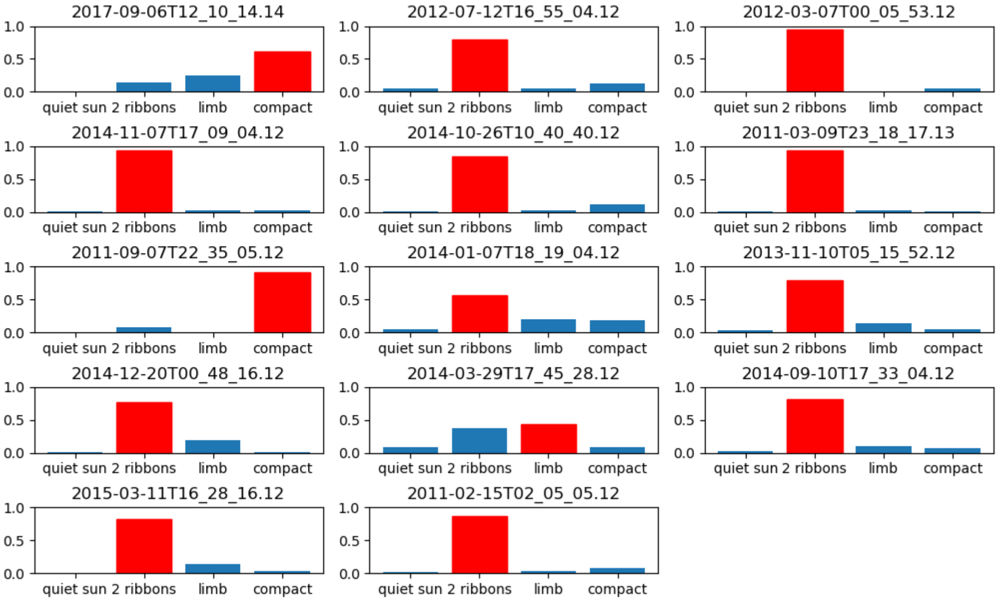

Figure 5.11: Classifications of X-class flares using the CNN. The classification output is highlighted in red.

by the network. However from human classification it is known that thirteen flares are known to be two-ribbon and only one is classified as a compact flare. With the compact flare also being classified correctly that leaves two flares which have been incorrectly classified by the network. These flares occur on 6th September 2017 and 29th March 2014.

The flare analysed that occurred on 6th September 2107 at 12:10pm UT was incorrectly classified as a compact flare. As shown in Figure 5.12, the flare ribbons at the peak of the flare bloom into other regions in the AIA data. It is thought that this may be the cause of the incorrect classification, with the network concentrating on the bright point of the blooming pixels. This lead to the classification of a compact flare ribbon. For comparison an AIA observation in the same wavelength but at a slightly later time was chosen to compare to the first classification. This observation was chosen due to the flare ribbons being clear in the observation with no blooming pixels present. The new data used is correctly classified as a two-ribbon flare, therefore it is thought that by taking a flare observation at a later time where there are less bright pixels and a clearer view of the H_α ribbons has lead to the correct classification using the neural network.

The other flare incorrectly classified occurred on 29th March 2014 with the original observation used occurring at 17:45UT. However as shown in Figures 5.11 and 5.13 it can be seen that the CNN gets confused and the flare is classified as a limb flare but with a 45% accuracy. The second largest class is the two-ribbon class with an

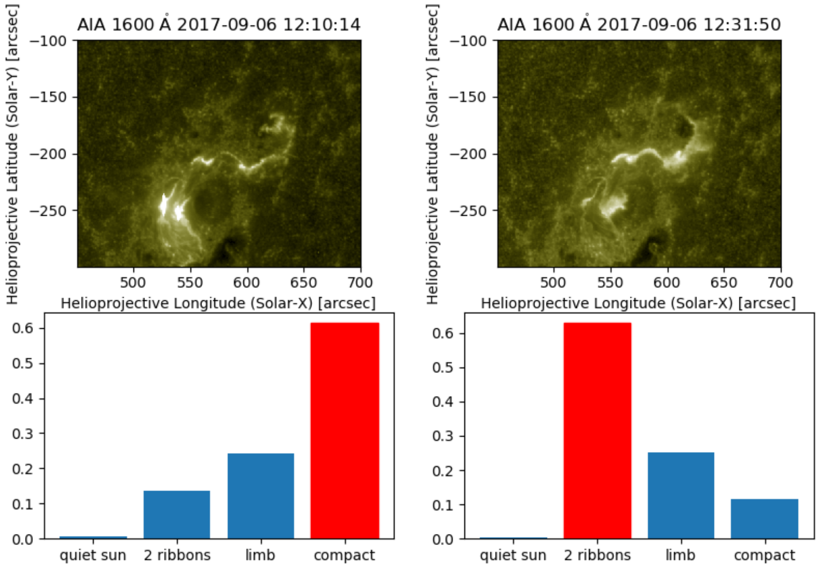

Figure 5.12: Both the original AIA image used for Figure 5.11 is shown and the new aia data processed through the CNN (which has no blooming pixels). The CNN classifications are shown as barplots with the output class shown in red.

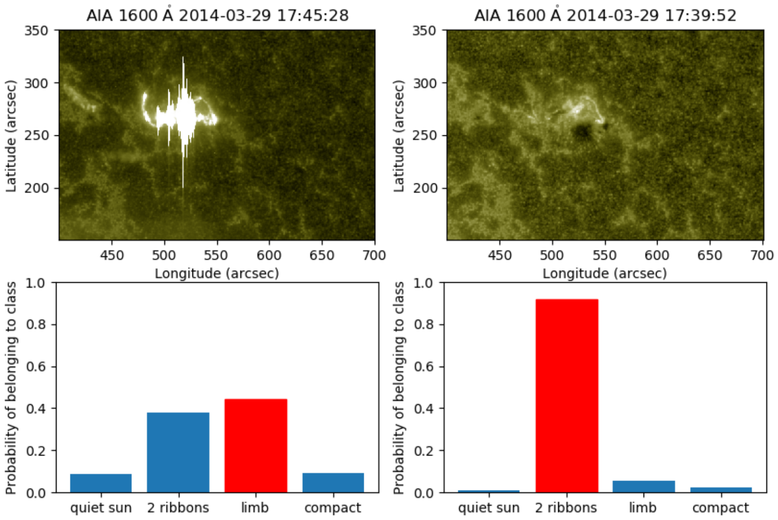

Figure 5.13: The original saturated AIA image and the unsaturated image taken on 29th March 2014. The saturated image shows the two ribbon flare being incorrectly classified as a limb flare - with the classification shown in red. The new observation used is shown with no pixel saturation and the model outputs a much higher confidence in the flare ribbons belonging to the two-ribbon class.

accuracy of approximately 40%. This shows that the network cannot give a definite classification on what the flare ribbons look like. From the AIA observation it is shown that at peak time the ribbons are not clearly visible due to pixel saturation. Due to this a second observation was chosen at 17:39UT which shows the ribbons more clearly. As shown in Figure 5.13 when this observation is processed by the network a more definite classification is reached with a 95% confidence in the flare belonging to the two-ribbon flare class.

5.3 Further Uses

5.3.1 Processing Numerical Parameters with Observational Data

After training the initial network to identify flares and their ribbon types - quiet sun, limb flares, two-ribbon flares and compact flares - there was confusion when identifying compact flares, as previously discussed in Section 5.2. This was due to two possible reasons;

1. Due to the flares occurring on the limb not having an associated "shape" many appear to look compact - however this is due to the angle of the observations.

2. When classifying limb flares some of the limbs are very close to the edge of the bounding box, this again may cause some confusion between compact and limb flares.

It was thought that this confusion could be corrected by allowing numerical and categorical parameters such as the position of the flares on the solar disk to be used during training. Hence to allow the use of non-image data, a second network was created with both the output from the original convolutional neural network (CNN) and a new neural network which processes the numerical data being used to classify the flare ribbons observed, see Figure 5.14

The network created to process the numerical and categorical data related to the flare observations, is known as a *single layer network*. This means that each node in the network is directly connected to an input variable and then connected to a single set of weights that contributes to an output variable. These types of networks are usually only applied to linearly separable data - data which when linked to each class could be separated by straight lines that indicate which class the data refers to.

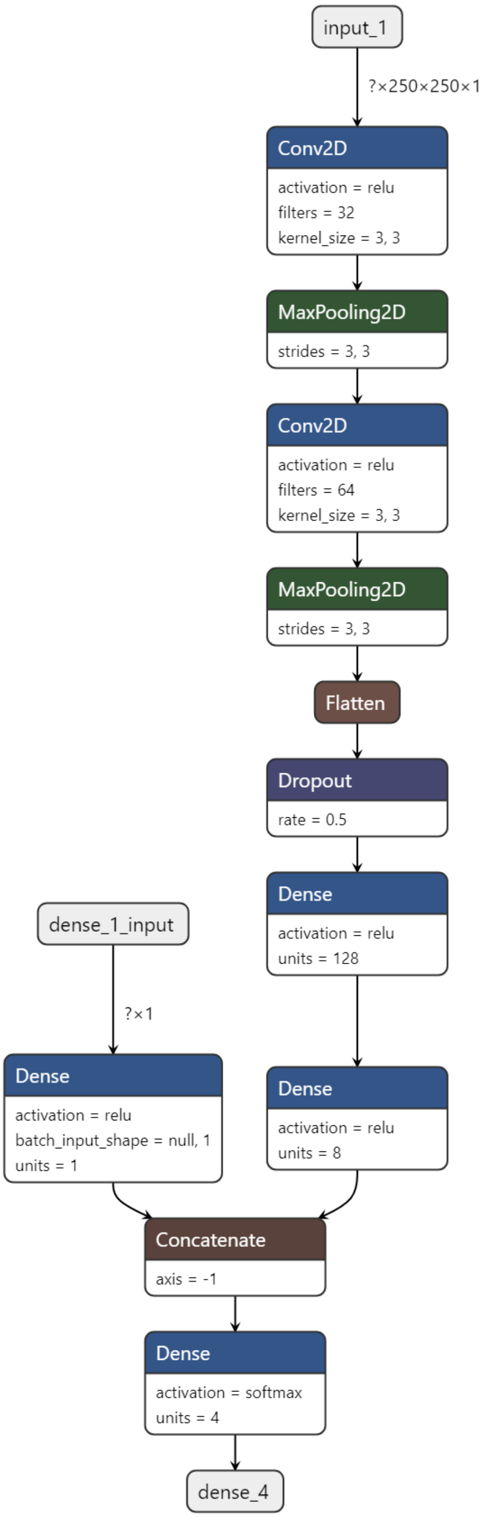

Figure 5.14: The model trained is shown here, with two input channels - one for numerical data and the other for image data - and outputs from both the CNN and single layer network combined before classifying a flare.

A single layer network was chosen here as we are going to test on positional data. It was thought that although the quiet sun, compact and two-ribbon flare classes could occur anywhere on the solar surface, the limb flare class will always have limb (outlying) positions which could be linearly separated from the other classes.

Hence using the *keras* python package, the single layer network used to process numerical data was chosen such that the number of nodes matched the number of numerical inputs. During the testing phase this was chosen to be one, with the input positional data chosen to be cosine of the longitude of the flare observation, i.e,; $\cos(\phi_{event})$. This was chosen as it would allow the positional data to be normalised between zero and one, whilst also allowing for the larger values to occur closest to the limb. The single layer network is shown at *input_2* in Figure 5.14. Once the input had been passed through the single dense layer (regular neural network layer) it is passed over to the main network again and concatenated with the convolutional neural network (CNN) output for the final stages of training which are discussed below.

The convolutional neural network (CNN) used to analyse the observational data, whilst the single layer network is analysing the numerical data, is very similar to the network used previously, see Figure 5.2. However due to eventually concatenating the output of both neural networks to classify the data, the final classification layer of the CNN previously used has been removed. Instead of a classification layer with softmax activation, the CNN was chosen to have a final dense layer with only eight nodes and ReLU activation. This was chosen to allow for the reduction in size of the CNN data at the dense layers before the output was merged with the much smaller outputs of the single layer network. The CNN with additional dense layer is shown at *input_1* in Figure 5.14.

Once both networks have trained on their respective input data, as previously mentioned the outputs are joined together and then processed through a final dense layer with four nodes and softmax activation, allowing the data to be classified into the four network classes previously defined.

The training process for this network is similar to that previously discussed for the original convolutional neural network in Section 5.1. The loss function used during training is again chosen to be *categorical cross-entropy*, see Eqn 5.4, which is updated throughout training using *backpropagation*. During training this loss function is minimised for each epoch - one forward and backward pass of the data through the network - with the probability density function for each classification calculated again using *softmax* distribution, see Eqn 5.3.

The network is trained on 400 $1600\mathring{A}$ AIA images which were previously used for

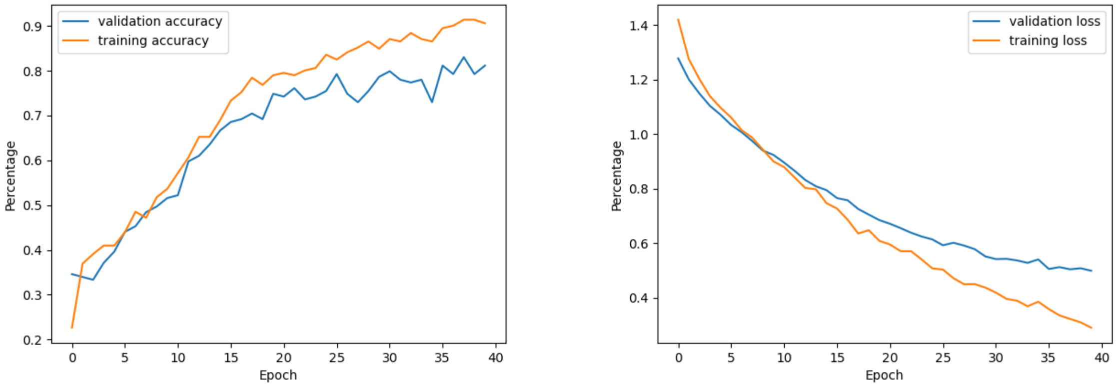

(i) Training Accuracies **(ii)** Training Losses

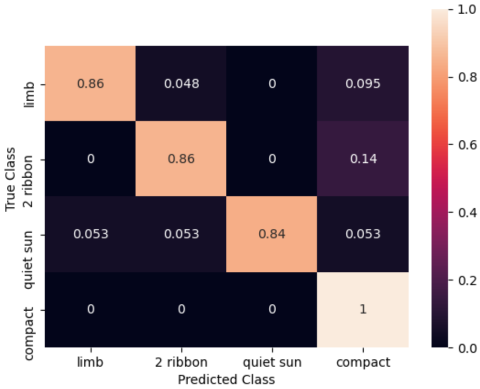

(iii) Confusion matrix using test data

Figure 5.15: Training outputs for the model combining a CNN and SLN.

training the original network. These images are prepared and normalised for training using the method discussed in Section 5.1.2, with the normalisation again carried out by calculating the z-scores of the data. In addition to the AIA data used, the positions of the flare ribbons were also needed to train the single layer network. To normalise the positional data for training it was decided that we would take cosine of the longitude of the positions allowing for a normalisation between 0 and 1 such that; $0 \leq \cos\phi \leq 1$. This was chosen after testing various normalisation schemes and picking which had the best training outcome for our network.

During training, 30% of the training data was used for validation and the remaining 70% were used to train the model. Unlike the previous network which was only trained over 10 epochs to prevent overfitting, due to the addition of the single layer network and the slight changes in the dense layers at the end of the CNN, the number of epochs was increased to 40. The need for this increase in epochs is shown in the training outputs in Figure 5.15 where we can see the training accuracy does not level off until higher epochs. In addition to the change in the number of epochs used the learning rate was chosen to be 10^{-3}.

Figure 5.15(a) shows the training and validation accuracies calculated over 40 epochs. Note that after epoch 25 the training accuracy continues to grow but the growth of the validation accuracy slows down causing a distance to appear between the curves. This increase in distance between both accuracies indicates that training should be stopped and, to get better results, more training data added. The training accuracy was found to be approximately 92% accurate with the validation accuracy levelling off at approxmiately 82%. In general this means our model will only be about 80% accurate on unseen test data.

This can be seen in Figure 5.15(c) where a test dataset was classified by the model. The confusion matrix shows that all compact flares in the test data were correctly classified. This shows that by adding in the positional data we have stopped the previous confusion in classifications of limb and compact flares seen in the confusion matrix in Figure 5.9. For all the other classes, the confusion matrix shows that they are correctly classified approximately $84 - 86\%$ of the time. When previously only using a CNN and image data, as previously noted the main confusion in classifications was between limb and compact flares. However, here when using a CNN with a SLN that processes positional data, instead of the previous misclassifications it seems that confusion now occurs when classifying two ribbon flares, where 14% of two ribbon flares in the test set are misclassified as compact. This could be due to both compact and two ribbons flares occurring at similar positions on the solar disc, and so we have introduced more ambiguity for these two classes.

The training and validation losses are shown in Figure 5.15(b) where we see a drop-off in both. Again to prevent overfitting of the dataset training should be stopped when a large gap appears between the validation and training loss curves as epochs increase.

5.4 Discussion

In this chapter we have demostrated a basic application of convolutional neural networks (CNNs) to solar image data. In particular, the first model created classifies the shapes of the solar flare ribbons that are visible in $1600\mathring{A}$ AIA observations into four classes. The four classes; quiet sun, two-ribbon flares, limb flares and compact ribbon flares were picked to allow for differences in the flare ribbons observed, with more complicated classifications possible, however it may also have introduced more confusion into the network created. The network trained resulted in an overall accuracy of approximately 94% in correctly classifying flares by the shape or location of their flare ribbons.

This initial network that was created and trained was a shallow CNN consisting of only two convolutional layers, unlike deeper neural networks that are typically used on solar image data; (e.g., Kucuk et al., 2017; Armstrong and Fletcher, 2019). The deeper CNNs are used to classify solar events such as coronal holes, solar flares and sunspots with varying instruments used. However, although a shallow CNN was used here the overall model accuracy when trained from scratch still ranges between $92.9\% \pm 2.98\%$. This model currently focuses on classifying flares by their ribbon shapes but the model could be generalised further for other solar events by including classes for sunspots or prominences which can be viewed in the current $1600\AA$ wavelength used, although the model would have to include further convolutional layers to classify these correctly. Varying the image wavelengths for the AIA data or using a different instrument such as SECCHI EUVI observations from STEREO (*Solar Terrestrial Relations Observatory*) or EIS EUV observations from Hinode could also make the model more robust.

If the network was to be made into a deep convolutional neural network, a CNN layout similar to the VGG network could be used; (Simonyan and Zisserman, 2014). This deeper network would take longer to train over more epochs and would need the training set for the current network to be increased - including more flare images for the current classes as well as adding any new images for other classes chosen. As well as increasing the number of convolutional layers used, other model parameters could be altered to achieve different training results, where any of the parameters discussed in Table 5.1 could be modified to affect the model training speed and accuracy.

The second CNN shows some of these changes in effect. The model implemented and discussed in Section 5.3 shows the inclusion of spatial parameters to the model, which increases the size of the training dataset as well as the number of epochs the model must train over. The inclusion of this neural network which can process numerical or categorical parameters with the addition of the original CNN created shows promising first results with the initial model accuracy found to be approximately 82%. **Showing that an expansion on the original CNN is possible.**

The main result from this chapter shows that although a shallow CNN is being used, we still get excellent accuracies when training the models to locate flaring regions based on their ribbon shapes and locations. Such a result is encouraging and shows a basic application of CNNs to solar image data, highlighting how they can be useful in analysing large datasets. Both the models created here could potentially be added to a pipeline which locates solar events from ground and space based instruments.

Chapter 6

Automated Edge Detection and Quantitative Distance Measures Applied to Observations of Flare Ribbons

The *Canny Edge Detection* method is an image processing method created by Canny (1986). This edge detection method was created to find the edges of an image, where the optimal output was found to be on a Gaussian smoothed image with the edges calculated corresponding to changes in pixel intensities.

This method has been used previously on solar image data (e.g., Hao et al., 2013), where the Canny edge detection method was used to find and track filaments present in Hα images. Here we will consider finding the edges of the flare ribbons observed during solar flares in 1600$\mathring{A}$ AIA data.

We chose to create our own version of the Canny edge detection method that would work specifically on the wavelength we have chosen, this includes setting unique threshold values in the edge detection process to reduce noise in the outputs. Hence if another wavelength is chosen the edge detector would have to have some of its parameters altered slightly to account for the new wavelength; with the parameters for another wavelength used it would still calculate the relevant edges but might pick up more noise.

There are five main steps carried out to complete the edge detection process which are; noise reduction, gradient calculations, non-maximum suppression, double threshold and edge tracing by hysteresis, with each step discussed below. Note that the algorithm works on greyscale images and so our algorithm normalises all the AIA data before processing through the edge detector.

The first step in the edge detection process is to apply some noise reduction algorithm to the image data. This step is needed as due to gradients being calculated in the next step, the edge detection process is very sensitive to noise and so the noise must be reduced within the data. A Gaussian blur is applied to the data to smooth it, such that;

$$G(x, y) = \frac{1}{2\pi\sigma^2} \exp\left\{ -\frac{x^2 + y^2}{2\sigma^2} \right\},$$

where σ is the standard deviation and x and y are the distances from the origin to the pixel being smoothed in both the horizontal and vertical directions. There is also a choice in what kernel size (grouping of pixels) to apply the blur over (i.e., 3×3, 5×5 etc.) and what the σ value should be. For our data the filter was applied with $\sigma = 1$. Hence G is calculated and applied to each pixel to smooth the image.

After the Gaussian filter has been applied to the data to reduce the noise, the second step of the edge detection process can be carried out. This is where the change in neighbouring pixel values is calculated to find potential edges within the image data. At this step the direction of these changes are also calculated (see Figure 6.2).

The edges in the images correspond to changes in the pixels intensities; these are calculated using filters that can be applied to the images to detect changes in both the horizontal and vertical directions. There are different types of filters that can be chosen here, however we use *Sobel filters* to calculate the gradients, (see Sobel and Feldman, 1973). The Sobel filters are two kernels of size 3×3 that calculate the gradients in both the horizontal (G_x) and vertical (G_y) directions by carrying out an image convolution on the smoothed AIA image data. Hence the derivative calculations to calculate theses changes are;

$$G_x = \begin{pmatrix} 1 & 0 & -1 \\ 2 & 0 & -2 \\ 1 & 0 & -1 \end{pmatrix} * I \quad \text{and} \quad G_y = \begin{pmatrix} -1 & -2 & -1 \\ 0 & 0 & 0 \\ 1 & 2 & 1 \end{pmatrix} * I, \tag{6.1}$$

where I is a 2D array containing the pixel intensities. Note that $*$ denotes an *image convolution* where the rows and columns in the kernels are flipped before being multipled element-wise. The Sobel filters are applied to each pixel in I and its surrounding eight pixels, and then summed together to give the overall value of the changes in pixel gradients in the horizontal and vertical directions which are stored in the G_x and G_y arrays. When the Sobel filters are applied to the first and last two columns and rows in the AIA data the filters must be modified as there are not the usual eight points around the pixel to calculate the gradients. However, due to the flare ribbons being located in the centre of the images a partial Sobel filter was applied as no important edges should be located at the edges of the AIA images.

Once the gradients in both the vertical and horizontal directions have been calculated, the magnitude of the gradient, G, can be found;

$$G = \sqrt{G_x^2 + G_y^2}, \tag{6.2}$$

and the slope, Θ of the gradient is also calculated;

$$\Theta = \arctan\left(\frac{G_y}{G_x}\right) \tag{6.3}$$

Figure 6.1 shows an example of AIA data which has been blurred using the Gaussian filter and shows what the output from the gradient calculations looks like. Notice that the gradient output has brighter and thicker white lines where possible edges of the data may be located. This gradient output matrix, G, is passed onto the next step in the edge detection process which is non-maximum suppression.

The non-maximum suppression step thins out the edges calculated in the gradient step. Here we analyse all the points on the edges found such that, only the points that

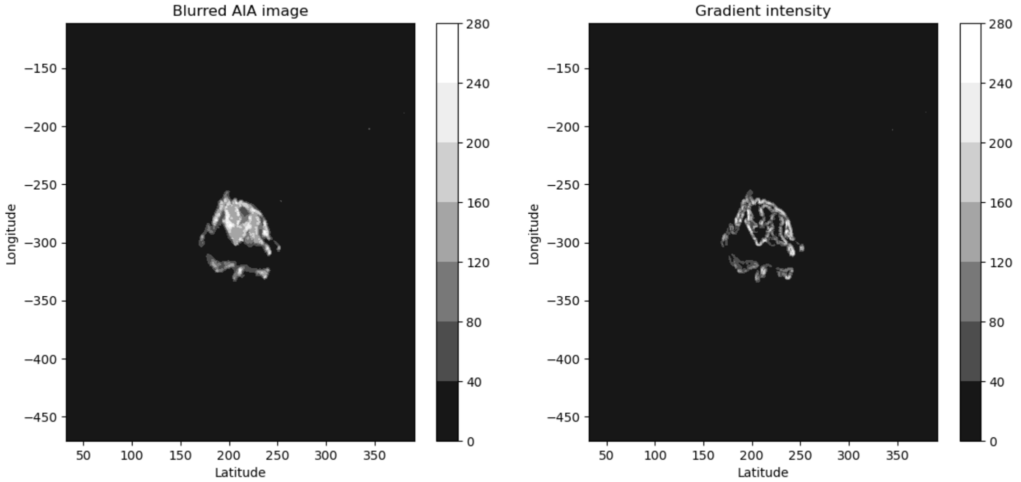

Figure 6.1: A flare ribbon observed on 10 November 2013 at 05:15:54UT, the first image shows the AIA data after the Gaussian blur has been applied. The second image shows the output from the gradient calculations i.e. matrix G, with the thicker white lines showing potential edges of the flare ribbons.

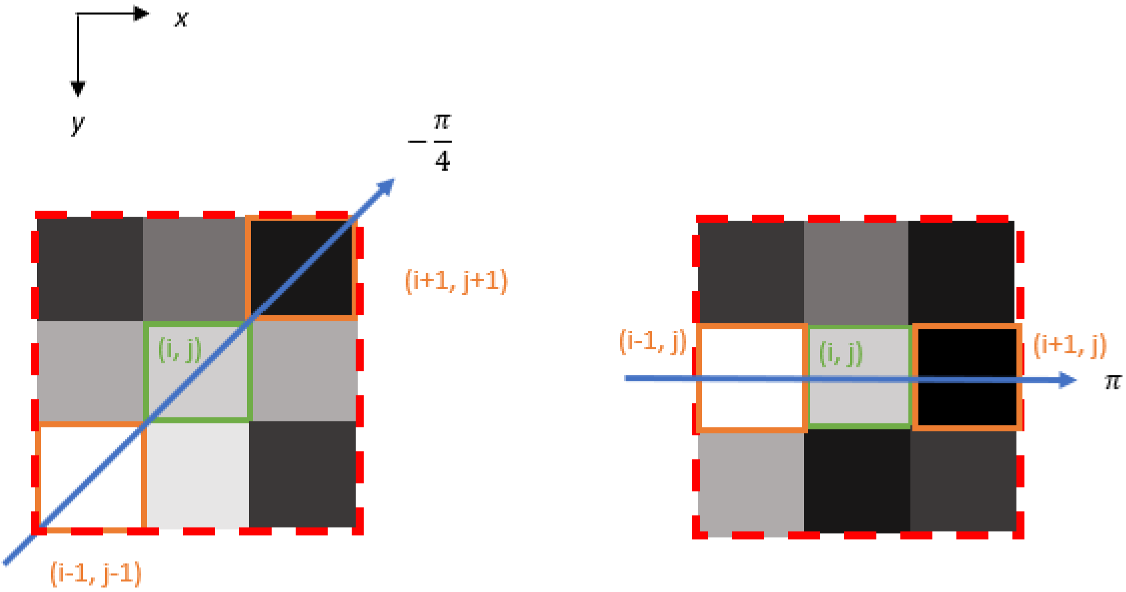

Figure 6.2: Two examples of non-maximum suppression are shown. The first shows the centre pixel gradient in a $-\frac{\pi}{4}$ direction with the maximum pixel value found to be at position (i-1, j-1). The second example shows the centre pixel gradient in a π direction with the maximum pixel value found to be at position (i-1, j).

are lying at an edge (e.g. surrounded by pixels of smaller G values) and in the correct direction (Θ array value for that pixel is pointing towards the nearest pixel with the next largest value) are marked as possible edge points.

Figure 6.2 shows two examples of non-maximum suppression being carried out on the gradient data. The Θ matrix is used to determine the direction the gradient, G is pointing to. Once this direction is found the non-maximum suppression method takes the surrounding eight pixels and looks at the pixels lying in this direction. For example, in Figure 6.2 the first example shows the centre pixel lying in the $-\frac{\pi}{4}$ direction, hence we take the maximum of the pixels lying on the blue direction arrow e.g. $max\{(i-1, j-1), (i, j), (i+1, j+1)\}$. In this example the maximum pixel value is found to lie at pixel (i-1, j-1), hence the pixel at position (i, j) is set to zero as there is no maximum gradient (edge) located there. The algorithm then moves onto the next pixel to be analysed using the surrounding eight pixels. If it is found that there is no pixel with a greater gradient than the centre pixel then that pixel value is kept and not set to zero.

In summary the main steps in the non-maximum suppression method is to identify whether an edge is present by using the angle matrix, Θ, then checking whether the pixels lying in the same direction have larger magnitudes than the pixel being analysed, returning zeros for pixels that are not maxima and the gradient intensities for pixels that are maxima. Finally, a new image is returned which should contain thinned out edges.

After non-maximum suppression has been carried out the double threshold step is applied. This step uses thresholds to determine whether pixels belong to the edge or not. There are three types of pixels we are looking for here; strong pixels that are definitely part of the edge as their intensities are large, weak pixels that may be part of the edge with intensities less than the strong pixels but not so small that they can be discounted and finally background pixels with low intensities that are not part of the edge.

The double thresholds chosen are used such that one is a strong threshold where any pixel with an intensity greater than the threshold is marked as a strong pixel. Weak pixels are marked such that they lie between the strong threshold value and the smaller second threshold, known as the weak threshold. Any pixels with values less than the weak threshold are marked as background pixels that definitely do not belong to any edge.

To determine what the thresholds should be set to, *survival functions* were calculated; see Section 6.1 for how these are used to determine the values of the strong and weak thresholds.

Note that here two groups of pixels are returned that are still relevant to the edge detection; strong and weak pixels. The strong pixels are already marked as definitely belonging to the edge of the flare ribbons and the final step in the edge detection process known as *edge tracing by hysteresis* determines what weak pixels should also belong to the edge.

This final step determines what is a true edge from the pixels marked as weak during the double threshold process. Here the weak pixels can be transformed into strong pixels if the weak pixel has at least one strong pixel as a direct neighbour. An example of this is shown in Figure 6.3, where the middle pixel is a weak pixel and has one strong pixel nearby (at position (i+1, j-1)). Hence the weak pixel is changed to a strong pixel to mark it as part of the final edge.

Figure 6.4 shows the inital input AIA image containing flare ribbons and the resultant edge detection output using the Canny edge detection method discussed above. Note that although the hysteresis step should thin out the edges those found are still thicker than usual, this is due to the noise lying around the saturated flare ribbons as the pixels go back down to the normal background value in the region.

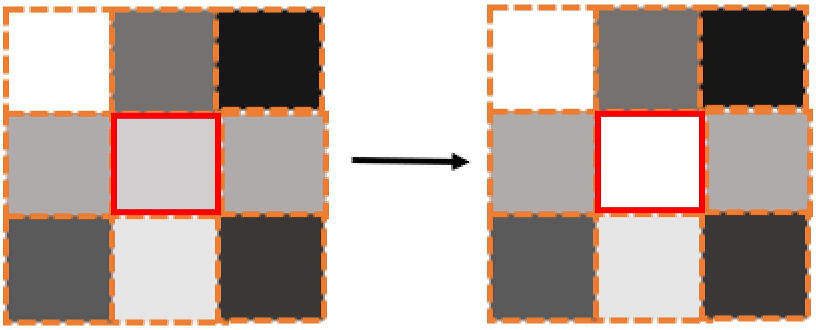

Figure 6.3: An example of hysteresis is shown. The middle pixel has been marked as a weak pixel in the double threshold step, by comparing it to the surronding pixels, one of which is a strong pixel, it is changed into a strong pixel itself.

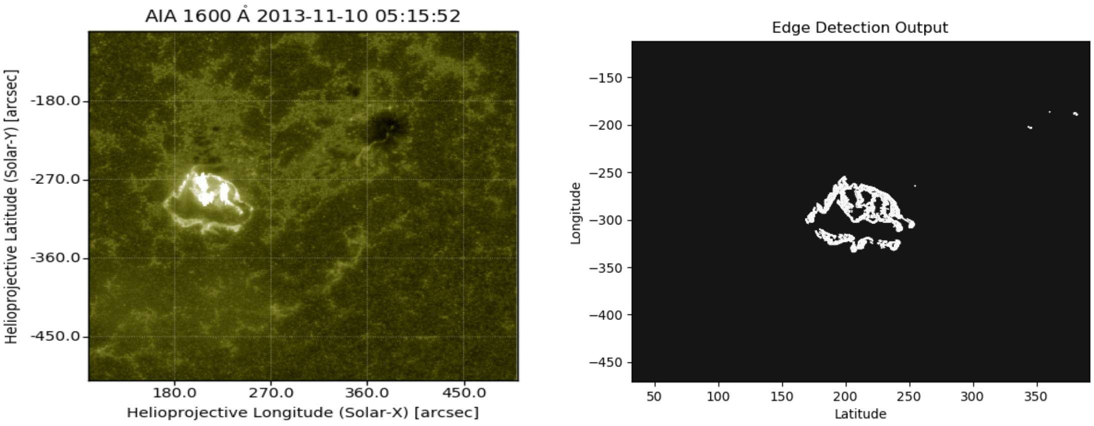

(i) (ii)

Figure 6.4: (a) shows the input $1600\mathring{A}$ AIA image and (b) shows the output of the Canny edge detection method.

6.1 Edge Detection Thresholds

There are two methods that we considered to find suitable values for the strong and weak edge detection thresholds. The first we considered but decided against was using percentages of the maximum values in the AIA data. Here the strong threshold was chosen to be $0.8I_{max}$ and the weak threshold was set to $0.75I_{max}$ to be slightly lower than the strong threshold. This would allow the thresholds to be individually set for each AIA image processed by the edge detector.

However with this method, depending on the AIA image processed, the thresholds chosen were either too large or too small and hence were picking up too much or too little of the ribbon edges. Due to this discrepancy it was decided to apply a different method to find the strong and weak thresholds. The alternative method would allow us to analyse pixel intensities that are too low to belong to the flare ribbons in each AIA image; by plotting histograms of the pixel intensities and producing subsequent survival functions.

For each AIA image a log-log histogram of the pixel intensity was produced. Examples of what these histograms look like are shown in Figure 6.5 where the histogram values are plotted as red + signs in the left-hand plots for each AIA image. A Gaussian of the form,

$$A \exp \frac{-(x - x_0)^2}{2\sigma^2},$$

was fitted to the AIA histogram using Python's *curvefit* function. This is fitted to the histogram data as the distribution is approximately gaussian. The variables A, x_0 and σ are extracted from the histogram data. For the AIA data considered in Figure 6.5ii these variables were found to be, $A = 0.1927, x_0 = 2.0799$ and $\sigma = 0.1079$, although they will vary depending on the histogram data for each AIA image. As well as the histogram and fitted Gaussian, the full-width half-max (FWHM) is shown in green to indicate where the fitted Gaussian reaches half of its amplitude.

Once a Gaussian had been fitted to each histogram, *survival functions* are also calculated for the Gaussian, the pixel count rate histogram and by taking the ratio between both. Note that the survival functions can also be thought of as the cumulative distribution functions (CDFs). In general a survival function shows how many elements of a particular data set are still present after a certain threshold. Here the survival functions, shown on the right-hand side of Figure 6.5, show how many pixels are still present if we pick a cut-off after a certain intensity.

The survival functions should be the same where the Gaussian is a good fit to the histogram and start to deviate where the Gaussian is no longer a good fit, typically at extremely large or extremely small intensities. Figure 6.5ii, shows that there is only 1 percent of pixels that have a log intensity $\gtrsim 2.5$.

We use these survival functions to find suitable values for the strong and weak thresholds. Typically the pixel values for the flare ribbons observed in the AIA data are of order $\geq 10^3$; these values coincide with the survival function values where only 1% of pixels are left with intensities falling within that range. Therefore we initially set the strong and weak thresholds to be equal to this 1% cut-off which we label, σ. Setting the thresholds to be equal will allow us to see whether too much or too little data is being picked up from the initial threshold values. An example of the edge detection output using these thresholds is shown in Figure 6.6i. Here, some of the smaller brighter background features are being picked up as well as the flare ribbons we are interested in. This indicates that one or both of the thresholds may not be large enough and hence is still picking up non-flare ribbon pixel intensities. This is unsurprising as we have picked the strong threshold to be $\leq 10^3$ whereas we previously stated that flare intensities are typically larger than this.

To reduce the amount of non-flare features being picked up by the edge detector it was decided to set the new thresholds as strong$= 3\sigma$ and weak$= \sigma$. This should allow the larger intensity flare pixels to be picked up by the strong threshold initially whilst the weaker threshold would pick up the other possible edge pixels before the hysteresis step. The results of the edge detection on the same flare data is shown in Figure 6.6ii. Note that by increasing the strong threshold by a factor of 3 the appearance of non-flare features have been reduced and a much cleaner edge has been picked up around the flare ribbons observed.

For the rest of this chapter, the edge detection thresholds are set to; strong$= 3\sigma$ and weak$= \sigma$. Figure 6.7 shows two other flaring regions analysed by the Canny edge detector. Figure 6.7i shows the edges of an X-class flare that occurred on 15 Feburary 2011, where two long flare ribbons were observed and Figure 6.7ii shows the edges of a circular flare ribbon and a corresponding j-shaped ribbon that were observed during an X-class flare on 9 March 2011. Note that both of these flares were also analysed in Chapter 4 where the magnetic field features around the flaring regions were investigated.

Both sets of flare ribbons detected in Figures 6.7i and 6.7ii, show the final edge output from the Canny edge detection process. However although hysteresis was carried out the final edges are still quite thick; thisf may be due to the fluctuation around the more highly saturated pixels with the intensity changing rapidly at the edges to convert back to the much lower background values. Hence a final step is taken to thin the edges out to get a single line of pixels denoting the ribbon edge. The pixels marked as edges are extracted and their positions averaged in the y-direction to get a single average position line for the ribbons detected. These averaged positions edges are shown for both the X-class flares previously analysed in Figures 6.7iii and 6.7iv.

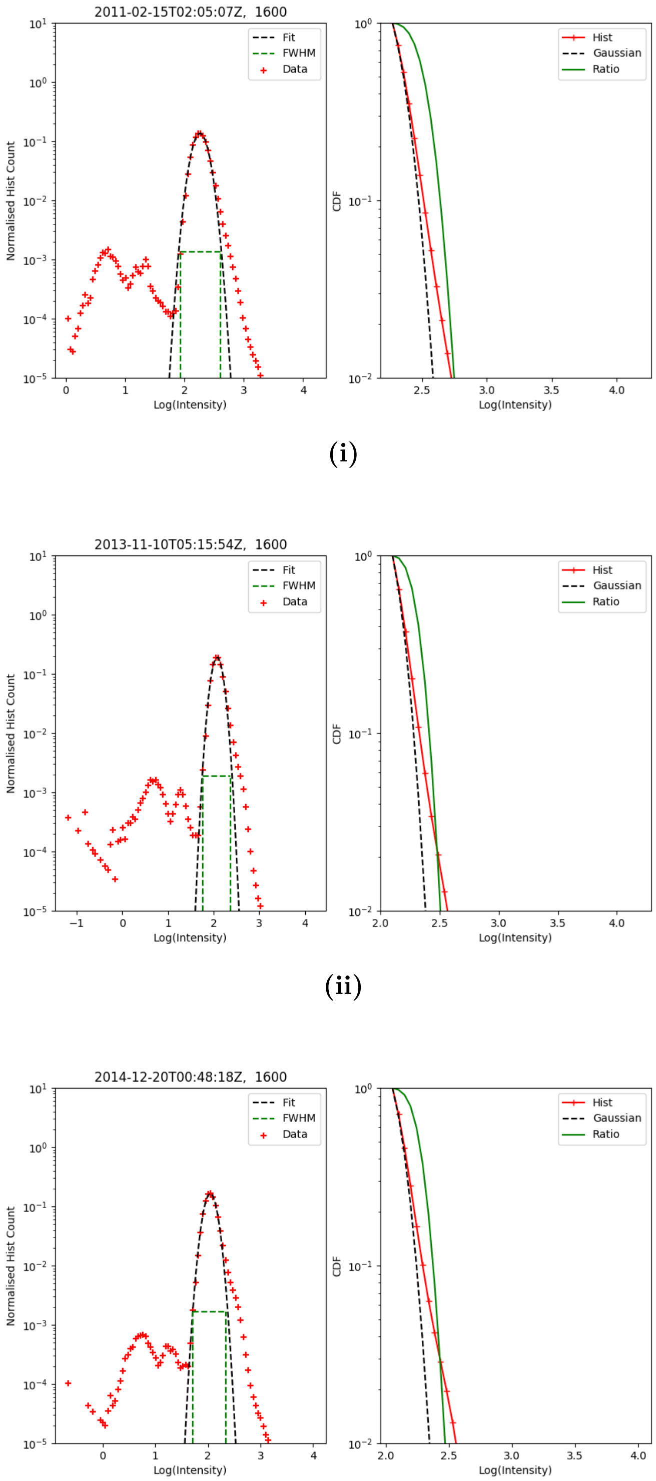

(i)

(ii)

(iii)

Figure 6.5: A histogram of count rates for each pixel and a fitted Gaussian are shown in the left plot. The right plots show CDFs (or survival functions) of count rates for each pixel (Hist) in red and the fitted Gaussian (using pythons curevefit method) in black. The ratio between the two are shown in green for various 1600 $\mathring{A}$ AIA images.

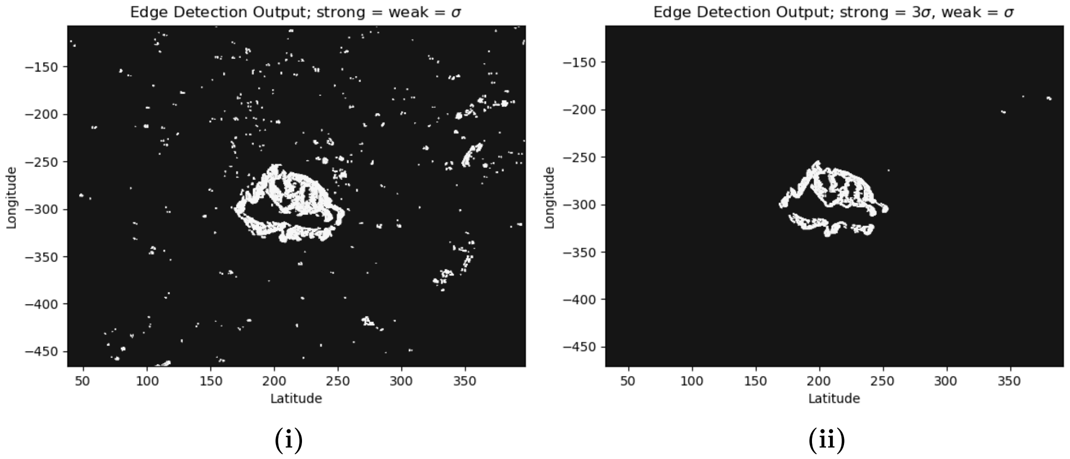

(i) **(ii)**

Figure 6.6: (a) shows the edge detection output when the strong and weak thresholds both equal σ. It shows some smaller bright feature being picked up as well as the flare ribbons; (b) shows the edge detection output where strong= 3σ and weak= σ, where the flare ribbon becomes almost the only feature being picked up.

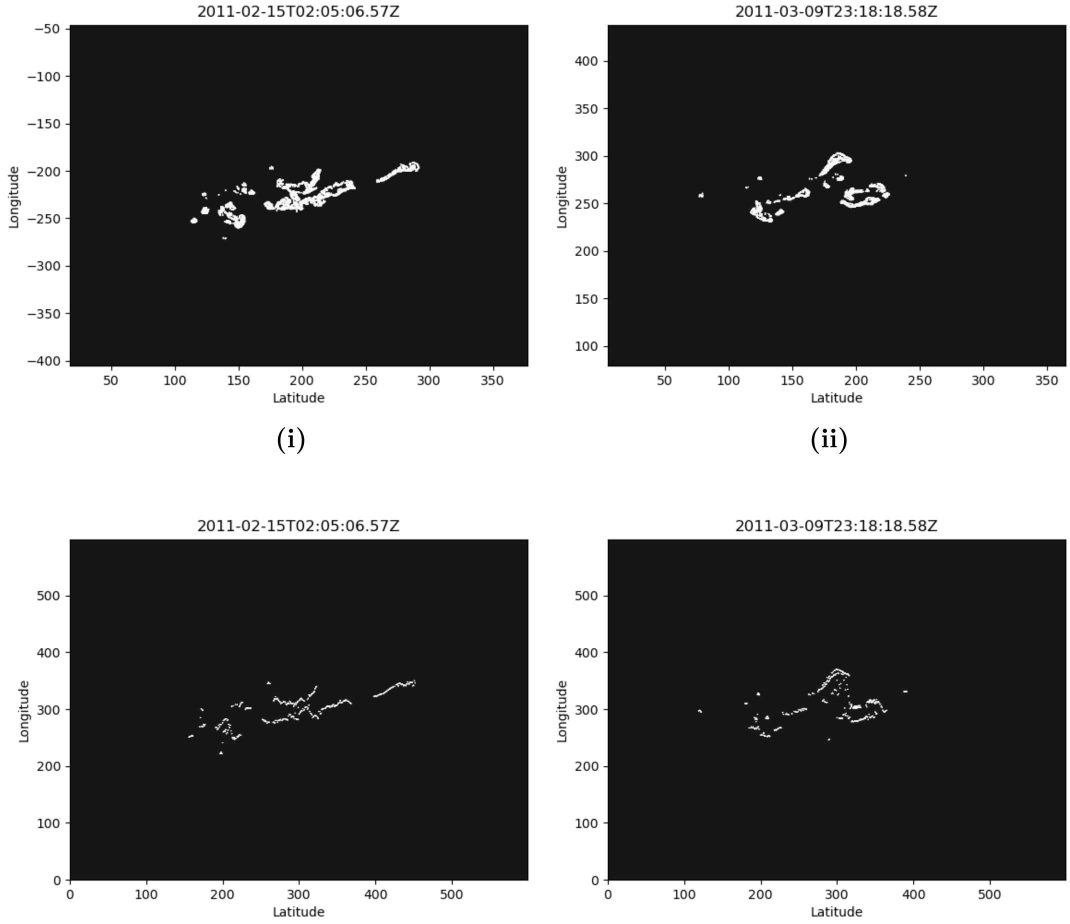

(i) (ii)

(iii) (iv)

Figure 6.7: Edge detection examples where strong = 3σ and weak = σ for two X-class flares that occurred on (a) 15 February 2011 and (b) 9 March 2011. (c) and (d) show the thinned out edges respectively.

6.2 Correction of Saturated Pixels in AIA data

Whilst using the Canny edge detector, the AIA images must have clear edges for the flare ribbons observed. However for some of the larger flares observed the AIA observations suffer from pixels bleeding into the surrounding image, causing the flare ribbons to become obscured. Two examples of bleeding pixels observed during two X-class flares are shown in Figure 6.8i, 6.8ii. Due to cases like this occurring in the AIA data that we want to analyse, a method must be developed that converts the saturated pixels back to their actual values and replaces the saturated values caused by surrounding large pixel values bleeding over into non-saturated pixels. This gives a clearer idea of what the flare ribbons look like without the saturation occurring.

There have been previous methods developed to reduce saturation of pixels in AIA images (e.g., Kazachenko et al., 2017), however many concentrate on correcting EUV images. Hence a similar method must be constructed to correct the pixel saturation occurring in the $1600\mathring{A}$ AIA images analysed here.

6.2.1 Method 1: Linear Interpolation using Timeseries of Pixel Intensities

The method discussed below is similar to that discussed in Kazachenko et al. (2017), however methods of desaturation of other solar image data have been discussed in other studies (e.g. Schwartz et al., 2015; Guastavino et al., 2019).

Initially the algorithm analyses each pixel in the AIA image to check whether they have a count rate greater than 5000 counts s^{-1}, this is a level where pixel saturation is usually seen. If the pixel count rate satisfies this condition a time series of the pixel value during the flare is taken, and the value at that point in time is linearly interpolated between the start and end pixels chosen such that their pixel count rates are not saturated. The linear interpolation is given by;

$$p_{n_{i,j}} = p_{start_{i,j}} + \frac{t_n - t_{start}}{t_{end} - t_{start}} \big(p_{end_{i,j}} - p_{start_{i,j}} \big), \tag{6.4}$$

where $p_{n_{i,j}}$ is the new value for the saturated pixel, $p_{start_{i,j}}$ and $p_{end_{i,j}}$ are the values of the start and end unsaturated pixels from the timeseries, t_n denotes the difference from when the inital unsaturated pixel occurred until the saturated pixel occurred with t_{start} and t_{end} denoting the start and end times of the timeseries of AIA data selected.

The surrounding pixels are also interpolated with two pixels in both positive and negative x-directions calculated, as well as ten pixels in both positive and negative

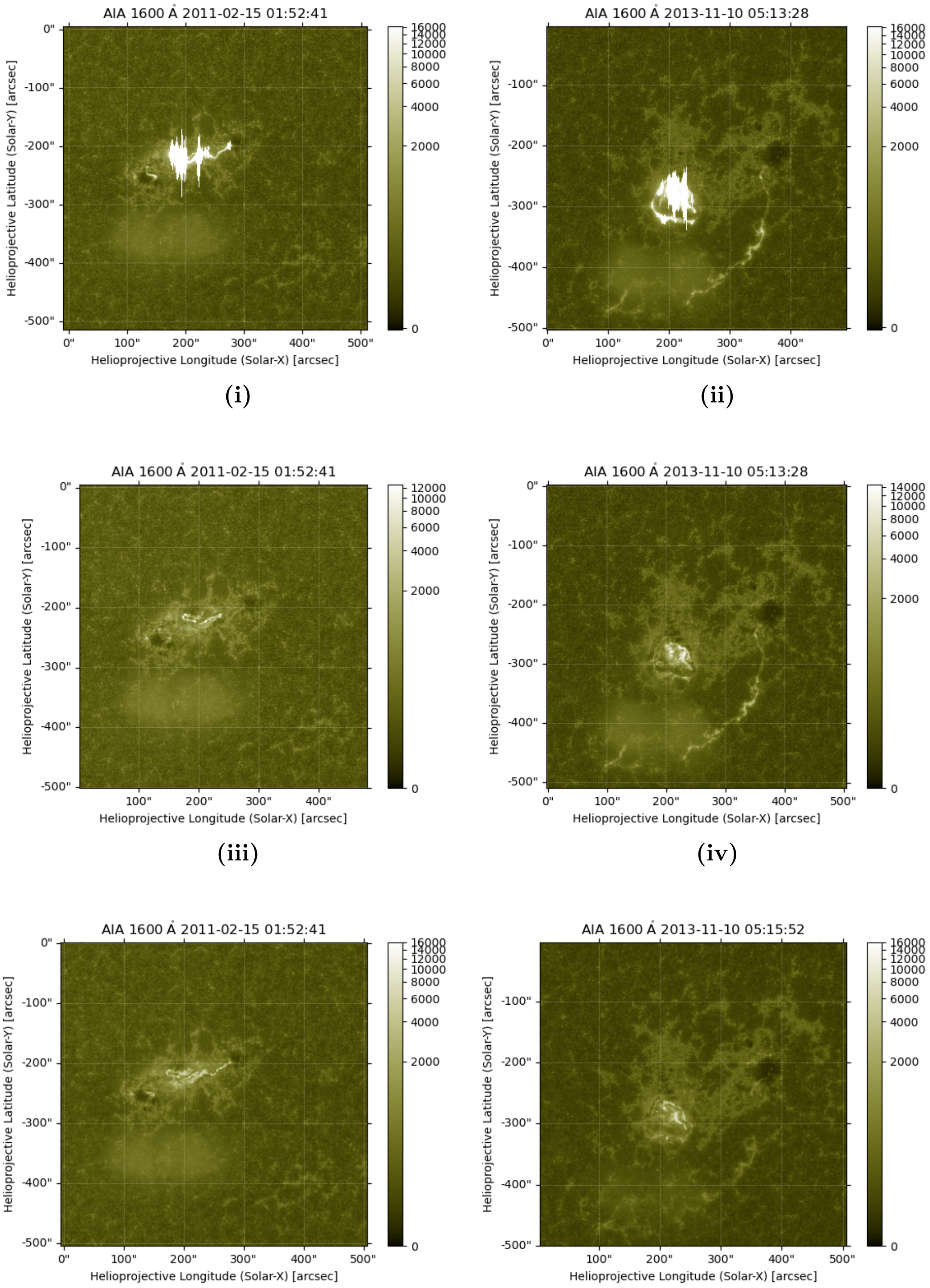

(i) (ii)

(iii) (iv)

(v) (vi)

Figure 6.8: (a) and (b) show two X-class flares that had pixels blooming into neighbouring pixels during the peak of the flare. Corrected AIA images (c) and (d) using method 1, (e) and (f) using method 2.

y-direction. This is to ensure the surrounding pixels, which might not be saturated but where blooming may have occurred, are also corrected.

Figure 6.8i shows an X-class flare where the flare ribbons are blooming into other pixels due to pixel saturation. These pixels are corrected using the method discussed above to produce a new *corrected* AIA image where two flare ribbons are more easily observed, with their shapes also visible, see Figure 6.8iii.

Figure 6.8ii shows another example of pixels blooming during a solar flare event, with figure 6.8iv showing the corrected AIA image. This flare was also the example used in figure 6.4 where we used an image at a later time to prevent the saturated pixels interfering with the edge detection, however we can now try to get cleaner edges for the flare ribbons observed at the peak time by using the corrected AIA images.

6.2.2 Method 2: Averaging Pixel Intensities

Similarly to method 1, this method utilises other AIA files to correct the pixel saturation during the peak of the flare. However only three files are needed here, the AIA image containing the saturated pixels, an AIA image during the same flare but before saturation occurs and a final AIA image during the same flare after the saturated image time. This method was implemented to try to see if a simpler method could result in suitable desaturation of AIA images.

Instead of correcting only saturated pixels the surrounding pixels must also be corrected. This is due to the surrounding pixels also having modified values due to blooming. The first step considers any pixels in the saturated image with a count rate greater than 6000 counts s^{-1}, this value was chosen through experimentation with various values. If this condition is satisfied a check is also done to evaluate the average pixel intensities surrounding the saturated pixel in the y direction, where if $avg_y > 5000$ then the saturated pixel is replaced by the average value of the two unsaturated AIA files such that;

$$p_{n_{i,j}} = \frac{p_{end_{i,j}} + p_{start_{i,j}}}{2}. \tag{6.5}$$

Note that the immediate surrounding pixels are also replaced by average values, even if the count rate is < 5000.

The next step considers any pixels such that $p_{n_{i,j}} > 1000$ and $avg_y > 750$ or where $p_{n_{i,j}} < 150$ and $avg_y > 500$, with these pixel values chosen through a trial and error process. These pixels also have to be corrected as surrounding the saturated pixels in the AIA data there is usually one or two pixels surrounding the edges of the saturation that are not normal background values but have been also been altered. These pixels

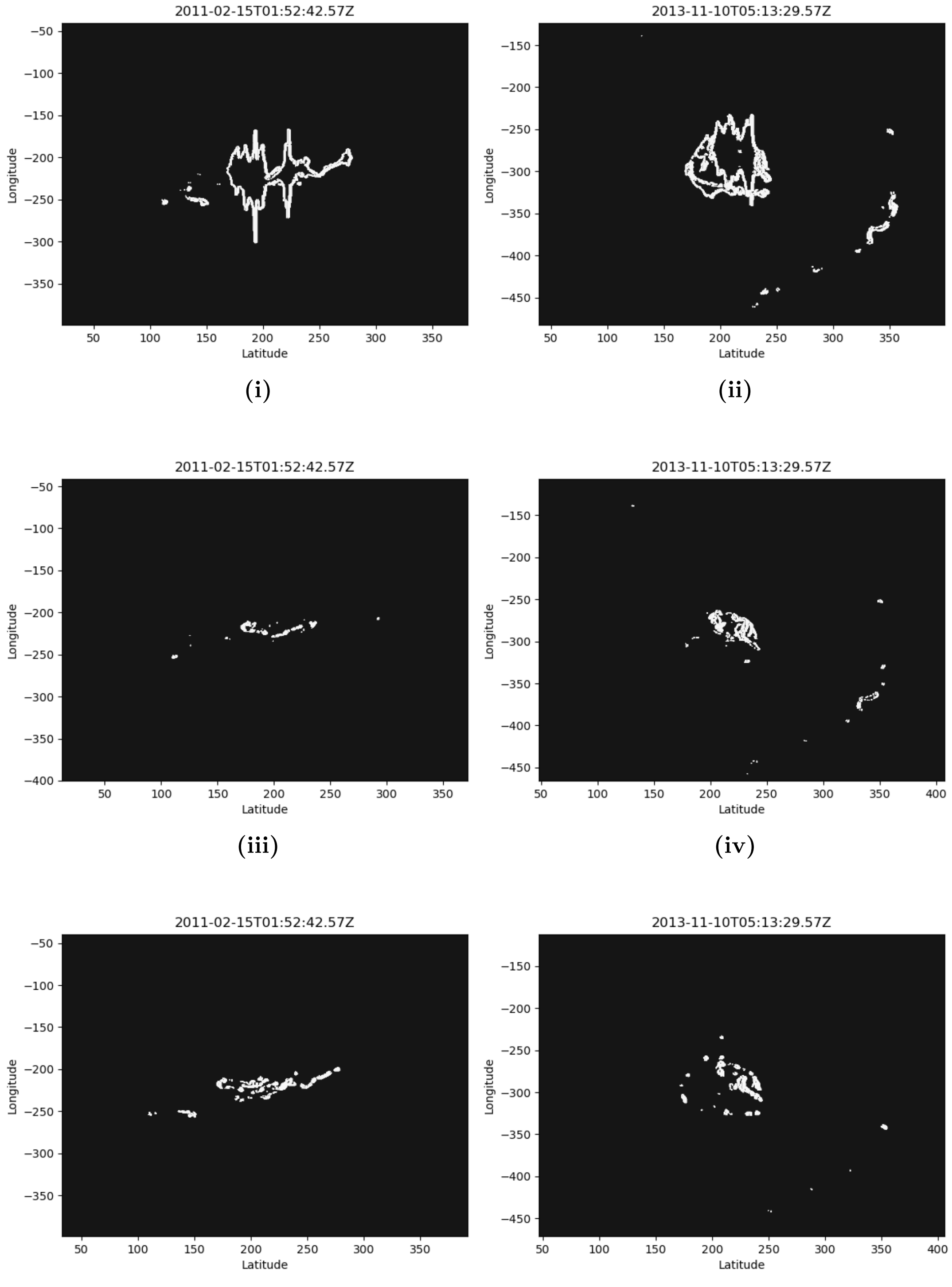

(i) (ii) (iii) (iv) (v) (vi)

Figure 6.9: Edge detection outputs; (a) and (b) using saturated AIA images, (c) and (d) using the timeseries method to smooth the saturated pixels (method 1), (e) and (f) using the averaging method to smooth the saturated pixels (method 2).

typically drop in count rate and mark the edges of the saturation region. Pixels that satisfy these conditions are averaged using the above equation.

This method is much simpler than the linear interpolation using timeseries method discussed in Section 6.2.1. However due to only averaging pixels of certain values chosen above, the output may not be as consistent for different flares. Examples of the smoothed AIA data outputs using this method are shown in Figures 6.8v and 6.8vi. Note that although the algorithm seems to produce a good result for the February 2011 flare, the output for the November 2013 flare is not as smooth and some ribbon definition has been lost which will affect the corresponding edge detection outputs. This is discussed in the next section, however highlights the problems with having varying intensities for each AIA image which makes it difficult to get consistent results.

6.2.3 Method Comparison

Figure 6.9iv shows the Canny edge detection outputs from a previously saturated two ribbon flare shown in figure 6.8ii. The edges detected from the corrected AIA data, shown in figure 6.8iv are found using method 1 discussed in Section 6.2.1. Using this method, for this example we lose definition on the bottom flare ribbon with the edge detector only picking up small sections of the corrected ribbon data. This may cause a problem when we try to compare the ribbon edges to the magnetic field features found in Chapter 4, with the comparison discussed later in Section 6.3.

Alternatively, figure 6.9vi shows the edge detection outputs for the same flare, where the pixel saturation has been corrected using method 2, see Section 6.2.2. Here the flare ribbons seem more broken apart with the averaging method not producing clean ribbon edges for the detector to work on.

Overall, method 1 should be used where possible to smooth saturated AIA images as the edge detection outputs produce better results, with more of the flare ribbons being detected. However where possible original unsaturated AIA images should be used to get the best edge detection results as shown in Figure 6.4ii.

6.3 Mapping Ribbon Edges to 3D Magnetic Field Features

As previously discussed, the Canny edge detection method can be used to find the edges of the flare ribbons observed in AIA data. Here, we look at the ribbon edges of some X-class flares that have been previously analysed in Chapter 4 to compare whether the ribbon edges can be mapped to some magnetic field features identified in the flaring active regions. This will allow us to deduce whether the position and shape of the flare ribbons observed and the separatrix surfaces found from the PFSS model are similar to each other, producing a more automated approach to mapping the separatrix surfaces to the flare ribbons observed.

To make suitable comparisons between the separatrix surfaces found and the ribbon edges detected, cuts taken along the solar surface from the extrapolations are used for comparison to identify where the magnetic field features intersect with the solar surface and could possibly correspond to the ribbon edges. Figure 6.10a and 6.10b show two examples of the 3D magnetic field features found overlying flaring active regions, with Figure 6.10c and 6.10d presenting the corresponding surface cuts which can be correlated to the flare ribbons observed. Note that these examples have been chosen to show the results of one flaring active region, observed on 7 January 2014, with no corresponding separatrix surface overlying the flare ribbons positions and another flaring active region, observed on 10 November 2013, with corresponding separatrix surface overlying the flare ribbons observed during an X-class flare. The first active region is surrounded by a separatrix dome but with no separatrix surfaces found lying close to the flare ribbons observed, see Figure 6.10i, whereas the other one looks as if a good correlation will be found between the separatrix dome present and the flare ribbons observed, see Figure 6.10ii.

To make a comparison between the separatrix surface cuts and the flare ribbon edges a couple of different distance metrics are calculated.

The first distance chosen to compare the flare ribbons and magnetic field features was the *Hausdorff* distance, (e.g. Birsan and Tiba, 2006). The Haussdorff distance between two curves C_1, C_2 is defined as;

$$D_H(C_1, C_2) = \max\left(\sup_{x\in C_1} D(x, C_2), \sup_{y\in C_1} D(y, C_1)\right), \tag{6.6}$$

where C_1 and C_2 are non-empty subsets of a metric space $(M,\ D)$ and $D(x, C_2)$ is the minimum distance between the point x and the curve C_2. An example of calculating the Hausdorff distance between two curves is shown in Figure 6.11.

Hence, the Hausdorff distance will calculate the minimum distance between a single point of the flare ribbons edges and the separatrix surface cut (this is connected to the closest null point if there is no separatrix surface immediately linked to the flare ribbons shape). These minimum distances are calculated for every point of the ribbons edges and then the overall minimum distance from that set is taken ($\sup_{x\in C_1} D(x, C_2)$). The

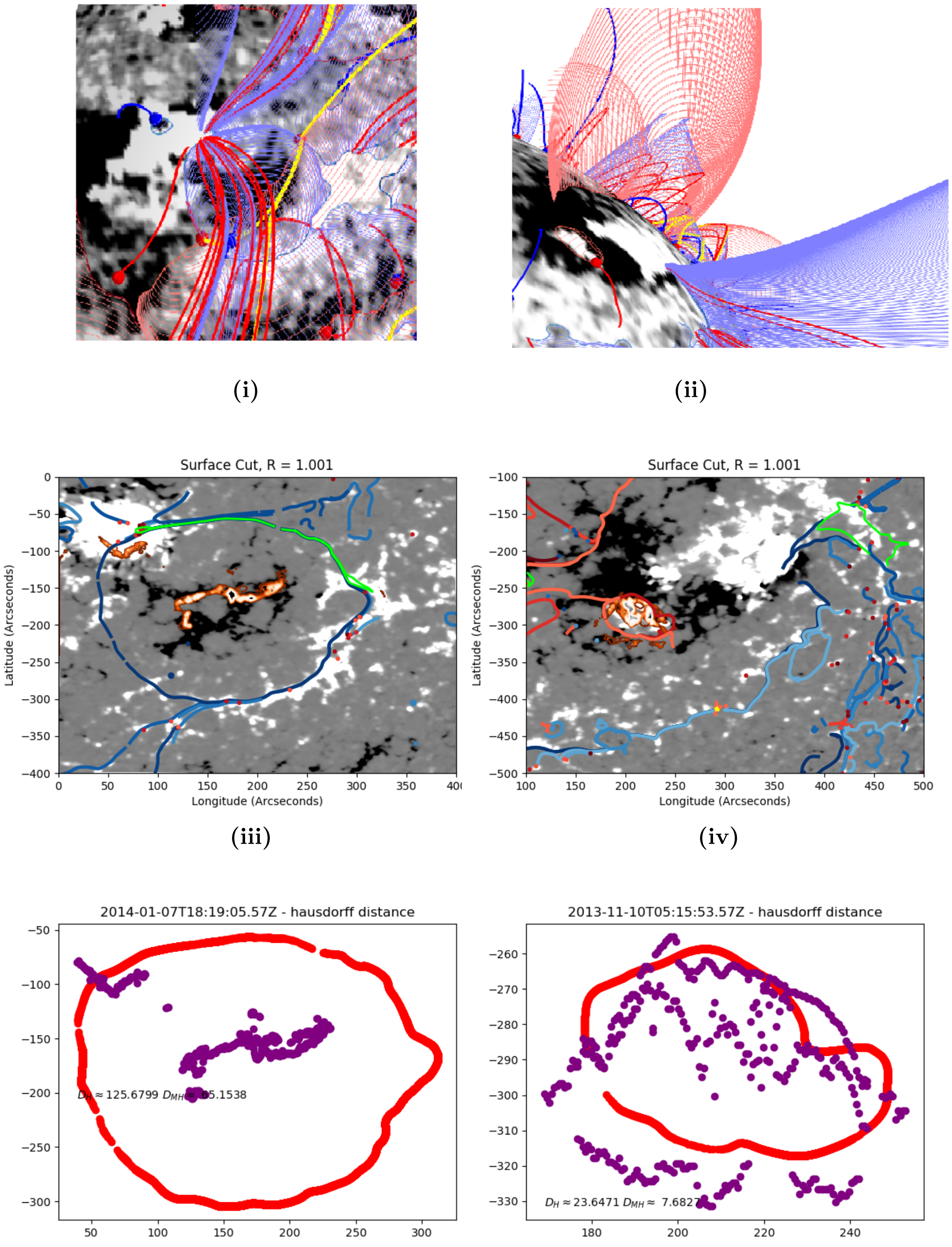

(i) **(ii)**

(iii) **(iv)**

(v) **(vi)**

Figure 6.10: Edge detection outputs; (a) and (b) show the 3D magnetic skeletons overlying flaring active regions, (c) and (d) show the corresponding cuts along the solar surface (at R=1.001$R_\odot$) with the flare ribbons shown contoured in orange, (e) and (f) show the flare ribbons in purple and the corresponding closest separatrix surface cut in red, with the Hausdorff distance (D_H) and modified Hausdorff distance (D_{MH}) calculated between the two.

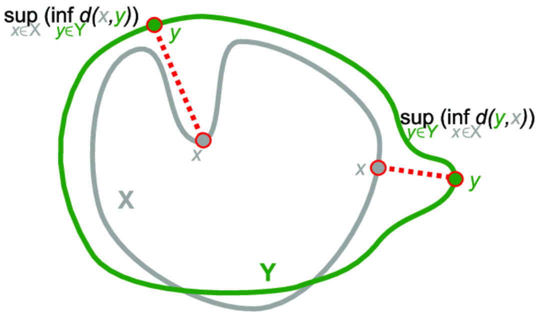

Figure 6.11: Illustration of calculating the Hausdorff distance between two metric spaces. This figure was originally produced by (Pellerin, 2014).

same operation is carried out for finding the overall minimum between every point of the separatrix surface cut and the whole flare ribbon edges ($\sup_{y \in C_1} D(y, C_1)$). Finally the maximum of the two minimum distances is taken to give the final Hausdorff distance. Note that only the parts of the separatrix structures thought to contribute to the flare ribbon positions or shapes are included in the Hausdorff calculations. These separatrix structures were intially selected by eye, however to make the selection process more automatic the separatrix surface found to lie the closest to the flare ribbons was selected using an automatic script to choose the nearest surface. This process may pick up the incorrect surface, however could be altered in the future to calculate the Hausdorff distance for all surfaces and then pick which has the best result for the flare ribbon that the surfaces are being compared to.

The Hausdorff distance D_H, will only equal zero if C_1 and C_2 have the same shape, here that would indicate that $C_1 = C_2$. Therefore the closer to zero the Hausdorff distance is, the better the match in shape and position between the flare ribbons and the separatrix surface cuts.

For the two examples shown in Figure 6.10 the Hausdorff distances were calculated. A closer look at the flare ribbons observed and the separatrix surfaces found closest to the ribbons are shown in Figures 6.10v and 6.10vi. The flare ribbons observed and subsequently processed by the Canny edge detector are shown in purple, with the nearest separatrix surface to the flare ribbons positions shown in red. For the X-class flare that occurred on 7 January 2014, shown in Figure 6.10v, a separatrix surface dome was found overlying the active region, with the flare ribbons observed from the flare occurring inside the separatrix surface. From these observations it looks like there is very little correlation between the separatrix dome position and shape and the flare ribbons observed. This is shown in the Hausdorff distance calculated which seems quite large at $D_H = 125.6799''$. As the distance calculated is much larger than $D_H = 0''$

it indicates that the flare ribbons and the separatrix surfaces are not well matched in position or shape.

The second example, shown in Figure 6.10vi, was of an X-class flare that occurred on 10 November 2013. Here a small separatrix surface dome is found overlying a small part of the active region. The flare ribbons observed seemed almost circular in shape and were found to lie in a similar position to the separatrix dome. The Hausdorff distance calculated for this example was found to be $D_H = 23.6471''$, which is much lower than the than the previous examples distance and also much closer to $D_H = 0''$ which indicates the two curves are the same. Therefore we could conclude that the flare ribbons observed may have obtained their shape from the separatrix surface dome present.

Date	**GOES Class**	**AR Number**	**Topological Feature (TF)**	**Hausdorff Distance (Arcsecs)**			**Modified Hausdorff**
				$\sup_{x\in ribbons} D(x,TF)$	$\sup_{x\in TF} D(x,ribbons)$	D_H	
15/02/11	X2.2	11158	Dome	49.3231	75.66	75.66	15.0651
07/09/11	X1.8	11283	Dome	19.6313	383.5266	383.5266	7.687
07/03/12	X1.3	11429	Cave	74.3363	350.1609	350.1609	28.8449
10/11/13	X1.1	11890	Dome	12.6159	23.6471	23.6471	7.6827
07/01/14	X1.2	11944	Dome	110.5935	125.6799	125.6799	65.1538
10/09/14	X1.6	12158	Dome	144.962	197.8599	197.8599	54.9553
07/11/14	X1.6	12205	Dome	18.1354	41.2723	41.2723	7.8196
20/12/14	X1.8	12242	Cave	72.9507	105.1416	105.1416	32.9456
11/03/15	X2.1	12297	Cave	79.4802	92.7212	92.7212	19.2195
06/09/17	X9.3	12673	Cave	43.2443	67.5452	67.5452	18.4557

Table 6.1: Summary of distance metric values calculated for X-class flares.

To draw a conclusion on which values of the Hausdorff distance indicate a good correlation between the flare ribbons observed and the separatrix domes found in the active regions, more than the two examples discussed above must be analysed. Therefore a subset of the flares analysed in Chapter 4 were used to give a more robust idea of what values the Hausdorff distances take; the regions where a feature was found that was thought to correspond to the flare ribbons observed were chosen. Table 6.1 shows a breakdown of the distances calculated for each flare along with the types of separatrix surfaces that were found in the flaring regions. Using the Hausdorff distances calculated it is suggested that the presence of the separatrix structures found may contribute to the ribbon position and shapes when $D_H < 75''$. Three of the active regions analysed satisfied this criteria, with active regions NOAA 11890, 12205 and 12673 all having lower D_H values. On further inspection as shown in Figure 6.10vi for active region NOAA 11890, these active regions all have separatrix surfaces that lie close to the flare ribbons observed for the X-class flares.

Active region NOAA 11158 has a Hausdorff distance of $D_H = 75.66''$, which is marginally larger than the cut-off value we have selected. On further inspection this active region looks to have a flare ribbon that does correspond to the separatrix structure found, however there is a second ribbon which does not lie close to the topological feature which could be having an impact on the distance value calculated, this active region is shown in Figures 4.2 and 6.12i. For some of the flares analysed the shape of the separatrix structure found was extremley similar to at least one of the flare ribbons observed. In these cases the separatrix structures could also have a position offset and this may be caused by the use of a potential field model rather than an MHS or NLFFF. For example active region NOAA 12242, see Figures 4.8 and 6.12ii, was found to have a separatrix structure lying very close to the flare ribbons observed on 20 December 2014. Although the shapes were similar, both almost semi-circular, the flare ribbons were offset from the topological features considered. These cases were found to have Hausdorff values that lay between $75'' < D_H < 100''$ here.

Note that for values where $D_H > 100''$, for example for active regions NOAA 11283 and NOAA 11429 both of these had one flare ribbon that could be mapped almost precisely to the separatrix structures found, however due to the separatrix structures being so large and spanning further across the solar surface the Hausdorff distances calculated were extremely large. Due to this and the previous cut-off ranges being so large ($D_H < 75''$ for flare ribbons mapping to the separatrix surfaces and $75'' < D_H < 100''$ for a partial match), a better distance metric was sought.

As well as the Hausdorff distances calculated, the modified Hausdorff distances

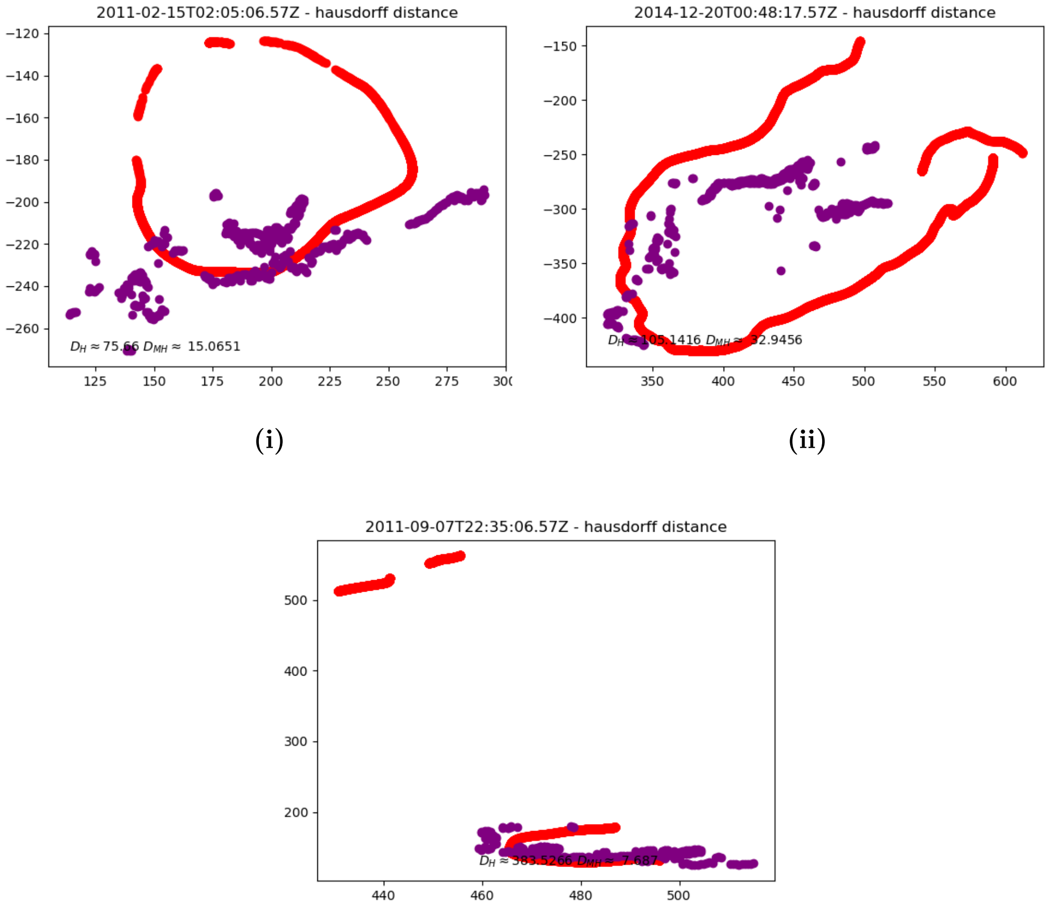

(i) **(ii)**

(iii)

Figure 6.12: Flare ribbons from an X-class flare are shown in purple and the corresponding closest separatrix surface cut is shown in red, with the Hausdorff distance (D_H) and modified Hausdorff distance (D_{MH}) calculated.

(Dubuisson and Jain, 1994) were also calculated where;

$$D_{MH}(C_1, C_2) = \max\left(\frac{1}{|C_1|}\sum_{x\in C_1}\sup D(x, C_2), \frac{1}{|C_2|}\sum_{y\in C_2}\sup D(y, C_1)\right). \tag{6.7}$$

This modified distance is used as it brings the values closer to the ideal case of $D_{MH} = 0''$. The data was previously found to have $D_H < 75''$ indicating a good correlation between the flare ribbons and the separatrix surfaces. Using the modified Hausdorff distance we find that flare ribbons that had similar shapes to the separatrix surfaces found but had an offset of position were found to have lower D_{MH} values. For example in Table 6.1 active regions NOAA 11283, 11890 and 12205 are all found to have $D_{MH} < 8''$ whereas previously all the D_H values were higher, with active region NOAA 11283 having a much larger Hausdorff distance of $D_H = 383.5266''$. This active region was found to have an almost exact mapping of flare ribbons to separatrix surfaces, however one section of the separatrix surface was found to lie across the solar disc, shown in Figure 6.12iii. This is thought to contribute to the previously higher D_H value.

Excluding active region NOAA 11283, most of the active regions analysed that previously had larger D_H values were found to also have the larger D_{MH} values, with active regions NOAA 11429, 11944 and 12242 found to have $D_{MH} > 30''$ and $D_H > 100''$. In general $D_H > D_{MH}$, however the modified Hausdorff distance picks up on ribbons and separatrix surfaces that seem to have a similar shape but are distanced further apart, for example NOAA 11242 as shown in Figure 6.12ii.

Overall we conclude that if the modified Hausdorff distance is found to be $D_{MH} < 20''$ then the flare ribbons observed may have their ribbon shapes and positions due to the separatrix surfaces found in the active regions, with the best cases found to have $D_{MH} < 10''$. Overall six out of the ten active regions were found to have $D_{MH} < 20''$, indicating that the separatrix surfaces could be the cause of the flare ribbon shapes and positions.

6.4 Discussion and Conclusions

In this chapter, we presented Canny edge detection as a method to detect flare ribbon edges in $1600\mathring{A}$ AIA images. This is a technique commonly used to find edges in images and it has been modified for our use. The method itself follows five main steps; noise reduction, gradient calculations, non-maximum suppression, double threshold and edge tracing by hysteresis.

The main differences implemented in our edge detector is how the edge detection thresholds are set. Typically a strong threshold is set at all pixels in the top 0.01% of the pixel intensities, with the weak threshold slighlty larger at approximately 0.05%. Here we present a method of plotting histograms of pixel intensities and subsequently calculating the survival functions associated with those. Examples of both these histograms and their subsequent survival functions are shown in Figure 6.5. These survival functions can give the approximate values of the pixel intensities in the top 1% which can be passed onto the edge detector to set both the strong and weak thresholds. The final implemented values of the strong and weak thresholds were chosen to be strong$= 3\sigma$ and weak$= \sigma$, where σ is the value found from the survival functions. For example if the weak threshold $\sigma = 1000$ counts s^{-1}, then the strong threshold would be $\sigma = 3000$ counts s^{-1}. This change in setting the thresholds allows the edge detector to work better and give clearer results for the flare ribbons analysed.

The detector obviously does not find ribbons when the pixels in the flaring regions are saturated. Hence two methods were presented as options to correct these saturated pixels and to see if the edge detector could give results closer to those found at unsaturated pixel times.

The first method suggested uses linear interpolation across a timeseries of the pixel intensities to correct pixels above a certain threshold. This threshold was set to be any pixels with an count rate greater than 5×10^3 counts s^{-1}. A timeseries containing the pixel count rates from an unsaturated AIA image before and after the peak time of the flare was taken and used to correct the saturated pixels using Equation 6.4 with the surrounding pixels also corrected. Note however that linear interpolation was used here instead of polynomial or Gaussian interpolation. These would perhaps have given a more realistic timeseries profile for the pixel values, with a peak occuring at the peak flare time and the the values on either side of the peak falling down to normal non-flare count rates.

The second method uses averaging of two previously unsaturated pixel values to correct the saturated pixel at the peak flare time. The two unsaturated pixels are taken from AIA images during the flaring time period where the pixels do not have an intensity greater than 5×10^3. The saturated pixel is replaced with the average of the two unsaturated pixel values.

Both methods were applied to X-class flares and the corrected images were processed by the Canny edge detector previously discussed. The comparisons shown in Figure 6.9 show the differences in the edges found by using an unsaturated AIA image, an image corrected using method one and an image corrected using method two. Overall it was found that although the correction methods are suitable to apply to the AIA data, when using the edge detector the best outcomes are found by using an unsaturated AIA image where the flare ribbons are visible. Of the two correction methods discussed, method one which uses a timeseries of pixel values was found to give the best results from the edge detector. This method would result in showing most of the original flare ribbons and not losing any ribbons by smoothing too much.

After the Canny edge detector thresholds were chosen to work on the AIA data, without picking up too much non-flare features; a more robust comparison between the ribbon edges observed and magnetic field features was undertaken. To make this comparison the magnetic field structures previously found in flaring active regions in Chapter 4 were used. As a method to correlate the flare ribbons and the separatrix structures found, two distance methods were implemented.

The first was to calculate the Hausdorff distance between the flare ribbons and separatrix surfaces. Ten X-class flares were analysed here to give a dataset with indications of what Hausdorff distance relates to a good correlation between the flare ribbons positions and shapes, and the separatrix surfaces that were found to intersect with the solar surface around the flaring active region. However to set definite thresholds more flaring regions would have to be analysed. Table 6.1 shows the Hausdorff values for the ten X-class flares. From the table and further image analysis, for example Figure 6.12, it was concluded that where $D_H < 75''$ the separatrix surfaces were thought to contribute to the flare ribbons shapes and positions. For flares where only one ribbon mapped or there was an offset in separatrix surface postion and ribbon positions, it was found that the Hausdorff distances had typical values of $75'' < D_H < 100''$. An example of this was found in particular for the X-class flare that occurred in active region NOAA 12242, see Figure 6.12iii, where there was an offset between the flare ribbons and separatrix surface positions resulting in a high Hausdorff distance. This would indicate that the separatrix surface present is unrelated to the presence and shape of the flare ribbons observed, however due to the closeness in position and similarity in shape it is thought otherwise. For flares that were found to have no ribbons correlating with the separatrix surface positions, the Hausdorff distances were typically, $D_H > 100''$. Some active regions, like NOAA 11283 found to have the ribbons lying along a separatrix surface, but due to the large reach of the surface across the solar disc the Hausdorff values were large, shown in Figure 6.12iii. The large differences in Hausdorff values needed to categorise whether the flare ribbons correlated to the separatrix surfaces produced a need for another distance metric which could make the range of values smaller and perhaps take into account some of the problems discussed here.

The second distance metric used was the modified Hausdorff distance, D_{MH}, which was chosen as an alternative to the Hausdorff distance. Again the lower values here indicated where there was a good correlation, with $D_{MH} < 20''$ chosen as the cut-off where the flare ribbons shape and position could be attributed at least in part to the separatrix surfaces present in the active region. This modified distance was found to include more of the flares that were observed, with flare ribbons found to match the shape of the separatrix surfaces but with an offset in the positions. Active region NOAA 11283 which had previously been shown to have a large Hausdorff distance, although the flare ribbons mapped to a portion of the separatrix surface was found to have a much smaller modified Hausdorff distance of $D_{MH} = 7.687''$. This shows that the modified Hausdorff distance is better at finding correlations between separatrix surfaces and flare ribbons where perhaps they are distanced further apart or only have one section of the separatrix surface or one flare ribbon mapping. It should be noted that for flare ribbons observed that were not found to lie along any separatrix surfaces the modified Hausdorff distances were still large. The X-class flare that occurred in active region NOAA 11944 which had been previously analysed, see Figure 6.10v, was found to have $D_H = 125.6799$ and $D_{MH} = 65.1538$ indicating that there was no correlation between the shape and position of the flare ribbons and the separatrix surfaces found.

These two distance metrics were chosen to take the shape and positions of the flare ribbons and separatrix surfaces into consideration and compare their similarities. Other distance metrics may have been more suitable for this comparison, however the modified Hausdorff distance was found to give a suitable range of values which corresponds to how the flare ribbons map to the topological features found.

Chapter 7

Conclusions and Future Work

In this thesis, we have presented a set of tools which can be used to automate the analysis of observational data and their interpretation using magnetic field models. Here, we have focused in particular on the application of these tools to flare ribbons observed with AIA, but one could envision other applications as well.

The ultimate aim would be to fully integrate the automation of the data analysis and interpretation. We achieved the automation of various analysis techniques, however we do not cover running the techniques together as a whole; which would be the natural next step.

In Chapters 2 and 3 the PFSS and MHS magnetic field models used in this thesis were discussed, together with a description of their implementation in the codes presented by Williams (2018a), which we employ for the numerical calculation of the magnetic fields analysed later. We use these global 3D magnetic field models to construct magnetic skeletons and their associated magnetic separatrix structures. These magnetic field models have been chosen because their calculation is straightforward and computationally cheap. Because it cannot be expected that potential fields will represent the magnetic field structure accurately, we also included magnetic field models using a family of simple MHS solutions. Chapter 3 presented an investigation of the dependence of these MHS solutions on the parameters they include, in particular the values of the parameter $\bar{\alpha}$ which represents one component of the field-aligned current density.

In Chapter 4, fourteen flaring active regions where X-class flares occurred were analysed using both PFSS and MHS models to investigate whether topological structures could be found to correlate to the flare ribbons observed. These models were created initially by using the PFSS models, where it was shown that around the active regions the main topological structures found were; separatrix domes, separatrix caves or a mixture of both, with no separatrix tunnels found in any of the active regions. However, some active regions were found to have no separatrix structures that could be correlated to the flare ribbons by eye. To investigate these regions, the squashing factor (Q) was also calculated for three regions, showing whether high Q values were found in all regions or only regions where separatrix structures had already been found. The active region where no separatrix structures were found was shown to have no regions of high Q which could be correlated to the flare ribbon positions, however for both active regions where separatrix structures had already been found, high Q values were present. Alternatively to both the PFSS model and squashing factor calculations, MHS models were also created and analysed in relation to the X-class flare ribbons observed in each active region. These MHS models however were found to show no major topological structure changes in the active regions and therefore it was concluded that PFSS models were sufficient to analyse these flaring active regions.

Note that in this chapter the mapping of topological features found from the 3D models and the flare ribbons observed was done by eye. However, this means that the results could be biased by subjectivity and so a more objective way to quantify and assess the correlation between observed and model-based structures is discussed in Chapter 6.

Following on from the magnetic field analysis, Chapter 5 discusses the creation and training of a CNN to classify flare ribbon types. Overall the CNN was trained and tested using data from AIA 1600$\mathring{A}$ and a mixture of C and M class flares were used for training with the X-class flares previously analysed tested after the CNN was trained. The CNN was shown to confuse circular flare ribbons with limb flares which was thought to occur due to the distortion of flare ribbons at the limb. Alternatively with the X-class flare analysis, flares which showed high levels of pixel saturation were shown to be misclassified, in particular as limb or compact flares. It was shown that by removing the pixel saturations by taking SDO data from an earlier time, the flare ribbons were subsequently conrrectly classified. Following on from this the CNN was merged with a single layer NN which would process numerical data. This feature was added to test the validity of adding numerical data to the observational classifier.

Finally, Chapter 6 considered using the Canny edge detection method to find the edges of flare ribbons which could be more easily mapped to the topological features found in the active regions analysed in Chapter 4. The main difference of this edge detector is that survival functions were used to set the detection thresholds for each AIA image processed. Following the use of the edge detector on X-class flares, this lead to developing a method which would smooth pixel saturation around flare ribbons to give a cleaner edge. Two methods were developed, one which had been trialled before by Kazachenko et al. (2017), which used linear interpolation using a timeseries of pixel intensities and the other which averaged across the timeseries to smooth the pixels. Of both of these methods, the first gives the best results when being subsequently processed by the Canny edge detector. Subsequently following on from the work in Chapter 4, these ribbon edges were mapped to the separatrix structures located in the flaring active regions by calculating the Hausdorff and modified Hausdorff distances. Thresholds could be set in both of these distance metrics to indicate whether the flare ribbons were considered to correlate to the topological structures analysed.

As previously discussed, all of the methods presented here could be combined into a pipeline to analyse flare ribbon observations. The intial step would be to process the AIA data through the CNN discussed in Chapter 5. This would allow for the detection of flare ribbons in the AIA observations. Subsequently the pipeline could take in corresponding magnetogram data to create a magnetic field model, the structure of which would then be analysed in the same way as those discussed in Chapter 4. Following the processing of data by the CNN and the construction of the magnetic field models, the automated edge detection process, shown in Chapter 6 could be implemented. This would allow a distance measure, like the Hausdorff distance, to be used to quantify whether the topological features found in the magnetic field models are related to the flare ribbons observed.

As well as implementing the methods as a data analysis pipeline, various aspects of the techniques themselves could be altered or improved to analyse different data or improve the analysis outputs. The magnetic fields considered in this thesis are potential and magnetohydrostatic and so improvements could be made by perhaps using a NLFFF model where the global topological structures may be more complex. This would allow a more dynamic magnetic field to be implemented around the active regions analysed, which would perhaps produce different topological structures or find structures where we found none. These more complex field features could be analysed similarly to the PFSS models presented in this thesis. The magnetic field models used throughout this work are also global models, with computing resources and time could be saved by using local magnetic field model which only consider the regions around where the flare ribbons are observed. This would allow for much quicker processing of the regions, however could lead to a loss in some of the larger structures found overlying some of the active regions that we analysed here.

The convolutional neural networks used to analyse the flare ribbon regions and classify them could also be altered such that a different and perhaps simplier techniques such as support vector machines (SVMs) could be used. This would allow for a comparison between models and a choice for which to use, and could also save some computing resources as well.

Further improvements could also be made to the distance metrics used, to compare the flare ribbons observed and the topological features found from a magnetic field model. However the Hausdorff distance was found to be the most suitable in this thesis, when compared with the Euclidean and the Fréchet distance which were also considered by us.

Finally, it should be remarked that parts or all of the overall methodology has the potential to be applied, maybe with modifications, to analyse observations of ribbons in other wavelengths or other solar structures altogether as well, such as filaments.

Appendix A

A.1 Solving the Laplace Equation for the PFSS Model

To solve Laplace's equation, separation of variables is used such that

$$f(r, \theta, \phi) = R(r)T(\theta)P(\phi). \tag{A.1}$$

This allows the Laplace equation, see Equation 2.4, to be written in the form

$$\frac{1}{R}\frac{\partial}{\partial r}\left(r^2\frac{\partial R}{\partial r}\right) + \frac{1}{T\sin(\theta)}\frac{\partial}{\partial \theta}\left(\sin(\theta)\frac{\partial T}{\partial \theta}\right) + \frac{1}{P\sin^2(\theta)}\frac{\partial^2 P}{\partial \phi^2} = 0. \tag{A.2}$$

We can then use separation of variables, with a separation constant λ to split this equation into one r-dependent part and one θ and ϕ dependent part.

$$\frac{1}{R}\frac{\partial}{\partial r}\left(r^2\frac{\partial R}{\partial r}\right) = \lambda, \tag{A.3}$$

$$\frac{1}{T\sin(\theta)}\frac{\partial}{\partial \theta}\left(\sin(\theta)\frac{\partial T}{\partial \theta}\right) + \frac{1}{P\sin^2(\theta)}\frac{\partial^2 P}{\partial \phi^2} = -\lambda. \tag{A.4}$$

To make Equation A.4 simpler to solve another separation constant, m, can be introduced. This allows the equation to split into two individual equations dependent only on θ and ϕ.

$$\frac{1}{P}\frac{\partial^2 P}{\partial \phi^2} = -m^2, \tag{A.5}$$

$$\frac{1}{T\sin(\theta)}\frac{\partial}{\partial \theta}\left(\sin(\theta)\frac{\partial T}{\partial \theta}\right) - \lambda\sin^2(\theta) = m^2. \tag{A.6}$$

Hence the equation for $P(\phi)$ becomes much easier to solve. Solving Equation A.5 results in P being written in terms of an exponential, $e^{\pm im\phi}$ with $0 \leq \phi \leq 2\pi$ and so m must be an integer. Although solving Equation A.5 is simple, to solve Equation A.6 Legendre polynomials and spherical harmonics must be introduced. These are discussed in the next section which discusses the Legendre polynomials used throughout the PFSS model calculations. Note that Equation A.3 must also be solved to find a solution for the Laplace equation, a substition of $r = e^u$ can be used to do this and the solution is shown later in Equation A.25.

A.1.1 Legendre Functions

Legendre functions are denoted as $P_l^m(x)$, where $l \geq 0$ and they are the solutions to the Legendre differential equation,

$$(1 - x^2)\frac{\mathrm{d}^2 y}{\mathrm{d}x^2} - 2x\frac{\mathrm{d}y}{\mathrm{d}x} + \left(l(l+1) - \frac{m^2}{1 - x^2}\right) = 0, \tag{A.7}$$

where, $m, l \in \mathbb{C}$. The Legendre functions exist when $-l \leq m \leq l$ and are both non-singular and orthogonal when $x \in (-1, 1)$. When $m = 0$ however, the Legendre polynomial is denoted as $P_l(x)$.

Calculating the Legendre functions can be done in various ways, however it is numerically easier to calculate them recursively with the initial Legendre polynomial already known. So with the initial polynomial,

$$P_0^0 = 1, \tag{A.8}$$

the following five equations can be used to calculate the subsequent Legendre functions needed.

$$P_l^l(x) = -\sqrt{1 - x^2}(2l + 1)P_{l-1}^{l-1}(x), \tag{A.9}$$

$$P_{l+1}^l(x) = x(2l + 1)P_l^l(x), \tag{A.10}$$

$$P_l^m(x) = \frac{x(2l + 1)P_{l-1}^m(x) - (l - 1 + m)P_{l-2}^m(x)}{l - m}, \tag{A.11}$$

$$P_l^{-m}(x) = (-1)^m \frac{(l - m)!}{(l + m)!} P_l^m(x), \tag{A.12}$$

$$P_l^m(-x) = (-1)^{l+m} P_l^m(x). \tag{A.13}$$

Note that in Equation A.12, $m < 0$ and for Equation A.11, $l \neq m$, otherwise the fraction would be undefined.

The Legendre differential equation (Equation A.7) can be used to help solve the Laplace equation for the θ dependence. This allows Equation A.6 to be solved by using the transformation $x = \cos(\theta)$, converting it into the Legendre differential equation and allowing it to be solved using Equations A.9 to A.13, to find the corresponding Legendre functions where $\theta \in (0, \pi)$.

To create *spherical harmonics*, the Legendre functions, P_l^m must be normalised using a normalising factor, N_l^m. Using this normalising factor produces the normalised Legendre functions,

$$Q_l^m(x) = N_l^m P_l^m(x). \tag{A.14}$$

The normalising factor used is,

$$N_l^m = \sqrt{\frac{2l+1}{4\pi}\frac{(l-m)!}{(l+m)!}}, \tag{A.15}$$

and is chosen as it allows for the orthonormalisation required. This orthogonality can be expressed by,

$$\int_{\theta=0}^{\pi}\int_{\phi=0}^{2\pi} Y_{l_1}^{m_1}(\theta,\phi)\overline{Y_{l_2}^{m_2}}(\theta,\phi)\mathrm{d}S = \delta_{l_1,l_2}\delta_{m_1,m_2}. \tag{A.16}$$

The $\delta_{i,j}$ denotes the Kronecker delta function and $\overline{Y_{m_2}^{l_2}}$ denotes the complex conjugate of $Y_{l_2}^{m_2}$. If a different normalising factor was used for the PFSS model it would not change the magnetic field components but alter the difficulty in finding them. Hence the normalising factor is chosen in its simplest form as in Equation A.16. The resulting spherical harmonics can be denoted by $Y_m^l(\theta,\phi)$ such that,

$$Y_l^m(\theta,\phi) = Q_l^m(\cos(\theta))e^{im\phi}, \tag{A.17}$$

where $Y_m^l(\theta,\phi)$ is the spherical harmonic of order m and degree l. These spherical harmonics are solutions of the Laplace equation (Equation 2.4). As the Legendre functions have been normalised Equations A.9 to A.13 can also be written in their normalised form where;

$$Q_0^0 = \sqrt{\frac{1}{4\pi}}, \tag{A.18}$$

$$Q_l^l(x) = -\sqrt{1-x^2}\sqrt{\frac{2l+1}{2l}}Q_{l-1}^{l-1}(x), \tag{A.19}$$

$$Q_{l+1}^l(x) = x\sqrt{2l+3}Q_l^l(x), \tag{A.20}$$

$$Q_l^m(x) = x\sqrt{\frac{4l^2-1}{l^2-m^2}}Q_{l-1}^m(x) - \sqrt{\frac{2l+1}{2l+3}\frac{(l-1)^2-m^2}{l^2-m^2}}Q_{l-2}^m(x), \tag{A.21}$$

$$Q_l^{-m}(x) = (-1)^m Q_l^m(x), \tag{A.22}$$

$$Q_l^m(-x) = (-1)^{l+m} Q_l^m(x). \tag{A.23}$$

These normalised Legendre functions are subsequently used as solutions to the θ dependent part of the Laplace equation.

In conclusion, equations A.3, A.5 and A.6 can now be solved to give the general solution for the Laplace equation. As previously stated Equation A.5 can be solved resulting in $P(\phi)$ becoming an exponential of the form, $e^{\pm im\phi}$. Equation A.6 can be solved for $T(\theta)$ by applying the substitution, $x = \cos(\theta)$. This substitution transforms Equation A.6 into the Legendre differential equation, Equation A.7. This transformation allows the spherical harmonics to be implemented into the PFSS model for $0 \leq \theta \leq \pi$, as the normalised Legendre functions, $Q_l^m(x)$, are solutions to Equation A.6. Hence the first separation constant, λ, is defined as

$$\lambda = l(l+1).$$

For each value of l there are $2l+1$ solutions to Legendre's equation, as each value of m ranges from $-l \leq m \leq l$. Hence the r-dependent solution for Laplace's equation can be solved given the expression for λ. Therefore Equation A.3 becomes,

$$\frac{\partial}{\partial r}\left(r^2 \frac{\partial R}{\partial r}\right) = l(l+1)R.$$

To solve this another substitution must be used where, $r = e^u$. This allows the R equation to be written as a second-order differential equation,

$$\frac{\mathrm{d}^2 R}{\mathrm{d}u^2} + \frac{\mathrm{d}R}{\mathrm{d}u} - l(l+1)R = 0. \tag{A.24}$$

This can easily be solved such that,

$$R(r) = a_l^m r^l + b_l^m r^{-(l+1)}. \tag{A.25}$$

Note the coefficients a_l^m and b_l^m are the constants of integration from the $T(\theta)$ and $P(\phi)$ equations and can be found using boundary conditions.

A.2 Further Mathematics for the Derivation of the Global MHS Model

Here we discuss further derivations and equations relating to the MHS magnetic field equations derived in Chapter 3.

To find the form of the free function F discussed in Equation 3.5 we must first take the curl of Equation (3.6):

$$\begin{aligned}\nabla \times (\nabla \times \mathbf{B}) &= \mu_0(\nabla \times (\alpha \mathbf{B}) + \nabla \times (\nabla F \times \nabla \psi)),\\ &= \mu_0(\alpha \nabla \times \mathbf{B} + \nabla \alpha \times \mathbf{B} + \nabla \times (\nabla F \times \nabla \psi)),\\ &= \mu_0(\alpha \mu_0 \mathbf{j} + \nabla \times (\nabla F \times \nabla \psi))\\ &= \mu_0(\alpha \mu_0(\alpha \mathbf{B} + \nabla F \times \nabla \psi) + \nabla \times (\nabla F \times \nabla \psi)),\\ &= \mu_0(\alpha^2 \mu_0 \mathbf{B} + \alpha \mu_0 \nabla F \times \nabla \psi + \nabla \times (\nabla F \times \nabla \psi)).\end{aligned} \tag{A.26}$$

Furthermore we can show,

$$\begin{aligned}\mathbf{r} \cdot (\nabla \times (\nabla \times \mathbf{B})) &= \mathbf{r} \cdot (\nabla(\nabla \cdot \mathbf{B}) - \nabla^2 \mathbf{B}),\\ &= \mathbf{r} \cdot (-\nabla^2 \mathbf{B}),\\ &= -\nabla^2(\mathbf{r} \cdot \mathbf{B}),\end{aligned} \tag{A.27}$$

where we use the following identity;

$$\begin{aligned}\nabla^2(\mathbf{r} \cdot \mathbf{B}) &= \mathbf{r} \cdot \nabla^2 \mathbf{B} - \mathbf{B} \cdot \nabla^2 \mathbf{r} + 2\nabla \cdot ((\mathbf{B} \cdot \nabla)\mathbf{r} + \mathbf{B} \times \nabla \times \mathbf{r}),\\ &= \mathbf{r} \cdot \nabla^2 \mathbf{B},\end{aligned}$$

with the final result shown in Equation 3.7. Following this F takes the form shown in Equation 3.8 and the gravitational potential (shown in Equation 3.1) is derived by,

$$\begin{aligned}\nabla \psi &= \frac{\partial \psi}{\partial r}\mathbf{e_r},\\ &= \frac{\partial \psi}{\partial r}\frac{\mathbf{r}}{r},\\ &= \frac{GM}{r^3}\mathbf{r}.\end{aligned}$$

A more in depth calculation of $\nabla F \times \nabla \psi$ (Equation 3.9) is also shown where;

$$\begin{aligned}
\nabla F \times \nabla \psi &= \nabla\Bigg(\kappa(\psi)\frac{GM}{r^3}\mathbf{r}\cdot\mathbf{B}\Bigg) \times \frac{GM}{r^3}\mathbf{r}, \\
&= \frac{GM}{r^3}\nabla\Bigg(\kappa(\psi)\frac{GM}{r^3}(\mathbf{r}\cdot\mathbf{B})\Bigg) \times \mathbf{r}, \\
&= \frac{GM}{r^3}\Bigg(\frac{GM}{r^3}(\mathbf{r}\cdot\mathbf{B})\nabla\kappa(\psi) + \kappa(\psi)(\mathbf{r}\cdot\mathbf{B})\nabla\Bigg(\frac{GM}{r^3}\Bigg) + \\
&\quad \kappa(\psi)\frac{GM}{r^3}\nabla(\mathbf{r}\cdot\mathbf{B})\Bigg) \times \mathbf{r}, \\
&= \kappa(\psi)\Bigg(\frac{GM}{r^3}\Bigg)^2 \nabla(\mathbf{r}\cdot\mathbf{B}) \times \mathbf{r}, \\
&= \xi(r)\nabla(\mathbf{r}\cdot\mathbf{B}) \times \mathbf{r}.
\end{aligned} \tag{A.28}$$

$\xi(r)$ is defined as;

$$\xi(r) = \kappa(\psi)\Bigg(\frac{GM}{r^3}\Bigg)^2. \tag{A.29}$$

To calculate the final forms for the magnetic field components two functions $v_{l,m}(r)$ and $w_{l,m}(r)$ are needed. The forms of both these functions are derived below.

Here we consider an element of;

$$\mathbf{L}\cdot\mathbf{B_t} = \frac{\bar{\alpha}}{i}\sum_{l=0}^{\infty}\sum_{m=-l}^{l} B_l^m(r)Y_l^m(\theta,\phi),$$

such that;

$$\begin{aligned}
(\mathbf{L}\cdot\mathbf{B_t})_l^m &= \frac{\bar{\alpha}}{i}(\mathbf{r}\cdot\mathbf{B})_l^m \\
\mathbf{L}\cdot(v_{l,m}\mathbf{L}Y_l^m(\theta,\phi) + w_{l,m}\nabla Y_l^m(\theta,\phi)) &= \frac{\bar{\alpha}}{i}B_l^m(r)Y_l^m(\theta,\phi) \\
v_{l,m}\mathbf{L}^2 Y_l^m + w_{l,m}\mathbf{L}\cdot\nabla Y_l^m &= \frac{\bar{\alpha}}{i}B_l^m Y_l^m \\
v_{l,m}l(l+1)Y_l^m &= \frac{\bar{\alpha}}{i}B_l^m Y_l^m \\
v_{l,m}(r) &= \frac{\bar{\alpha}}{i}\frac{B_l^m}{l(l+1)}
\end{aligned} \tag{A.30}$$

Furthermore consider $\nabla\cdot\mathbf{B} = 0$ to find the form of $w_{l,m}(r)$;

$$\begin{aligned}
\nabla\cdot\mathbf{B} = \frac{1}{r^2}\frac{\partial}{\partial r}\Bigg(r^2\frac{B_l^m(r)}{r}Y_l^m(\theta,\phi)\Bigg) + \nabla\cdot(v_{l,m}\mathbf{L}Y_l^m(\theta,\phi)) \\
+\nabla\cdot(w_{l,m}(r)\nabla Y_l^m(\theta,\phi)) = 0
\end{aligned}$$

$$\begin{aligned}
\frac{1}{r^2}\frac{\partial}{\partial r}(rB_l^m)Y_l^m + v_{l,m}\nabla\cdot\mathbf{L}Y_l^m + \nabla v_{l,m}\cdot\mathbf{L}Y_l^m \\
+w_{l,m}\nabla^2 Y_l^m + \nabla w_{l,m}\cdot\nabla Y_l^m = 0 \\
\frac{1}{r^2}\frac{d}{dr}(rB_r)Y_l^m + w_{l,m}\frac{l(l+1)}{r^2}Y_l^m = 0 \\
w_{l,m}(r) = \frac{1}{l(l+1)}\frac{d}{dr}(rB_l^m) \qquad \text{(A.31)}
\end{aligned}$$

A.3 Further Flares Analysed

Active Region NOAA 11166

On the 9 March 2011 a X1.5 solar flare was observed in active region NOAA 11166. Lasting for just under one hour, the flare produced a circular flare ribbon as shown in Figure A.1a. The PFSS model was used to analyse this region for corresponding topological features.

In Figures A.1a and b, the flare ribbons observed during the X-class event are shown. There is a small circular-shaped ribbon present over a small bipolar region, with a larger sigmodial ribbon lying to the side. A cut along the solar surface was taken at a height of 1.001R$_\odot$ shown in Figure A.1c. The separatrix cut does not show any features lying in the active region at $R = 1.001R_\odot$, however when investigating further, the 3D model shown in Figure A.1d shows a small separatrix dome lying across a small part of the active region where one of the circular flare ribbons looks to be located. It is thought this was not picked up in our surface cut as it lies very close to the solar surface. This separatrix dome corresponds to one of the AIA 1600 $\AA$ ribbons observed, with a comparison between the location of the separatrix dome, the active region and the flare ribbons observed shown in Figures A.1e and A.1f. The separatrix dome found only is thought to correspond to the smaller circular flare ribbon observed with no other topological feature found in the region which could correspond to the larger flare ribbon. Note also that this active region lies within a partially closed field region, with the edge of the HCS lying in the middle of the active region, although the smaller bipolar region that the separatrix dome lies upon is within a region of open magnetic field.

Although a second topological feature was not found in this active region, this could be due to smoothing of the magnetic field by the PFSS model with only a limited spatial resolution being used in the magnetic field calculations. The use of a potential magnetic field instead of a MHS or NLFFF extrapolation may also have an effect on

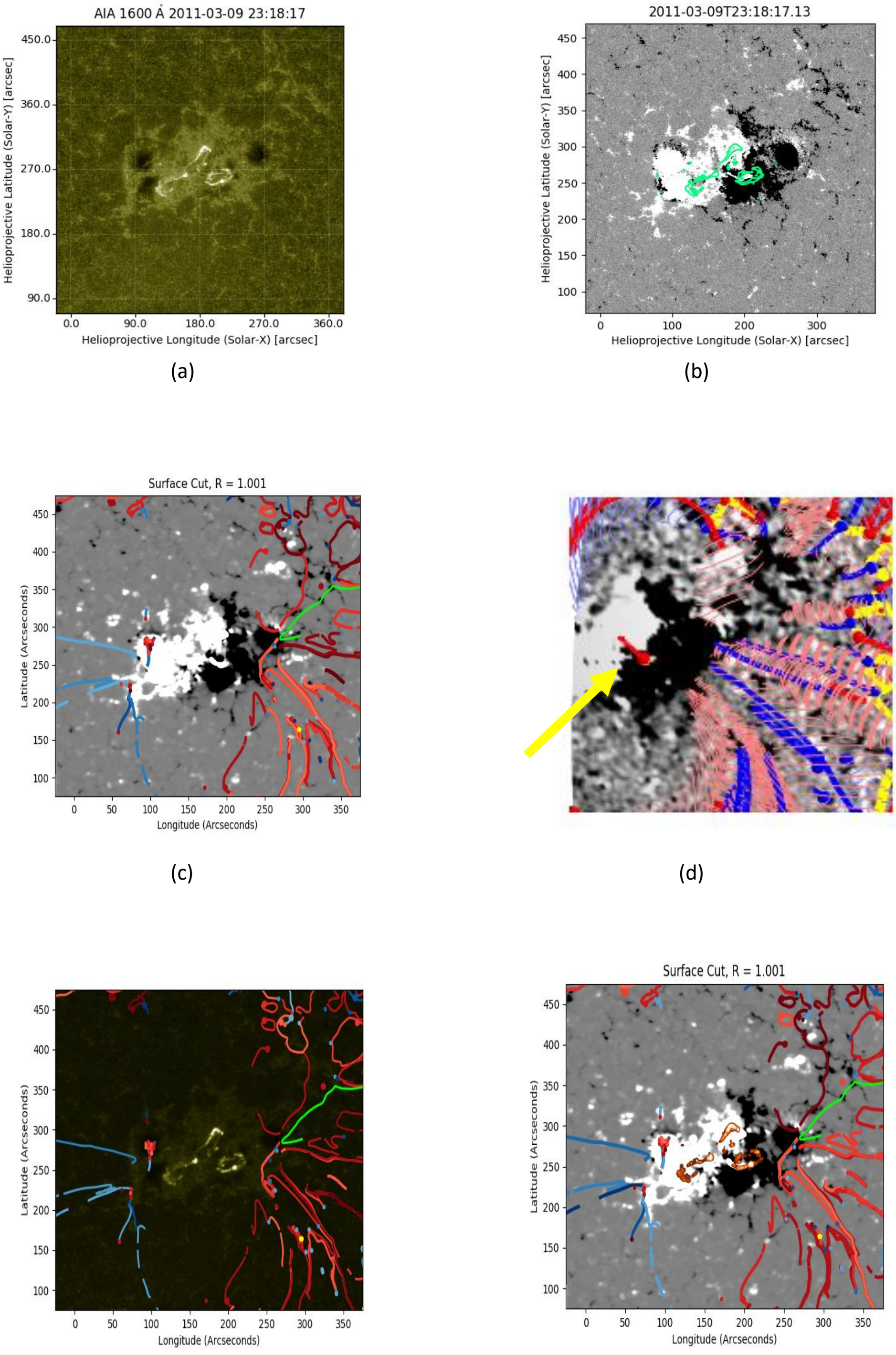

(a) (b)

(c) (d)

(e) (f)

Figure A.1: Analysis of AR NOAA 11166. (a) AIA observation taken during the X1.6 flare. (b) shows the HMI data at the time of the flare with the corresponding flare ribbons contoured (green). (c) the surface cut of the PFSS model at $R = 1.001$ is shown around the active region, with features on the edges of the active region but none lying across the active region. (d) the 3D magnetic skeleton showing a single low lying positive null in the active region. (e) the separatrix cut is imposed onto the AIA image. (f) Surface cut of the 3D model at $R = 1.001$ with the ribbons contoured (orange).

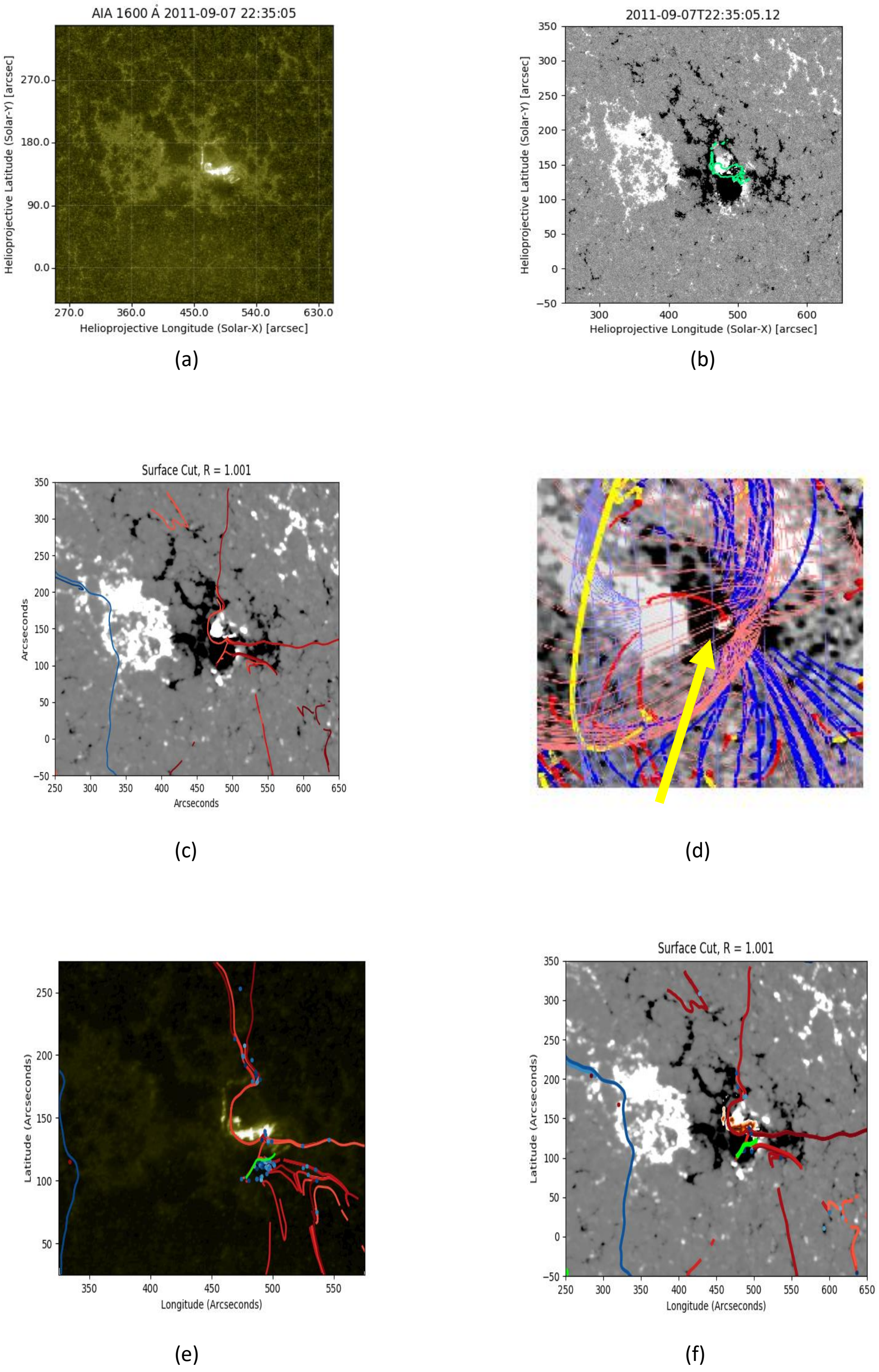

(a) (b) (c) (d) (e) (f)

Figure A.2: Analysis of AR NOAA 11283. (a) AIA observation taken during the X1.8 flare on 7 November 2011. (b) HMI data at the time of the flare with the corresponding flare ribbons contoured (green). (c) the surface cut of the PFSS model at $R = 1.001$, showing positive null features around the active region. (d) the 3D magnetic skeleton, showing a large positive separatrix cave in a portion of the active region. (e) the separatrix cut is shown on an AIA image. (f) Surface cut of the 3D model at $R = 1.001$ with the ribbons contoured (orange).

what features were found.

The Q map was also calculated for this region and is shown in Figure A.3a nd A.3b. Note that where the circular ribbon lies, there are high Q values also in the region, this could indicate the presence of a QSL or could relate to the low lying null and its associated small separatrix dome which was previously discussed. For the second flare ribbon, there is no high region of Q nearby which could relate to a QSL being present where the flare ribbon lies.

In relation to the other magnetic fields analysed and discussed, due to the separatrix dome found here, this region is similar to active region NOAA 11890 (see Section 4.2.2) which was found to have a circular flare ribbon that could correspond to the presence of a separatrix dome present in the flaring active region.

Active Region NOAA 11283

Two X-class solar flares were observed in active region NOAA 11283, which crossed the solar disc from 30 August 2011 to 12 September 2011, with the X-class flares observed on 6 and 7 September 2011. Here, the data analysed is from the 7 September, however both flares occurred in the same region and had the same flare ribbon emission in AIA 1600 $\AA$. When the X1.8 flare studied here occurred, the active region was past disc centre and moving towards the western limb of the solar surface.

This flare produced a small semi-circular ribbon as shown in Figure A.2a. The PFSS model was used over the active region and surrounding surface to find the topological structures present. The resultant features around the active region are shown in the cut taken at $1.001R_\odot$ as in Figure A.2c. A small separatrix cave-like structure was present over the smaller bipolar region within the active region. This structure is classified as cave-like, due to many spine lines intersecting at the solar surface close to the edge of the structure, clearly shown in Figure A.2d, however none of them seem to lie along the cave opening as expected. The 3D model also shown the active region lying within a large separatrix dome structure indicating an area of closed magnetic field. From Figures A.2e and A.2f, it is shown that the semi-circular contours of the flare ribbons map around the edge of the bipolar region corresponding to the base of the separatrix dome present. The Q map that was calculated for this region showed high values of Q ($\approx 10^8$) where the separatrix structure intersects with the surface and where the flare ribbons were observed. Note the Q map is not shown here as the output was very similar to other regions previously analysed (e.g. see Section 4.2).

In comparison to the other active regions analysed this region was the only region

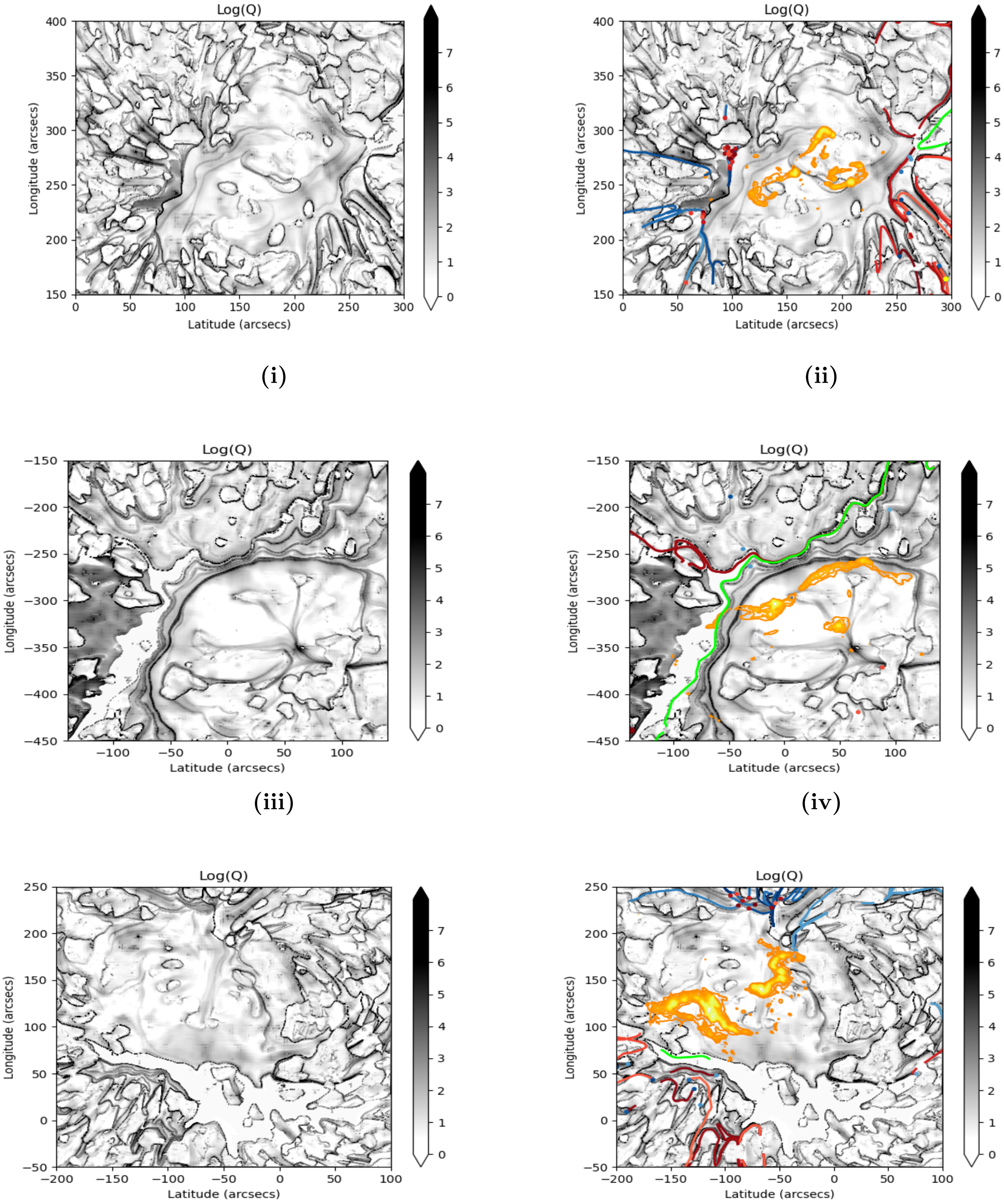

(i) (ii)

(iii) (iv)

(v) (vi)

Figure A.3: Q maps calculated for some of the active regions analysed in Section A.3, with the PFSS surface cuts also shown to investigate whether the high Q values correlate to separatrix surfaces already located or QSLs, flare ribbons also contoured (orange). (a) Q map for AR NOAA 11166 with (b) showing the associated PFSS model surface cut, where Q values of $\approx 10^6$ were found around the smaller flare ribbon. (c) Q map for AR NOAA 11520 with (d) showing the associated PFSS model surface cut. Q $\approx 10^7$ close to the flare ribbon indicating a possible QSL. (e) Q map for AR NOAA 12158 with (f) showing the associated PFSS model surface cut. No large Q values were found around the flare ribbons.

which had a *cave-like* structure rather than a definite separatrix cave or dome. However, the semi-circular flare ribbons observed could be most closely compared to those observed in active region NOAA 11158 where almost semi-circular ribbons were present and mapped to the edge of a separatrix dome located in the region, see Section 4.2.1.

Active Region NOAA 11429

Active region NOAA 11429 crossed the solar disc from 4 March 2012 to 14 March 2012, with a X1.3 solar flare occurring on 7 March 2012. This large X-class flaring event is analysed here, with the flare itself being observed by SDO in all wavelengths.

Two flare ribbons were observed in the active region during the flaring period, with the 1600$\mathring{A}$ AIA image shown in Figure A.4a. When the flare ribbon is contoured onto the HMI magnetogram it is shown that the ribbons lie on the edge of the bipolar region, Figure A.4b. The global 3D magnetic skeleton is extrapolated and inspected around the active region to investigate whether any topological structures could contribute to the presence of the flare ribbons observed. This active region is quite noisy with many separatrix surfaces and their spines lines intersecting along the edge of the active region, shown in Figure A.4d. The surface cut taken along R=1.001$R_{\odot}$, shown in Figure A.4c, shows a small separatrix cave lying along the active region, with a larger separatrix dome also present with both surfaces intersecting the solar surface at the same points. The smaller, more vertical, ribbon lies along the edge of where the separatrix cave intersects with the solar surface with the other flare ribbon not found to lie along any separatrix surface intersection. The comparison between the flare ribbons observed and the separatrix surface cut is shown in Figures A.4e and A.4f. Along the separatrix cave intersection and where the smaller vertical ribbon was observed, high Q values were also found ($\approx 10^9$) which was to be expected.

This region was found to be similar to active region NOAA 12673, where both active regions were found to have separatrix surfaces lying in the active region around where the flare ribbons were observed. However, in both regions the separatrix surfaces were not a similar shape to the flare ribbons observed, although they were found to be in close proximity to each other.

Active Region NOAA 11520

On 12 July 2012 in active region NOAA 11520 an X1.4 solar flare was observed. This active region crossed the solar disc from 6 July 2012 to 18 July 2012 and was at disc centre when the flare occurred. The flare ribbons observed by SDO AIA 1600 $\mathring{A}$, see

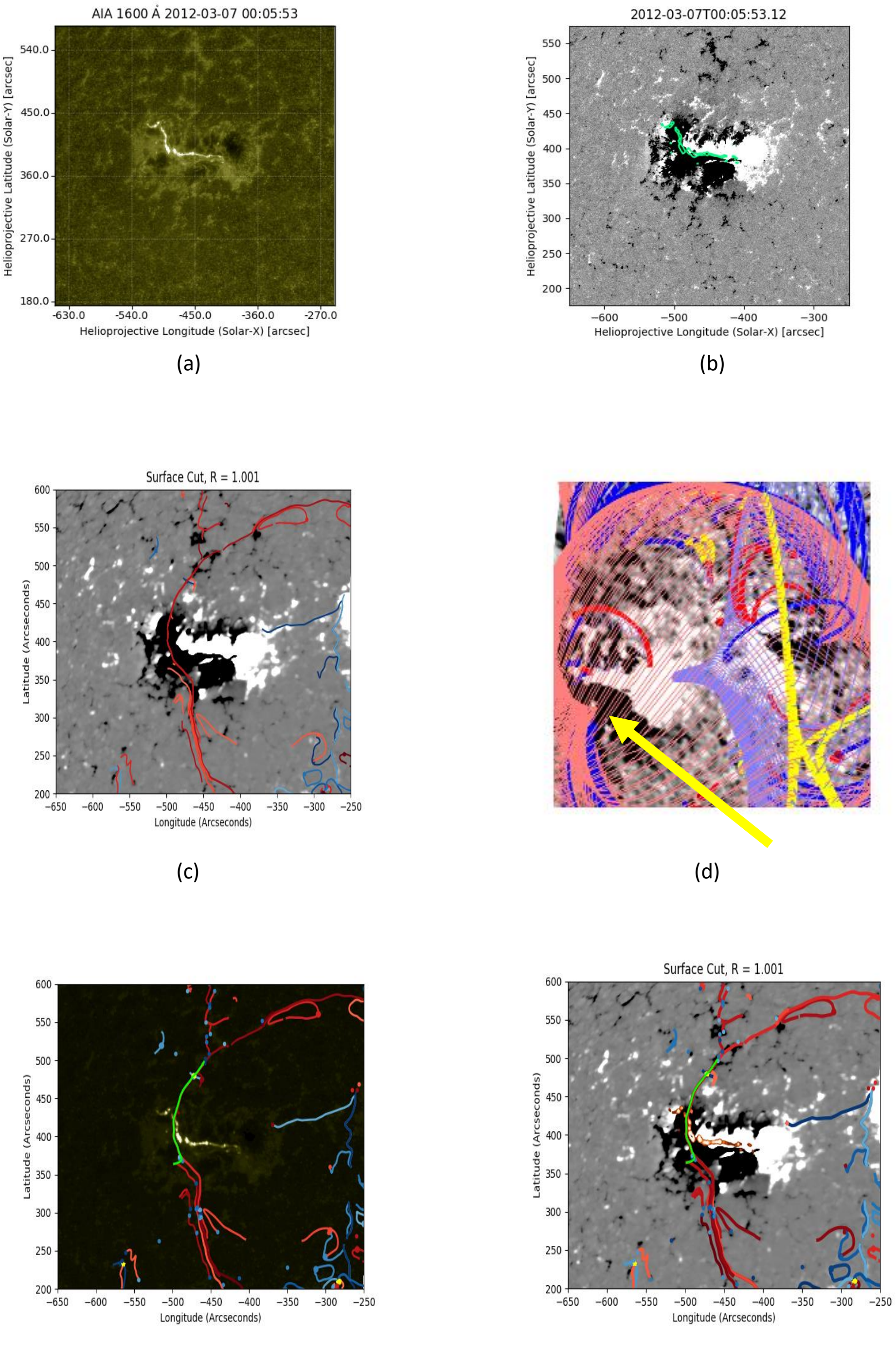

(a) (b)

(c) (d)

(e) (f)

Figure A.4: Analysis of AR NOAA 11429. (a) AIA observation taken during the X1.3 flare. (b) HMI data at the time of the flare with the corresponding flare ribbons contoured (green). (c) the surface cut of the PFSS model at $R = 1.001$ shows a large topological feature lying across the active region. (d) the 3D magnetic skeleton shows a large positive separatrix dome overlying the region with smaller structures enclosed. (e) the separatrix cut shown on the AIA image. (f) surface cut of the 3D model at $R = 1.001$ with the ribbons contoured (orange).

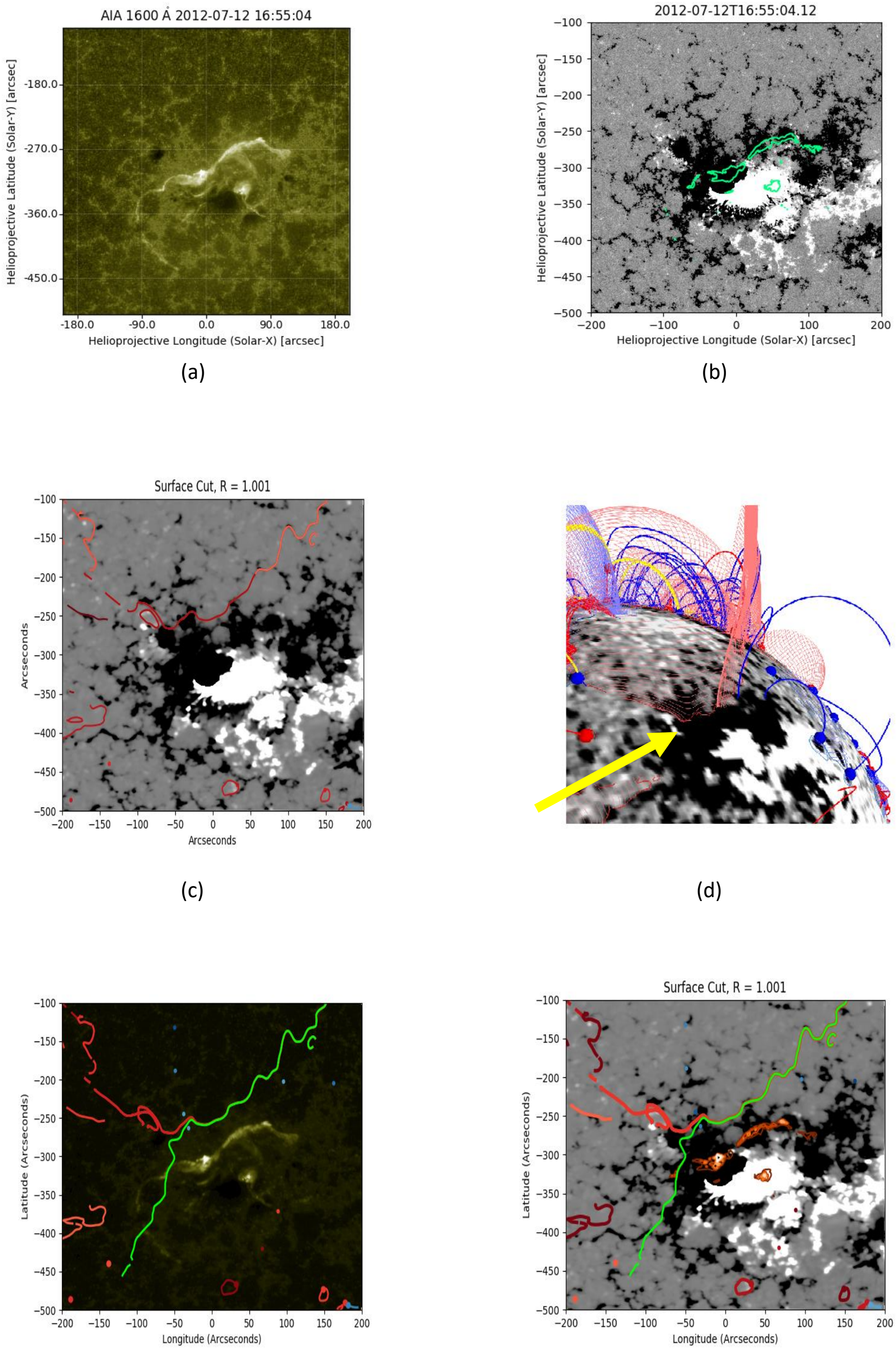

(a) (b) (c) (d) (e) (f)

Figure A.5: Analysis of AR NOAA 11520. (a) shows an AIA observation taken during a X1.4 flare. (b) HMI data at the time of the flare with the corresponding flare ribbons contoured (green). (c) the surface cut of the PFSS model at $R = 1.001$, with no features found lying in the active region and a single structure lying along the upper edge. (d) the 3D magnetic skeleton shows a large separatrix dome lying at the top of the region. (e) the separatrix cut is shown with the AIA image. (f) Surface cut of the 3D model at $R = 1.001$ with the ribbons contoured (orange).

Figure A.5a, were sigmoidal in shape with a smaller circular ribbon also present. No nulls or related topological features were found directly over the active region when the PFSS model was used, see Figure A.5d. However, there was a large separatrix dome system found further north on the surface which extended down to the upper edge of the flaring active region. The surface cut taken at $R = 1.001R_{\odot}$, shown in Figure A.5 shows the lack of separatrix surfaces present in this active region. Figures A.5e and A.5f show the comparison between the flare ribbons observed and the surface cut, no obvious correlation is found however it is possible that the separatrix dome edge may correspond to the larger ribbons observed. Due to the distance between the ribbons and this separatrix dome, the correlation between the two cannot be made for certain.

A Q map was also created to analyse whether there could be QSLs present in the region where there were few separatrix structures found. Figure A.3c shows the Q map for this region, with the flare ribbons observed and the separatrix features previously found shown in Figure A.3d. In these plots it was shown that regions of high Q were found around the separatrix structures. However note that just above the observed flare ribbons and below where the HCS curtains intersect with the surface, there is also a region of large Q ($\approx 10^7$) which could indicate the presence of a QSL. This QSL would lie much closer to the flare ribbons than any of the previous separatrix structures found and could correspond to why the flare ribbons have the shape and positions observed.

Due to the lack of separatrix structures in this active region, no definite conclusion could be made between their presence here and the X-class flare ribbons observed by SDO. This is a very similar result to that discussed later for active region NOAA 12192, which also was found to have no separatrix surfaces in the active region although the region was the site of four X-class flares.

Active Region NOAA 11944

On 7 January 2014 a X1.2 solar flare occurred in active region NOAA 11944, which crossed the solar disc from 1 January 2014 to 14 January 2014. The flare produced two flare ribbons which were observed by SDO lying on the edge of the active region, see Figures A.6a and A.6b.

A 3D magnetic skeleton was created from the potential field extrapolation, see Figure A.6d, with a cut along the surface $R = 1.001R_{\odot}$ taken to inspect where the separatrix surfaces intersect with the solar surface, see Figure A.6c. Over the small section of the active region where the X-class flare occurred, a separatrix dome was

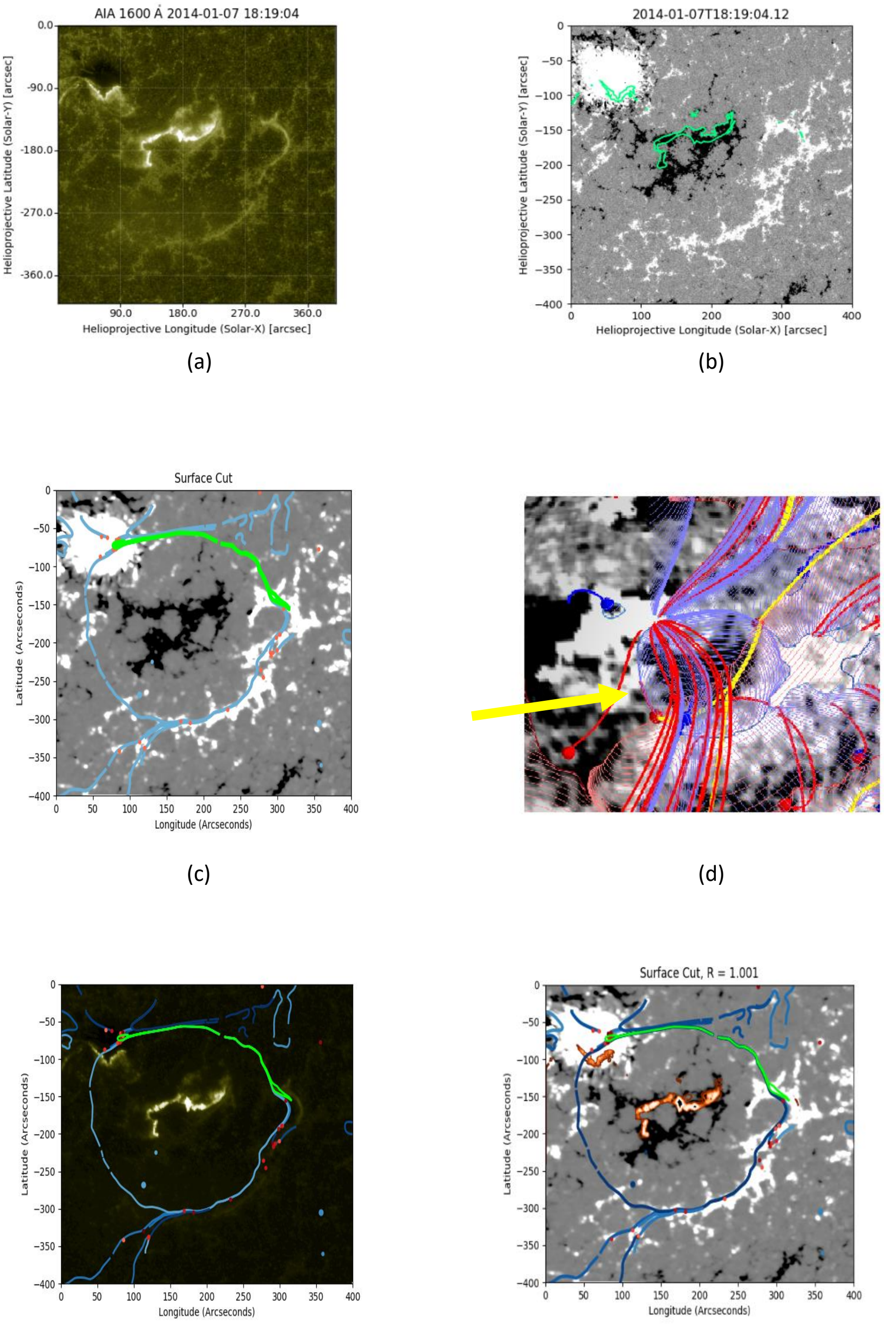

(a) (b)

(c) (d)

(e) (f)

Figure A.6: Analysis of AR NOAA 11944. (a) AIA observation taken during a X1.2 flare. (b) HMI data at the time of the flare with the corresponding flare ribbons contoured (green). (c) the surface cut of the PFSS model at $R = 1.001$ shows a large topological structure originating from a negative null lying around the active region. (d) the 3D magnetic skeleton shows a separatrix dome lying in the active region surrounded by other features. (e) the separatrix cut is shown on the AIA image. (f) Surface cut of the 3D model at $R = 1.001$ with the ribbons contoured (orange).

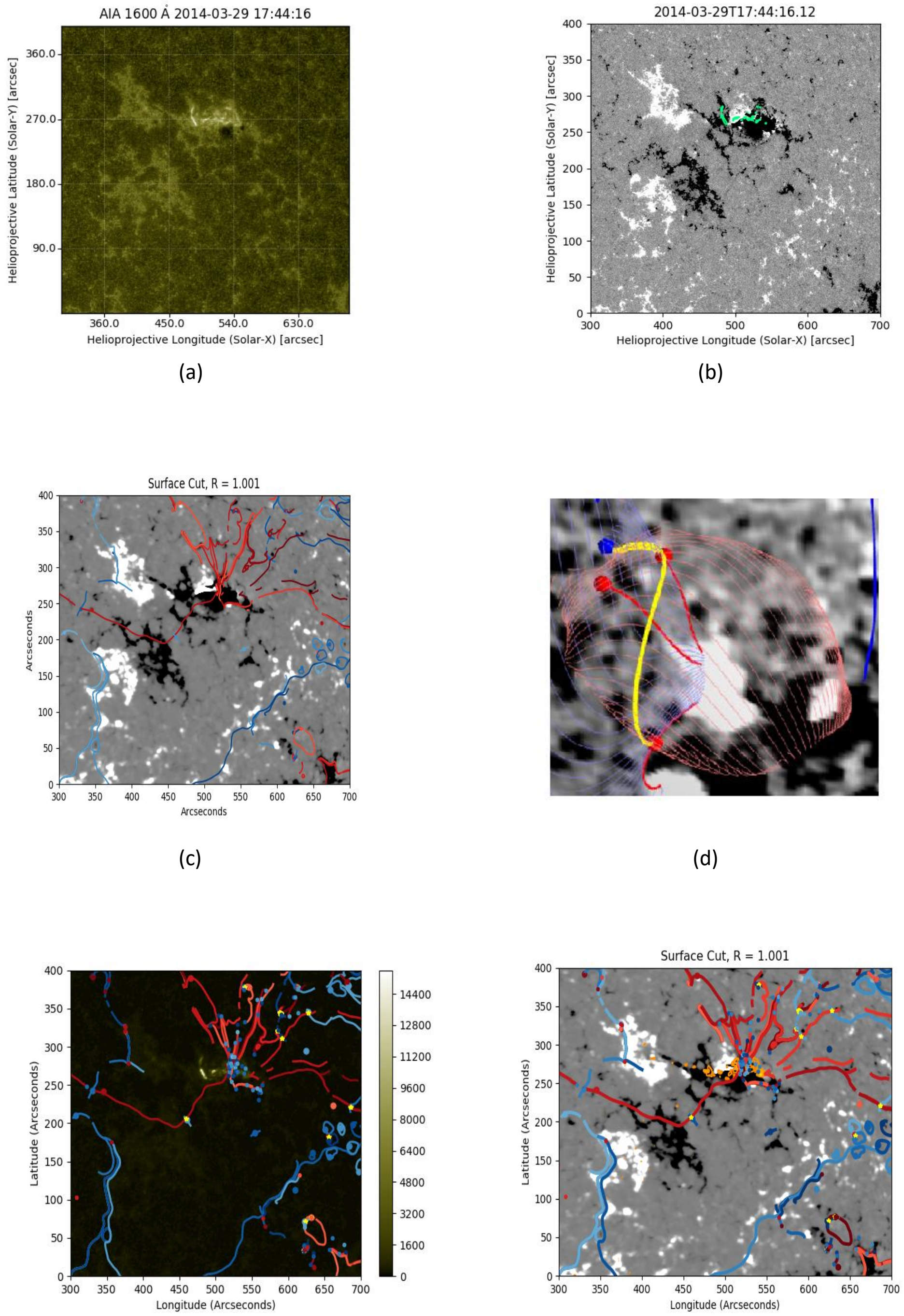

(a) (b)

(c) (d)

(e) (f)

Figure A.7: Analysis of AR NOAA 12017. (a) AIA observation taken during a X-class flare. (b) HMI data at the time of the flare with the corresponding flare ribbons contoured (green). (c) the surface cut of the PFSS model at $R = 1.001$, positive separatrix structures intersect around where the flare ribbons were observed. (d) the 3D magnetic skeleton shows a positive separatrix cave lying in the region the flare ribbons were observed. (e) the separatrix cut is shown along with AIA image. (f) Surface cut of the 3D model at $R = 1.001$ with the ribbons contoured (orange).

present along with multiple spine lines and separatrices originating from other separatrix structures. These structures were compared to the shape and position of the flare ribbons observed during the X-class flare, see Figures A.6e and A.6f. Here it is shown that although the separatrix dome is present in the region there is no obvious correlation between its presence and the presence of the flare ribbons observed. This could be due to multiple things such as too low a resolution when extrapolating the potential magnetic fields or the exclusion of the flaring dynamics in the region. The Q values were also calculated for this region, however although high Q values were found around separatrix surfaces there were no high Q values in the region where the ribbons were observed.

Compared to the other active regions analysed, this region is similar to active region NOAA 12158, which is analysed later in this section. Both regions have clear sigmodial flare ribbons present during the X-class flares, however although separatrix structure were found lying around both active regions no structures were found close to the flare ribbons observed by SDO.

Active Region NOAA 12017

On the 29 March 2014 a X1.0 solar flare was observed in active region NOAA 12017. Occurring between 17:35UT and 17:54UT, the flare produced a semi-circular flare ribbon as shown in Figure A.7a. A clearer analysis of where the ribbon sits with respect to the active region is shown in Figure A.7b, with the ribbons marked in green.

The magnetic skeleton produced from the PFSS model, see Figure A.7d, shows a cave-like separatrix structure present in the flaring active region. The separatrix structure originates from a positive null point, however is surrounded by a further two positive nulls and one negative null point which leads to the presence of two null-null separators in the region. Where this structure intersects with the solar surface is shown in the surface cut (Figure A.7c), where the whole active region is covered by a large positive separatrix structure (thought to be the positive separatrix dome found in the 3D model), with the other separatrix structure lying at the edge of a small bipolar region (this correlates to the cave shown in the 3D model). The comparison between the flare ribbons observed and the separatrix structures found is shown in Figures A.7e and A.7f. The flare ribbons observed lie extremely close to where the separatrix cave intersects with the solar surface. It is thought this structure could give rise to the shape and position of the flare ribbons observed. The Q map was also calculated for this region, with large Q values ($\approx 10^7$) found around the flaring site. These Q values are thought to correspond to the separatrix structures already found in the active region.

This active region analysis and results is very similar to that found for active region NOAA 11429, with both regions found to have *cave-like* structures. Both regions had more complex cave structures present in the active region which possibly contributed to the flare ribbons observed during the X-class flaring events.

Active Region NOAA 12158

On 10 September 2014 a X1.6 solar flare was observed from 17:21UT to 17:45UT in active region NOAA 12158, which crossed the Solar disc from 5 September 2014 to 17 September 2014. Two sigmoidal flare ribbons were observed by AIA 1600 $\mathring{A}$, as in Figure A.8a. The flare ribbons were found to lie across the centre of the active region when compared to the HMI magnetogram, see Figure A.8b.

Figure A.8d shows the 3D magnetic skeleton found around the flaring active region with its associated surface cut taken at $R = 1.001R_{\odot}$ shown in Figure A.8c. There are many separatrix surfaces lying around the edges of the active region and a large positive separatrix structure marking that the active regon is lying within a closed magnetic field structure, however there are no structures lying around the positions of the flare ribbons observed, as shown in Figure A.8e. Again this could be due to the use of a potential magnetic field instead of more sophisticated field configurations such as an MHS or NLFF field being modelled.

The Q maps were calculated here to investigate the possibility of QSLs in the active region where no separatrix structures were found. Figure A.3e shows the Q values around the flaring active region and Figure A.3f shows these values with respect to the flare ribbons observed during the X-class flare. Very small Q values are found in the active region with one or two sections with slightly higher values. However, there are no regions of large Q which could correspond to the indication that there is separatrix surfaces or QSLs present in the region where the flare ribbons were observed.

As with active region NOAA 11944, which was previously discussed in this section, there are lots of separatrix structures lying around the active region but none present in the active region itself that could contribute to the shape or position of the flare ribbons observed.

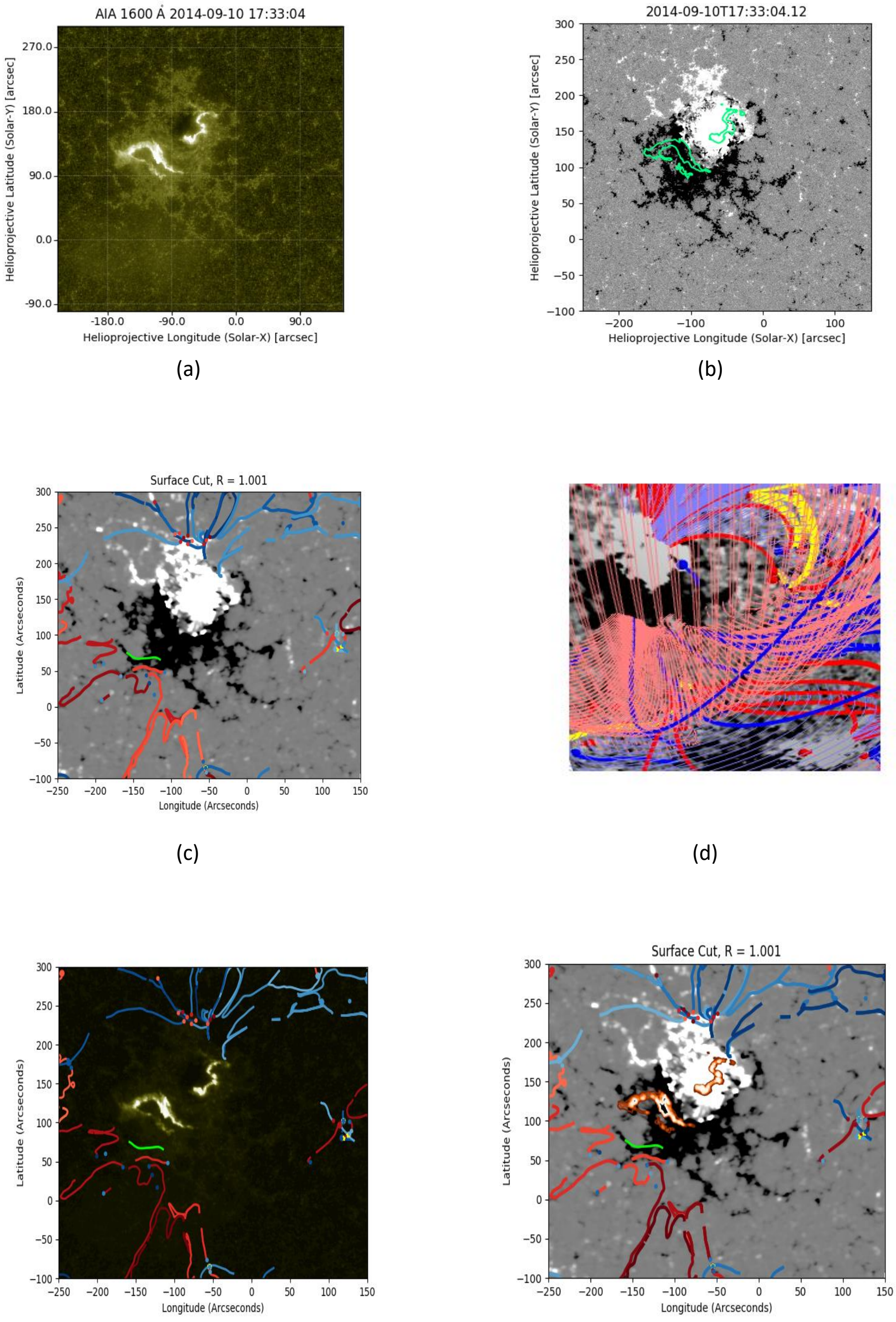

(a) (b)

(c) (d)

(e) (f)

Figure A.8: Analysis of AR NOAA 12158. (a) AIA observation taken during the X1.6 flare. (b) HMI data at the time of the flare with the corresponding flare ribbons contoured (green). (c) the surface cut of the PFSS model at $R = 1.001$, there are features lying on the edge of the region but none lying across the centre where the ribbons were observed. (d) the 3D magnetic skeleton shows no features across the active region and a large positive structure lying overhead. (e) the separatrix cut is shown with the AIA image. (f) Surface cut of the 3D model at $R = 1.001$ with the ribbons contoured (orange).

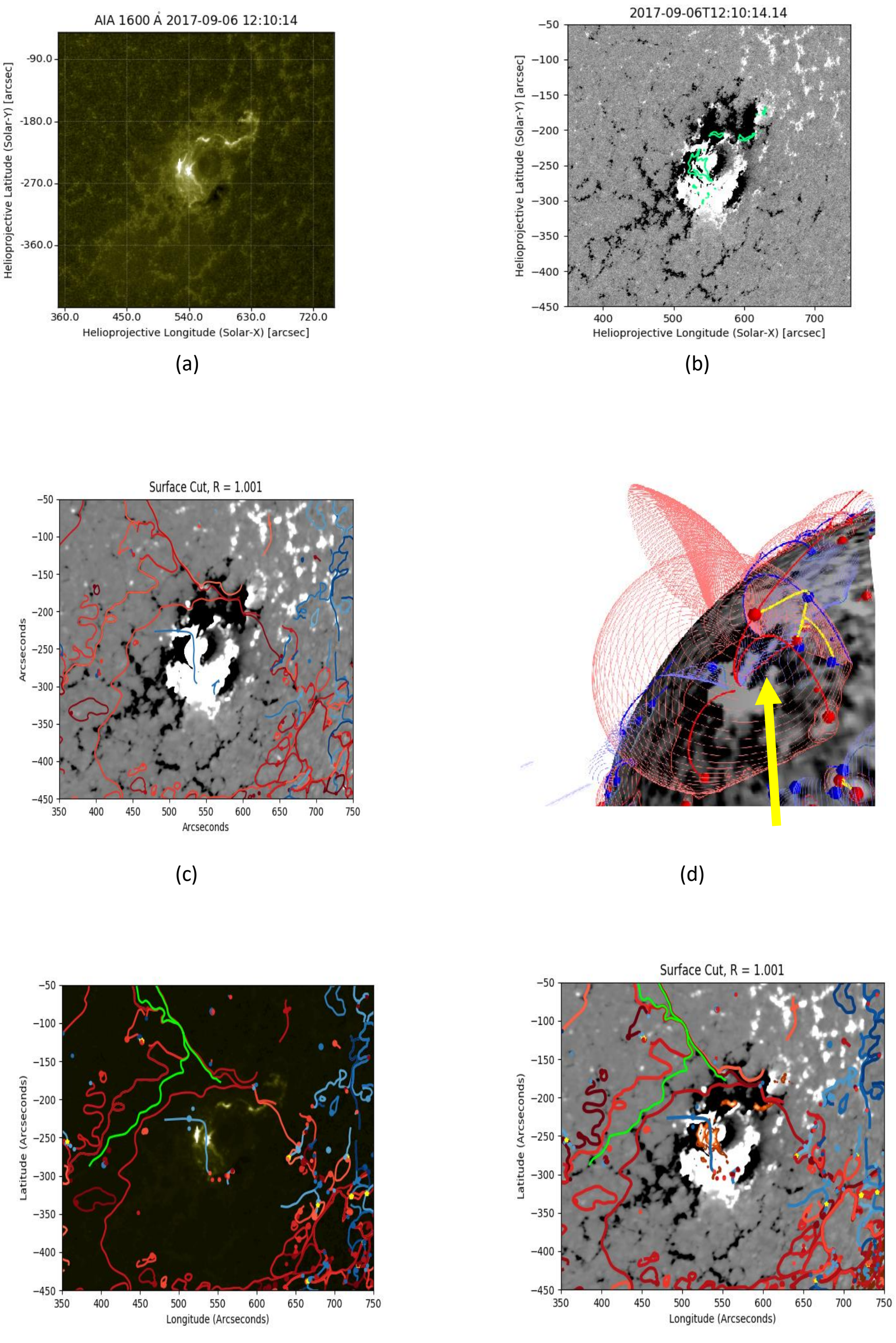

(a) (b)

(c) (d)

(e) (f)

Figure A.9: Analysis of AR NOAA 12673. (a) AIA observation taken during the X9.3 flare. (b) HMI data at the time of the flare with the corresponding flare ribbons contoured (green). (c) the surface cut of the PFSS model at $R = 1.001$ shows a negative separatrix structure lying in the active region with positive structures lying around the edges. (d) the 3D magnetic skeleton shows a small negative cave (blue) enclosed within a larger positive separatrix dome (red). (e) the separatrix cut is shown with the AIA image. (f) Surface cut of the 3D model at $R = 1.001$ with the ribbons contoured (orange).

Active Region NOAA 12673

On 6th September 2017 a X9.3 solar flare occurred in active region NOAA 12673, which emerged on the solar disc on 30 August 2017 and crossed the remainder of the disc until the 10 September 2017. Over the 12 days as it crossed the solar disc, 4 X-class flares and 2 large CMEs were observed. The data in Figure A.9 was taken from the largest of these flares which occurred on the 6th September from 11:53UT to 12:10UT.

Two flare ribbons were observed by SDO, which merge together in the final stages of the flare, see Figures A.9a and b with the flare ribbons observed lying across the centre of the active region. A separatrix dome originating from a positive null point was found overlying the active region, see Figure A.9d. However it is a smaller negative null and its separatrix cave that lie within the separatrix dome, that may contribute to the flare ribbons observed. A surface cut taken along $R = 1.001R_\odot$ gives a clearer insight into where the separatrix surfaces intersect with the solar surface, see Figure A.9c. This surface cut is compared to the flare ribbons observed in Figures A.9e and A.9f, where it is shown that the flare ribbons and the separatrix cave lie in the same part of the active region. Although they share a close position, there is a difference in the shape of the flare ribbons observed and the separatrix cave. Similarly to the other active regions analysed, the Q values in this region where found to be high in the presence of the footpoints of the separatrix surfaces detected and low in other parts of the active region.

This difference in the shape of the flare ribbons observed and the separatrix surfaces found in the active region is similar to what was found during the analysis of active region NOAA 11429 discussed previously. However the almost squashed cave structure observed here is similar to another structure found in active region NOAA 12297, discussed in Section 4.2.6.

A.4 Backpropagation derivation

To calculate the gradients needed to minimise the loss function, a process known as *backpropagation* (Hecht-Nielson, 1989) is carried out. There are four main steps to the backpropagation process; forward pass, calculating the loss function, backwards pass and the weight update. Throughout we will denote the kernel containing the model weights as $w^l_{m,n}$ where l is the layer the weight matrix is implemented to connect the neuron to layer $l - 1$. The aim of the backpropagation process is to calculate how each of the weights affects the loss function calculation and find a way to minimise them such that the overall loss decreases. To do this we need to calculate, $\frac{\partial E}{\partial w^l_{m',n'}}$. During the forward pass, each pixel included in the weight kernels, $w^l_{m',n'}$, makes a contribution to each convolution carried out. So, each weight will be applied to all the image pixels during the convolutional layers; this means that the feature map outputs are all affected by what value each weight initially has. The chain rule is used to calculate the gradient for each weight with respect to the loss function such that;

$$\begin{aligned}\frac{\partial E}{\partial w^l_{m',n'}} &= \sum_{i=0}^{H-k_h}\sum_{j=0}^{W-k_w} \frac{\partial E}{\partial x^l_{i,j}} \frac{\partial x^l_{i,j}}{\partial w^l_{m',n'}} \\ &= \sum_{i=0}^{H-k_h}\sum_{j=0}^{W-k_w} \delta^l_{i,j} \frac{\partial x^l_{i,j}}{\partial w^l_{m',n'}}\end{aligned} \tag{A.32}$$

In Equation A.32 the $x^l_{i,j}$ term denotes the input into convolutional layer, l, with the i, j iterators denoting the pixels in that array. The input into this convolutional layer can be written as;

$$x^l_{i,j} = \sum_m \sum_n w^l_{m,n} o^{l-1}_{i+m,j+n} + b^l, \tag{A.33}$$

where $o^l_{i,j}$ denotes the output feature map at layer l and b^l denotes the optional bias parameter that can be included at layer l. We can calculate the $\frac{\partial x^l_{i,j}}{\partial w^l_{m',n'}}$ term in equation A.32 by expanding equation A.33 to remove the summations and calculating the partial derivatives such that;

$$\begin{aligned}\frac{\partial x^l_{i,j}}{\partial w^l_{m',n'}} &= \frac{\partial}{\partial w^l_{m',n'}}\left(\sum_m \sum_n w^l_{m,n} o^{l-1}_{i+m,j+n} + b^l\right) \\ &= \frac{\partial}{\partial w^l_{m',n'}}\left(w^l_{0,0} o^{l-1}_{i+0,j+0} + \cdots + w^l_{m',n'} o^{l-1}_{i+m',j+n'} + \cdots + b^l\right) \\ &= \frac{\partial}{\partial w^l_{m',n'}}\left(w^l_{m',n'} o^{l-1}_{i+m',j+n'}\right) \\ &= o^{l-1}_{i+m',j+n'}\end{aligned} \tag{A.34}$$

As shown in the previous equation, the only term that contributes to the partial derivatives is where $m = m'$ and $n = n'$. Using equation A.34, we can write Equation A.32 as,

$$\frac{\partial E}{\partial w^l_{m',n'}} = \sum_{i=0}^{H-k_h}\sum_{j=0}^{W-k_w} \delta^l_{i,j} o^{l-1}_{i+m',j+n'} \tag{A.35}$$

Once the data has been passed through the network in the forward pass and the loss function, E, has been calculated the backwards pass in the backpropagation process starts. This is where the gradients, $\delta^l_{i,j}$, for each layer, l, are calculated such that;

$$\delta^l_{i,j} = \frac{\partial E}{\partial x^l_{i,j}},$$

allowing the weights to be updated such that the loss function is minimsed using Equation A.35. These gradients are measuring how a small change in one pixel in the input feature maps, $x_{i',j'}$, affects the overall value of the loss function calculated. If we denote the output region affected by the input pixel by Q, then we can express the gradients as,

$$\begin{aligned}
\frac{\partial E}{\partial x^l_{i',j'}} &= \sum_{i,j \in Q} \frac{\partial E}{\partial x^{l+1}_Q} \frac{\partial x^{l+1}_Q}{\partial x^l_{i',j'}} \\
&= \sum_{i,j \in Q} \delta^{l+1}_Q \frac{\partial x^{l+1}_Q}{\partial x^l_{i',j'}} \\
&= \sum_{m=0}^{k_h-1} \sum_{n=0}^{k_w-1} \delta^{l+1}_{i'-m,j'-n} \frac{\partial x^{l+1}_{i'-m,j'-n}}{\partial x^l_{i',j'}},
\end{aligned} \tag{A.36}$$

where Q has a height range of $0 \leq Q_{height} \leq i^{'} - (k_h - 1)$ and a width ranging from $0 \leq Q_{width} \leq j^{'} - (k_w - 1)$.

The activation function, act, and its derivative, $act^{'}$, along with Equation A.33 are used to expand the partial derivative term in Equation A.36 such that;

$$\begin{aligned}
\frac{\partial x^{l+1}_{i'-m,j'-n}}{\partial x^l_{i',j'}} &= \frac{\partial}{\partial x^l_{i',j'}} \left(\sum_{m'} \sum_{n'} w^{l+1}_{m',n'} o^l_{i-m+m',j-n+n'} + b^{l+1} \right) \\
&= \frac{\partial}{\partial x^l_{i',j'}} \left(\sum_{m'} \sum_{n'} w^{l+1}_{m',n'} act\left(x^l_{i-m+m',j-n+n'}\right) + b^{l+1} \right) \\
&= \frac{\partial}{\partial x^l_{i',j'}} \left(w^{l+1}_{m',n'} act\left(x^l_{0-m+m',0-n+n'}\right) + \cdots + w^{l+1}_{m,n} act\left(x^l_{i',j'}\right) + \cdots + b^{l+1} \right) \\
&= \frac{\partial}{\partial x^l_{i',j'}} \left(w^{l+1}_{m,n} act\left(x^l_{i',j'}\right) \right) \\
&= w^{l+1}_{m,n} \frac{\partial}{\partial x^l_{i',j'}} \left(act\left(x^l_{i',j'}\right) \right) \\
&= w^{l+1}_{m,n} act^{'}\left(x^l_{i',j'}\right).
\end{aligned} \tag{A.37}$$

This equation can now be substituted back into Equation A.36 to calculate the gradients needed in the backwards pass;

$$\frac{\partial E}{\partial x^{l}_{i',j'}} = \sum_{m=0}^{k_h-1} \sum_{n=0}^{k_w-1} \delta^{l+1}_{i'-m} w^{l+1}_{m,n} act'\left(x^{l}_{i',j'}\right). \tag{A.38}$$

The final step in the backwards pass calculations is converting these gradients into convolutions that can be applied at the convolutional layers to update the weights. Hence, equation A.38 can be expressed as a convolution such that;

$$\begin{aligned} \frac{\partial E}{\partial x^{l}_{i',j'}} &= rot_{180^\circ}\left(\sum_{m=0}^{k_h-1} \sum_{n=0}^{k_w-1} \delta^{l+1}_{i'-m} w^{l+1}_{m,n}\right) act'\left(x^{l}_{i',j'}\right) \\ &= \delta^{l+1}_{i',j'} * rot_{180^\circ}(w^{l+1}_{m,n}) act'\left(x^{l}_{i',j'}\right) \end{aligned} \tag{A.39}$$

Therefore in the backpropagation process for the error function to be minimised, Equation A.35 and the gradients needed to update the weights are calculated using Equation A.39. Once the gradients have been calculated they can be passed back into the SGD routine described in Equation 5.5.

Bibliography

V. E. Abramov-Maximov, V. N. Borovik, L. V. Opeikina, A. G. Tlatov, and L. V. Yasnov. Features of Microwave Radiation and Magnetographic Characteristics of Solar Active Region NOAA 12242 Before the X1.8 Flare on December 20, 2014. *Geomagnetism and Aeronomy*, 57(8):978–987, December 2017. doi: 10.1134/S0016793217080023.

M. D. Altschuler and G. Newkirk. Magnetic Fields and the Structure of the Solar Corona. I: Methods of Calculating Coronal Fields. *SolPhys*, 9:131–149, September 1969. doi: 10.1007/BF00145734.

Laith Alzubaidi, Jinglan Zhang, Amjad J Humaidi, Ayad Al-Dujaili, Ye Duan, Omran Al-Shamma, J Santamaría, Mohammed A Fadhel, Muthana Al-Amidie, and Laith Farhan. Review of deep learning: concepts, CNN architectures, challenges, applications, future directions. *Journal of big data*, 8(1):53–53, 2021.

J.A. Armstrong and L. Fletcher. Fast solar image classification using deep learning and its importance for automation in solar physics. *Sol Phys*, 294, 06 2019. doi: https://doi.org/10.1007/s11207-019-1473-z.

M. J. Aschwanden, P. Boerner, C. J. Schrijver, and A. Malanushenko. Automated Temperature and Emission Measure Analysis of Coronal Loops and Active Regions Observed with the Atmospheric Imaging Assembly on the Solar Dynamics Observatory (SDO/AIA). *SolPhys*, 283(1):5–30, March 2013. doi: 10.1007/s11207-011-9876-5.

A. Asensio Ramos, I. S. Requerey, and N. Vitas. Deepvel: Deep learning for the estimation of horizontal velocities at the solar surface. *Astronomy & Astrophysics*, 604:A11, Jul 2017. ISSN 1432-0746. doi: 10.1051/0004-6361/201730783. URL `http://dx.doi.org/10.1051/0004-6361/201730783`.

G. Aulanier. Coronal heating and flaring in QSLs. In D. Prasad Choudhary and K. G.

Strassmeier, editors, *Physics of Sun and Star Spots*, volume 273 of *IAU Symposium*, pages 233–241, August 2011. doi: 10.1017/S1743921311015304.

G. Aulanier, E. E. DeLuca, S. K. Antiochos, R. A. McMullen, and L. Golub. The Topology and Evolution of the Bastille Day Flare. *ApJ*, 540(2):1126–1142, Sep 2000. doi: 10.1086/309376.

A. A. Ballegooijen, N. P. Cartledge, and E. Priest. Magnetic flux transport and the formation of filament channels on the sun. *The Astrophysical Journal*, 501:866–881, 1998.

J. M. Banda and R. A. Angryk. Unsupervised learning techniques for detection of regions of interest in solar images. In *2015 IEEE International Conference on Data Mining Workshop (ICDMW)*, pages 582–588, 2015. doi: 10.1109/ICDMW.2015.61.

G. Barnes, N. Schanche, K. D. Leka, A. Aggarwal, and K. Reeves. A comparison of classifiers for solar energetic events. *Proceedings of the International Astronomical Union*, 12(S325):201–204, 2016. doi: 10.1017/S1743921316012758.

L. Beauregard, M. Verma, and C. Denker. Horizontal flows concurrent with an X2.2 flare in the active region NOAA 11158. *Astronomische Nachrichten*, 333(2):125, February 2012. doi: 10.1002/asna.201111631.

M. A. Berger. Structure and stability of constant-alpha force-free fields. *Astrophys. J. Suppl.*, 59:433–444, November 1985. doi: 10.1086/191079.

T. Birsan and D. Tiba. One hundred years since the introduction of the set distance by dimitrie pompeiu. In F. Ceragioli, A. Dontchev, H. Futura, K. Marti, and L. Pandolfi, editors, *System Modeling and Optimization*, pages 35–39, Boston, MA, 2006. Springer US. ISBN 978-0-387-33006-8.

M. G. Bobra and S. Couvidat. Solar Flare Prediction Using SDO/HMI Vector Magnetic Field Data with a Machine-learning Algorithm. *ApJ*, 798(2):135, Jan 2015. doi: 10.1088/0004-637X/798/2/135.

T. J. Bogdan and B. C. Low. The Three-dimensional Structure of Magnetostatic Atmospheres. II. Modeling the Large-Scale Corona. *Astrophys. J.*, 306:271, July 1986. doi: 10.1086/164341.

T. N. Bungey, V. S. Titov, and E. R. Priest. Basic topological elements of coronal magnetic fields. *A&A*, 308:233–247, April 1996.

P. Bushby and J. Mason. Understanding the solar dynamo. *Astronomy & Geophysics*, 45(4):4.7–4.13, 08 2004. ISSN 1366-8781. doi: 10.1046/j.1468-4004.2003.45407.x. URL `https://doi.org/10.1046/j.1468-4004.2003.45407.x`.

J. Canny. A computational approach to edge detection. *IEEE Transactions on Pattern Analysis and Machine Intelligence*, PAMI-8(6):679–698, 1986. doi: 10.1109/TPAMI.1986.4767851.

H. Carmichael. *A Process for Flares*, volume 50, page 451. 1964.

F. Chollet et al. Keras. https://github.com/fchollet/keras, 2015.

E. L. Chupp, D. J. Forrest, P. R. Higbie, A. N. Suri, C. Tsai, and P. P. Dunphy. Solar Gamma Ray Lines observed during the Solar Activity of August 2 to August 11, 1972. *Nature*, 241(5388):333–335, February 1973. doi: 10.1038/241333a0.

R. Close, C. Parnell, and E. Priest. Separators in 3d quiet-sun magnetic fields. *Solar Physics*, 225:21–46, 11 2004. doi: 10.1007/s11207-004-3259-0.

T. Colak and R. Qahwaji. Automated solar activity prediction: A hybrid computer platform using machine learning and solar imaging for automated prediction of solar flares. *Space Weather*, 7:12, 06 2009. doi: 10.1029/2008SW000401.

Y. Le Cun, B. Boser, J. S. Denker, R. E. Howard, W. Habbard, L. D. Jackel, and D. Henderson. *Handwritten Digit Recognition with a Back-Propagation Network*, page 396–404. Morgan Kaufmann Publishers Inc., San Francisco, CA, USA, 1990. ISBN 1558601007.

I. De Moortel and P. Browning. Recent advances in coronal heating. *Philosophical Transactions of the Royal Society A: Mathematical, Physical and Engineering Sciences*, 373(2042):20140269, May 2015. ISSN 1471-2962. doi: 10.1098/rsta.2014.0269. URL `http://dx.doi.org/10.1098/rsta.2014.0269`.

P. Demoulin, L. G. Bagala, C. H. Mandrini, J. C. Henoux, and M. G. Rovira. Quasi-separatrix layers in solar flares. II. Observed magnetic configurations. *A&A*, 325: 305–317, September 1997.

S. K. Dhakal and J. Zhang. Evolution of ARs with contrasting sunspot areas and contrasting flare activity. In *Solar Heliospheric and INterplanetary Environment (SHINE 2018)*, page 156, July 2018.

M. . Dubuisson and A. K. Jain. A modified hausdorff distance for object matching. In *Proceedings of 12th International Conference on Pattern Recognition*, volume 1, pages 566–568 vol.1, 1994. doi: 10.1109/ICPR.1994.576361.

S.J. Edwards. *On the topology of global coronal magnetic fields*. PhD thesis, University of St Andrews, 2014.

ESA. Anatomy of our sun. `https://www.esa.int/ESA_Multimedia/Images/2019/10/Anatomy_of_our_Sun`, 2019.

F. Fárník and S. K. Savy. Soft X-Ray Pre-Flare Emission Studied in Yohkoh-SXT Images. *Solar Phys.*, 183(2):339–357, December 1998. doi: 10.1023/A:1005092927592.

F. Fárník, H. Hudson, and T. Watanabe. Spatial Relations between Preflares and Flares. *Solar Phys.*, 165(1):169–179, April 1996. doi: 10.1007/BF00149096.

L. Fletcher and H. Hudson. The magnetic structure and generation of euv flare ribbons. *Solar Physics*, 204:69–89, 2001. doi: 10.1023/A:1014275821318.

L. Fletcher, B. R. Dennis, H. S. Hudson, S. Krucker, K. Phillips, A. Veronig, M. Battaglia, L. Bone, A. Caspi, Q. Chen, P. Gallagher, P. T. Grigis, H. Ji, W. Liu, R. O. Milligan, and M. Temmer. An observational overview of solar flares. *Space Science Reviews*, 159(1):19, Aug 2011. ISSN 1572-9672. doi: 10.1007/s11214-010-9701-8. URL `https://doi.org/10.1007/s11214-010-9701-8`.

Sébastien Galtier. *Introduction to Modern Magnetohydrodynamics*. Cambridge University Press, 2016. doi: 10.1017/CBO9781316665961.

G. A. Gary. Plasma Beta above a Solar Active Region: Rethinking the Paradigm. *Solar Phys.*, 203(1):71–86, October 2001. doi: 10.1023/A:1012722021820.

V. S. Gorbachev and B. V. Somov. Photospheric vortex flows as a cause for two-ribbon flares - A topological model. *SolPhys*, 117:77–88, March 1988. doi: 10.1007/BF00148574.

S. Guastavino, M. Piana, A. M. Massone, R. Schwartz, and F. Benvenuto. Desaturating SDO/AIA Observations of Solar Flaring Storms. *Astrophys. J.*, 882(2):109, September 2019. doi: 10.3847/1538-4357/ab35d8.

Q. Hao, C. Fang, and P. F. Chen. Developing an Advanced Automated Method for Solar Filament Recognition and Its Scientific Application to a Solar Cycle of

MLSO Hα Data. *Solar Phys.*, 286(2):385–404, September 2013. doi: 10.1007/s11207-013-0285-9.

R Hecht-Nielson. Theory of the backpropagation neural network. *International 1989 Joint Conference on Neural Networks*, 1:593–605, 1989. doi: 10.1109/IJCNN.1989.118638.

G. E. Hinton, N. Srivastava, A. Krizhevsky, I. Sutskever, and R. R. Salakhutdinov. Improving neural networks by preventing co-adaptation of feature detectors. *arXiv e-prints*, art. arXiv:1207.0580, July 2012.

T. Hirayama. Theoretical Model of Flares and Prominences. I: Evaporating Flare Model. *Solar Phys.*, 34(2):323–338, February 1974. doi: 10.1007/BF00153671.

Y. Hou, T. Li, S. Yang, and J. Zhang. A Secondary Fan-spine Magnetic Structure in Active Region 11897. *ApJ*, 871(1):4, Jan 2019. doi: 10.3847/1538-4357/aaf4f4.

H. S. Hudson. Thick-Target Processes and White-Light Flares. *Solar Phys.*, 24(2):414–428, June 1972. doi: 10.1007/BF00153384.

N. Hurlburt, M. Cheung, C. Schrijver, L. Chang, S. Freeland, S. Green, C. Heck, A. Jaffey, A. Kobashi, D. Schiff, J. Serafin, R. Seguin, G. Slater, A. Somani, and R. Timmons. Heliophysics Event Knowledgebase for the Solar Dynamics Observatory (SDO) and Beyond. *SolPhys*, 275(1-2):67–78, January 2012. doi: 10.1007/s11207-010-9624-2.

S. Inoue, K. Hayashi, T. Magara, G. S. Choe, and Y. D. Park. Magnetohydrodynamic Simulation of the X2.2 Solar Flare on 2011 February 15. I. Comparison with the Observations. *ApJ*, 788(2):182, June 2014. doi: 10.1088/0004-637X/788/2/182.

J.D. Jackson. *Classical Electrodynamics*. Wiley, 1975.

M. Janvier, A. Savcheva, E. Pariat, S. Tassev, S. Millholland, V. Bommier, P. McCauley, S. McKillop, and F. Dougan. Evolution of flare ribbons, electric currents, and quasi-separatrix layers during an X-class flare. *A&A*, 591:A141, Jul 2016. doi: 10.1051/0004-6361/201628406.

Janvier, M., Aulanier, G., Pariat, E., and Démoulin, P. The standard flare model in three dimensions - iii. slip-running reconnection properties. *A&A*, 555:A77, 2013. doi: 10.1051/0004-6361/201321164. URL `https://doi.org/10.1051/0004-6361/201321164`.

jefkine. Backpropagation in convolutional neural networks, 2016. URL `https://www.jefkine.com/general/2016/09/05/backpropagation-in-convolutional-neural-networks/`.

M. D. Kazachenko, B. J. Lynch, B. T. Welsch, and X. Sun. A Database of Flare Ribbon Properties from the Solar Dynamics Observatory. I. Reconnection Flux. *Astrophysical Journal*, 845:49, August 2017. doi: 10.3847/1538-4357/aa7ed6.

M.D. Kazachenko, B. J Lynch, B. T. Welsch, and X. Sun. A database of flare ribbon properties from the solar dynamics observatory. i. reconnection flux. *ApJ*, 845, 2017.

R. A. Kopp and G. W. Pneuman. Magnetic reconnection in the corona and the loop prominence phenomenon. *Solar Phys.*, 50(1):85–98, October 1976. doi: 10.1007/BF00206193.

A. Krizhevsky, I. Sutskever, and G. E. Hinton. Imagenet classification with deep convolutional neural networks. *Commun. ACM*, 60(6):84–90, May 2017. ISSN 0001-0782. doi: 10.1145/3065386. URL `https://doi.org/10.1145/3065386`.

A. Kucuk, J. Banda, and R. Angryk. Solar Event Classification Using Deep Convolutional Neural Networks. 06 2017. doi: 10.1007/978-3-319-59063-9_11.

D. A. Lacatus, A. Donea, and P. G. Judge. The March 11, 2015 X2.1 flare: peculiar post-flare spectral signatures. In *Solar Heliospheric and INterplanetary Environment (SHINE 2016)*, page 207, July 2016.

K. R. Lang. Solar flare model. `https://ase.tufts.edu/cosmos/view_picture.asp?id=660`, 2010.

Y. LeCun, Y. Bengio, and G. Hinton. Deep learning. *Nature*, 521:436–44, 05 2015a. doi: 10.1038/nature14539.

Yann LeCun and Yoshua Bengio. *Convolutional Networks for Images, Speech, and Time Series*, page 255–258. MIT Press, Cambridge, MA, USA, 1998. ISBN 0262511029.

Yann LeCun, Yoshua Bengio, and Geoffrey Hinton. Deep learning. *Nature*, 521(7553): 436–444, May 2015b.

R. B. Leighton. The solar granulation. *Annual Review of Astronomy and Astrophysics*, 1(1):19–40, 1963. doi: 10.1146/annurev.aa.01.090163.000315. URL `https://doi.org/10.1146/annurev.aa.01.090163.000315`.

R. Li, Y. Cui, H. He, and H. Wang. Application of support vector machine combined with K-nearest neighbors in solar flare and solar proton events forecasting. *Advances in Space Research*, 42(9):1469–1474, November 2008. doi: 10.1016/j.asr.2007.12.015.

C. Liu, J. Lee, and H. Wang. The Eruption of Outer Spine-like Loops Leading to a Double-Stage Circular-Ribbon Flare. In *American Astronomical Society Meeting Abstracts #234*, volume 234 of *American Astronomical Society Meeting Abstracts*, page 204.05, June 2019.

C. Liu, A. Prasad, J. Lee, and H. Wang. An Eruptive Circular-ribbon Flare with Extended Remote Brightenings. *ApJ*, 899(1):34, August 2020. doi: 10.3847/1538-4357/ab9cbe.

W. Liu, T. E. Berger, A. M. Title, T. D. Tarbell, and B. C. Low. CHROMOSPHERIC JET AND GROWING "LOOP" OBSERVED BYHINODE: NEW EVIDENCE OF FAN-SPINE MAGNETIC TOPOLOGY RESULTING FROM FLUX EMERGENCE. *The Astrophysical Journal*, 728(2):103, jan 2011. doi: 10.1088/0004-637x/728/2/103. URL `https://doi.org/10.1088/0004-637x/728/2/103`.

Y. Liu and P. W. Schuck. Magnetic Energy and Helicity in Two Emerging Active Regions in the Sun. *ApJ*, 761(2):105, December 2012. doi: 10.1088/0004-637X/761/2/105.

T. Love, T. Neukirch, and C. E. Parnell. Analyzing aia flare observations using convolutional neural networks. *Frontiers in Astronomy and Space Sciences*, 7:34, 2020. ISSN 2296-987X. doi: 10.3389/fspas.2020.00034. URL `https://www.frontiersin.org/article/10.3389/fspas.2020.00034`.

B. C. Low. Three-dimensional Structures of Magnetostatic Atmospheres. III. A General Formulation. *Astrophys. J.*, 370:427, March 1991. doi: 10.1086/169829.

C. H. Mandrini, P. Demoulin, J. C. Henoux, and M. E. Machado. Evidence for the interaction of large scale magnetic structures in solar flares. *A&A*, 250:541–547, October 1991.

C. H. Mandrini, M. G. Rovira, P. Demoulin, J. C. Henoux, M. E. Machado, and L. K. Wilkinson. Evidence for magnetic reconnection in large-scale magnetic structures in solar flares. *A&A*, 272:609, May 1993.

S. Masson, E. Pariat, G. Aulanier, and C. J. Schrijver. The Nature of Flare Ribbons in Coronal Null-Point Topology. *Astrophysical Journal*, 700:559–578, July 2009. doi: 10.1088/0004-637X/700/1/559.

R. A. Maurya, P. Vemareddy, and A. Ambastha. Velocity and Magnetic Transients Driven by the X2.2 White-light Flare of 2011 February 15 in NOAA 11158. *ApJ*, 747(2):134, March 2012. doi: 10.1088/0004-637X/747/2/134.

V. Nair and G. E. Hinton. Rectified linear units improve restricted boltzmann machines. In *Proceedings of the 27th International Conference on International Conference on Machine Learning*, ICML'10, page 807–814, Madison, WI, USA, 2010. Omnipress. ISBN 9781605589077.

T. Neukirch. On self-consistent three-dimensional analytic solutions of the magnetohydrostatic equations. *Astronomy and Astrophysics*, 301:628, 08 1995.

C. E. Parnell, J. M. Smith, T. Neukirch, and E. R. Priest. The structure of three-dimensional magnetic neutral points. *Physics of Plasmas*, 3(3):759–770, 1996. doi: 10.1063/1.871810. URL `https://doi.org/10.1063/1.871810`.

J. Pellerin. *Accounting for the geometrical complexity of geological structural models in Voronoi-based meshing methods*. PhD thesis, 03 2014.

W. D. Pesnell, B. J. Thompson, and P. C. Chamberlin. The Solar Dynamics Observatory (SDO). *SolPhys*, 275(1-2):3–15, January 2012. doi: 10.1007/s11207-011-9841-3.

G. J. D. Petrie. A Spatio-temporal Description of the Abrupt Changes in the Photospheric Magnetic and Lorentz-Force Vectors During the 15 February 2011 X2.2 Flare. *SolPhys*, 287(1-2):415–440, October 2013. doi: 10.1007/s11207-012-0071-0.

Phung and Rhee. A high-accuracy model average ensemble of convolutional neural networks for classification of cloud image patches on small datasets. *Applied Sciences*, 9:4500, 10 2019. doi: 10.3390/app9214500.

S. J. Platten, C. E. Parnell, A. L. Haynes, E. R. Priest, and D. H. Mackay. The solar cycle variation of topological structures in the global solar corona. *A&A*, 565:A44, May 2014. doi: 10.1051/0004-6361/201323048.

Platten, S. J., Parnell, C. E., Haynes, A. L., Priest, E. R., and Mackay, D. H. The solar cycle variation of topological structures in the global solar corona. *A&A*, 565:

A44, 2014. doi: 10.1051/0004-6361/201323048. URL `https://doi.org/10.1051/0004-6361/201323048`.

D. Pontin, K. Galsgaard, and P. Démoulin. Why Are Flare Ribbons Associated with the Spines of Magnetic Null Points Generically Elongated? *SolPhys*, 291:1739–1759, August 2016. doi: 10.1007/s11207-016-0919-9.

David Pontin, Eric Priest, and Klaus Galsgaard. On the nature of reconnection at a solar coronal null point above a separatrix dome. *The Astrophysical Journal*, 774, 07 2013. doi: 10.1088/0004-637X/774/2/154.

E. R. Priest and P. Démoulin. Three-dimensional magnetic reconnection without null points. 1. Basic theory of magnetic flipping. *JGR*, 100:23443–23464, December 1995. doi: 10.1029/95JA02740.

E. R. Priest and V. S. Titov. Magnetic reconnection at three-dimensional null points. *Philosophical Transactions: Mathematical, Physical and Engineering Sciences*, 354 (1721):2951–2992, 1996. ISSN 1364503X. URL `http://www.jstor.org/stable/54745`.

Eric Priest. *Magnetohydrodynamics of the Sun.* Cambridge University Press, 2014. doi: 10.1017/CBO9781139020732.

Y. Qiu, Y. Guo, M. Ding, and Z. Zhong. The Magnetic Topology and Eruption Mechanism of a Multiple-ribbon Flare. *ApJ*, 901(1):13, September 2020. doi: 10.3847/1538-4357/abae5b.

H. A. S. Reid, N. Vilmer, G. Aulanier, and E. Pariat. X-ray and ultraviolet investigation into the magnetic connectivity of a solar flare. *Astron. Astrophys.*, 547:A52, November 2012. doi: 10.1051/0004-6361/201219562.

Ihab S. Mohamed. *Detection and Tracking of Pallets using a Laser Rangefinder and Machine Learning Techniques.* PhD thesis, 09 2017.

A. Savcheva, E. Pariat, S. McKillop, P. McCauley, E. Hanson, Y. Su, E. Werner, and E. E. DeLuca. The Relation between Solar Eruption Topologies and Observed Flare Features. I. Flare Ribbons. *ApJ*, 810(2):96, Sep 2015. doi: 10.1088/0004-637X/810/2/96.

K. H. Schatten, J. M. Wilcox, and N. F. Ness. A model of interplanetary and coronal magnetic fields. *Solar Physics*, 6(3):442–455, Mar 1969. ISSN 1573-093X. doi: 10.1007/BF00146478. URL `https://doi.org/10.1007/BF00146478`.

J. Schou, P. H. Scherrer, R. I. Bush, R. Wachter, S. Couvidat, M. C. Rabello-Soares, R. S. Bogart, J. T. Hoeksema, Y. Liu, T. L. Duvall, D. J. Akin, B. A. Allard, J. W. Miles, R. Rairden, R. A. Shine, T. D. Tarbell, A. M. Title, C. J. Wolfson, D. F. Elmore, A. A. Norton, and S. Tomczyk. Design and Ground Calibration of the Helioseismic and Magnetic Imager (HMI) Instrument on the Solar Dynamics Observatory (SDO). *Solar Phys.*, 275(1-2):229–259, January 2012. doi: 10.1007/s11207-011-9842-2.

C. J. Schrijver, G. Aulanier, A. M. Title, E. Pariat, and C. Delannée. The 2011 February 15 X2 Flare, Ribbons, Coronal Front, and Mass Ejection: Interpreting the Three-dimensional Views from the Solar Dynamics Observatory and STEREO Guided by Magnetohydrodynamic Flux-rope Modeling. *ApJ*, 738(2):167, September 2011. doi: 10.1088/0004-637X/738/2/167.

M. A. Schuh, R. A. Angryk, K. G. Pillai, J. M. Banda, and P. C. Martens. A large-scale solar image dataset with labeled event regions. In *2013 IEEE International Conference on Image Processing*, pages 4349–4353, 2013. doi: 10.1109/ICIP.2013.6738896.

R. A. Schwartz, G. Torre, A. M. Massone, and M. Piana. DESAT: A Solar SoftWare tool for image de-saturation in the Atmospheric Image Assembly onboard the Solar Dynamics Observatory. *Astronomy and Computing*, 13:117–123, November 2015. doi: 10.1016/j.ascom.2015.10.006.

Paulo J. A. Simões, Hamish A. S. Reid, Ryan O. Milligan, and Lyndsay Fletcher. The spectral content of sdo/aia 1600 and 1700 å filters from flare and plage observations. *The Astrophysical Journal*, 870(2):114–128, January 2019. ISSN 0004-637X. doi: 10.3847/1538-4357/aaf28d.

K. Simonyan and A. Zisserman. Very Deep Convolutional Networks for Large-Scale Image Recognition. *arXiv e-prints*, art. arXiv:1409.1556, Sep 2014.

E. J. Smith. The heliospheric current sheet. *Journal of Geophysical Research: Space Physics*, 106(A8):15819–15831, 2001. doi: https://doi.org/10.1029/2000JA000120. URL `https://agupubs.onlinelibrary.wiley.com/doi/abs/10.1029/2000JA000120`.

I. Sobel and G. Feldman. A 3×3 isotropic gradient operator for image processing. *Pattern Classification and Scene Analysis*, pages 271–272, 01 1973.

M. Sobotka, J. Dudík, C. Denker, H. Balthasar, J. Jurčák, W. Liu, T. Berkefeld, M. Collados Vera, A. Feller, A. Hofmann, F. Kneer, C. Kuckein, A. Lagg, R. E. Louis, O. von der Lühe, H. Nicklas, R. Schlichenmaier, D. Schmidt, W. Schmidt, M. Sigwarth, S. K. Solanki, D. Soltau, J. Staude, K. G. Strassmeier, R. Volkmer, and T. Waldmann. Slipping reconnection in a solar flare observed in high resolution with the GREGOR solar telescope. *A&A*, 596:A1, November 2016. doi: 10.1051/0004-6361/201527966.

Y. Song and H. Tian. Investigation of White-light Emission in Circular-ribbon Flares. *ApJ*, 867(2):159, November 2018. doi: 10.3847/1538-4357/aae5d1.

E. A. Spiegel and J. P. Zahn. The solar tachocline. *Astron. Astrophys.*, 265:106–114, November 1992.

P. A. Sturrock. Model of the High-Energy Phase of Solar Flares. *Natur*, 211:695–697, August 1966. doi: 10.1038/211695a0.

X. Sun, J. T. Hoeksema, Y. Liu, Q. Chen, and K. Hayashi. A Non-radial Eruption in a Quadrupolar Magnetic Configuration with a Coronal Null. *ApJ*, 757(2):149, October 2012a. doi: 10.1088/0004-637X/757/2/149.

X. Sun, J. T. Hoeksema, Y. Liu, T. Wiegelmann, K. Hayashi, Q. Chen, and J. Thalmann. Evolution of Magnetic Field and Energy in a Major Eruptive Active Region Based on SDO/HMI Observation. *ApJ*, 748(2):77, April 2012b. doi: 10.1088/0004-637X/748/2/77.

X. Sun, J. T. Hoeksema, Y. Liu, G. Aulanier, Y. Su, I. G. Hannah, and R. A. Hock. Hot Spine Loops and the Nature of a Late-phase Solar Flare. *Astrophys. J.*, 778(2): 139, December 2013. doi: 10.1088/0004-637X/778/2/139.

X. Sun, J. T. Hoeksema, Y. Liu, and J. Zhao. On Polar Magnetic Field Reversal and Surface Flux Transport During Solar Cycle 24. *Astrophys. J.*, 798(2):114, January 2015. doi: 10.1088/0004-637X/798/2/114.

I. Sutskever, J. Martens, G. Dahl, and G. Hinton. On the importance of initialization and momentum in deep learning. In Sanjoy Dasgupta and David McAllester, editors, *Proceedings of the 30th International Conference on Machine Learning*, volume 28 of *Proceedings of Machine Learning Research*, pages 1139–1147, Atlanta, Georgia, USA, 17–19 Jun 2013. PMLR. URL `http://proceedings.mlr.press/v28/sutskever13.html`.

C. Szegedy, W. Liu, Y. Jia, P. Sermanet, S. Reed, D. Anguelov, D. Erhan, V. Vanhoucke, and A. Rabinovich. Going deeper with convolutions. In *The IEEE Conference on Computer Vision and Pattern Recognition (CVPR)*, June 2015.

A. Tei, T. Sakaue, T. J. Okamoto, T. Kawate, P. Heinzel, S. UeNo, A. Asai, K. Ichimoto, and K. Shibata. Blue-wing enhancement of the chromospheric Mg II h and k lines in a solar flare. *ASJ*, 70(6):100, December 2018. doi: 10.1093/pasj/psy047.

V. Titov. Quasi-Separatrix Layers: Refined Theory and its Application to Solar Flares. In A. Wilson and et al., editors, *Magnetic Fields and Solar Processes*, volume 448 of *ESA Special Publication*, page 715, December 1999.

V. S. Titov, G. Hornig, and P. Démoulin. Theory of magnetic connectivity in the solar corona. *Journal of Geophysical Research: Space Physics*, 107(A8):SSH 3–1–SSH 3–13, 2002. doi: https://doi.org/10.1029/2001JA000278. URL `https://agupubs.onlinelibrary.wiley.com/doi/abs/10.1029/2001JA000278`.

V.S. Titov. Generalized Squashing Factors for Covariant Description of Magnetic Connectivity in the Solar Corona. *ApJ*, 660:863–873, May 2007. doi: 10.1086/512671.

P. Tree, L. Xu, L. Chen, Y. Yan, and L.Y. Duan. Mask-pix2pix network for overexposure region recovery of solar image. *Advances in Astronomy*, 2019:1–10, 09 2019. doi: 10.1155/2019/5343254.

B.M. Williams. *The dynamic topology of the Solar corona: mapping the Sun's three dimensional magnetic skeleton.* PhD thesis, University of St Andrews, 2018a.

D. R. Williams. Sun fact sheet. `https://nssdc.gsfc.nasa.gov/planetary/factsheet/sunfact.html`, 2018b.

Z. Xu, Y. Jiang, J. Yang, B. Yang, and Y. Bi. Rapid Penumbra and Lorentz Force Changes in an X1.0 Solar Flare. *ApJl*, 820(1):L21, March 2016. doi: 10.3847/2041-8205/820/1/L21.

J. Zhao, S. A. Gilchrist, G. Aulanier, B. Schmieder, E. Pariat, and H. Li. Hooked Flare Ribbons and Flux-rope Related QSL Footprints. *ApJ*, 825:80, July 2016. doi: 10.3847/0004-637X/825/1/80.

G. Zhou and J. Zhan. Observations of a large-scale chain solar activity. In *Solar Heliospheric and INterplanetary Environment (SHINE 2015)*, page 98, July 2015.

C. Zhu, J. Qiu, K. Yang, A. Takeda, and K. Yoshimura. Loop Heating in Recurrent Circular-Ribbon Flares. In *Solar Heliospheric and INterplanetary Environment (SHINE 2018)*, page 24, July 2018.

F. Zuccarello, S. L. Guglielmino, V. Capparelli, M. Mathioudakis, P. Keys, L. Fletcher, S. Criscuoli, M. Falco, and M. Murabito. Continuum emission enhancements and penumbral changes observed during flares by IRIS, ROSA, and Hinode. *Nuovo Cimento C Geophysics Space Physics C*, 42(1):13, January 2019. doi: 10.1393/ncc/i2019-19013-2.